Enabling Microscopic Simulators to Perform System-Level Analysis of Viscoelastic Flows

by

Zubair Anwar

B.Sc. Chemical Engineering
Georgia Institute of Technology (2002)

S.M. Chemical Engineering Practice
Massachusetts Institute of Technology (2004)

Submitted to the Department of Chemical Engineering
in partial fulfillment of the requirements for the degree of

Doctor of Philosophy in Chemical Engineering

at the

MASSACHUSETTS INSTITUTE OF TECHNOLOGY

May 2008

Author . . . .
Department of Chemical Engineering
May 20, 2008

Certified by. . . . .
Robert C. Armstrong
Chevron Professor of Chemical Engineering
Thesis Supervisor

Accepted by . . . .
William M. Deen
Professor of Chemical Engineering
Chairman, Committee for Graduate Students

Enabling Microscopic Simulators to Perform System-Level Analysis of Viscoelastic Flows

by

Zubair Anwar

Submitted to the Department of Chemical Engineering
on May 20, 2008, in partial fulfillment of the
requirements for the degree of
Doctor of Philosophy in Chemical Engineering

Abstract

State-of-the-art methods for simulating viscoelastic flows couple the conservation equations for mass and momentum with a model from kinetic theory that describes the microstructural state of the polymer. Introduction of appropriate numerical discretization and boundary conditions for these equations leads to a hybrid simulation for studying the dynamic behavior of polymeric liquids in complex geometries. This approach represents a rare example of a successful multiscale solution of a physical problem, as it allows investigation of arbitrary models of kinetic theory.

The simulations, however, are not amenable to standard numerical techniques for system-level stability, bifurcation, and control analysis as this requires closed form equations. These simulation either use stochastic descriptions for the polymer microstructure that cannot be reduced to closed form, or involve equations for the evolution of a distribution of polymer conformations, which can only be written in closed form by invoking mathematical closure approximations that can have a significant qualitative impact on the predictive ability of these simulations.

The focus of this thesis was to develop a novel numerical method that can enable hybrid simulations to perform system-level analysis of polymeric flows. This numerical approach has been applied directly to kinetic theory models and hybrid simulations to obtain stationary states and associated bifurcations and stability information. The method is general in its applicability in that it treats kinetic theory models and hybrid simulations as black boxes that are then used to obtain system-level information without any modification.

The methods developed here are illustrated in a variety of problems. Steady state results have been obtained for the non-interacting rigid dumbbell model in steady shear, and for the free-draining bead-spring chain model in both steady shear and uniaxial elongation that are in excellent agreement with previous studies and steady state computed from direct integration. The method is also applied to a hybrid simulation for the pressure-driven flow of non-interacting rigid dumbbells in a planar channel with a linear array of equally spaced cylinders. The computed steady state is in agreement with direct integration and qualitatively matches previous computations

with closed models.

Bifurcation analysis has been performed for the Doi model at equilibrium with the Onsager excluded volume potential. This analysis agrees with previous studies and accurately predicts the isotropic-nematic transition and turning point for the unstable to stable transition on the prolate solution branch. Bifurcation analysis has also been performed for the Doi model in the weak shear flow limit for the Maier-Saupe excluded volume potential. It is found that stable stationary solutions are lost at a limit point beyond which time-periodic tumbling orbits are the only stable solution. This transition occurs via an infinite period global bifurcation, while the limit point approaches a threshold value as the shear rate approaches zero. This result matches a recently published scaling analysis and demonstrates the ability of the method to provide general bifurcation analysis of kinetic theory models.

Stability analysis of the fiber-spinning process for polymeric fluids has also been performed by using a hybrid simulation that couples the one-dimensional conservation equations for mass and momentum with a stochastic description for the configuration fields of the Hookean dumbbell model. The steady-state velocity profiles are in good agreement with previous studies with the Oldroyd-B model. The analysis predicts onset of the draw resonance instability via a Hopf bifurcation and subsequent stabilization via second Hopf bifurcation in draw ratio parameter space. This result is in good agreement with experimentally observed behavior during polymer fiber-spinning.

Thesis Supervisor: Robert C. Armstrong
Title: Chevron Professor of Chemical Engineering

Dedicated to

Nasim Akhter and Mohammad Anwar,

and

Bushra Mahmood

my parents, and wife

Acknowledgments

I find myself a very different person from the time I walked onto MIT campus, definitely having changed for the better. Working on this thesis got frustrating at times, but such moments were always followed by something to rejoice. While I was afforded an opportunity to develop greater depth of understanding about a scientific topic, there were several lessons provided by the process of carrying out doctoral research that should serve me well for the rest of my life. The foremost lesson was taught to me by my advisor, Prof. Armstrong. His mild and calm nature and disposition has been absolutely contagious, a trait that can be so useful when dealing with any challenge. On top of that, he has been thoroughly supportive of my efforts, and always given me the freedom to try things out and chart my own path. For that I will always be indebted to him. I would like to thank my committee member, Professors Yip and Doyle, for their helpful advice and input, and for finding time from their busy schedule to meet. I would also like to thank all the assistants Bob had over the years, Melanie, Margaret, Katie, Alina, and Patty, who made sure I continued to meet Bob despite all his engagements.

A special thank you goes to Arvind, for helping me get started on research and for teaching me about kinetic theory. I can't even remember how many times I've bugged him with questions, and every single time he not only accomodated me but I walked away having learned something new. It was a lot of fun to collaborate, and I'll always be grateful for his suggestion of a great problem to develop my thesis.

I am also indebted to David, who was an excellent sounding board as I tried out different things in my thesis. His understanding of numerical linear algebra, and transport phenomenon is remarkable and I'm sure I'll be hearing good things about him in the near future.

Life at MIT would not have been so much fun without great friends like Saif, Adnan, Zaid, and Faisal Kashif, who were there in happiness and sorrow. Faisal Kashif was always willing to make his excellent chai, and spend hours discussing the vagaries of life. Thank you for all the great conversations we've had over the years.

When I felt like leaving MIT or Boston, Zubair Pasha and Faisal Kassim were always there, with the latter always more eager. His passion to drive and my need to get some respite from MIT was a perfect combination. I was saddened when he decided to leave US, but am glad he's now part of family.

Words can never describe the support, encouragement, and prayers of my family: ammi, abu, shanda, and baji. Their sacrifices have been immense in the entire period. Just hearing ammi's voice on the phone was sufficient to achieve calmness, while abu's advice was instrumental is helping me develop better judgement. Truly, I don't know where I would be without their support.

Finally, I would like to thank my wife, Bushra, for her love, support, encouragment, and inspiration. She put her academic career on hold for me, and continued to support me when I struggled, and things got difficult. Despite all obstacles and adversities, she has stood by me during thick and thin, and I hope to give her a better life as we move to New Jersey. Bushra is by far the best thing that has ever happened to me, and having started our life together at MIT, I look forward to more exciting times ahead.

Contents

List of Figures

14

18

List of Tables

Chapter 1

Introduction

1.1 Polymer Processing

In popular usage the word polymer is often understood to mean plastic, a material that is fairly ubiquitous in the twenty first century. Common examples include items of daily usage, such as food containers, soft-drink bottles, toys, sports equipment etc. In addition to consumer goods, plastics are also used extensively in high-tech engineering applications, such as aerospace parts, as components of high-speed machinery, and housings for electronic devices. This diversity of application stems from the diverse mechanical and thermal properties of the finished product. The word polymer, however, is not restricted to refer to plastics and synthetic materials only, since polymers also exist naturally. These are often called bio-polymers and include materials such as natural rubber, ivory, amber, protein-based polymers such as DNA, and cellulosic based materials. The common feature of all polymers, whether synthetic or natural, is that they are composed of molecules with very large molecular mass that results from chemical bonding of a large number of repeating units or *monomers*. A simple example is that of polyethylene with ethylene as the repeating unit in the polymer molecule.

Initial interest in polymers originated from the ability to cheaply create synthetic materials of complicated shapes and good appearance with relative ease. While chemistry dictates the potential properties such materials can possess, it is inevitably the

processing that determines whether those properties can be realized in an economically feasible manner. To that end, advances in polymer processing have led to the creation of materials with versatile performance and appearance. Examples include polymeric fibers of considerable slenderness and strength created by fiber-spinning and electro-spinning processes, compact discs with intricate features on the order of a micron that are created using injection molding, and multilayer films and sheets that can be formed by using the co-extrusion process. These processes typically involve heating the polymers above their glass transition or melting temperatures, followed by some forming process, such as extrusion or drawing, and subsequent cooling to obtain the desired shape. At that point, the crystallization and molecular orientation of the polymer that results from the processing history dominates the material properties and performance of the finished product. Clearly, how the polymer flows in the molten state or in solution significantly affects the processing conditions that can be imposed on it. For this reason, fluid dynamics of polymers plays a pivotal role in accurately understanding the effect of various polymer processes on final product properties.

Advances in polymer processing have significantly increased the complexity of the flows that are imposed on a given polymer. This complexity emerges either in the form of a complex geometry through which the polymer is being processed or in terms of processing conditions, such as high extrusion rates. More recently, there is also a greater desire to understand how natural polymers such as DNA flow in novel processing geometries that have been designed for biomedical applications. The major challenge posed by these processes is the ability to describe how the microstructure of polymer molecules evolves in a given process. Polymer molecules are by definition large molecules, often consisting of 10,000 monomer units in a single polymer chain. This property leads to significantly different flow behavior when compared with standard Newtonian fluids, such as water. For example, in the molten state a polymer molecule may either be stiff or flexible depending on the chemical nature of the monomer units, their physical arrangement, and the resulting forces they experience from neighboring molecules. These forces could arise either due to

excluded volume effects or entanglements among polymer molecules. Even in a dilute solution, polymer molecules take a finite time to respond to changes in the bulk flow depending on how the polymer structure adjusts to the prevalent flow field. For this reason, any attempt at understanding how polymeric materials flow, must take into account the structure of the fluid, as opposed to the ideal of structureless, small–molecule fluids, and how stresses develop in these fluids as a result of some imposed deformation.

The science of rheology addresses this primary issue of how flow-induced deformation affects fluid behavior. Even though rheologists study a wide variety of materials, polymers have been found to be the most interesting and complex. Rheology recognizes that the stresses that may develop in polymeric fluids can have a nonlinear or temporal dependence on the rate of deformation, or both. This behavior is strikingly different from that of Newtonian fluids where stress depends linearly and instantaneously on the rate of deformation. As a result, polymeric materials are also known as *non-Newtonian* fluids, and non-Newtonian fluid dynamics then focuses on rheologically complex flows typical of most laboratory and polymer processing operations. Even though the science of rheology may focus on specific flows that are designed to measure material properties for developing better molecular theories, non-Newtonian fluid dynamics aims to study more general flows. As a consequence, such an approach invariably requires numerical methods and computational techniques, since analytical solutions can rarely be obtained. This is exactly the focus of this thesis, as it introduces a new numerical approach that furthers the ability of state-of-the-art methods for studying complex polymeric flows.

1.2 Computational Rheology

The field of computational rheology is concerned with the design, implementation, and use of numerical methods for the computer simulation of the flow of non-Newtonian fluids in complex geometries [56]. Even though the field has been under development for more than 30 years, it has only recently begun to reach a state of relative

maturity. Earlier efforts to model the flows of polymers took a continuum approach by assuming that the macroscopic features of polymer behavior could be described without a detailed consideration of molecular configuration. The microstructure is assumed to exist over a sufficiently small spatial scale to permit averaging and the use of a continuum approximation. This approach was inspired by the approach taken to model Newtonian fluids where a linear relationship between fluid stresses and deformation rate is sufficient to describe the flow behavior without any knowledge of the behavior of the molecules that make up the fluid. Non-Newtonian fluid dynamics, therefore, makes use of a *constitutive equation* that relates the stress tensor to the rate of deformation. When combined with the conservation laws for mass and momentum, the constitutive equation yields a coupled set of partial differential or integro-differential field equations that must be solved for a specified flow geometry and defined boundary conditions.

In most cases the constitutive equations are not connected with the underlying microstructure and therefore have diverse predictive ability. An exception to this are equations that although continuum in form, have some basis in molecular theory as they are derived in terms of certain averages of the distribution of polymer conformations within a macroscopic fluid element. Despite their basis in molecular theory, such equations invariably make use of mathematical closure approximations for these averages that can have a significant qualitative impact [109] on their predictive ability.

Despite these significant drawbacks, large scale simulations of polymeric flow that use the continuum approach have led to significant accomplishments in describing the stresses and velocities that develop in complicated geometries. A variety of polymeric flow behavior and non-trivial problems have been modelled with this approach even though the continuum constitutive models in use give rise to stress boundary layers and singularities in complex flow geometries [57]. The nonlinear qualitative behavior of the resulting solutions can indeed be very rich. Most importantly, however, the formidable mathematical and numerical challenges posed by this approach and the advantage of solving for a limited number of variables (pressure, the components of velocity and stress) make continuum modelling the mainstream of the discipline even

28

today.

As already discussed, the interesting behavior of polymeric liquids is primarily due to their underlying molecular structure. Liquid crystal fibers, for example, gain their strength from the extremely high degree of molecular alignment induced during processing, while many coating polymers such as those contained in paints and adhesives derive their properties from a carefully engineered lack of molecular alignment. Hence, it seems natural to incorporate molecular information in complex flow simulations, which is exactly the focus in the emerging and complementary *micro-macro* or *hybrid* approach to polymeric flow modelling. In this approach, the equations for the evolution of polymer microstructure are directly coupled to the field equations for mass and momentum conservation. The evolution equation for the the microstructure is typically available in the form of a Fokker-Planck equation from polymer kinetic theory or an equivalent stochastic description. Whereas earlier efforts with this approach were restricted to elementary flow fields, such as plane Couette flow and well-understood molecular models, the approach has shown great promise when extended to more complex flows and kinetic theory models with better description of the polymer microstructure, since the approach circumvents the need to invoke mathematical closure approximations of doubtful validity.

Despite this significant advantage, the hybrid approach is more demanding in computer resources than the continuum approach. This can be easily understood by considering the rigid dumbbell molecular model, which describes the behavior of a rigid rod with a fixed length. This model molecule can neither stretch nor entangle and hence has only two orientational degrees of freedom. Typically $\mathcal{O}(10)$ discretization points are needed in orientation space for each degree of freedom to accurately capture the distribution that describes the probable orientation of the large number of molecules within a fluid element. This leads to $\mathcal{O}(100)$ discrete equations that must be solved at each material point in a flow geometry. If we contrast this with the continuum approach that only requires solution of six components of the stress at each spatial point, it is immediately obvious that a move from continuum to even the simplest of molecular models leads to a significant increase in computational

resources. Although this may not have been feasible in the past, computational resources have increased significantly in the last decade and a half to allow preliminary computations of 3D transient flows with elementary models of kinetic theory [89] and more detailed computations of 2D transient flows with kinetic theory models that incorporate significantly larger degrees of freedom for the microstructural model [61]. More importantly, work has also been carried out to predict the inception of flow instabilities in plane Couette flow using the hybrid approach without having to resort to closed form constitutive equations [102].

While these results represent significant developments in polymer flow modelling, the hybrid approach is currently unsuitable for true system-level analysis of polymer flows, which requires a closed set of equations to yield detailed information, i.e. bifurcations and stability of the computed solutions. As such, by avoiding closure approximations, the model is rendered unamenable to system-level stability, operability, bifurcation, parameter sensitivity, design and control analysis that standard numerical techniques allow. For example, the work done to predict inception of polymeric flow instabilities makes use of precise time-dependent computations to carry out linear stability analyses by deriving linearized equations for the perturbation to a Fokker-Planck equation. Although this may be reasonable for a simple molecular model, the approach is clearly infeasible for kinetic theory models with larger internal degrees of freedom. Also, the method does not provide for a general approach to obtaining a sequence of solutions that may be otherwise be possible with closed-form equations. Hence, having developed stable and efficient algorithms to carry out hybrid simulations, there is then a clear need for algorithms and numerical methods that may bridge the gap between state-of-the-art simulations and system-level analysis to elucidate the nonlinear coupling between rheological behavior, flow-induced evolution of the microstructure, flow parameters (such as geometry and boundary conditions), and final product properties.

To that end, this thesis focuses on proposing a new numerical approach that can bridge this gap by enabling hybrid simulations to perform system-level analysis of polymeric flows. In particular, the numerical approach is applied directly to kinetic

theory models and hybrid simulations to obtain stationary states and associated bifurcations and stability information. The method is general in its applicability in that it treats kinetic theory models and hybrid simulations as black boxes that are then used to obtain system-level information without any modification. This is a significant advantage of this approach as it allows a theoretical rheologist to study the impact of a new molecular model on the richness of macroscopic scale behavior for the polymeric material of interest. In industrial practice, on the other hand, the polymer engineer could predict production problems, such as extrusion instabilities, which can then be partially overcome with improved design. Most importantly, however, such an approach may eventually lead to physics-based process control techniques for polymeric flows typical of processing operations.

1.3   Thesis Outline

The thesis begins in Chapter 2 with a brief review of rheometric experiments that highlight the non-Newtonian character of polymeric fluids and form the basis for development of constitutive equations suitable for studying polymeric flows. In particular, some of the most commonly used constitutive equations in continuum modelling are presented along with equations that have some basis in kinetic theory. The presentation of constitutive equations is accompanied with discussion of their inherent limitations, which provides the necessary motivation for considering kinetic theory models to study the flow of polymeric liquids. This is followed by a brief discussion of two simple kinetic theory models, the rigid and elastic dumbbell, which have been used extensively in hybrid simulations of polymeric flows, even though they represent significant simplifications to real polymer molecules. The equations developed for the rigid and elastic dumbbell form the core of the discussion relating to standard numerical methods that are employed in the hybrid approach, namely the direct solution of the associated Fokker-Planck equations or the equivalent stochastic description. In particular, the presentation highlights the current state-of-the-art in computational techniques that has led to 3D simulations with hybrid methods.

The numerical approach that allows for bridging the gap between hybrid methods and system-level analysis of polymeric flows is presented in Chapter 3. The discussion presents the ingredients of the computational approach, namely the coarse time-stepper framework and iterative methods from numerical linear algebra, along with two examples that illustrate the application of the approach to models from polymer kinetic theory. In particular, we consider a dilute solution of rigid dumbbells in simple shear and a stochastic simulation of polymer chain in simple rheometric flows. These examples specifically illustrate how the numerical method may be applied to both deterministic and stochastic descriptions from kinetic theory without any modification to well developed computational techniques that represent the state-of-the-art for such descriptions. In addition to discussion of the novel numerical approach, Chapter 3 also presents a short review of the finite element method, including specific formulations for discretization of the momentum conservation balance and hyperbolic partial differential equations that arise in kinetic theory models used in this thesis. The chapter concludes with the presentation of an algorithm for performing stability and bifurcation analysis of nonlinear dynamical systems that has been used extensively in this thesis.

Chapter 4 considers three example problems: (1) the equilibrium behavior of the Doi model with the Onsager excluded volume potential, (2) pressure-driven flow of non-interacting rigid dumbbells in a planar channel, and (3) pressure-driven flow of non-interacting rigid dumbbells through a planar channel with a linear array of equally spaced cylinders. The first example clearly demonstrates that models from kinetic theory of polymeric liquids possess a compact spectrum of eigenvalues for the Jacobian matrix associated with the dynamical description. This property of kinetic theory descriptions makes them specifically suitable for obtaining stationary states and performing stability and bifurcation analyses with the methods proposed in this thesis. Whereas the first examples considers a model at equilibrium with a highly nonlinear excluded volume potential, the next two examples show that the numerical methods proposed in this thesis may also be used in the context of a hybrid simulation of a non-homogeneous flow without any significant modification to the simulation

algorithm. Although the focus is on converging to stable stationary states in order to facilitate comparison with dynamic simulations, the results are very encouraging both for incorporation of higher numbers of configurational degrees of the freedom for the kinetic theory models and for performing stability and bifurcation analyses with hybrid simulations of benchmark flows.

Chapter 5 investigates flow induced transitions from steady aligned states to periodic, tumbling states in a linear, weak shear flow for a model suspension of hard rods in two dimensions. In particular, the Doi-Hess diffusion equation with the Maier-Saupe excluded volume interaction potential serves as the starting point for the study. Although the Doi model shows spontaneous alignment even in the absence of flow, approximations typically made in the solution of the Doi model act to alter its predictions in flow situations. For this reason, the discussion in Chapter 5 considers the unapproximated Doi model as a black box simulator which is then wrapped in the numerical approach presented in this thesis to perform detailed bifurcation analysis. While bifurcation analysis for the unapproximated model has been carried out previously [73, 80] for shear flow with moderate to large shear rates, the presentation in Chapter 5 focuses on the solution behavior in the weak shear limit. Specifically, imposition of a weak shear flow has two main ramifications. First, the shear flow unravels the pitchfork bifurcation obtained at equilibrium, selects the director and results in two steady branches - one stable and the other unstable. Second, imposition of shear results in loss of steady aligned solutions beyond a critical value of the dimensionless potential, the value of which depends on imposed shear rate and the shape factor that takes into account the aspect ratio of the rods. The results specifically elaborate on the mechanism by which the time periodic states originate from the steady solution families in the weak shear limit, and the existence of a limiting value for the critical point. The results validate previous asymptotic results in the limit of infinite aspect ratio and extend the results to arbitrary values of the shape factor.

Chapter 6 considers the isothermal fiber spinning process for polymeric melts with specific focus on predicting the onset of draw resonance instability. Mathematical modeling of the process has been carried out in the past using a variety of

constitutive equations that include the White-Metzner model, Phan-Thien and Tanner fluid model, and the Oldroyd-B fluid. The presentation in Chapter 6, however, develops black box simulators for the fiber spinning process for Oldroyd-B and elastic dumbbell models. While closed set of equations are available for the Oldroyd-B fluid, the simulation of the elastic dumbbell model employs a hybrid approach whereby a stochastic description is evolved with the macroscopic conservation equations. These black box descriptions are then wrapped in the computational approach presented in this thesis to obtain steady state results and perform stability and bifurcation analysis of the fiber spinning process. In particular, the results obtained for the onset of draw resonance show that the computational framework presented in this thesis not only yields results consistent with previous studies but also extends the analysis to unclosed kinetic theory descriptions.

Finally, Chapter 7 presents a summary of the contributions of the work carried out in this thesis and ideas for exploration in future research efforts.

Chapter 2

Constitutive Modelling of Polymers

In order to build reliable predictive power for the modelling of polymer flow processes, it is important to develop constitutive equations for polymeric fluids that describe how these large molecules interact with each other and with an imposed flow field. The earliest pioneers in this area, such as Kuhn, Flory, Rouse, and Kramers recognized that the chemical details of the monomers that constitute the building blocks of a polymer chain are not as important as the sheer size of the polymer chain in determining overall impact on flow behavior. In fact, the first major advance came from Kuhn [62] who took a step back from the atomic detail of polymeric structure to look at larger length scales characteristic of these macromolecules. We now know that behavior of polymers in flow, such as non-constant viscosity, differences in normal stresses in shear flow, other elastic effects, and instabilities, are a direct consequence of the large length and time scale response of these materials.

An attempt to understand how all these effects come together in a typical industrial process is then an extremely difficult task given the disparity in scales between the molecular level description and polymer process of interest. Consequently, much of the work done in the field of polymer flow modelling has been based on the continuum approach rather than molecular-based descriptions. In fact, it has only recently become feasible to use molecular descriptions to solve macroscopic flow problems as a

result of rapid rise in computational power and the advent of sophisticated numerical methods.

The aim of this chapter is to provide an overview of flow behavior that is characteristic of polymeric systems and a brief review of continuum and kinetic theory approaches to modelling this behavior. The chapter is organized as follows. Section 2.1 presents those characteristics of polymeric rheological behavior that distinguish them from more familiar Newtonian fluids while Section 2.2 reviews continuum constitutive equations that form the core of modelling efforts for capturing this behavior. While both differential and integral constitutive equations have been used to describe polymer rheological behavior, the presentation here will focus exclusively on differential constitutive equation. This is followed by Section 2.3, which discusses the development of the configurational distribution function and the Fokker-Planck equation that governs its evolution for the most basic molecular models, namely the elastic and rigid dumbbells. This discussion forms the basis for description of two complementary computational approaches: the direct solution of the Fokker-Planck equation and the solution of its stochastic equivalent to obtain stress and structure information in simple rheological and complex flows.

2.1   Viscoelastic Fluid Flow Behavior

There are three important phenomena seen in polymeric liquids that make them different from simple fluids: a non-Newtonian viscosity, normal stresses in shear flow, and elastic effects. All theses effects are a result of the complex molecular structure of polymer macromolecules and its inetraction with the flow. First consider a simple steady shear flow as shown in Fig. 2-1. For a Newtonian fluid, the shear stresses that develop during deformation are directly proportional to the shear rate $\dot{\gamma}_{yx}$ such that

$$\tau_{yx} = -\mu \dot{\gamma}_{yx} \tag{2.1}$$

Top plate velocity $= V$

$v_x = (V/L)y = \dot{\gamma}y$

L

y

x

z
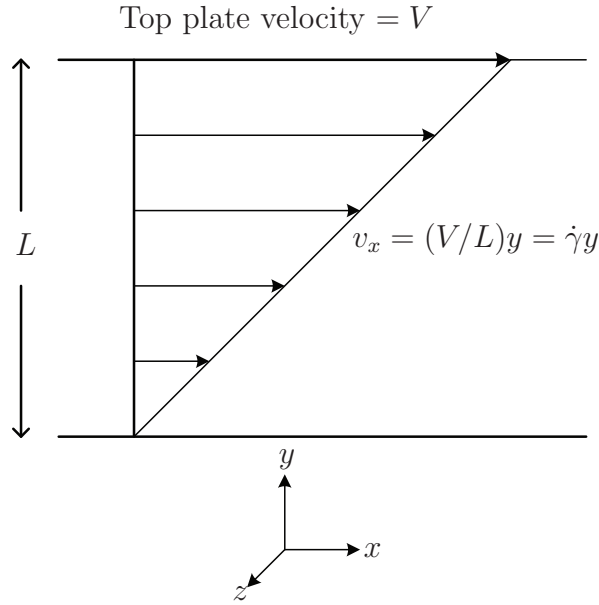
Figure 2-1: Schematic diagram of simple shear flow

where the proportionality constant μ is the Newtonian viscosity, which is considered to be dependent only on temperature. However, the viscosity of most polymer melts is *shear thinning* in addition to being temperature dependent. The shear thinning refers to a decrease in the viscosity with increasing shear rate. This results from a disentanglement of polymer molecules at high shear rates as they are stretched out and begin to slide past each other with greater ease. For a dilute polymer solution this occurs simply due to stretching and alignment of the polymer molecules with the flow. This clearly can be a desirable phenomenon as it benefits polymer processing by relieving the stresses that may develop in these fluids in high shear rate regions of a process. The shear stress that develops in a non-Newtonian fluid in steady simple shear flow may then be expressed as

$$\tau_{yx} = -\eta(\dot{\gamma})\dot{\gamma}_{yx} \tag{2.2}$$

where $\dot{\gamma}$ is the magnitude of the strain-rate or the rate-of-deformation tensor $\dot{\boldsymbol{\gamma}}$.

In addition to the shear thinning viscosity, the polymer molecules tend to stretch in shear flow, which results in normal stresses in the fluid. This is in contrast with a Newtonian fluid where the normal stresses τ_{xx}, τ_{yy}, and τ_{zz} are all zero in steady shear

37

flow. The measurable normal stress differences in an incompresible non-Newtonian fluid, $\tau_{xx} - \tau_{yy}$ and $\tau_{yy} - \tau_{zz}$ are referred to as the first and second normal stress differences. These normal stress differences are material dependent and are used to define two normal stress coefficients, or material functions,

$$\tau_{xx} - \tau_{yy} = -\Psi_1 \dot{\gamma}_{xy}^2$$
$$\tau_{yy} - \tau_{zz} = -\Psi_2 \dot{\gamma}_{xy}^2$$

(2.3)

where Ψ_1 and Ψ_2 are called the first and second normal stress coefficients, respectively. These are also functions of the magnitude of the strain-rate tensor and temperature; and, like the viscosity, decrease in magnitude with increasing shear rate. The first normal stress coefficient, Ψ_1, is typically large and positive, whereas Ψ_2 is small and negative. The second normal stress coefficient is difficult to measure and is often approximated by

$$\Psi_2 \approx -(\text{const})\Psi_1$$

(2.4)

where the constant is between 0.05 and 0.2. The viscosity and the two normal stress coefficients are collectively referred to as steady shear flow or viscometric material functions.

Another type of flow that is used to characterize non-Newtonian behavior is uniaxial elongational flow, as shown in Fig. 2-2. The elongational viscosity measured in this flow is defined as

$$\bar{\eta} = -\frac{(\tau_{zz} - \tau_{xx})}{\dot{\epsilon}}$$

(2.5)

where $\dot{\epsilon}$ is the elongation rate. For Newtonian fluids, the elongational viscosity is equal to three times the the zero-shear-rate viscosity and is also known as Trouton viscosity. Non-Newtonian fluids, on the other hand, exhibit a variety of behavior such that $\bar{\eta}$ may increase or decrease with increasing elongation rate, that is the fluid exhibits *extension thickening* or *thinning*, or have elongational viscosity independent of elongation rate. It must be emphasized that measuring elongational or extensional viscosity is an extremely difficult task since in order to maintain a constant strain rate, the specimen must be deformed exponentially in a uniform manner. Instead,

$$v_z = \dot{\epsilon}z$$

$$v_x = -\frac{\dot{\epsilon}}{2}x$$

$$v_y = -\frac{\dot{\epsilon}}{2}y$$
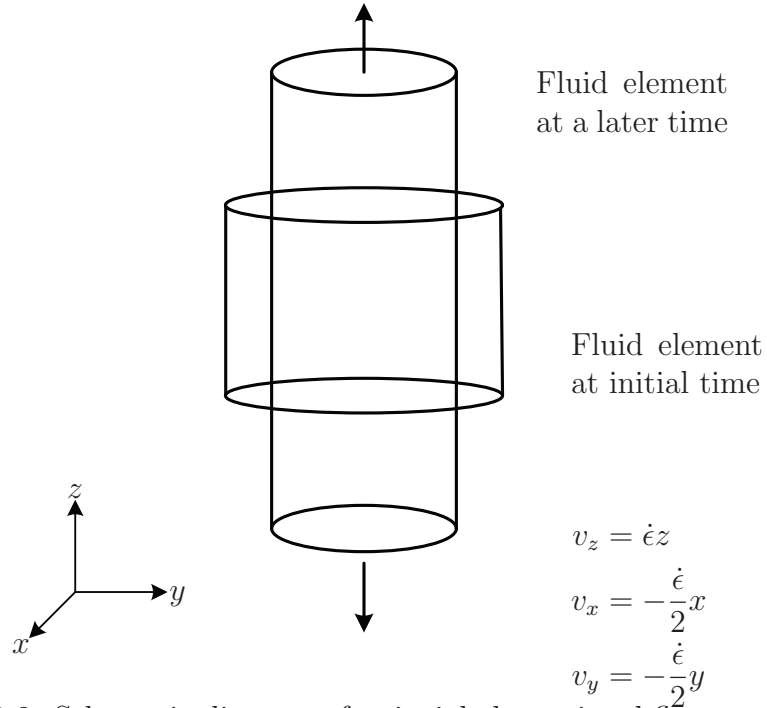
Figure 2-2: Schematic diagram of uniaxial elongational flow

unsteady elongational data are often used for fluid characterization by studying the transient behavior of the specimen in the startup of elongational flow [8].

A third type of flow that is used to characterize polymer flow behavior is small amplitude oscillatory shear [8]. When polymer molecules are subjected to this flow, it is found that for sufficiently small amplitude, the shear stresses oscillate with the same frequency as the shear rate, but display a phase lag, This is an indication of viscoelastic behavior since a purely viscous or inelastic material displays no phase lag. The shear stress can then be expressed as a linear combination of in-phase and out-of-phase contributions. In this representation, two material functions are defined: η', the viscosity associated with the in-phase part of the stress, and η'', the viscosity associated with the out-of-phase part of the stress. These are often called the linear viscoelastic properties of the material and depend on the frequency.

The phase lag displayed by viscoelastic materials in the oscillatory shear experiment indicate that these fluids have memory, that is, the behavior of the fluid at a given time is dependent on the history of the strain experienced by the fluid in the past. This idea can be better understood by considering a molecular argument. When

39

a polymer melt is deformed either by stretching, shearing, or a combination of these, the polymer molecules are stretched, oriented, and untangled. If the deformation is maintained for a short period of time, the molecules can then nearly recover their initial shape and position, as if they remembered their initial state. On the other hand, if the deformation continues for an extended period of time, the polymer molecules cannot recover the initial shape and adjust to their new state of deformation. This behavior is clearly observed experimentally in a stress relaxation experiment, where a polymeric fluid at rest after deformation possesses non-zero stress for some time after flow has ceased, as the conformations of the polymer molecules return gradually to their equilibrium state. Consequently, the time it takes for a molecule to fully relax and adjust to its new state of deformation is known as the relaxation time of the polymeric material and often denoted by λ. This leads to a useful dimensionless number or parameter, De, known as the Deborah number, that is used to estimate the elastic or memory effects during flow

$$\text{De} = \frac{\lambda}{t_{\text{process}}} \qquad (2.6)$$

where t_{process} is a characteristic process time. For example, in an extrusion die, a characteristic process time can be defined by the ratio of characteristic die dimension and average speed through the die [82]. A Deborah number of zero represents a viscous fluid, that is a fluid with no memory, whereas a Deborah number of infinity represents an elastic solid.

The effects discussed so far highlight the primary differences between Newtonian and polymeric fluids, which are basically a manifestation of differences in molecular size. A collection of experiments that illustrate interesting non-Newtonian behavior is compiled in the photo gallery by Boger and Walters [11], and several of these are discussed in the text by Bird et al. [8]. Among them is the phenomenon of 'rod-climbing' in which a polymeric fluid travels up a spinning rod placed within it, despite centrifugal and gravitational forces. This effect is directly related to normal stress differences that counter inertial effects to push the fluid inward from the streamlines

and upward. Another example is that of the 'tubeless siphon' in which a polymeric fluid can empty itself out of a beaker without the aid of a siphoning tube. This is a result of molecular alignment along the streamlines that allows the fluid to form a long thread without breaking. One behavior that is observed in industrial applications is the phenomenon of 'extrudate-swell', in which a viscoelastic fluid exiting a tube exhibits an increase in diameter of up to 300% compared with an increase of about 13% for a Newtonian fluid. Although many factors affect the amount of extrudate swell, fluid memory and normal stress effects are the most significant ones. Other factors include abrupt changes in boundary conditions such as the separation point of the extrudate from the die. In practice, the fluid memory contribution to die swell can be mitigated by lengthening the land length of the die [82]. A long die land separates the polymer from the manifold for enough time to allow it to forget its past shape.

In polymer processing operations the characteristics of viscoelastic fluid flow described here can have significant impact on the quality of the product. The property of fading memory of the fluid specifically gives rise to many problems. If the Deborah number is $\mathcal{O}(1)$ the polymer does not have enough time to relax during the process, which can result in possible deviations in the dimensions of the final product. A well known phenomenon of this type is known as 'shark skin' where waves appear in the extrudate as a result of high speeds during extrusion. One postulate for this behavior proposes that at high extrusion speeds the polymer is not allowed to relax sufficently, and the accompanying extrudate swell leads to waves on the product surface. Additionally, if the fluid has been highly stressed during processing, the residual stresses can remain in the finished product, causing anisotropy, weakness, and defects. Excellent reviews of the origins of some of these instabilities are given by Larson [65], Shaqfeh [99], and Denn [25].

In summary, the Deborah number and the magnitude of the deformation imposed on the polymer during processing strongly affects the modeling of non-Newtonian flows. For flows with De $\sim \mathcal{O}(1)$, small deformations can be captured with linear viscoelasticity [8]. However, large deformations that are typical of most processing

operations require the use of constitutive equations that can reproduce the nonlinear viscoelastic behavior described above.

2.2 Continuum Approaches

In order to model the flow of polymeric liquids one naturally begins with the conservation equations of mass and momentum to calculate the velocity and pressure fields within the fluid. However, in order to successfully complete such a calculation one must also introduce a constitutive equation that relates the stresses in the fluid to the flow kinematics. As one of the obvious deviations of polymeric liquids from Newtonian fluids is the property of shear rate dependent viscosity, first attempts at describing their behavior considered the generalized Newtonian fluid approach that retains the form of the Newtonian constitutive equation but makes the viscosity dependent on the shear rate.

Models based on the generalized Newtonian fluid approach are some of the most widely used models by polymer engineers on a day-to-day basis. Prominent examples include the power law, Bird-Carreau-Yasuda, and the Bingham fluid models [8]. The power law model originally proposed by Ostwald and de Waale is a simple model that accurately represents the shear thinning region in the viscosity versus strain rate curve but neglects the Newtonian plateau present at small strain rates. This model postulates a viscosity of the form

$$\eta = m\dot{\gamma}^{n-1} \tag{2.7}$$

where m is referred to as the consistency index and n the power law index. The consistency index is typically used to capture the temperature dependence of the viscosity while the power law index represents the shear thinning behavior of the polymer melt.

While such models work very well for predicting shear stresses in steady shearing flows, they are unable to provide good predictions in general flows as they do

not incorporate either normal stresses of fading memory of the fluid in the constitutive equation. Although fading memory has its basis in molecular configurational dynamics, its effects must nevertheless be captured by the constitutive equation, regardless of whether this equation is derived from molecular descriptions or not. This is discussed next for both flexible and rigid polymers.

2.2.1 Flexible Polymers

Two types of nonlinear viscoelastic flow models have been used when describing the behavior of polymers in complex flow systems: differential and integral models. Of these the differential type are discussed here, as they represent the bulk of modelling effort.

The process of developing rheologically admissible constitutive equations was laid out by the work of Oldroyd, who postulated that two requirements should be satisfied by any constitutive equation. The first was the simple fluid assumption: the stresses in a given fluid element should not be affected by the deformation history in any other fluid element. The second was the property of *frame invariance*: rheological predictions should not be affected by rigid body rotations of the material. Oldroyd proposed that frame invariance could be enforced by writing the constitutive equations in a coordinate system that deformed with the fluid, thus introducing a new time derivative known as the *convected derivative*. The most commonly used convected derivative in the upper-convected derivative defined for a second order tensor $\boldsymbol{\tau}$ as

$$\boldsymbol{\tau}_{(1)} \equiv \frac{\partial \boldsymbol{\tau}}{\partial t} + \boldsymbol{v} \cdot \boldsymbol{\nabla}\boldsymbol{\tau} - [(\boldsymbol{\nabla}\boldsymbol{v})^T \cdot \boldsymbol{\tau} + \boldsymbol{\tau} \cdot (\boldsymbol{\nabla}\boldsymbol{v})] \tag{2.8}$$

This process was very useful in improving upon early efforts to model flexible polymers, which were based on the idea of elastic behavior modified by viscous damping. The mechanical analogue for this is the dynamic response of a spring and dashpot in series [8]. This leads to the well-known Maxwell model

$$\boldsymbol{\tau} + \lambda \frac{\partial \boldsymbol{\tau}}{\partial t} = -\eta \dot{\boldsymbol{\gamma}} \tag{2.9}$$

that captures the idea of a finite response time for the molecule. Since the Maxwell model does not satisfy the frame invariance property, the time derivative in Eq. 2.9 was changed to the upper-convected derivative to yield the upper-convected Maxwell model that has received most attention from computational rheologists. Differential constitutive equations that represent the bulk of the published literature can be described by the general form

$$a\boldsymbol{\tau} + \lambda_1\boldsymbol{\tau}_{(1)} + \lambda_3\{\dot{\boldsymbol{\gamma}}\cdot\boldsymbol{\tau} + \boldsymbol{\tau}\cdot\dot{\boldsymbol{\gamma}}\} + \lambda_4\{\boldsymbol{\tau}\cdot\boldsymbol{\tau}\} = -\eta_0\{\dot{\boldsymbol{\gamma}} + \lambda_2\dot{\boldsymbol{\gamma}}_{(1)}\} \qquad (2.10)$$

where the constants in Eq. 2.10 are defined in Table 2.1 for various viscoelastic models. One additional model is the White-Metzner model, which is very similar to

Constitutive model	a	λ_1	λ_2	λ_3	λ_4
Upper convected Maxwell	1	λ_1	0	0	0
Convected Jeffreys (Oldroyd-B)	1	λ_1	λ_2	0	0
Phan-Thien Tanner 1	$e^{-\text{tr}\boldsymbol{\tau}(\epsilon\lambda/\eta_0)}$	λ	0	$\xi\lambda/2$	0
Phan-Thien Tanner 2	$1 - \text{tr}\boldsymbol{\tau}(\epsilon\lambda/\eta_0)$	λ	0	$\xi\lambda/2$	0
Giesekus	1	λ_1	0	0	$-\alpha\lambda_1/\eta_0$

Table 2.1: Definition of constants in general differential constitutive equation

the upper convected Maxwell model except that η_0 and λ_1 in the upper convected Maxwell model are replaced by $\eta(\dot{\gamma})$ and $\lambda_1(\dot{\gamma}) = \eta(\dot{\gamma})/G$ where $\eta(\dot{\gamma})$ is the shear-rate dependent viscosity and G is the constant modulus. While both models provide a first order approximation to flows in which shear rate dependence and memory effects are important, they predict zero second normal stress coefficients.

In contrast with introducing shear rate dependence, the convected Jeffreys or Oldroyd-B model improves over the Maxwell model by including a convected time derivative of the rate-of-strain tensor. While this model does have a molecular basis, it fails to produce shear thinning or a non-zero second normal stress coefficient. To remedy this, Oldroyd proposed including all possible quadratic terms in $\boldsymbol{\tau}$ and $\dot{\boldsymbol{\gamma}}$ that are linear in $\boldsymbol{\tau}$, and produced the Oldroyd-8 constant model, which does indeed give qualitatively correct behavior for material functions. Such an approach has formed the basis of most constitutive models that introduce higher-order terms with additional

adjustable parameters or variations of functional forms in order to reproduce observed behavior empirically and provide greater predictive capability.

More successful models, such as Phan-Thien Tanner and Giesekus models, were obtained by considering the physics of the flow at the molecular level for a suitable molecular model and using the insights to suggest important effects that could be included in the constitutive equation. The Giesekus model, for example, is based on the two bead molecular model for an elastic dumbbell with the argument that the forces on each bead are likely to be anisotropic and biased in a particular flow direction. Further assuming that this anisotropy is proportional to the stress introduces nonlinear stress terms in the constitutive equation. The Phan-Thien Tanner model is similarly based on network theory and gives nonlinear terms for the stress tensor. While both these models are based on molecular arguments, they are nevertheless continuum models since they treat the stress tensor as a field quantity, with no restriction imposed by the existence of a molecular length scale. Similar attempts at developing continuum models from molecular arguments have required the introduction of closure approximations [18] to cast the equations in continuum form for the stress tensor and tensorial quantities for averages over the microstructure. Unfortunately, these approximation tend to be purely mathematical in nature, and the modifications they introduce in the predictions of the molecular model cannot be known a priori. A more complete review of the existing viscoelastic models is provided by Bird and Wiest [10].

2.2.2 Rigid Polymers

The most well studied continuum constitutive equation for the modeling of rigid polymers comes from Leslie-Ericken theory, although it is only valid for low deformation rates. By assuming that the fluid is anisotropic, a director vector $\boldsymbol{n}$ describing the anisotropy is defined at every point in space and assumed to be a continuum property of the fluid. The constitutive equation provided by the theory is

$$\boldsymbol{\tau} = -[\alpha_1 \boldsymbol{nnnn} : \dot{\boldsymbol{\gamma}} + \alpha_2 \boldsymbol{nN} + \alpha_3 \boldsymbol{Nn} + \alpha_4 \dot{\boldsymbol{\gamma}} + \alpha_5 \boldsymbol{nn} \cdot \dot{\boldsymbol{\gamma}} + \alpha_6 \dot{\boldsymbol{\gamma}} \cdot \boldsymbol{nn}] \qquad (2.11)$$

where $\boldsymbol{N} \equiv \dot{\boldsymbol{n}} - \boldsymbol{n} \cdot \boldsymbol{\omega}$, and $\boldsymbol{\omega}$ is the vorticity tensor. The coefficients α_2 and α_3 determine the torque exerted by the fluid on the director aligned with the velocity gradient and flow direction, respectively. If α_3 is negative, the director tumbles continuously in the flow and reaches no steady state. Since Eq. 2.11 contains only linear terms in $\dot{\boldsymbol{\gamma}}$ it is only valid for low $\dot{\gamma}$ and does not describe rheological properties like shear thinning. Additionally, the theory has nothing to say about the extent of molecular ordering around the director. Despite these deficiencies, the theory has been used extensively in both experimental and theoretical work to interpret the constants from a molecular point of view for liquid crystal polymers [75].

In developments similar to those for flexible polymers, several molecular based continuum equations have been proposed for rigid polymers that incorporate effects such as an intermolecular potential. The resulting molecular theories require resorting to closure approximations to obtain closed equations for the stress tensor. Unfortunately, these equations also suffer from similar advantages and disadvantages as those for flexible molecules. While they are computationally easy to solve in conjunction with momentum and continuity equations, they are difficult to interpret rigorously from a molecular viewpoint.

2.3 Micromechanical Models and Kinetic Theory

While continuum constitutive equations have demonstrated considerable predictive power, a more realistic simulation of polymeric flow necessitates a more comprehensive picture of molecular configurations and its interaction with macroscopic flow. Even the simplest linear polymer molecule has many internal degrees of freedom that result from up to 10^3 to 10^6 repeating monomer units in the polymer backbone. These monomer units are connected by bonds that can rotate and stretch to various degrees, giving rise to a large number of possible configurations. This problem is exacerbated by the diversity of polymer structure that results from side chains and ring-like conformations. In addition, most polymers have a distribution of molecular weights. This makes it important to consider averaged properties of the polymer and existence of

molecular interactions such as entanglements, excluded volume, and hydrodynamic interactions.

As a consequence, a hierarchy of theoretical models have been considered to model this diversity. Given the large number of degrees of freedom in the polymer molecule, a modeling approach based on quantum mechanics and related *ab initio* computational techniques is clearly impossible with current computational resources, which leaves atomistic modeling and the associated techniques of *non-equilibrium molecular dynamics* as the most detailed level of description that may be applied in rheological studies. In fact, most early molecular models described polymer molecules as long chains of beads connected either by rigid rods or extensible springs, in which the beads represent carbon atoms in the polymer backbone, while the rods represent massless interatomic bonds. Variations on this model include allowing some amount of rotation in each bond, as proposed by Flory [34]. While such an approach has been used to study the behavior of polymers near walls [52, 51] and geometrical singularties such as re-entrant corners, the atomistic approach to flow simulation is currently limited to very simple non-equilibrium situations and flow geometries of molecular dimension.

A more coarse-grained description of the polymer was first introduced by Kuhn [62] that ignores atomistic processes altogether while producing many of the essential features of polymer behavior. Kuhn introduced the idea of the *persistence length* or Kuhn length, which is an effective segment length of the polymer molecule over which the position of two monomers can be considered uncorrrelated. The size of this persistence length determines the flexibility of the polymer chain as a whole. Typical flexible polymers have Kuhn lengths which are 5-10 times the monomer length, while rigid rod polymers have Kuhn lengths which are of the order of the molecule length.

The definition of the Kuhn length led to modeling of the polymer molecule as a freely jointed chain with links of one Kuhn length, in which the orientation of each link is uncorrelated with that of every other link. The model describes a polymer molecule as a chain of N beads, each of mass m, connected by $N-1$ massless rods of Kuhn length a. Each bead represents the mass of some finite length of the polymer

47

chain rather than of one individual carbon atom or monomer unit. However, the total mass of the beads is equal to the mass of the molecule and the contour length of the chain is equal to the length of the polymer molecule. The freely jointed bead rod chain is often refered to as the *Kramers* model and is completely described by the center-of-mass position vector and the two spherical polar angles associated with each link in the chain. The equilibrium distribution function for each link in the chain can be shown to be that for a random walk [8], which allows one to obtain the average root mean square end-to-end distance of the N-bead chain at equilibrium as

$$\sqrt{\langle r^2 \rangle_{\text{eq}}} = a\sqrt{N - 1} \tag{2.12}$$

While this was a major step in the development of micromechanical models for polymers it suffered from three major limitations. First, the model does not describe molecules that are highly extended in flow since the result in Eq. 2.12 shows that a polymer chain at equilibrium is highly coiled. Second, it does not take into account steric hindrances from other atoms along the polymer backbone; and third, it does not describe the effect of solvent on polymer conformation. Flory [34] was the first to introduce thermodynamic understanding of such models by introducing solvent-polymer interactions. This led to definition of good' and 'poor' solvents that produce maximum and minimum contact of the polymer chain with the solvent, respectively.

The next level coarse-graining was introduced by Rouse who described the polymer molecule as a chain of beads connected not by rods but by springs. It can be shown that at small extensions, a sufficient number of Kuhn segments behaves like a Hookean spring [9] leading to this natural simplification of the freely jointed chain. Rouse studied the motion of the bead-spring chain and showed that the molecule possesses a spectrum of relaxation times or modes, that is it responds to changes in its conformation on a variety of different time scales that result from the large size of the molecule. This does make intuitive sense as one would expect the overall molecular conformation to respond slowly to changes in flow field when compared with orientation of a Kuhn length or a bond length. This is the central idea in de-

veloping constitutive equations of better predictive power by incorporating more and more modes in the model. In fact, the parameter λ_1 in Table 2.1 may be thought of as the longest relaxation time of the polymer molecule. Most importantly, however, it is this existence of a spectrum of relaxation times in polymer dynamics that forms the basis of the work carried out in this thesis. Following the work of Rouse, Zimm and Kirkwood separately introduced hydrodynamic interactions into the chain model to account for changes in flow field experienced by a given bead in the chain due to flow field modifications by other beads. This was further extended to incorporate anisotropy in the forces experienced by the beads as a result of both hydrodynamic interactions and Brownian forces. An excellent review of such work is given by Larson [66].

In contrast with flexible polymers, the freely jointed model is not applicable for rigid polymers as the Kuhn length is comparable to the molecular size. Instead, the dominant balance of forces acting on these molecules is between the rotational action of the flow field and Brownian motion. Just as for flexible polymers, there is a spectrum of relaxation times; but molecular models assume a dominant relaxation time that governs the orientational rather than the extensional state of the polymer. Both hydrodynamic interactions and anisotropic drag effects have also been considered in development of these models [8], including contributions from studies of suspensions of rigid ellipsoidal particles [48].

The treatment of polymer molecules through construction of micromechanical models and consideration of forces that act on a large collection of such model molecules forms the basis of polymer kinetic theory. The goal of kinetic theory of macromolcules, then, is the same as the kinetic theory for gases or small liquid molecules, that is, to derive macroscopic constitutive equations based on assumptions regarding the structure of the molecules and their interactions. The additional complication arises from the need to consider flowing or non-equilibrium systems, which makes the field particularly challenging. While details of general phase-space polymer kinetic theory are given in the text by Bird et al. [8], the following discussion presents the kinetic theory development for the dumbbell model, which represents

the simplest mathematical coarse-grained molecular description.

2.3.1 Dumbbell models

In the dumbbell model each polymer molecule is represented as two beads joined by a rigid or elastic connector. The justification for the latter representation comes from the fact that for small deformations a freely jointed chain model behaves effectively like a Hookean spring. Thus, a dumbbell with a spring connector has some of the features of a more detailed model. Dumbbells with rigid connectors can be used to model polymers with stiff backbones, such as liquid crystals. Illustrations of the two dumbbells is shown in Fig. 2-3. While these models are mathematically more tractable than the models already discussed, they do not display a spectrum of relaxation times and can be inaccurate in describing true rheological behavior, such as the shear thinning viscosity. Nevertheless, they have been used extensively in flow calculation, as dumbbells represent a drastic reduction in the number of degrees of freedom.

Rigid dumbbell   Elastic dumbbell

Bead "+1"

u

Q

Bead "-1"
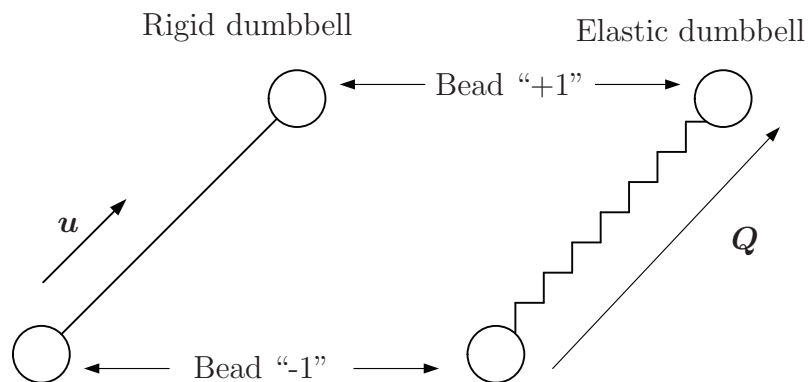
Figure 2-3: Schematic diagrams for the rigid and elastic dumbbells. The beads represent mass points of zero volume

In kinetic theory, beads are denoted by the Greek letter ν with position vectors r_ν to obtain the simplest representation of the model. Alternatively, the vector along the connecting link, Lu for the rigid dumbbell (L is the length of the rod and u is a unit vector pointing from bead -1 to 1) and Q for the flexible dumbbell, can be specified as well, as shown in Fig. 2-3, along with the position vector for the center of mass, r_c. From this it is evident that the rigid and elastic dumbbells possess 5

and 6 configurational degrees of freedom per molecule, respectively. The difference results from the additional constraint of constant length for the rigid dumbbell. The orientation vector for the rigid dumbbell, $\boldsymbol{u}$, is therefore generally expressed in polar coordinates θ and ϕ. Finally, the beads are assumed to be mass points, each of mass m with no volume. This information is then sufficient to build a description of the molecular configuration.

Distribution function and microstructural averages

In order to obtain information about the macroscopic flow properties of a polymeric fluid described by a dumbbell model we use kinetic theory to understand the dynamical state of a dumbbell molecule. This state can in general be characterized by a two attributes: the configuration of the dumbbell as defined by the position of each bead, and its momentum, which is defined by the momentum $\boldsymbol{p}_\nu$ of each bead. Since $\boldsymbol{p}_\nu = m\dot{\boldsymbol{r}}_\nu$, specifying $\dot{\boldsymbol{r}}_\nu$ is equivalent to specifying $\boldsymbol{p}_\nu$. In addition, the dumbbell model is being used to describe a large collection of polymer molecules. Hence, a distribution of configurations and momenta over the whole range of $\boldsymbol{r}_1$, $\boldsymbol{r}_2$, $\dot{\boldsymbol{r}}_1$, and $\dot{\boldsymbol{r}}_2$ is defined in position-velocity space. This distribution, denoted by $F(\boldsymbol{r}_1, \boldsymbol{r}_2, \dot{\boldsymbol{r}}_1, \dot{\boldsymbol{r}}_2, t)$, is customarily factored into a configuration space distribution function $\Psi(\boldsymbol{r}_1, \boldsymbol{r}_2, t)$, and a velocty space distribution funtion $\Xi(\boldsymbol{r}_1, \boldsymbol{r}_2, \dot{\boldsymbol{r}}_1, \dot{\boldsymbol{r}}_2, t)$

$$F(\boldsymbol{r}_1, \boldsymbol{r}_2, \dot{\boldsymbol{r}}_1, \dot{\boldsymbol{r}}_2, t) = \Psi(\boldsymbol{r}_1, \boldsymbol{r}_2, t)\Xi(\boldsymbol{r}_1, \boldsymbol{r}_2, \dot{\boldsymbol{r}}_1, \dot{\boldsymbol{r}}_2, t) \tag{2.13}$$

In polymer kinetic theory, the collection of molecules associated with every material point is assumed to equilibrate in momentum space, that is the time scale of momentum fluctuations is much smaller than the time scale of position and orientational changes. If the fluid is observed on a position-fluctuation time-scale, the particle momenta have already equilibrated to a value described by a Maxwellian velocity distribution for the particles. This leads to a major simplification, as only the configuration distribution function Ψ is sufficient to obtain a kinetic theory description. If we make the additional assumption that the flow is locally homogeneous, that

is the velocity field does not change significantly over the length scale of a molecule, then the configuration distribution function is independent of the physical position $\boldsymbol{r}_c$ of the molecules in space. Hence, the configuration distribution function for the dumbbell may be written as

$$\Psi(\boldsymbol{r}_1,\boldsymbol{r}_2,t) \equiv \begin{cases} \Psi(\boldsymbol{r}_c,\boldsymbol{u},t) = nf(\boldsymbol{u},t) & \text{rigid dumbbell} \\ \Psi(\boldsymbol{r}_c,\boldsymbol{Q},t) = n\psi(\boldsymbol{Q},t) & \text{elastic dumbbell} \end{cases} \tag{2.14}$$

where n is the number of molecules per unit volume, and $f(\boldsymbol{u},t)$ or $\psi(\boldsymbol{Q},t)$ is the orientation distribution function. In a locally homogeneous flow, the velocity field may be written locally as $\boldsymbol{v} = \boldsymbol{v}_0 + \boldsymbol{\kappa} \cdot \boldsymbol{r}$, where $\boldsymbol{v}$ is the local solution velocity, $\boldsymbol{v}_0$ is a position independent vector, and $\boldsymbol{\kappa} \equiv \boldsymbol{\nabla}\boldsymbol{v}^T$, which may be time dependent but not position dependent. The local homogeneity requirement does not mean that $\boldsymbol{\kappa}$ must be constant everywhere in the flow. It simply means that it should be constant within a material point containing a statistically significant number of polymer molecules. In some sense three length scales are being assumed here: a macroscopic scale for the flow, a microscopic scale for a material point of the fluid, and a molecular scale for a polymer molecule. The work done in this thesis deals only with locally homogeneous flows, which is a standard assumption in hybrid simulations of viscoelastic flows.

If the distribution function F is known, one can calculate average values of any property $B(\boldsymbol{r}_c,\boldsymbol{u})$ or $B(\boldsymbol{r}_c,\boldsymbol{Q})$ by first using the Maxwellian velocity distribution to obtain the velocty space average

$$[[B]] \equiv \int B\Xi d\dot{\boldsymbol{r}}_1 d\dot{\boldsymbol{r}}_2 \tag{2.15}$$

followed by the configuration space average, which is given by

$$\langle B \rangle \equiv \frac{1}{nV} \int \int [[B]] f d\boldsymbol{r}_c d\boldsymbol{u} \tag{2.16}$$

for a rigid dumbbell, where nV is the total number of macromolecules. For a flexible
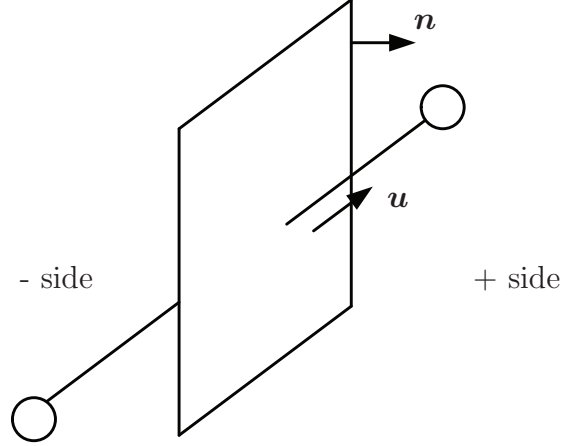
Figure 2-4: A fluid plane straddled by a rigid dumbbell

dumbbell, the equivalent expression is

$$\langle B \rangle \equiv \frac{1}{nV} \int \int [[B]] \psi \, d\boldsymbol{r}_c d\boldsymbol{Q} \tag{2.17}$$

If B depends only on $\boldsymbol{u}$ or $\boldsymbol{Q}$, then $\langle B \rangle \equiv \int B f(\boldsymbol{u}, t) d\boldsymbol{u}$ or $\int B \psi(\boldsymbol{Q}, t) d\boldsymbol{Q}$. Knowledge of the orientational distribution function and the ability to compute associated averages forms the basis for obtaining constitutive equations for the polymer contribution to the fluid stress.

Constitutive equation for stress tensor

The total stress tensor for a fluid is written as the sum of the equilibrium and deviatoric parts

$$\boldsymbol{\pi} = p\boldsymbol{\delta} + \boldsymbol{\tau} \tag{2.18}$$

where $\boldsymbol{\tau} = -\eta_s \dot{\boldsymbol{\gamma}} + \boldsymbol{\tau}_p$. The solvent contribution to the deviatoric stress is taken to be Newtonian with viscosity η_s and strain rate tensor $\dot{\boldsymbol{\gamma}} \equiv (\boldsymbol{\nabla v} + \boldsymbol{\nabla v}^T)$. The task then for kinetic theory is to develop a constitutive equation for $\boldsymbol{\tau}_p$ in terms of the average configuration of a large number of dumbbell models, that is, interms of $\boldsymbol{u}$ for a rigid dumbbell or $\boldsymbol{Q}$ for an elastic dumbbell.

Rigid dumbbell To develop the constitutive equation for a rigid dumbbell consider a plane, as shown in Fig. 2-4, with normal vector $\boldsymbol{n}$. The plane is straddled by a dumbbell with rigid connector of length L and orientation $\boldsymbol{u}$ such that one of its beads is on the '+ side' of the plane, while the others is on the '- side'. The number of dumbbells oriented within the range $d\boldsymbol{u}$ about the direction $\boldsymbol{u}$ that penetrate unit area of this plane is $nL(\boldsymbol{u}\cdot\boldsymbol{n})f\boldsymbol{u}$, where n is the total number of dumbbells per unit volume of solution, and $fd\boldsymbol{u}$ is the probability of finding a dumbbell in the orientation range $d\boldsymbol{u}$ about $\boldsymbol{u}$. Now, suppose the force that is exerted by the positive-side bead on the solvent is given by $\boldsymbol{F}^+$. Then the total contribution of all dumbbells to the force on unit area of the plane on the positive side is

$$\int_{\boldsymbol{u},\boldsymbol{u}\cdot\boldsymbol{n}>0} nL(\boldsymbol{u}\cdot\boldsymbol{n})\boldsymbol{F}^+ f d\boldsymbol{u} \tag{2.19}$$

Similarly, force contribution by all the negative side beads on the negative side is

$$\int_{\boldsymbol{u},\boldsymbol{u}\cdot\boldsymbol{n}<0} nL(-\boldsymbol{u}\cdot\boldsymbol{n})\boldsymbol{F}^- f d\boldsymbol{u} \tag{2.20}$$

Since the forces on the plane from either side must be equal and opposite, we must have $\boldsymbol{F}=\boldsymbol{F}^+=-\boldsymbol{F}^-$ and the total force per unit area of the plane is

$$\int_{\boldsymbol{u}} nL(\boldsymbol{u}\cdot\boldsymbol{n})\boldsymbol{F} f d\boldsymbol{u} \tag{2.21}$$

Two types of forces act on the bead: Brownian forces that cause random fluctuations of the bead relative to the solvent, and hydrodynamic forces, which only exist if the bead experiences systematic motion relative to its surrounding solvent. Since the dumbbell is of fixed length, motion of the bead in the $\boldsymbol{u}$ direction relative to the center of mass is impossible. But rotational Brownian forces produce non-zero bead velocities in the angular direction relative to the immediately surrounding solvent. This rotational Brownian velocity may be written as

$$\boldsymbol{v}^{\mathrm{Br}} = \frac{kT}{L\zeta}\frac{\partial \ln f}{\partial \boldsymbol{u}} \tag{2.22}$$

where ζ is a friction coefficient. Note that $\boldsymbol{v}^{\mathrm{Br}}$ only has components in the polar and azimuthal direction, $\boldsymbol{s}$ and $\boldsymbol{t}$, respectively. Hydrodynamic forces, on the other hand, play a role in the translational velocity of the bead relative to the center of mass as the dumbbell cannot stretch. Since the velocity of the solvent at a bead position relative to the center of the mass of the dumbbell is just $\boldsymbol{v} = \frac{L}{2}\boldsymbol{\kappa} \cdot \boldsymbol{u}$, the translational velocity of the bead relative to its immediately surrounding solvent is just the component of $\boldsymbol{v}$ in the $\boldsymbol{u}$ direction. Hence,

$$\frac{L}{2}(\boldsymbol{\kappa} \cdot \boldsymbol{u}){\cdot}\boldsymbol{uu}$$
$$= \frac{L}{2}(\boldsymbol{\kappa} : \boldsymbol{uuu}) \tag{2.23}$$

There should be a Brownian components to the translational velocity as well, since the entire dumbbell is subject to some translational diffusivity. However, for this thesis this effect is assumed to be small.

The force exerted by the bead on the fluid is then given by the product of the friction coefficient (assumed to be isotropic) and the velocity of the bead relative to the solvent

$$\boldsymbol{F} = \zeta \boldsymbol{v}^{\mathrm{rel}} = \zeta \frac{L}{2}\left(\boldsymbol{\kappa} : \boldsymbol{uuu} + \frac{2kT}{\zeta L^2}\frac{\partial \ln f}{\partial \boldsymbol{u}}\right) \tag{2.24}$$

The total force contribution from dumbbells in all possible orientations, per unit area of the plane is then

$$\boldsymbol{n} \cdot \boldsymbol{\tau}_p = \int_{\boldsymbol{u}} nL(\boldsymbol{u} \cdot \boldsymbol{n})\boldsymbol{F} f d\boldsymbol{u}$$
$$= \boldsymbol{n}{\cdot}\left[n\zeta\frac{L^2}{2}\int_{\boldsymbol{u}} \boldsymbol{u} f\left(\boldsymbol{\kappa} : \boldsymbol{uuu} + \frac{2kT}{\zeta L^2}\frac{\partial \ln f}{\partial \boldsymbol{u}}\right)d\boldsymbol{u}\right] \tag{2.25}$$

After integration by parts and the substitution $\zeta = \frac{12kT\lambda}{L^2}$ we get the final expression for the stress

$$\boldsymbol{\tau}_p = -3nkT\langle\boldsymbol{uu}\rangle - 6nkT\lambda\,\boldsymbol{\kappa} : \langle\boldsymbol{uuuu}\rangle + nkT\boldsymbol{\delta} \tag{2.26}$$

This expression represents the constitutive equation for the stress of a dilute solution of rigid dumbbells that does not take into account external forces. If external forces

are described by a potential $\phi^{(e)}$ then this expression becomes

$$\boldsymbol{\tau}_p = -3nkT\langle\boldsymbol{uu}\rangle - 6nkT\lambda\,\boldsymbol{\kappa}:\langle\boldsymbol{uuuu}\rangle + nkT\boldsymbol{\delta} + n\left\langle\boldsymbol{u}\frac{\partial\phi^{(e)}}{\partial\boldsymbol{u}}\right\rangle \tag{2.27}$$

which is known as the Kramers expression [9]. It can be noted that the stress depends only on the second and fourth moment of the orientational distribution function.

Elastic dumbbell   For an elastic dumbbell, there are no constraints on the motion of the bead relative to the center of mass of the dumbbell. Hence, the contribution to stress from bead motion across a fluid plane is governed solely by Brownian forces and turns out to be simply isotropic if a Maxwellian distribution is assumed. However, the elastic spring in the dumbbell model contributes to stress through tensile or compressive force transmitted across the plane.

Here we follow the development given in Bird et al. [9] and denote this stress by $\boldsymbol{\tau}_p^{(c)}$, that is the polymer stress from the connector spring. Consider a plane in the fluid similar to that in Fig. 2-4 that is straddled by a dumbbell with configuation $\boldsymbol{Q}$ and beads numbered '1' on the negative side and '2' on the positive side. Also, let the force exerted on bead '1' through the connector spring be $\boldsymbol{F}_1^{(\phi)}$, which is equal and opposite to the force exerted on the positive side due to this one dumbbell. The total number of dumbbells with orientation $\boldsymbol{Q}$ across the plane is $n(\boldsymbol{n}\cdot\boldsymbol{Q})\psi(\boldsymbol{Q},t)d\boldsymbol{Q}$, where $\boldsymbol{n}\cdot\boldsymbol{Q}$ is the volume in which bead '1' must be contained and $\psi(\boldsymbol{Q},t)d\boldsymbol{Q}$ is the probability that the dumbbell with have an orientation $\boldsymbol{Q}$ within $d\boldsymbol{Q}$. Thus, the total force acting on the positive and negative materials is

$$\int_{\boldsymbol{Q},\boldsymbol{n}\cdot\boldsymbol{Q}>0} n(\boldsymbol{n}\cdot\boldsymbol{Q})\psi(\boldsymbol{Q},t)(\boldsymbol{F}_2^{(\phi)})d\boldsymbol{Q} \tag{2.28}$$

and

$$\int_{\boldsymbol{Q},\boldsymbol{n}\cdot\boldsymbol{Q}<0} n(\boldsymbol{n}\cdot\boldsymbol{Q})\psi(\boldsymbol{Q},t)(-\boldsymbol{F}_1^{(\phi)})d\boldsymbol{Q} \tag{2.29}$$

Defining a connector force $\boldsymbol{F}^{(c)} = \boldsymbol{F}_1^{(\phi)} = -\boldsymbol{F}_2^{(\phi)}$ leads to the following expression for

the contribution of the connectors to the polymer stress

$$\boldsymbol{n} \cdot \boldsymbol{\tau}_p^{(c)} = -\boldsymbol{n} \cdot \int_{\boldsymbol{Q}} n\psi(\boldsymbol{Q}, t)\boldsymbol{Q}(-\boldsymbol{F}^{(c)})d\boldsymbol{Q} \tag{2.30}$$

or

$$\boldsymbol{\tau}_p^{(c)} = -n \int_{\boldsymbol{Q}} \psi(\boldsymbol{Q}, t)\boldsymbol{Q}(-\boldsymbol{F}^{(c)})d\boldsymbol{Q} = -n \left\langle \boldsymbol{Q}\boldsymbol{F}^{(c)} \right\rangle \tag{2.31}$$

If external forces act on the beads, the corresponding stress, $\boldsymbol{\tau}_p^{(e)}$ can be expressed as

$$\boldsymbol{\tau}_p^{(e)} = \frac{1}{2}n \left\langle \boldsymbol{Q}(\boldsymbol{F}_2^{(e)} - \boldsymbol{F}_1^{(e)}) \right\rangle \tag{2.32}$$

The sum of the connector, external and Brownian contributions to the stress yields the following equation for the polymer contribution to the stress tensor

$$\boldsymbol{\tau}_p = -n \left\langle \boldsymbol{Q}\boldsymbol{F}^{(c)} \right\rangle + \frac{1}{2}n \left\langle \boldsymbol{Q}(\boldsymbol{F}_2^{(e)} - \boldsymbol{F}_1^{(e)}) \right\rangle + nkT\boldsymbol{\delta} \tag{2.33}$$

Diffusion equation

Since the calculation of the distribution function and its averages is essential for calculation of the polymer contribution to the stress tensor, an equation must be derived that describes the evolution of the orientational distribution function for dumbbell models.

Rigid dumbbell   The forces that act on a given rigid dumbbell molecule are the Brownian force, the hydrodynamic force, and forces due to an external potential. The sum of these forces for each bead is then zero for the dumbbell. This yields

$$\boldsymbol{F}_1^{(h)} + \boldsymbol{F}_{-1}^{(h)} + \boldsymbol{F}_1^{(b)} + \boldsymbol{F}_{-1}^{(b)} + \boldsymbol{F}_1^{(e)} + \boldsymbol{F}_{-1}^{(e)} = 0 \tag{2.34}$$

where the subscripts refer to the bead number in Fig. 2-3 and the superscripts refer to the type of force. This equation describes the translational motion of the dumbbell. However, since we are only intereseted in equation of motion for the rotational degrees of freedom, we add up the differences of the various types of forces $\boldsymbol{F}_1^{()} + \boldsymbol{F}_{-1}^{()}$ and

then project this in the polar and azimuthal directions by forming a dot product with the quantity $ss + tt$. Here s is the unit vector in θ direction while t is the unit vector in the ϕ direction. Since $ss + tt + uu = \delta$, where δ is the unit tensor, the balance for the θ and ϕ components of the force balance can be written as

$$(\delta - uu) \cdot [(F_1^{(h)} - F_{-1}^{(h)}) + (F_1^{(b)} - F_{-1}^{(b)}) + (F_1^{(e)} - F_{-1}^{(e)})] = 0 \tag{2.35}$$

We now substitute the following expressions for the Brownian

$$F_\nu^{(b)} = -\nu \frac{kT}{L} \frac{\partial \ln f}{\partial u} \qquad (\nu = \pm 1) \tag{2.36}$$

and hydrodynamic force [9]

$$
\begin{aligned}
F_\nu^{(h)} &= -\zeta([[\dot{r}_\nu]] - v_\nu) \\
&= -\zeta([[\dot{r}_c]] + \frac{1}{2}\nu L[[\dot{u}]] - v_0 - [\kappa \cdot r_c] - \frac{1}{2}\nu L[\kappa \cdot u])
\end{aligned}
\qquad (\nu = \pm 1) \tag{2.37}
$$

in Eq. 2.35 to obtain the following expression for $[[\dot{u}]]$

$$[[\dot{u}]] = [\kappa \cdot u - \kappa : uuuu] - \frac{1}{6\lambda} \frac{\partial \ln f}{\partial u} - \frac{1}{\zeta L}[(\delta - uu) \cdot (F_1^{(e)} - F_{-1}^{(e)})] \tag{2.38}$$

where $\lambda = \zeta L^2/12kT$ is the time constant for the rigid dumbbell. This expression is then substituted in the continuity equation for the orientation distribution function which is a conservation equation that states that dumbbells leaving one orientation must end up in another. Mathemetically, this is expressed by the following relation

$$\frac{\partial f}{\partial t} = -\left(\frac{\partial}{\partial u} \cdot [[\dot{u}]]f\right) \tag{2.39}$$

Substituting Eq. 2.38 in Eq. 2.39 leads to the diffusion equation for the rigid dumbbell

$$\frac{\partial f}{\partial t} = \frac{1}{6\lambda}\left(\frac{\partial}{\partial u} \cdot \frac{\partial f}{\partial u}\right) - \frac{\partial}{\partial u} \cdot \left([\kappa \cdot u - \kappa : uuu]f - \frac{1}{6kT\lambda}\frac{\partial}{\partial u}\phi^{(e)}f\right) \tag{2.40}$$

where $[(\boldsymbol{\delta} - \boldsymbol{uu}) \cdot (\boldsymbol{F}_1^{(e)} - \boldsymbol{F}_{-1}^{(e)})]$ has be set to $(2/L)\partial\phi^{(e)}/\partial\boldsymbol{u}$, for an external interaction potential $\phi^{(e)}$. The diffusion equation in Eq. 2.40 is a partial differential equation for the orientational distribution function f and is periodic in orientation variables θ and ϕ. Since the equation is homogeneous in f, it is solved is conjunction with the normalization condition $\int_{\boldsymbol{u}} f d\boldsymbol{u} = 1$ to uniquely specify the solution.

Elastic dumbbell To develop the diffusion equation for the elastic dumbbell we follow a discussion similar to that for the rigid dumbbell. Since there are no constraints in the elastic dumbbell, we begin with a force balance on each bead rather than the whole dumbbell

$$\boldsymbol{F}_\nu^{(h)} + \boldsymbol{F}_\nu^{(b)} + \boldsymbol{F}_\nu^{(\phi)} + \boldsymbol{F}_\nu^{(e)} = 0 \qquad (\nu = 1, 2) \tag{2.41}$$

where as before, $\boldsymbol{F}_\nu^{(h)}$ is the hydrodynamic drag force, $\boldsymbol{F}_\nu^{(b)}$ is the Brownian force, $\boldsymbol{F}_\nu^{(\phi)}$ is the intramolecular force felt through the connecting spring, and $\boldsymbol{F}_\nu^{(e)}$ is an external force. Each of these forces can be written in a more explicit form as

$$\boldsymbol{F}_\nu^{(h)} = -\zeta[[[\dot{\boldsymbol{r}}_\nu]] - (\boldsymbol{v}_0 + \boldsymbol{\kappa} \cdot \boldsymbol{r})] \tag{2.42}$$

$$\boldsymbol{F}_\nu^{(b)} = -kT(\partial \ln \Psi / \partial \boldsymbol{r}_\nu) \tag{2.43}$$

$$\boldsymbol{F}_\nu^{(\phi)} = -\partial\phi^{(c)}/\partial \boldsymbol{r}_\nu \tag{2.44}$$

where $\phi^{(c)}$ is the connector potential. Again the velocity space is assumed to be equilibrated and hydrodynamic effects are neglected to obtain

$$-\zeta[[[\dot{\boldsymbol{r}}_\nu]] - (\boldsymbol{v}_0 + \boldsymbol{\kappa} \cdot \boldsymbol{r})] - kT(\partial \ln \Psi / \partial \boldsymbol{r}_\nu) + \boldsymbol{F}_\nu^{(\phi)} + \boldsymbol{F}_\nu^{(e)} = 0 \qquad (\nu = 1, 2) \tag{2.45}$$

Since $\boldsymbol{Q} = \boldsymbol{r}_2 - \boldsymbol{r}_1$, subtracting the equations for the two beads yields

$$[[\dot{\boldsymbol{Q}}]] = [\boldsymbol{\kappa} \cdot \boldsymbol{Q}] - \frac{2kT}{\zeta} \frac{\partial}{\partial \boldsymbol{Q}} \ln \psi - \frac{2}{\zeta} \boldsymbol{F}^{(c)} + \frac{1}{\zeta}[\boldsymbol{F}_2^{(e)} - \boldsymbol{F}_1^{(e)}] \tag{2.46}$$

59

This expression is then substituted in the continuity equation for the elastic dumbbell, which is of the same form as Eq. 2.39

$$\frac{\partial \psi}{\partial t} = -\left(\frac{\partial}{\partial \boldsymbol{Q}} \cdot [[\dot{\boldsymbol{Q}}]]\psi\right) \tag{2.47}$$

to obtain the diffusion equation for the elastic dumbbell

$$\frac{\partial \psi}{\partial t} = -\left(\frac{\partial}{\partial \boldsymbol{Q}} \cdot \left\{[\boldsymbol{\kappa} \cdot \boldsymbol{Q}]\psi - \frac{2kT}{\zeta}\frac{\partial}{\partial \boldsymbol{Q}}\psi - \frac{2}{\zeta}\boldsymbol{F}^{(c)}\psi + \frac{1}{\zeta}[\boldsymbol{F}_2^{(e)} - \boldsymbol{F}_1^{(e)}]\psi\right\}\right) \tag{2.48}$$

Here it is relevant to mention two types of elastic dumbbells that have been used extensively in flow modeling. The first is the Hookean dumbbell. In this model, the connector is a Hookean spring and the connector force is given by $\boldsymbol{F}^{(c)} = H\boldsymbol{Q}$ where H is the Hookean spring constant. It can be shown that this model is equivalent to the continuum Oldroyd-B model. However, this model is quite unrealistic, as this spring is infinitely extensible, which is not the case with real polymer molecules. More importantly, the Hookean dumbbell is incapable of reproducing the strain-rate dependent material functions that are characteristic of polymers. Instead, a second model that corrects this shortcoming by imposing finite extensibility has been used in complex viscoelastic flow simulations. The corresponding connector force is given by

$$\boldsymbol{F}^{(c)} = \frac{H\boldsymbol{Q}}{1 - (Q/Q_0)^2} \tag{2.49}$$

where the connector length Q has an upper limiting length of Q_0. This is known as the Finitely Extensile Non-linear Elastic or FENE dumbbell, and was first proposed by Warner [116] as an approximation to the inverse Langevin force law, which can be derived from molecular arguments [9].

The discussion in this section has focused on the diffusion equations for the rigid and elastic dumbbells that can be solved to obtain the orientation distribution function of these micromechanical models for real polymer molecules. Once the orientation distribution function has been obtained, one can evaluate the polymer contribution to the stress tensor by calculating the necessary averages of this distribution. The next

60

two section review this approach and an alternative that uses the stochastic equivalent of the diffusion equation to calculate the polymer contribution to the stress tensor.

2.3.2   Direct Solution of the Diffusion Equation

Direct solution of the diffusion equation for micromechanical models represents an approach that does not rely on mathematical closure approximation for the moments of the orientation distribution function. In doing so, one obtains more accurate predictions of the physical model. However, such an approach necessitates a suitable discretization for the distribution in both physical and configuration space in addition to the discretization of the conservation equations for mass and momentum. The dimensionality of the resulting problem can be large, even for the simple dumbbell models described so far, as enough basis functions must be introduced at each point in space to capture the key features of the distribution function. For this reason, direct solution of the diffusion equation has been restricted to either simple rheometric flows or hybrid simulation with dumbbell models.

Rheometric flows

In rheometric flows, the velocity field is specified and the distribution function only depends on the molecular configuration and time. One, therefore, solves for the distribution function in configuration space with a suitable discretiztion scheme. The earliest computational study with this approach was done by Stewart and Sørensen [105] who used Galerkin's method and spherical harmonics to study the steady shear flow of a dilute suspension of rigid dumbbells. Motivated by the Laplacian term in the diffusion equation (see Eq. 2.40), Stewart and Sørensen used spherical harmonics basis function as these are the eigenfunctions of the operator. In particular, the choice of basis functions was optimal for describing the distribution function in the diffusion dominated limit of small deformation rates. Stewart and Sørensen were able to compute viscosity and normal stress differences for various values of the shear rate. A similar approach has also been used for the analysis of the Doi model for rod-like

61

polymers in the nematic phase. Due to the mean-field interaction potential between rods, the Doi model is a nonlinear partial differential equation for the distribution function, but retains the Laplacian term for the dilute case. Several publications that explore the rich nonlinear dynamical behavior of nematic polymers have used this approach, including the pioneering work of Larson and Öttinger [67], and we use the same later in the thesis.

Warner [116] was the first to extend the work of Stewart and Sørensen [105] to flexible polymers by studying the steady and small-amplitude oscillatory shear flow of FENE dumbbells. This work was later extended by Fan [30] who used spherical harmonics for the orientational degrees of freedom and Jacobi polynomials for the dumbbell length. In this work, Fan had to solve a system of 506 equations to obtain results for flows with a Deborah number of up to 100. This was the same issue faced by Stewart and Sørensen who had to retain upto 144 spherical harmonic terms to accurately capture the highly peaked distribution at high shear rates. At high deformation rates the flow tends to align the model molecules in a prefered direction, which results in a highly localized distribution function. Since spherical harmonics have global support, they are no longer the most appropriate basis functions to use when solving the diffusion equation. Additionally, for models with a configuration dependent diffusivity, spherical harmonics are no longer eigenfunctions of any operator is the diffusion equation. The only significant improvement over spherical harmonics was proposed by Nayak [80] and Suen et al. [107] who used Daubechies wavelets as alternative basis functions, in view of their localization properties and compact support.

Hybrid simulations

The first major work that incorporated the direct solution of the diffusion equation in studying a complex flow was carried out by Nayak [80] who studied two-dimensional flows of rigid dumbbells either in the dilute or nematic phase. She discretized the convection operator in the diffusion equation by means of the discontinuous Galerkin finite element method, and used Daubechies wavelets for the discretization in con-

figuration space. This work has been recently extended by several authors (Suen [108], Chauviere and Lozinski [17, 16]).

In particular, Lozinski et al. use a Galerkin spectral element technique to solve the conservation equations and decouple the problem in physical and configuration space by splitting each time step update into two consecutive sub-steps. The first step updates the solution locally in configuration space with a subsequent global update of the distribution function in physical space. This methods has been used to study both the three dimensional configuration space of the FENE dumbbell [16] and an artificial two-dimensional case where planar dumbbell orientation is assumed [17, 71].

In contrast, Suen [108] has built on the work of Nayak [80] and used a mixed finite-element/wavelet-Galerkin method for computing two-dimensional flows of rigid dumbbells and the double reptation tube model Bird et al. [9]. He uses the DEVSS-G finite element technique [110] to solve the conservation equations along with the discontinuous Galerkin method to solve the diffusion equation in physical space. A semi-implicit time-stepping scheme is used for the configurational degrees of freedom, such that orientational diffusion is treated implicitly and all other operators in the diffusion equation are treated explicitly. This leads to a particularly efficient solution within each finite element and can be parallelized very easily. The same approach has been used in this thesis to develop a hybrid viscoelastic flow simulation of non-interacting rigid dumbbells.

2.3.3   Brownian Dynamics

Brownian dynamics simulations follow a different approach to the computation of molecular orientations and the distribution function. The technique does not invole the solution of the diffusion equation for the distribution function, but instead uses the $3N$ Langevin equations to describe the motion of each bead in a N bead micromechanical model of the polymers. The Langevin equations for the motion of a collection of polymer molecules are the stochastic equivalent, both physically and mathematically, of the Fokker-Planck or diffusion equations for the evolution of the configuration distribution function [83]. In particular, the motion is described by an

Itô stochastic differential equation [83]

$$d\boldsymbol{X}(t) = \boldsymbol{A}(t, \boldsymbol{X}(t))dt + \boldsymbol{B}(t, \boldsymbol{X}(t)) \cdot d\boldsymbol{W}(t) \tag{2.50}$$

that governs the evolution of a vector variable $\boldsymbol{X}$ under the influence of deterministic drift and random Brownian forces such that $\boldsymbol{A}$ is the vector representing the deterministic drift velocity, $\boldsymbol{W}$ is a Wiener stochastic process, and $\boldsymbol{B} \cdot \boldsymbol{W}$ is the change in $\boldsymbol{X}$ due to random forces. In a complex flow the stochastic differential equation applies along flow trajectories and the time derivateive in Eq. 2.50 becomes a material derivative. Instead of solving the Fokker-Planck or diffusion equation for the distribution function, one solves Eq. 2.50 for a large ensemble of realizations of the stochastic process $\boldsymbol{X}$ by means of a suitable numerical technique. The polymer contribution to the stress tensor is then obtained as an ensemble average.

For purpose of illustration, we obtain the stochastic equivalent of the diffusion equation for elastic dumbbell by considering the general Fokker-Planck equation

$$\frac{D\psi}{Dt} = -\frac{\partial}{\partial \boldsymbol{X}} \cdot [\boldsymbol{A}\psi] + \frac{1}{2}\frac{\partial}{\partial \boldsymbol{X}}\frac{\partial}{\partial \boldsymbol{X}} : [\boldsymbol{D}\psi] \tag{2.51}$$

where $\boldsymbol{D}$ is the diffusion matrix given by $\boldsymbol{D} = \boldsymbol{B} \cdot \boldsymbol{B}^T$ and D/Dt denotes the Lagrangian or material derivative. The diffusion equation in Eq. 2.48 cast in the form of Eq. 2.51 reads

$$\frac{D\psi}{Dt} = -\frac{\partial}{\partial \boldsymbol{Q}} \cdot \left[\left\{\boldsymbol{\kappa} \cdot \boldsymbol{Q} - \frac{2}{\zeta}\boldsymbol{F}^{(c)}\right\}\psi\right] + \frac{2kT}{\zeta}\frac{\partial}{\partial \boldsymbol{Q}} \cdot \frac{\partial}{\partial \boldsymbol{Q}}\psi \tag{2.52}$$

where the time derivative in Eq. 2.48 has been changed to a material derivative and external forces have been ignored. Comparing Eq. 2.50 and Eq. 2.52 gives the following Itô stochastic differential equation for the dumbbell connector vector

$$d\boldsymbol{Q} = \left[\boldsymbol{\kappa} \cdot \boldsymbol{Q} - \frac{2}{\zeta}\boldsymbol{F}^{(c)}\right]dt + \sqrt{\frac{4kT}{\zeta}}d\boldsymbol{W} \tag{2.53}$$

This simple example illustrates the relative ease with which one can construct the

stochastic differential equation for a Fokker-Planck equation from kinetic theory. As the stochastic approach does not require explicit solution of the distribution function, a task that can quickly become intractable for diffusion equations that describe micromechanical models with increasingly larger degrees of freedom, it has been used extensively to study the dynamical behavior of multi-link bead-rod and bead-spring chains [27, 104, 40]. Most of these studies have focused on testing various closure approximations that are used to obtain closed form constitutive equations. For example, direct measurements of stresses in a filament stretching rheometer have clearly demonstrated the existence of a stress conformation hysteresis in startup of uniaxial elongational flows of dilute polymeric solutions [28]. Brownian dynamics simulation of the stochastic differential eqution in Eq. 2.53 with the FENE model can capture this phenomenon, while the FENE-P model that preaverages the nonlinear force law does not.

In particular, a very comprehensive examination of the Kramer's bead-rod chain using Brownian dynamics was carried out by Doyle et al. [27]. They were able to show that the stress optical law, which postulates a linear relationship between stress and birefringence of a polymer sample and is used extensively by experimentalists, is only valid in the limit of small alignment of molecules when Brownian motions are dominant. They also found that at high shear rates, there is considerable, and qualitative, discrepancy between the behavior of a FENE dumbbbell and a bead-rod chain. A similar study was carried out by Ghosh [40] that found that a bead-spring chain with 5 springs is sufficient to produce a stress-birefringence loop that is in excellent agreement with prediction of Kramer's chain. Even though a 5 spring chain is still computationally expensive to simulate, it represents a significant coarse graining of the Kramer's chain.

All these studies deal with molecular models in simple homogeneous flow, so that only a single constant strain rate is being considered. In a practical flow, the strain rate will vary with position and the Brownian dynamics simulation must be combined with a discretization in physical space to compute flow field for viscoelastic fluids. We now discuss a method that pioneered this approach and a subsequent significant

improvement.

CONNFFESSIT

Öttinger and Laso [84] were the first to combine finite element techniques with Brownian dynamics simulation in a method known as CONNFFESSIT, which stands for "**C**alculation **O**f **N**on-**N**ewtonian **F**low: **F**inite **E**lements and **S**tochastic **SI**mulation **T**echnique." The method is most naturally exploited as a time marching scheme, and the steady state flow, if it exists, is then obtained as the long time limit of the calculation. At the start of the simulation, a large number of model molecules (such as dumbbells, bead-spring chains, or any other coarse-grained model) are distributed uniformly over the flow domain with initial configuration drawn from the equilibrium distribution. At each time step of the simulation, the conservation equations for mass and momentum are solved first, followed by the integration of the stochastic differential equation as molecules are convected along flow trajectories. This decouples the conservation laws from the stochastic process. The polymer contribution to the stress tensor at a given time is then obtained by means of averaging over the local ensemble of molecules located within each element.

The CONNFFESSIT method has been used to study two-dimensional flows of dumbbell models of dilute polymeric solutions, colloidal dispersions, and liquid crystalline polymers [32, 68, 69]. The method is found to capture all the important qualitative aspects of viscoelastic flow. Furthermore, it has an attractive interpretation in terms of mimicking how real molecules contribute to stress in a polymeric flow. The method is able to accomodate many different types of force laws and molecular models without significant modification. However, it has three major drawbacks. First, the intrinsically Lagrangian formulation of the method requires a great deal of effort and book-keeping to track all the molecules in the flow as they move from element to element. Given the large number of molecules and elements, typically on the order of 10^6 and 10^3, respectively, in a two-dimensional simulation, the associated brute force search of a molecule cannot be justified at each time step. Second, the error in the calculation of the polymer contribution to the stress tensor converges as

$N^{-1/2}$, where N is the number of molecules in a given element of the flow domain. Clearly, each element of the finite element mesh must then contain enough model molecules during the entire simulation for local ensemble averaging. Ideally a simulation should have $N \sim \mathcal{O}(10^3)$, which is not easy to insure especially in flow regions where large spatial gradients develop in the flow field. Third, it has been shown that CONNFFESSIT can exhibit spurious oscillation in the stress field [69], which can affect the numerical accuracy of the computed velocity. For these reasons several improvements were proposed to the CONNFFESSIT algorithm, the most significant being that of Brownian configuration fields.

Brownian Configuration Fields

(a)   (b)
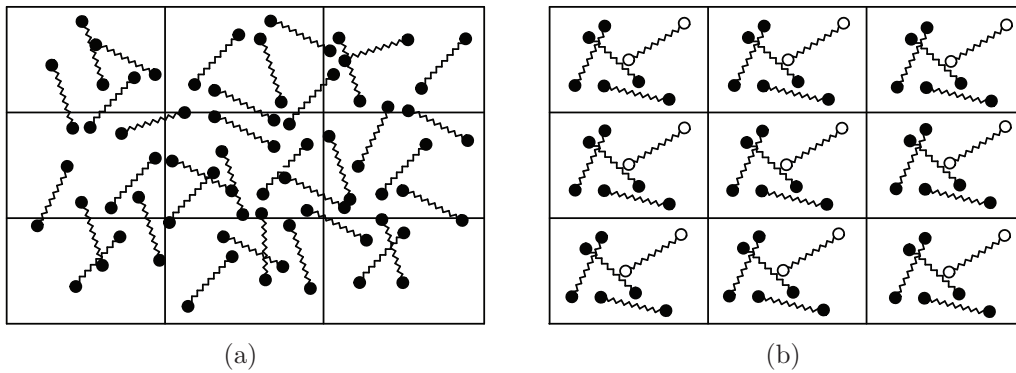
Figure 2-5: Comparison between Lagrangian (CONNFFESSIT) and Eulerian (Brownian configuration fields) implementations. (a) Lagrangian implementation, in which ensembles at adjacent nodes are uncorrelated. (b) Eulerian implementation, where the same ensemble of random numbers is generated at each node in the physical domain.

The method of Brownian configuration fields was introduced by van den Brule [114] and Hulsen et al. [49] to replace the large ensemble of independent molecules in the CONNFFESSIT approach with an ensemble of configuration fields. The main idea is to use correlated ensembles so that instead of tracking the configuration of individual molecules along flow trajectories, the method determines the evolution of a finite number of Eulerian configuration fields such that each field is subjected to a random Wiener process that is uniform in space. This key difference is illustrated in the schematic in Fig. 2-5.

In the original CONNFFESSIT implementation, adjacent points in space were subjected to different random processes at a given time step, which resulted in noisy spatial gradients for the polymer contribution to the stress tensor. By constructing a configuration field in space that is subjected to the same Wiener process results in adjacent points in space that have strongly correlated fluctuations. Consequently, in computing the divergence of the stress tensor for use in the momentum equation, differences are taken for the configurational averages taken over an ensemble of fields, which reduces fluctuations. With the assumption of correlated ensembles in space, the Brownian configuration field method in essence behaves as a variance reduced formulation of the original CONNFFESSIT approach.

The stochastic differential equation that governs the evolution of these configuration fields is given by

$$d\boldsymbol{X}_k = \{-\boldsymbol{v} \cdot \boldsymbol{\nabla}\boldsymbol{X}_k + A(\boldsymbol{X}_k)\}dt + B(\boldsymbol{X}_k) \cdot d\boldsymbol{W}_k(t) \qquad (2.54)$$

where $\{\boldsymbol{X}_k\}_{k=1}^{N_f}$ denotes an ensemble of N_f configuration fields defined over the entire flow domain. This is indeed the Eulerian formulation of the stochastic differential equation Eq. 2.50 with the addition of the convective term $\boldsymbol{v} \cdot \boldsymbol{\nabla}\boldsymbol{X}_k$. The stochastic factor $d\boldsymbol{W}_k$, however, only depends on time. As a result, the spatial gradient of the configuration field is a well defined function of the spatial coordinates. The discretization of a field $\boldsymbol{X}_k$ can be constructed by means of a standard finite element, and the polymer contribution to the stress tensor can be computed as an ensemble average over all configuration fields

$$\boldsymbol{\tau}_p = \frac{1}{N_f}\sum_{k=1}^{N_f}\boldsymbol{g}(\boldsymbol{X}_k) \qquad (2.55)$$

where $\boldsymbol{g}$ is a model dependent tensorial function of configuration. In the original paper by van den Brule et al. [114], the authors performed simulations of a solution of Hookean dumbbells (the Oldroyd-B model) flowing past a cylinder in a channel, and obtained smooth stress fields that matched extremely well with simulations performed

using a conventional, continuum, Oldroyd-B constitutive equation. The simulation employed the discontinuous Galerkin finite element method to discretize Eq. 2.54, which allows for element by element solution of the problem through parallel algorithms.

There are, however, two drawbacks to the Brownian configuration field method. First, it has been shown recently that while the use of correlated ensembles reduces the variance of the velocity, it increases the variance of the viscoelastic stress (see work of Bonvin and Picasso [12]). This counter intuitive finding must be due to the nonlinear coupling between the conservation laws and the stochastic differential equation, since the variance of the approximate stress should not be affected by the spatial dependence of the Wiener process for a deterministic velocity field. Second, the approach cannot be applied to problems that are dominated by physical fluctuations, such as flows on a molecular length scale, since real molecular orientations are not continuous and Brownian forces on real molecules are not spatialy correlated.

Despite these two drawbacks, the Brownian configuration field method has been improved upon with the idea of control variates, which introduces a parallel stochastic simulation of a quantity that has about the same fluctuations as the original problem, but with a vanishing average. Subtracting this quantity from the true stochastic process provides the correct average of the original problem but with reduced variance. This approach was first demonstrated by Melchior and Ottinger [79] and has been implemented within the framework of Brownian configuration fields for a complex flow calculation where a FENE dumbbell model was simulated with a closed FENE-P model defined as a control variate [112]. This approach has now become standard and has been used to study two-dimensional flow of bead-spring chains [61] and three-dimensional flows of Hookean dumbbells [89], which represent significant achievements in hybrid simulations.

Chapter 3

System-Level Analysis of Viscoelastic Flows

3.1 State-of-the-Art Approaches

When the constitutive models described in the last chapter are combined with the conservation of mass and momentum, one obtains a set of partial differential (or integro-differential) equations that can be solved by means of a suitable grid-based numerical method. This is the primary approach adopted by computational rheologists to elucidate the nonlinear coupling between rheological behavior, flow-induced evolution of the polymer microstructure, flow parameters (such as geometry and boundary conditions) and final product properties.

While the majority of publications for simulations of complex viscoelastic flow are based on continuum approaches, significant work has been done to couple the conservation equations at the macroscopic level with kinetic theory models (both Fokker-Planck and stochastic models) in order to describe the polymer contribution to the fluid stress tensor. While such an approach is more demanding in terms of computer resources, it allows for the direct use of kinetic theory models in complex flows, without having to resort to closure approximations, which often are of doubtful validity [57]. An extensively studied example is the Doi model in shear flow, where it is well known that closure approximations suppress tumbling effects observed ex-

perimentally with liquid crystals [60], a phenomenon that is qualitatively matched by the unclosed model [67].

Consequently, sizeable effort has been devoted to the development of hybrid methods that allow the study of more detailed molecular models in complex flows. Until recently, such methods were restricted to the computation of molecular orientation for low-dimensional models in complex, two-dimensional, time-dependent flows [109], but the work of Koppol et al. [61] has extended hybrid simulations to include more realistic models, by carrying out stochastic simulation of a bead-spring chain with up to 6 springs in a circular channel with smooth contraction-expansion geometry. Despite this significant improvement over the state-of-the-art, such simulations have been made possible primarily due to availability of better computational resources with time. Even though they make efficient use of massively parallel computers, no new numerical approach or method has been proposed. More importantly, however, such simulations are only able to carry out stability analyses by running very precise time-dependent computations for perturbations to the base flow [100, 101, 102]. As a result, it remains impossible to apply the traditional computational tools used to perform system-level stability and bifurcation analysis of closed macroscopic equations to these hybrid simulators.

This chapter begins by describing a computational framework that can enable the computational rheologist to perform system-level analysis with viscoelastic flows by running computational "experiments" on the well-developed hybrid simulators. The computational framework will be described with a simple dynamical system serving as the example. This is followed by a quick review of the fast developing area of iterative matrix-free numerical analysis, which is particularly suited to the task of avoiding closure approximation when bridging microscopic simulations with macroscopic system-level modelling. In particular, it will be shown how one can enable microscopic simulators (kinetic theory models and Brownian dynamics) to obtain stationary states without the need to pass through an intermediate, macroscopic-level explicit evolution equation description of the dynamics of viscoelastic fluid flow. The application of the finite element method for studying viscoelastic flows will be de-

scribed next, followed by a review of numerical bifurcation analysis and the algorithm used to generate results in this thesis.

3.2   Coarse Time-stepper Framework

In building hybrid simulators one typically obtains a large system of ordinary differential equations that describe the detailed dynamics of the polymer microstructure. This could result either from an appropriate discretization of a Fokker-Planck equation or from a stochastic description of the internal degrees of freedom of the polymer molecule. Let us denote these microscopic unknowns by $\boldsymbol{y}(t)$ such that

$$\frac{d\boldsymbol{y}}{dt} = \boldsymbol{f}(\boldsymbol{y}), \qquad \boldsymbol{y} \in \mathbb{R}^m, \quad \text{and} \qquad m \gg 1 \tag{3.1}$$

This system of ODE's can be written as a black-box *time stepper* code that gives the time-t map ($\mathcal{T}_d^t$, subscript d corresponds to *detailed*) for the system, if provided initial data and the integration time t. In other words,

$$\boldsymbol{y}(t_0 + t) = \mathcal{T}_d^t \boldsymbol{y}(t_0),$$

where $\boldsymbol{y}$ is a solution to Eq. 3.1. Computations to extract information about the coarse dynamics of the system given in Eq. 3.1 are the current state-of-the-art in viscoelastic flow modelling as the dynamical equations of the corresponding coarse unknowns can only be obtained via closure approximations. These coarse unknowns are typically averages of the polymer microstructure or simply the polymer contribution to the fluid stress tensor. While one may obtain these coarse unknowns during the detailed simulation, the inability to write close equations for these unknowns limits the utility of direct simulation of Eq. 3.1 to yielding only the dynamical behavior and stable solutions. The computational framework presented in this section is the primary enabling step within the framework for obtaining the behavior of the coarse unknowns and performing system-level analysis.

Clearly, as a first step, we need to define what constitutes an appropriate macro-

scopic/coarse representation. In general, our coarse formulation takes the form

$$\frac{d\boldsymbol{Y}}{dt} = \boldsymbol{F}(\boldsymbol{Y}), \qquad \boldsymbol{Y} \in \mathbb{R}^M, \quad \text{and} \qquad M \ll m, \tag{3.2}$$

where the function $\boldsymbol{F}$ is not available, but once we choose a coarse variable set, $\boldsymbol{Y}$, we can also define a *restriction* operator $\mathcal{R}$ that takes the microscopic description $\boldsymbol{y}$ to the chosen macroscopic description $\boldsymbol{Y}$. This operator could involve averaging over microstructural state or the ensemble of simulations in a stochastic description. If the detailed system can be successfully modelled at the coarse/macroscopic level through the coarse variable set $\boldsymbol{Y}$, even though the function $\boldsymbol{F}$ is unavailable in closed form, this suggests that any other coarse variables that may be derived from the detailed set can be approximated as functionals of the $\boldsymbol{Y}$. This is indeed the primary assumption in writing closed equations for the microstructural state of a polymer in terms of a few low order averages or moments by assuming that higher moments of the microstructural state can be approximated as functionals of these low order moments.

Within dynamical systems theory this corresponds to the existence of a fast-attracting "slow" manifold, parameterized by the selected set $\boldsymbol{Y}$. This manifold embodies a closure of Eq. 3.1 such that all components of $\boldsymbol{Y}$ vary slowly on this manifold when observing the dynamics of the detailed time-stepper. Similar assumptions also underpin the theory of Inertial Manifolds, Approximate Inertial Manifolds [39] and many singularly perturbed systems that arise in engineering modelling. In particular, the reduced dynamical models for many chemical and physical processes hinge on the existence of a low-dimensional, attracting, invariant "slow" manifold that characterizes the long-term process dynamics. When the dynamics of the problem approach this manifold, it becomes possible to describe the full state of the system in terms of the unknowns that parameterize this manifold. As a result many model reduction schemes are developed around identification of this manifold without invoking pseudo steady-state or equilibrium assumptions for the "fast" unknowns that are not mathematically rigorous and may not always result in an accurate model [92]. An example

of such a scheme is the Intrinsic Low-Dimensional Manifold approach of Mass and Pope [77] that has been used extensively in problems associated with combustion.

Suppose now for example that a "slow" manifold exists for the physical problem in Eq. 3.1. Using the theory of singularly perturbed systems, it can then be shown that there exists a change of variables, $\boldsymbol{y} \mapsto \boldsymbol{u} = (\boldsymbol{u}_1, \boldsymbol{u}_2)$ in Eq. 3.1 such that

$$\frac{d\boldsymbol{u}_1}{dt} = \boldsymbol{g}_1(\boldsymbol{u}_1, \boldsymbol{u}_2) \qquad \boldsymbol{u}_1 \in \mathbb{R}^N, \boldsymbol{u}_2 \in \mathbb{R}^{m-N} \qquad (3.3)$$
$$\frac{d\boldsymbol{u}_2}{dt} = \frac{1}{\epsilon}\boldsymbol{g}_2(\boldsymbol{u}_1, \boldsymbol{u}_2)$$

with $\epsilon \ll 1$. If we also assume that $\boldsymbol{u}_2$ can be expressed in terms of $\boldsymbol{u}_1$ such that $\boldsymbol{u}_2 = \boldsymbol{h}(\boldsymbol{u}_1)$ and $\boldsymbol{g}_2(\boldsymbol{u}_1, \boldsymbol{h}(\boldsymbol{u}_1)) = 0$, this is sufficient to identify $\boldsymbol{u}_1$ as the coarse variable. The evolution equation for the coarse variable is then given by

$$\frac{d\boldsymbol{Y}}{dt} = \boldsymbol{F}(\boldsymbol{Y}) = \frac{d\boldsymbol{u}_1}{dt} = \boldsymbol{g}_1(\boldsymbol{u}_1, \boldsymbol{h}(\boldsymbol{u}_1)) \qquad (3.4)$$

It is important to note that the functions $\boldsymbol{g}_1, \boldsymbol{g}_2$ and $\boldsymbol{h}$ are unknown and cannot be used as a basis for direct numerical simulation. It will be demonstrated in a numerical example that a dynamical system in the form of Eq. 3.3 exhibits dynamic behavior evolving over two vastly different time scales, and for an integration time longer that the "fast" time scale leads to a good approximation of the "slow" manifold.

The main tool that allows the use of microscopic descriptions to perform numerical tasks at the coarse/macroscopic level is the coarse time-stepper [111], denoted by $\mathcal{T}_c^\tau$, which implements an approximation of the time-τ map for Eq. 3.2 such that the equation for macroscopic evolution is unavailable in closed form. Since we do not have the function $\boldsymbol{F}$, we can only approximate the coarse behavior. More importantly, the time horizon for the coarse time stepper, τ, should be chosen such that it captures the true macroscopic dynamics without making the computation of $\mathcal{T}_d^\tau$ too expensive. At a minimum τ should be large enough so that "fast" dynamics have decayed and the solution has approached the "slow" manifold.

In addition to the restriction operation described previously, another operator

links the *detailed* and *coarse* time steppers: $\mathcal{L}$ is the non-unique *lifting* operator that maps the macroscopic description $\boldsymbol{Y}$ onto a consistent microscopic description $\boldsymbol{y}$. Consistency requires $\mathcal{RL} = I$ so that lifting from the macroscopic to the microscopic and then restricting back to the macroscopic has no effect on the macroscopic state. Hence, given an initial macroscopic condition for the macroscopic state, $\boldsymbol{Y}(t_0)$, the coarse time stepper consists of the following steps:

- Construct a single or an ensemble of microscopic states such that $\boldsymbol{y}(t_0) = \mathcal{L}\boldsymbol{Y}(t_0)$.

- Use the detailed time-stepper, Eq. 3.1 to evolve the microscopic states for a short macroscopic time τ to generate $\boldsymbol{y}(t_0 + \tau) = \mathcal{T}_d^\tau \boldsymbol{y}(t_0)$.

- Obtain the restriction of the evolved microscopic state such that $\boldsymbol{Y}(t_0 + \tau) = \mathcal{R}\boldsymbol{y}(t_0 + \tau)$.

In essence, the coarse time stepper can be defined as

$$\mathcal{T}_c^\tau = \mathcal{R}\mathcal{T}_d^\tau \mathcal{L}$$

If the detailed time-stepper Eq. 3.1 has an equivalent coarse description Eq. 3.4, then independent of the initial condition provided by the lifting operator, the solution should quickly approach the slow manifold for $\tau \gg \epsilon$, at which point, the dynamics of Eq. 3.1 should approximate the real dynamics of the unavailable Eq. 3.4.

Example   Let's consider a simple example where the microscopic equation Eq. 3.1 has the form

$$\begin{aligned}
\frac{dy_1}{dt} &= 1 - y_1 \\
\frac{dy_2}{dt} &= 50(1 - y_1^3 - y_2)
\end{aligned} \tag{3.5}$$

Eq. 3.5 is already in the form of Eq. 3.3 with $\epsilon = 1/50 = 0.02$. The results of numerically integrating Eq. 3.5 are shown in Fig. 3-1 where the solution rapidly moves to the slow manifold $y_2 = 1 - y_1^3$ for initial data far from the manifold. We also build a coarse time-stepper for Eq. 3.5 by defining $\mathcal{L}Y = (Y, 1/2)$ and $Y = \mathcal{R}(y_1, y_2)^T = y_1$.

The results for this coarse time-stepper are shown in Fig. 3-2. For $\tau = 0.1$ and $Y(0) = -1$ it can be observed that the lifted solutions rapidly approach the slow manifold at each call to the coarse time-stepper where the solution from the previous call at $t = n\tau$ has been restricted and lifted such that y_2 is always initialized to $1/2$. In addition, the restricted solution at $t = n\tau$ is also shown as function of time along with the exact solution obtained from solving Eq. 3.5.
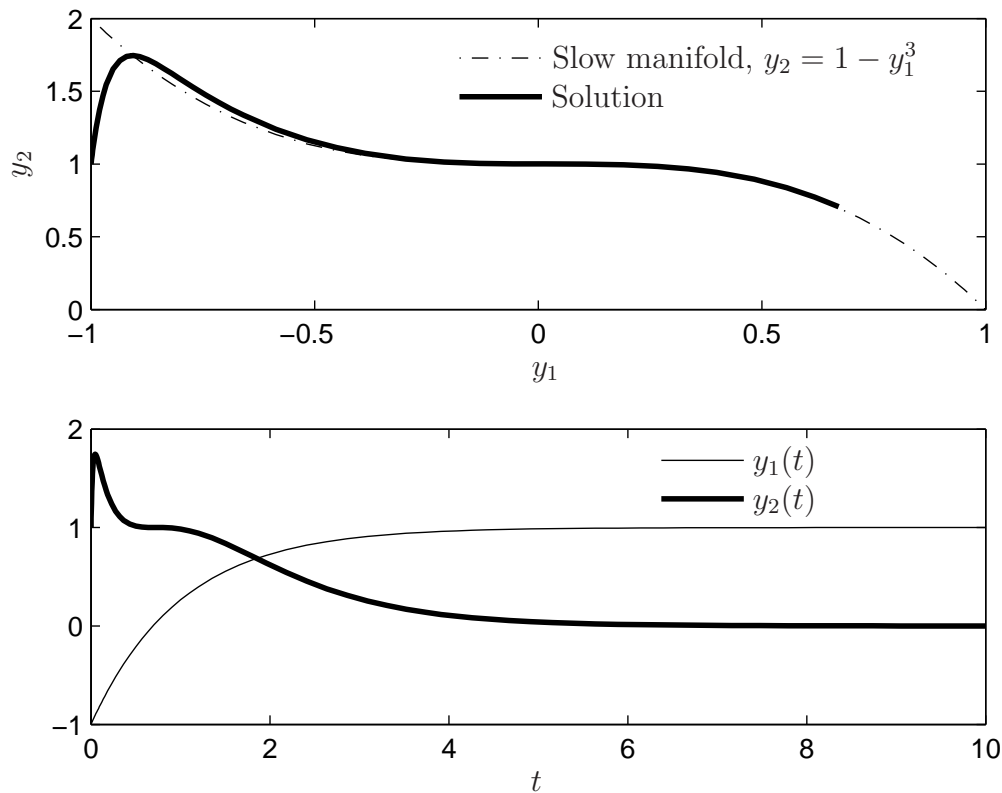
Figure 3-1: Solution of Eq. 3.5 with $\epsilon = 0.02$, $y_1(0) = -1$, $y_2 = 1$. The top figure shows the solution plotted in (y_1, y_2) phase space while the bottom figure shows the solution as a function of time.

In this example, the dynamics evolve at vastly different time scales that can be estimated by the inverse of the eigenvalues of the Jacobian of Eq. 3.5 at steady state $(1, 0)^T$. The eigenvalues, which are equal to -1 and -50, have a significant spectral gap. Here we use $\tau = 0.1$, which is 5 times the characteristic timescale of the faster eigenmode but only 1/10th of the slower eigenmode. Since τ must be large enough for
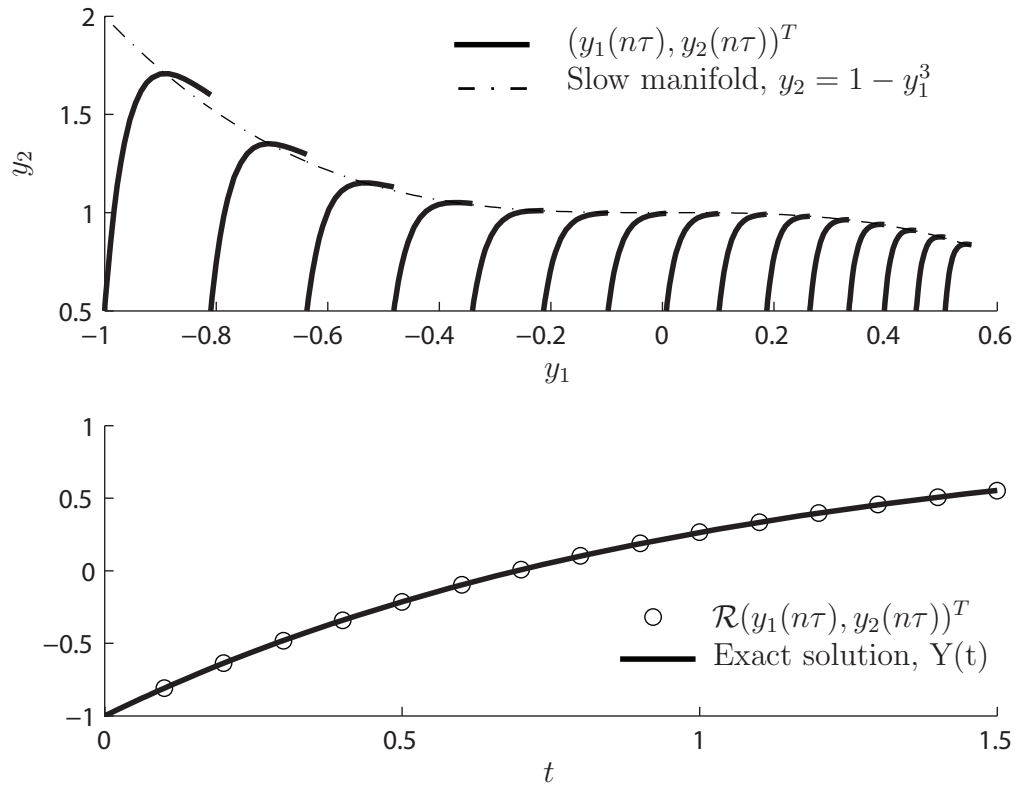
Figure 3-2: Solution of Eq. 3.5 with coarse time-stepper using $\tau = 5\epsilon = 0.1$ and $Y(0) = -1$. The top figure shows the lifted solution in (y_1, y_2) phase space while the bottom figure shows the restricted solution as a function of time along with the exact solution.

the "fast" dynamics to approach the slow manifold, this suggests that problems with large gaps in the eigenspectrum, or small ϵ, will be especially amenable to numerical analysis with the coarse time-stepper.

To begin with, we will be primarily interested is using the coarse time-stepper for Eq. 3.1 to obtain the stationary states of Eq. 3.2. One naive way is to use the coarse time-stepper $\mathcal{T}_c^\tau$ to evolve an initial condition in time through direct simulation. However, this would be no different from the existing state-of-the-art in computational rheology. In addition, if the coarse system of Eq. 3.2 also includes a real parameter λ such that

$$\frac{d\boldsymbol{Y}}{dt} = \boldsymbol{F}(\boldsymbol{Y};\lambda), \qquad \boldsymbol{Y} \in \mathbb{R}^M, \quad \text{and} \quad M \ll m, \tag{3.6}$$

then we are also interested in how the qualitative behavior of the stationary solutions change with λ. This task initially appears impossible since we cannot apply the standard numerical tools used to study closed equations to $\boldsymbol{F}$, which is unknown in explicit form. All we have access to is an approximate coarse time-stepper that provides evolution of $\boldsymbol{Y}$ for short times $\tau \ll 1$. However, since construction of the coarse time-stepper requires clear separation of timescales, exhibited in the eigenspectrum of the system at steady state, this fact can be exploited by combining Newton's method with iterative methods for linear systems, in what is known as Newton iterative methods [54]. The following section describes how such a structure of the eigenspectrum is particularly well suited for this approach.

3.3   Newton's Method with Coarse Time-stepper

Let us assume that Eq. 3.6 has a steady state $\boldsymbol{Y}^*(\lambda)$. Since $\frac{d\boldsymbol{Y}}{dt} = \boldsymbol{0}$ at steady state, it is then obvious that $\boldsymbol{Y}^*(\lambda)$ is also a fixed point for the coarse time-stepper, i.e.

$$\boldsymbol{Y}^* - \mathcal{T}_c^\tau \boldsymbol{Y}^* = \boldsymbol{0} \tag{3.7}$$

This relationship suggests that one approach to obtaining the steady state $\boldsymbol{Y}^*$ is to start with some initial guess $\boldsymbol{Y}^0$ and use the coarse time-stepper to evolve this guess

in time such that

$$\boldsymbol{Y}^{k+1} = \mathcal{T}_c^\tau \boldsymbol{Y}^k \tag{3.8}$$

for $k \geq 0$. There are several problems with this approach. First, by assumption the coarse time-stepper $\mathcal{T}_c^\tau$ can only be called for short τ making this approach clearly infeasible. Second, it is well-known that convergence rate for the error in fixed-point iterations is only linear. And finally, fixed-point iterations of the form in Eq. 3.8 will be unable to find unstable solutions of Eq. 3.6.

For this reason we consider Newton's method, which gives quadratic convergence in the error and can also locate unstable solutions to Eq. 3.7. We begin by defining the nonlinear residual

$$\boldsymbol{G}(\boldsymbol{Y}; \lambda) = \boldsymbol{Y} - \mathcal{T}_c^\tau \boldsymbol{Y} \tag{3.9}$$

which leads to the following sequence for Newton iterations

$$\boldsymbol{Y}^{k+1} = \boldsymbol{Y}^k - \left[\boldsymbol{I} - \frac{\partial \mathcal{T}_c^\tau}{\partial \boldsymbol{Y}}\right]^{-1} \left(\boldsymbol{Y} - \mathcal{T}_c^\tau \boldsymbol{Y}\right) \tag{3.10}$$

The sequence for Newton iterations can also be expressed as a linear system

$$\boldsymbol{G}'(\boldsymbol{Y}; \lambda)\boldsymbol{s} = -\boldsymbol{G}(\boldsymbol{Y}; \lambda) \tag{3.11}$$

where $\boldsymbol{s} = \boldsymbol{Y}^{k+1} - \boldsymbol{Y}^k$ denotes the Newton step, and $\boldsymbol{G}'$ is the Jacobian of Eq. 3.9 with respect to $\boldsymbol{Y}$. As a consequence, the process of obtaining Newton iterates requires computation of the Newton step via solution of Eq. 3.11. If the evaluation, storage and factorization of the Jacobian matrix is not prohibitive, one can proceed by using direct methods, such as Gaussian elimination to compute the Newton step. For our problem, however, this requires the computation of the Jacobian of $\mathcal{T}_c^\tau$, which is not available in closed form and is expensive to approximate numerically. Additionally, we are also concerned with obtaining the eigenvalues of the Jacobian of the coarse time-stepper in order to ascertain stability of the computed steady states. We address this issue by invoking iterative methods from numerical linear algebra that only require the product of the matrix on a given vector to solve the linear system rather than

the matrix itself. For the linear system in Eq. 3.11 this is equivalent to evaluating the nonlinear residual in Eq. 3.9, with the negative sign. More importantly, iterative methods converge in far fewer iterations than the dimension of the linear system and provide excellent estimates for the extreme eigenvalues of the associated matrix, that is, eigenvalues near the edge of the spectrum of the matrix. Fortunately, these are precisely the eigenvalues of interest in determining stability with the coarse time-stepper framework.

3.3.1 Review of Iterative Methods

Consider the prototypical linear system

$$\boldsymbol{Ax} = \boldsymbol{b} \tag{3.12}$$

and eigenvalue problem

$$\boldsymbol{Ay} = \lambda \boldsymbol{y} \tag{3.13}$$

where $\boldsymbol{A}$ is a $n \times n$ matrix, and $\boldsymbol{x}$ and $\boldsymbol{b}$ are n-dimensional column vectors. Additionally, $\boldsymbol{y}$ is the nonzero n-dimensional *eigenvector*, and λ is the corresponding *eigenvalue.* Most algorithms in numerical linear algebra are concerned with obtaining the solution of either Eq. 3.12 or 3.13. Some of the well-known techniques, also known as direct methods, include Gaussian elimination, QR factorization, and Schur factorization. These algorithms typically require $\mathcal{O}(n^3)$ floating point operations, which can be especially prohibitive as n becomes large, which is typical for most practical problems including the problems that form the topic of this thesis. In particular, the large dimension of the matrix under consideration arises indirectly through discretization of differential or integral equations, even though most large matrices of computational interest are simpler than their vast number of individual entries might suggest. For example, a finite element discretization of a partial differential equation may lead to a matrix with a large dimension, say $n = 10^5$, but with only $m = 10$ nonzero entries per row. This gives special structure to the matrix, often referred to

as the *sparsity* of the matrix. Iterative methods exploit this very fact to solve matrix problems in Eqs. 3.12 and 3.13 in $\mathcal{O}(n^2)$ rather than $\mathcal{O}(n^3)$ operations. The primary distinguishing feature of iterative methods is that they require nothing more than the ability to compute $\boldsymbol{Ax}$ for any given $\boldsymbol{x}$, which can be easily obtained in only $\mathcal{O}(mn)$ rather than $\mathcal{O}(n^2)$ operations. This is clearly different from the algorithms of direct linear algebra, which explicitly manipulate matrix entries so as to introduce zeros, but in the process generally destroy sparsity.

Even though sparsity is the most often exploited structure of these large matrices, primarily due to the discretization of partial differential equations to study physical phenomenon, more recently it has become apparent that other kinds of matrix structure may also be exploitable, even though the matrices involved are dense (the opposite of sparse) [113]. In this thesis, the motivation for using iterative methods is derived from two reasons. First, only matrix-vector products can be readily obtained for the problem in Eq. 3.11 by making calls to the coarse time-stepper, as the computation, storage and factorization of the Jacobian matrix for a large-scale problem is clearly prohibitive. Second, the unknown Jacobian matrix is expected to contain gaps in its eigenspectrum. This argument follows from the construction of the coarse time-stepper that exploits the existence of a slow manifold or closure, albeit an unknown one, for the underlying dynamical system.

Projecting to Krylov Subspaces   The iterative methods used in this thesis are based on the idea of constructing a low-dimensional Krylov subspace for the n-dimensional problem in Eq. 3.12. Given a matrix $\boldsymbol{A}$ and a vector $\boldsymbol{b}$, the associated Krylov sequence is the set of vectors $\boldsymbol{b}$, $\boldsymbol{Ab}$, $\boldsymbol{A^2b}$, $\boldsymbol{A^3b}$, ... that can be readily obtained by calling a black box code for computing matrix vector products. The corresponding Krylov subspaces are then the spaces spanned by successively larger groups of these vectors. While there are several iterative algorithms that are built on Krylov subspace methods [95], we will focus on two algorithms, namely the GMRES and Arnoldi procedures, that solve Eqs. 3.12 and 3.13, respectively, for general non-hermitian matrices ($\boldsymbol{A} \neq \boldsymbol{A^*}$), where $\boldsymbol{A^*}$ denotes the transpose of the complex conjugate of $\boldsymbol{A}$.

In either procedure, the projection to Krylov subspaces reduces the original matrix problem to a sequence of matrix problems of dimensions $m = 1, 2, 3, \ldots$. For nonhermitian $\boldsymbol{A}$, this reduction results in matrices that have Hessenberg form, that is they are almost triangular, with zeros entries either above or below the first superdiagonal or subdiagonal, respectively. As will be described next, the Arnoldi algorithm approximates eigenvalues of $\boldsymbol{A}$ by computing the eigenvalues of certain Hessenberg matrices of successively larger dimensions.

3.3.2 Arnoldi Method for Computing Eigenvalues

All algorithms for eigenvalue computation of a matrix are based on the basic idea of carrying out a factorization of the matrix that reduces it to either a diagonal or triangular matrix such that the eigenvalues of the original matrix explicitly appear on the diagonal of the resulting matrix. The most widely used and general algorithm for this is the Schur factorization

$$\boldsymbol{A} = \boldsymbol{Q}\boldsymbol{T}\boldsymbol{Q}^* \tag{3.14}$$

where $\boldsymbol{Q}$ is unitary, that is $\boldsymbol{Q}^*\boldsymbol{Q} = \boldsymbol{I}$, and $\boldsymbol{T}$ is a upper-triangular. The Schur factorization is accomplished by first producing an upper Hessenberg matrix $\boldsymbol{H}$ from $\boldsymbol{A}$, with zeros below the first subdiagonal, followed by a sequence of iterations to convert the Hessenberg matrix to a triangular form $\boldsymbol{T}$. The complete reduction of $\boldsymbol{A}$ to Hessenberg form is expressed as

$$\boldsymbol{A} = \boldsymbol{Q}\boldsymbol{H}\boldsymbol{Q}^* \tag{3.15}$$

or $\boldsymbol{A}\boldsymbol{Q} = \boldsymbol{Q}\boldsymbol{H}$. This form is analogous to factorizing the matrix $\boldsymbol{A}\boldsymbol{Q}$ into a unitary and triangular matrix in what is known as QR factorization. The two most popular approaches for obtaining the QR factorization are Householder reflections and Gram-Schmidt orthogonalization [113]. Householder reflections obtain this reduction, by carrying out transformations that reveal the factorization only at the end of the

procedure, as it true of all direct methods. In contrast, the Gram-Schmidt process has the advantage that it can be stopped part-way, leaving one with a reduced QR factorization of the first m columns of the matrix. The Arnoldi method is essentially a modified Gram-Schmidt procedure for transforming a matrix to Hessenberg form when n is large.

Algorithm The Arnoldi iteration uses the stabilized Gram-Schmidt process to produce a sequence of orthonormal vectors, $\boldsymbol{q}_1, \boldsymbol{q}_2, \boldsymbol{q}_3, \ldots$, called the Arnoldi vectors, such that for every m, the vectors $\boldsymbol{q}_1, \boldsymbol{q}_2, \ldots, \boldsymbol{q}_m$ span the Krylov subspace $\mathcal{K}_m = \langle \boldsymbol{b}, \boldsymbol{A}\boldsymbol{b}, \boldsymbol{A^2}\boldsymbol{b}, \ldots, \boldsymbol{A}^{m-1}\boldsymbol{b} \rangle$. The algorithm starts with an arbitrary vector $\boldsymbol{b}$ such that $\boldsymbol{q}_1 = \boldsymbol{b}/\|\boldsymbol{b}\|$ and computes

$$
\begin{aligned}
&\textbf{for } m = 1, 2, 3, \ldots \\
&\qquad \boldsymbol{v} = \boldsymbol{A}\boldsymbol{q}_m \\
&\qquad \textbf{for } j = 1, \ldots, m \\
&\qquad\qquad h_{jm} = \boldsymbol{q}_j^* \boldsymbol{v} \\
&\qquad\qquad \boldsymbol{v} = \boldsymbol{v} - h_{jm}\boldsymbol{q}_j \\
&\qquad \textbf{end for} \\
&\qquad h_{m+1,m} = \|\boldsymbol{v}\| \\
&\qquad \boldsymbol{q}_{m+1} = \boldsymbol{v}/h_{m+1,m} \\
&\textbf{end for}
\end{aligned}
\tag{3.16}
$$

In the algorithm, the j-loop implements Gram-Schmidt process by projecting out the components of $\boldsymbol{q}_{m+1}$ in the directions of $\boldsymbol{q}_1, \boldsymbol{q}_2, \ldots, \boldsymbol{q}_m$ to ensure the orthogonality of all the generated vectors. From the quantities generated by the algorithm one obtains the following equality

$$
\boldsymbol{A}\boldsymbol{q}_m = \sum_{j=1}^{m+1} h_{jm}\boldsymbol{q}_j
\tag{3.17}
$$

84

This equality can be written in matrix form as

$$AQ_m = Q_{m+1}\tilde{H}_m \tag{3.18}$$

or as

$$AQ_m = Q_m H_m + h_{m+1,m} q_{m+1} e_m^* \tag{3.19}$$

where, $e^* \equiv (0, 0, \ldots, 1)$ is the m-dimensional unit vector. This introduces two matrices: the $n \times m$ matrix Q_m whose columns are the first m columns of Q,

$$Q_m = \begin{bmatrix} q_1 & q_2 & \cdots & q_m \end{bmatrix} \tag{3.20}$$

and the $(m+1) \times m$ upper-left section of H denoted by $\tilde{H}_m$, which is also a Hessenberg matrix

$$\tilde{H}_m = \begin{bmatrix} h_{11} & h_{12} & \cdots & & h_{1m} \\ h_{21} & h_{22} & \cdots & & \vdots \\ & \ddots & \ddots & & \vdots \\ & & h_{m,m-1} & h_{mm} \\ & & & & h_{m+1,m} \end{bmatrix} \tag{3.21}$$

Writing out the algorithm in matrix form shows that the product $Q_m^* Q_{m+1}$ is the $n \times (n+1)$ identity matrix, i.e. the $n \times (n+1)$ matrix with 1 on the main diagonal and 0 elsewhere. Multiplying the right hand side of Eq. 3.18 from the left by Q_m^* yields $Q_m^* Q_{m+1} \tilde{H}_m$, which is the $m \times m$ Hessenberg matrix obtain by removing the last row of $\tilde{H}_m$

$$H_m = \begin{bmatrix} h_{11} & h_{12} & \cdots & & h_{1m} \\ h_{21} & h_{22} & \cdots & & \vdots \\ & \ddots & \ddots & & \vdots \\ & & h_{m,m-1} & h_{mm} \end{bmatrix} \tag{3.22}$$

Eq. 3.18, therefore, yields the Hessenberg matrix via this simplification as

$$\boldsymbol{H}_m = \boldsymbol{Q}_m^* \boldsymbol{A} \boldsymbol{Q}_m \qquad (3.23)$$

While we have just shown how the Arnoldi procedure generates the Hessenberg reduction of $\boldsymbol{A}$, one can make several interpretations from the process. First, the relationship in Eq. 3.17 suggests that the vectors $\boldsymbol{q}_j$ generated by the process form an orthonormal bases of the successive Krylov subspaces, i.e.

$$\mathcal{K}_m = \left\langle \boldsymbol{b}, \boldsymbol{A}\boldsymbol{b}, \boldsymbol{A^2}\boldsymbol{b}, \ldots, \boldsymbol{A}^{m-1}\boldsymbol{b} \right\rangle = \left\langle \boldsymbol{q}_1, \boldsymbol{q}_2, \ldots, \boldsymbol{q}_m \right\rangle$$

Hence, if we were to explicitly form a Krylov matrix

$$\boldsymbol{K}_m = \left[\begin{array}{c|c|c|c} \boldsymbol{b} & \boldsymbol{A}\boldsymbol{b} & \ldots & \boldsymbol{A}^{m-1}\boldsymbol{b} \end{array} \right] \qquad (3.24)$$

with a QR factorization $\boldsymbol{K}_m = \boldsymbol{Q}_m \boldsymbol{R}_m$, then the matrix $\boldsymbol{Q}_m$ will be same matrix as given in Eq. 3.20. In the Arnoldi process the matrices $\boldsymbol{K}_m$ and $\boldsymbol{R}_m$ are never formed explicitly, even though one would expect the Krylov matrix to contain good information about the eigenvalues of $\boldsymbol{A}$. This is because the columns of the Krylov matrix approximate the same dominant eigenvector of $\boldsymbol{A}$ and in doing so result in an exceedingly ill-conditioned matrix.

The desired eigenvalues are instead revealed by the Hessenberg matrix $\boldsymbol{H}_m$, which has eigenvalues, $\lambda_i^{(m)}$ that constitute very good approximation for corresponding eigenvalues λ_i for the matrix $\boldsymbol{A}$. These approximate eigenvalues are also known as *Ritz values* and provide better agreement with the exact eigenvalues as m is increased. Each Ritz value also has an associated *Ritz approximate eigenvector* defined by $\boldsymbol{y}_i^{(m)} = \boldsymbol{Q}_m \boldsymbol{u}_i^{(m)}$, where $\boldsymbol{u}_i^{(m)}$ is an eigenvector associated with the eigenvalue $\lambda_i^{(m)}$. The Ritz values and corresponding eigenvectors can be obtained easily using a standard direct algorithm for computing eigenvalues and eigenvectors, since $m \ll n$ for

a typical computation. Of course, one cannot expect to compute all the eigenvalues of $\boldsymbol{A}$ by this process since that would be equivalent to using direct methods. Instead one uses a stopping criteria while increasing m until reasonably accurate eigenvalues have been obtained. This criteria is derived by using Eq. 3.19 to obtain an estimate for the residual of the eigenvalue problem, Eq. 3.13

$$(\boldsymbol{A} - \lambda_i^{(m)} \boldsymbol{I}) \boldsymbol{y}_i^{(m)} = h_{m+1,m} (\boldsymbol{e}_m^* \boldsymbol{u}_i^{(m)}) \boldsymbol{q}_{m+1} \tag{3.25}$$

and the associated norm

$$\|(\boldsymbol{A} - \lambda_i^{(m)} \boldsymbol{I}) \boldsymbol{y}_i^{(m)}\|_2 = h_{m+1,m} |(\boldsymbol{e}_m^* \boldsymbol{u}_i^{(m)})| \tag{3.26}$$

This relationship then provides the basic criteria for stopping the Arnoldi process, even though the residual norm is not always indicative of the actual error in $\lambda_i^{(m)}$ [95]. The only time this is not possible is when the Arnoldi algorithm breaks down for $h_{m+1,m} = 0$. However, this is a desired breakdown since the approximate eigenvalues are then exact and the iteration can be terminated.

3.3.3 GMRES Method for Linear Systems

While the Arnoldi process can be used to find eigenvalues, it can also be readily adapted to solve linear systems. The resulting method is commonly known as GMRES or "generalized minimal residuals." Assuming that the linear system in Eq. 3.12 has a solution $\boldsymbol{x}^*$, GMRES approximates the solution with a vector $\boldsymbol{x}_m \in \mathcal{K}_m$ by minimizing the norm of the residual, $\boldsymbol{r}_m = \boldsymbol{b} - \boldsymbol{A}\boldsymbol{x}_m$. Since $\boldsymbol{x}_m \in \mathcal{K}_m$, we can write $\boldsymbol{x}_m = \boldsymbol{Q}_m \boldsymbol{y}$, and state a least squares problem to find $\boldsymbol{y} \in \mathbb{C}^m$ such that

$$\|\boldsymbol{A}\boldsymbol{Q}_m \boldsymbol{y} - \boldsymbol{b}\| = \text{minimum} \tag{3.27}$$

where $\boldsymbol{Q}_m$ is the matrix in Eq. 3.20. The only difference here is that while the Arnoldi procedure typically starts with a random vector, for the solution of a linear system of equations, the Arnoldi process instead starts with the right-hand side vector $\boldsymbol{b}$. We

further simplify the least squares problem in Eq. 3.27 by using Eq. 3.18 to obtain

$$\|\boldsymbol{Q}_{m+1}\tilde{\boldsymbol{H}}_m\boldsymbol{y} - \boldsymbol{b}\| = \text{minimum} \tag{3.28}$$

which further simplifies by multiplication on the left by $\boldsymbol{Q}^*_{m+1}$ to

$$\|\tilde{\boldsymbol{H}}_m\boldsymbol{y} - \boldsymbol{Q}^*_{m+1}\boldsymbol{b}\| = \text{minimum} \tag{3.29}$$

Since the matrices $\boldsymbol{Q}_m$ have been constructed by starting with $\boldsymbol{b}$, the term $\boldsymbol{Q}^*_{m+1}\boldsymbol{b}$ in Eq. 3.29 can be written as $\|\boldsymbol{b}\|\boldsymbol{e}_1$ where $\boldsymbol{e}_1 \equiv (1, 0, 0, \ldots)^*$. This leaves us with the final form of the GMRES least squares problem

$$\|\tilde{\boldsymbol{H}}_m\boldsymbol{y} - \|\boldsymbol{b}\|\boldsymbol{e}_1\| = \text{minimum} \tag{3.30}$$

which is a problem of dimension $(m + 1) \times m$ as opposed to $n \times m$ in Eq. 3.27. The final algorithm can be expressed as

$$
\begin{aligned}
&\boldsymbol{q}_1 = \boldsymbol{b}/\|\boldsymbol{b}\| \\
&\textbf{for } m = 1, 2, 3, \ldots \\
&\qquad \langle\text{Step } m \text{ of Arnoldi iteration, Eq. 3.16}\rangle \\
&\qquad \text{Find } y \text{ to minimize} \|\tilde{\boldsymbol{H}}_m\boldsymbol{y} - \|\boldsymbol{b}\|\boldsymbol{e}_1\| \\
&\qquad \boldsymbol{x}_m = \boldsymbol{Q}_m\boldsymbol{y} \\
&\textbf{end for}
\end{aligned}
\tag{3.31}
$$

At each step of the algorithm, GMRES minimizes the norm of the residual $\boldsymbol{r}_m = \boldsymbol{b} - \boldsymbol{A}\boldsymbol{x}_m$ over all vectors $\boldsymbol{x}_m \in \mathcal{K}_m$, while the least squares problem for finding $\boldsymbol{y}$ can be solved via standard QR factorization that takes advantage of the Hessenberg structure of the problem.

The discussion in the section was aimed at providing a basic overview of the Arnoldi and GMRES procedures. The actual implementation of either algorithms is not trivial and special attention must be paid when implementing them for use

with Newton's method, which is the case in this thesis. In particular, two issues are of critical importance: the convergence criteria for Newton's iterations and the computation of Newton steps that lead to convergence. The two issues are intimately tied in that the Newton step computed from solution of Eq. 3.11 is never taken in full in an actual implementation and a sufficient decrease in the residual is appropriate when computing the Newton step using GMRES. This leads to the inexact Newton condition

$$\|(\boldsymbol{G}'(\boldsymbol{Y}_k; \lambda)\boldsymbol{s} + \boldsymbol{G}(\boldsymbol{Y}_k; \lambda))\| \leq \eta \|\boldsymbol{G}(\boldsymbol{Y}_k; \lambda)\| \qquad (3.32)$$

where $\boldsymbol{Y}_k$ is the kth iterate, and η is a forcing term that can be varied as the Newton iteration progresses. A very small value of η makes the iteration more like Newton's method, but makes the computation of the Newton step more expensive. Good implementations of a Newton iterative method always make use of Eq. 3.32 as a termination criteria along with an appropriate choice for η [29]. For this reason, calculations in this thesis were performed using public domain legacy codes for Newton's method that use Krylov subspace iterations. Specifically, medium-sized problems with $n \sim \mathcal{O}(100)$, were solved on MATLAB by using the freely-available code `nsoli.m` by Kelley [54]. In contrast, larger problems implemented in FORTRAN were solved using the SNES solver in the PETSc library [5].

3.4   Examples

In this section we present two examples from the kinetic theory of polymeric liquids to build coarse time-steppers and obtain stationary states. The first example uses the Fokker-Planck equation for non-interacting rigid dumbbells in steady shear as the detailed time-stepper, while the second example uses the stochastic simulation of a free draining bead-spring chain as the black-box microscopic code. The latter example is considered in standard rheometric flows, i.e. steady shear and steady uniaxial elongation, and serves to demonstrate that Newton iterative methods may be used to obtain macroscopic steady states even if there is no true microscopic steady state for the stochastic model.

3.4.1 Non-interacting Rigid Dumbbell In Steady Shear

Problem Formulation

Diffusion Equation We begin with the diffusion equation for the rigid dumbbell model (Eq. 3.33), which is a differential equation that describes the time evolution of the distribution of rigid dumbbell orientations, $f(\boldsymbol{u}, t)$ or $f(\theta, \phi, t)$ (z-axis is $\theta = 0$ and x-axis is $\theta = \frac{\pi}{2}, \phi = 0$), when the imposed time-dependent, homogeneous velocity field is described by $\boldsymbol{\kappa}(t) = \nabla v^T$. In Eq. 3.33, λ is the time constant of the rigid dumbbell and $\boldsymbol{u}$ is the orientation vector while Eq. 3.34 is the normalization condition.

$$\frac{\partial f}{\partial t} = \frac{1}{6\lambda}\left(\frac{\partial}{\partial \boldsymbol{u}} \cdot \frac{\partial f}{\partial \boldsymbol{u}}\right) - \frac{\partial}{\partial \boldsymbol{u}} \cdot ([\boldsymbol{\kappa} \cdot \boldsymbol{u} - \boldsymbol{\kappa} : \boldsymbol{uuu}])f \tag{3.33}$$

$$\int_{\boldsymbol{u}} f d\boldsymbol{u} = 1 \tag{3.34}$$

For simple shearing flow in the x-y plane ($v_x = \dot{\gamma}(t)y$) the only non-zero component of the tensor $\boldsymbol{\kappa}$ is $\boldsymbol{\kappa}_{xy} = \dot{\gamma}$. The diffusion equation can then be written as:

$$6\lambda \frac{\partial f}{\partial t} = \left[\frac{1}{S}\frac{\partial}{\partial \theta}\left(S\frac{\partial f}{\partial \theta}\right) + \frac{1}{S^2}\frac{\partial^2 f}{\partial \phi^2}\right] - (6\lambda\dot{\gamma})\left[\frac{sc}{S}\frac{\partial}{\partial \theta}(S^2 Cf) - \frac{\partial}{\partial \phi}(s^2 f)\right]$$

$$= \boldsymbol{\Lambda} f - (6\lambda\dot{\gamma})\boldsymbol{\Omega}_s f \tag{3.35}$$

where $\boldsymbol{\Lambda}$ and $\boldsymbol{\Omega}_s$ are linear operators with $S = \sin\theta, C = \cos\theta, s = \sin\phi$ and $c = \cos\phi$. Stewart and Sørensen [105] studied this diffusion equation by expanding f in term of spherical harmonics and we have done the same. When the operator $\boldsymbol{\Lambda}$ acts on the spherical harmonics it returns the same spherical harmonic multiplied by a constant, while $\boldsymbol{\Omega}_s$ yields a linear combination of spherical harmonics. As a result, the partial differential equation reduces to an ordinary differential equation with these basis functions. The Mth order spherical harmonic approximation to f is, therefore, constructed as:

$$f^{(M)} = \sum_{n=0}^{M}\sum_{m=0}^{n}(A_n^m P_n^m \cos(m\phi) + B_n^m P_n^m \sin(m\phi)) \tag{3.36}$$

where the coefficients A_n^m and B_n^m are functions of the dimensionless shear rate $\lambda\dot\gamma$ and have to be determined for each approximation $f^{(M)}$ so as to make it close to the actual f and P_n^m are the Legendre polynomials, $P_n^m(\cos\theta)$. Substituting Eq. 3.36 in Eq. (3.35) and using the orthogonality relationships of spherical harmonics we obtain:

$$\frac{dA_q^p}{dt} = q(q+1)A_q^p + (6\lambda\dot\gamma)\sum_{n=0}^{M}\sum_{m=0}^{n} a_{nq}^{mp} B_n^m, \qquad (p = 0, 1, \ldots, q)$$
$$\frac{dB_q^p}{dt} = q(q+1)B_q^p - (6\lambda\dot\gamma)\sum_{n=0}^{M}\sum_{m=0}^{n} a_{nq}^{mp} A_n^m, \qquad (q = 0, 1, \ldots, M) \tag{3.37}$$

The coefficients a_{nq}^{mp} in Eq. 3.37 are given by Bird et. al[1]. Once we choose the order of the expansion, M, the resulting system of ordinary differential equations for A_n^m and B_n^m is used as the microscopic time-stepper within the coarse time-stepper framework.

Moment Equations Instead of evolving Eq. 3.37 in time, one may obtain the equation of change for any function of dumbbell orientation $B(\boldsymbol{u})$ that is periodic in ϕ by multiplying the diffusion equation by B and integrating over all the configuration space. The equations for the second and fourth moment of f, i.e. $\langle\boldsymbol{uu}\rangle$ and $\langle\boldsymbol{uuuu}\rangle$, are obtained accordingly and are given as:

$$\frac{d\langle u_i u_j\rangle}{dt} = \frac{1}{3\lambda}\delta_{ij} - \frac{1}{\lambda}\langle u_i u_j\rangle - 2\kappa_{im}\langle u_m u_j u_k u_l\rangle + \kappa_{im}\langle u_m u_j\rangle + \langle u_i u_m\rangle\kappa_{mj}^T$$

$$\tag{3.38a}$$

$$\frac{d\langle u_i u_j u_k u_l\rangle}{dt} = -\frac{20}{6\lambda}\langle u_i u_j u_k u_l\rangle + \frac{1}{3\lambda}[\delta_{ij}\langle u_k u_l\rangle + \delta_{jk}\langle u_i u_l\rangle + \delta_{kl}\langle u_i u_j\rangle + \delta_{il}\langle u_j u_k\rangle$$
$$+ \delta_{jl}\langle u_i u_k\rangle + \delta_{ik}\langle u_j u_l\rangle] - 4\kappa_{mn}\langle u_n u_m u_i u_j u_k u_l\rangle + \kappa_{im}\langle u_m u_j u_k u_l\rangle$$
$$+ \langle u_i u_j u_k u_m\rangle\kappa_{ml}^T + \langle u_i u_j u_l u_p\rangle\kappa_{kp} + \kappa_{jp}\langle u_p u_i u_k u_l\rangle$$

$$\tag{3.38b}$$

Eq. 3.38b contains an additional unknown term $\langle\boldsymbol{uuuuuu}\rangle$, the sixth moment of f. Of course, an equation for this sixth moment may be derived by taking the sixth moment of the diffusion equation, but it can easily be seen that this equation

---

[1] R.B. Bird, H.R. Warner, Jr., and D.C. Evans (1971), *Adv. Polym. Sci.*, **8** 1-90, Table 1 on p. 23

will include yet higher moments of f. As a result, an appropriate approximation of $\langle uuuuu \rangle$ has to be found to derive the evolution of $\langle uuuu \rangle$. This problem of closure approximation has been frequently studied in recent years but a definitive recipe for the closure problem has not been found. Rather, acceptable approximations specific for each special problem considered have been constructed. Here we follow the work of Maffettone [72], which proposes:

$$\langle uuuuuu \rangle \approx \langle uuuuuu \rangle^{\text{approx}} = (1 - s) \langle uuuuuu \rangle^{\text{isotropic}} + s \langle uuuuuu \rangle^{\text{anisotropic}}$$

(3.39)

where $\langle uuuuuu \rangle^{\text{isotropic}}$ represents an accurate approximation of $\langle uuuuuu \rangle$ in the proximity of isotropy, $\langle uuuuuu \rangle^{\text{anisotropic}}$ is the approximation valid in the strongly aligned limit and the parameter $s = 1 - 27|\langle uu \rangle|$ is a scalar measure of the orientation. With the closed set of equations for the second and fourth moment, we have sufficient information to calculate the stress tensor as given by Kramer's equation

$$\boldsymbol{\tau} = -\eta \dot{\boldsymbol{\gamma}} - 3nkT \langle uu \rangle - 6nkT\lambda\boldsymbol{\kappa} : \langle uuuu \rangle + nkT\boldsymbol{\delta}$$

(3.40)

The form of the Kramer's equation suggests that one may define the second and fourth moments of the orientational distribution as a coarse set in order to obtain material functions for steady shear flow. While Eqs. 3.38a and 3.38b are a closed set of equations for these coarse variables, in order to use the formulation in Eq. 3.37 one must build a coarse time-stepper for the second and fourth moments. We will use this approach to illustrate how the coarse time-stepper yields solution in good agreement with direct simulation of Eq. 3.37.

Lifting and Restriction Steps

The restriction step for the coarse time-stepper involves obtaining the second and fourth moments in terms of the spherical harmonic coefficients A_n^m and B_n^m. This can be expressed in exact form using certain orthogonality relations for spherical

harmonics

$$\int_0^{2\pi} \int_0^{\pi} P_n^m \begin{bmatrix} \cos m\phi \\ \sin m\phi \end{bmatrix} P_{n'}^{m'} \begin{bmatrix} \cos m'\phi \\ \sin m'\phi \end{bmatrix} \sin\theta \, d\theta \, d\phi = \frac{2\pi(n+m)!}{(2n+1)(n-m)!} \delta_{nn'} \delta_{mm'} (1 \pm \delta_{m0})$$

(3.41)

where the positive sign in the factor $(1 \pm \delta_{m0})$ is to be used when $\cos m\phi$ and $\cos m'\phi$ appear in the integrals, and the negative sign when $\sin m\phi$ and $\sin m'\phi$ appear. Note that the product of two spherical harmonics integrated over the surface of a unit sphere is zero unless the two spherical harmonics are identical. Using this approach, it can be shown that the spherical harmonic coefficients for $M = 0, \ldots, 4$ constitute a sufficient set to describe the second and fourth moments. While the tensors $\langle \boldsymbol{uu} \rangle$ and $\langle \boldsymbol{uuuu} \rangle$ have 9 and 81 components, respectively, only 5 and 15 of them are independent, respectively. In particular, one obtains a linear equation relating the 15 independent components of $\langle \boldsymbol{uuuu} \rangle$ to the coefficients in the spherical harmonic expansion Eq. 3.36

$$\boldsymbol{y} = \boldsymbol{Ax}$$

(3.42)

where $\boldsymbol{x} = \{A_0^0, A_2^0, A_2^1, A_2^2, A_4^0, A_4^1, A_4^2, A_4^3, A_4^4, B_2^1, B_2^2, B_4^1, B_4^2, B_4^3, B_4^4\}^T$

$$\boldsymbol{y} = \begin{pmatrix} \langle u_x u_x u_x u_x \rangle \\ \langle u_x u_x u_x u_y \rangle \\ \langle u_x u_x u_x u_z \rangle \\ \langle u_x u_x u_y u_y \rangle \\ \langle u_x u_x u_y u_z \rangle \\ \langle u_x u_y u_y u_y \rangle \\ \langle u_x u_x u_z u_z \rangle \\ \langle u_x u_y u_y u_z \rangle \\ \langle u_y u_y u_y u_y \rangle \\ \langle u_x u_y u_z u_z \rangle \\ \langle u_y u_y u_y u_z \rangle \\ \langle u_x u_z u_z u_z \rangle \\ \langle u_y u_y u_z u_z \rangle \\ \langle u_y u_z u_z u_z \rangle \\ \langle u_z u_z u_z u_z \rangle \end{pmatrix} \tag{3.43}$$

and

$$
\boldsymbol{A} =
\begin{pmatrix}
\frac{1}{5} & -\frac{2}{35} & 0 & \frac{12}{35} & \frac{1}{105} & 0 & -\frac{4}{21} & 0 & \frac{8}{3} & 0 & 0 & 0 & 0 & 0 & 0 \\
0 & 0 & 0 & 0 & 0 & 0 & 0 & 0 & 0 & 0 & \frac{6}{35} & 0 & -\frac{2}{21} & 0 & \frac{8}{3} \\
0 & 0 & -\frac{3}{35} & 0 & 0 & \frac{1}{21} & 0 & -\frac{2}{3} & 0 & 0 & 0 & 0 & 0 & 0 & 0 \\
\frac{1}{15} & -\frac{2}{105} & 0 & 0 & \frac{1}{315} & 0 & 0 & 0 & -\frac{8}{3} & 0 & 0 & 0 & 0 & 0 & 0 \\
0 & 0 & 0 & 0 & 0 & 0 & 0 & 0 & 0 & -\frac{1}{35} & 0 & \frac{1}{63} & 0 & -\frac{2}{3} & 0 \\
0 & 0 & 0 & 0 & 0 & 0 & 0 & 0 & 0 & 0 & \frac{6}{35} & 0 & -\frac{2}{21} & 0 & -\frac{8}{3} \\
\frac{1}{15} & \frac{1}{105} & 0 & \frac{2}{35} & -\frac{4}{315} & 0 & \frac{4}{21} & 0 & 0 & 0 & 0 & 0 & 0 & 0 & 0 \\
0 & 0 & -\frac{1}{35} & 0 & 0 & \frac{1}{63} & 0 & \frac{2}{3} & 0 & 0 & 0 & 0 & 0 & 0 & 0 \\
\frac{1}{5} & -\frac{2}{35} & 0 & -\frac{12}{35} & \frac{1}{105} & 0 & \frac{4}{21} & 0 & \frac{8}{3} & 0 & 0 & 0 & 0 & 0 & 0 \\
0 & 0 & 0 & 0 & 0 & 0 & 0 & 0 & 0 & 0 & \frac{2}{35} & 0 & \frac{4}{21} & 0 & 0 \\
0 & 0 & 0 & 0 & 0 & 0 & 0 & 0 & 0 & -\frac{3}{35} & 0 & \frac{1}{21} & 0 & \frac{2}{3} & 0 \\
0 & 0 & -\frac{3}{35} & 0 & 0 & -\frac{4}{63} & 0 & 0 & 0 & 0 & 0 & 0 & 0 & 0 & 0 \\
\frac{1}{15} & \frac{1}{105} & 0 & -\frac{2}{35} & -\frac{4}{315} & 0 & -\frac{4}{21} & 0 & 0 & 0 & 0 & 0 & 0 & 0 & 0 \\
0 & 0 & 0 & 0 & 0 & 0 & 0 & 0 & 0 & -\frac{3}{35} & 0 & -\frac{4}{63} & 0 & 0 & 0 \\
\frac{1}{5} & \frac{4}{35} & 0 & 0 & \frac{8}{315} & 0 & 0 & 0 & 0 & 0 & 0 & 0 & 0 & 0 & 0
\end{pmatrix}
\tag{3.44}
$$

This relationship suggests that these 15 independent components of $\langle \boldsymbol{uuuuuu} \rangle$ can serve as the coarse set, since one can obtain the corresponding set of spherical harmonic coefficients for $M = 0, \ldots, 4$ directly. As for the remaining coefficients in the spherical harmonic expansion, we explicitly set them to zero.

Initial Condition and Guess

The isotropic state was chosen as both the initial condition and guess for the moment equations and the coarse set of 15 unknowns, respectively. In particular, the initial condition for the second and fourth moments was set to

$$
\frac{1}{4\pi} \int \boldsymbol{uu}\, d\boldsymbol{u} = \frac{1}{3}\boldsymbol{\delta}
\tag{3.45}
$$

$$
\frac{1}{4\pi} \int \boldsymbol{uuuu}\, d\boldsymbol{u} = \frac{1}{15}\left(\boldsymbol{\delta\delta} + \mathbf{I} + \mathbf{I}^{\dagger}\right)
\tag{3.46}
$$

where $(\boldsymbol{\delta\delta})_{ijkl} = \delta_{ij}\delta_{kl}$, $\mathbf{I}_{ijkl} = \delta_{ik}\delta_{jl}$ and $\mathbf{I}^{\dagger}_{ijkl} = \delta_{il}\delta_{jk}$. Eqs. 3.38a and 3.38b were then solved using an adaptive step size Cash-Karp Runge-Kutta method [87]. A similar integrator was used to evolve the spherical harmonic coefficients within the coarse

time-stepper, which was then wrapped in a Newton-GMRES solver to obtain the steady state results.

Results

The steady state for the shear viscosity and first normal stress coefficient are given in Table 3.4.1 for the moment equations, Eqs. 3.38a and 3.38b, along with the results of Stewart and Sørensen [105], which were obtained by direct solution of Eq. 3.37 for $M = 22$. It is immediately clear from these results that even though the closure approximation yields results in agreement with direct simulation for small Deborah numbers, the agreement gets worse with increasing De. In the direct simulation of

	Stewart and Sørensen [105]		Moment Equations	
De	$(\eta - \eta_s)/nkT\lambda$	$\Psi_1/nkT\lambda^2$	$(\eta - \eta_s)/nkT\lambda$	$\Psi_1/nkT\lambda^2$
0.1	0.9949	1.1872	0.9949	1.1855
1.0	0.7676	0.6467	0.7940	0.6634
10.0	0.3344	0.0517	0.3071	0.0881

Table 3.1: Comparison of steady state $(\eta - \eta_s)/nkT\lambda$ and $\Psi_1/nkT\lambda^2$ from moment equations and simulation of Stewart and Sørensen [105]

.

the diffusion equation Stewart and Sørensen [105] used an expansion with $M = 22$, which is equivalent to introducing a closure approximation for the 22nd order moment of the orientational distribution function. In doing so they avoid the need to introduce a closure approximation for the sixth moment. In this example, however, we avoid the closure approximation by building a coarse time-stepper for 15 independent components of the fourth moment. Doing so will allow for determination of the material functions, which are a function of second and fourth moments only, by evolving the diffusion equation for a fixed and short time-horizon.

For the purpose of illustration we exclusively focus on De = 1.0 and De = 10 in the remaining discussion since there is good agreement between the moment equations and direct simulation for De = 0.1. We begin by observing the eigenspectrum for the Jacobian of the right hand side of the diffusion equation at steady state. This is shown in Fig. 3-3. The first and most important thing to observe is the existence

(a) De = 0.1   (b) De = 10.0
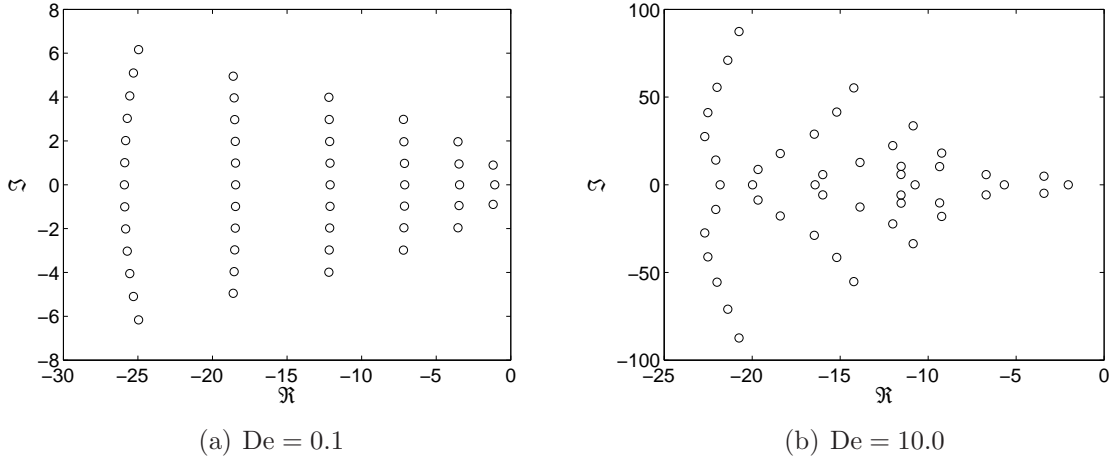
Figure 3-3: Eigenspectrum for the Jacobian of the diffusion equation at De = 1.0 and De = 10.0 with $M = 22$

De	Stewart and Sørensen [105]	Coarse Time-stepper				
		$\tau = 0.05$	$\tau = 0.1$	$\tau = 0.2$	$\tau = 0.3$	$\tau = 0.5$
1	0.7676	0.7681	0.7680	0.7677	0.7677	0.7677
10	0.3344	0.3514	0.3613	0.3363	0.3325	0.3403

Table 3.2: Steady state of shear viscosity from coarse time-stepper for varying time horizons

of gaps in the eigenspectrum at De = 1.0 and how this changes for De = 10.0. As discussed already, these gaps suggest that a coarse time-stepper may be constructed with a time horizon dictated by the inverse of the eigenvalues. In particular, for De = 1.0 there are gaps between the first three eigenvalues at approximately -1, the next five eigenvalues at approximately -3 and so on. For this reason, we use time horizons of $\tau = \{0.05, 0.1, 0.2, 0.3, 0.5\}$ for our simulations. The steady state results for the shear viscosity and first normal stress coefficient for these time horizons are summarized in Tables 3.2 and 3.3, respectively. It can be observed that the results from the coarse time-stepper are in better agreement with direct simulation

De	Stewart and Sørensen [105]	Coarse Time-stepper				
		$\tau = 0.05$	$\tau = 0.1$	$\tau = 0.2$	$\tau = 0.3$	$\tau = 0.5$
1	0.6467	0.6495	0.6490	0.6482	0.6477	0.6470
10	0.0517	0.0380	0.0451	0.0511	0.0495	0.0516

Table 3.3: Steady state of first normal stress coefficient from coarse time-stepper for varying time-horizons

when compared with those of the moment equations. Additionally, the agreement improves with increasing time horizon. In particular, it can be observed that the agreement is better for De = 1.0 than that for De = 10.0. This can be understood clearly by considering that even though there are 15 independent unknowns in the coarse time-stepper, the actual dimension of the coarse time-stepper is 8. This is because we can eliminate A_0^0 due to the normalization conditions and all coefficients with odd m due to fore-aft symmetry of the dumbbell. Even though the spherical harmonics corresponding to these remaining coefficients are not necessarily equal to the eigenfunctions corresponding to the 8 right most eigenvalues in Fig. 3-3(a), the existence of a gap after these eigenvalues does suggest existence of a closure in term of 8 spherical harmonic coefficients. On the other hand, a similar gap does not exist for the eigenspectrum at De = 10.0, suggesting that our assumed closure will never converge to the exact solution, which is exactly what is observed in Tables 3.2 and 3.3.

In addition to the steady state results, we also obtain the eigenspectrum for the coarse time-stepper at steady state in Figs. 3-4 and 3-5, where the exact eigenvalues are compared with the Ritz values obtained from the Arnoldi process at the last Newton step before convergence. First, it can be observed that the eigenvalues begin to cluster around unity with increasing time horizon for the coarse time-stepper, which is beneficial for GMRES iterations. Second, the number of Ritz values returned by Arnoldi iterations at the last Newton iteration are not always equal to the number of exact eigenvalues. This is because GMRES iterations never compute the full Newton step, and instead accept a step that satisfies the inexact Newton condition, or a sufficient decrease in the nonlinear residual. Better estimates can be obtained for the eigenvalues by increasing the number of Arnoldi iterations at the last Newton step. To illustrate this, improved Ritz values are shown in Fig. 3-6 for De = 1.0 and De = 10.0. These new estimates should be compared to Figs. 3-4(d) and 3-5(c) where four and five Arnoldi iterations, respectively, were sufficient to converge to steady state. In contrast, in Figs. 3-6(a) and 3-6(b), we used nine and eight Arnoldi iterations, respectively, which yield Ritz values in far better agreement with the exact

(a) $\tau = 0.1$
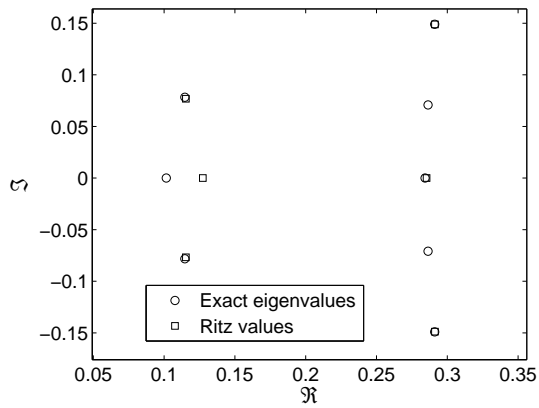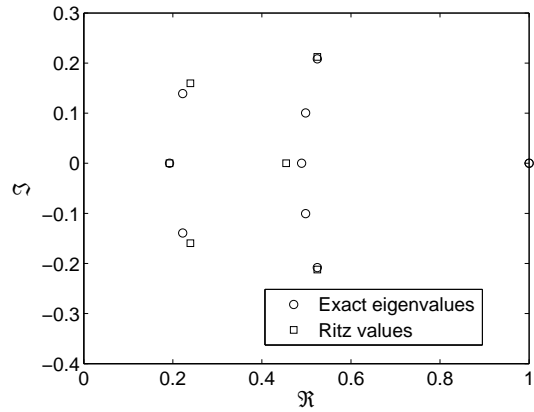
(b) $\tau = 0.2$
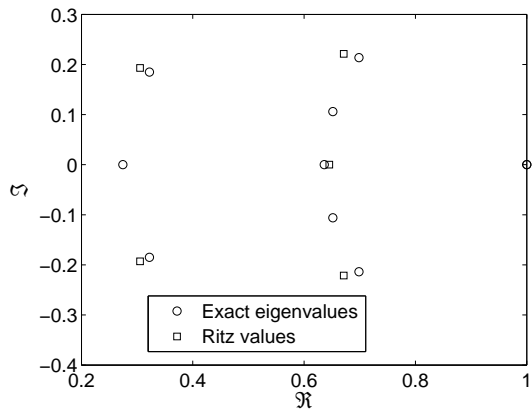
(c) $\tau = 0.3$
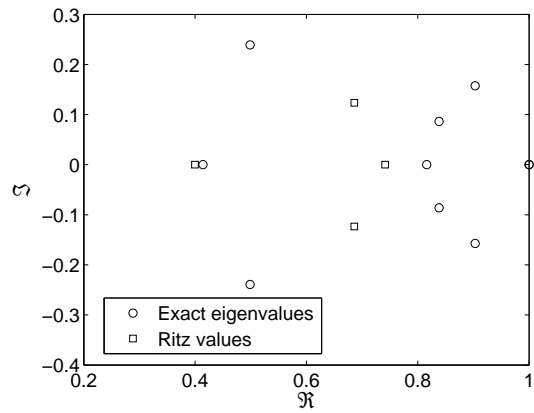
(d) $\tau = 0.5$

Figure 3-4: Comparison of exact eigenvalues and Ritz values from Arnoldi iterations for the coarse time-stepper at De= 1.0

(a) $\tau = 0.1$
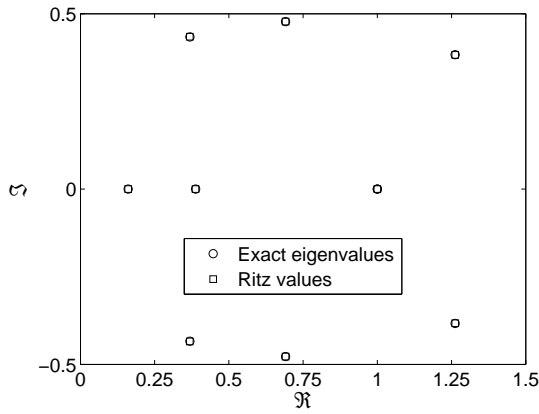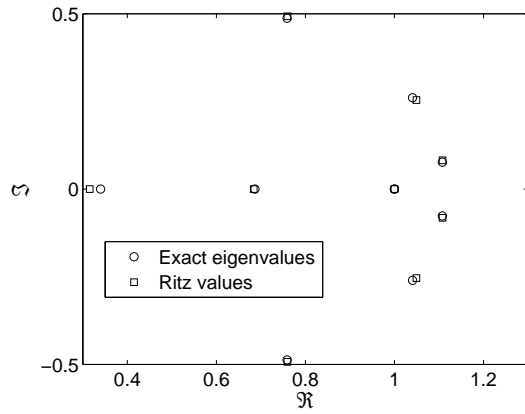
(b) $\tau = 0.2$
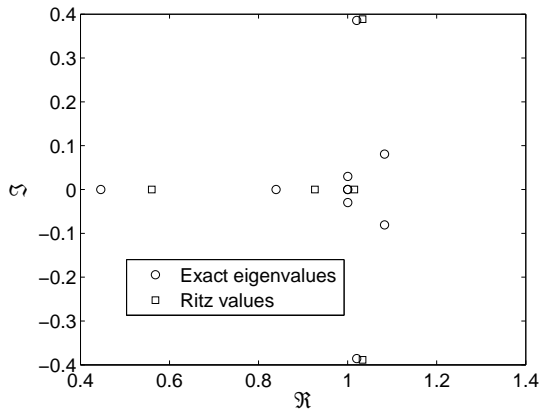
(c) $\tau = 0.3$
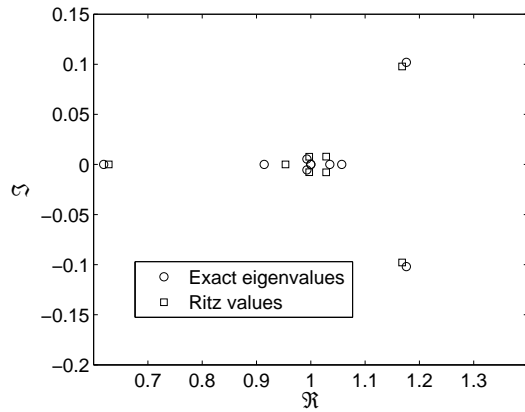
(d) $\tau = 0.5$

Figure 3-5: Comparison of exact eigenvalues and Ritz values from Arnoldi iterations for the coarse time-stepper at De= 10.0
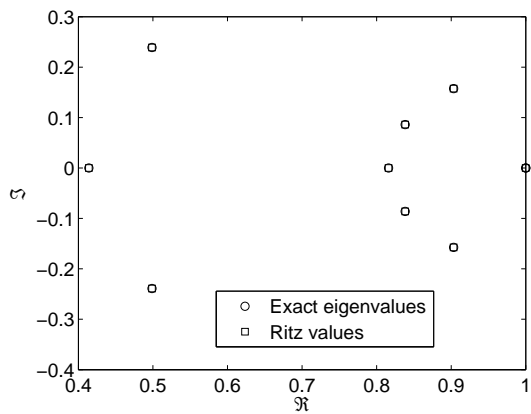
(a) De = 1.0, $\tau = 0.5$
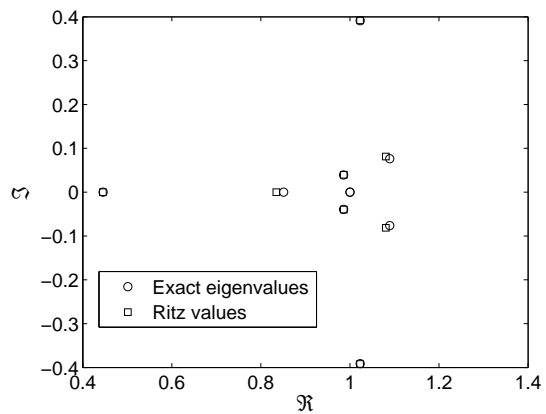
(b) De = 10.0, $\tau = 0.3$

Figure 3-6: Comparison of exact eigenvalues and Ritz values with increased Arnoldi iterations

eigenvalues. This shows that by increasing the number of Arnoldi iterations, one can obtain sufficiently accurate estimates for the exact eigenvalues of the coarse time-stepper and use them to perform stability/bifurcation analysis.
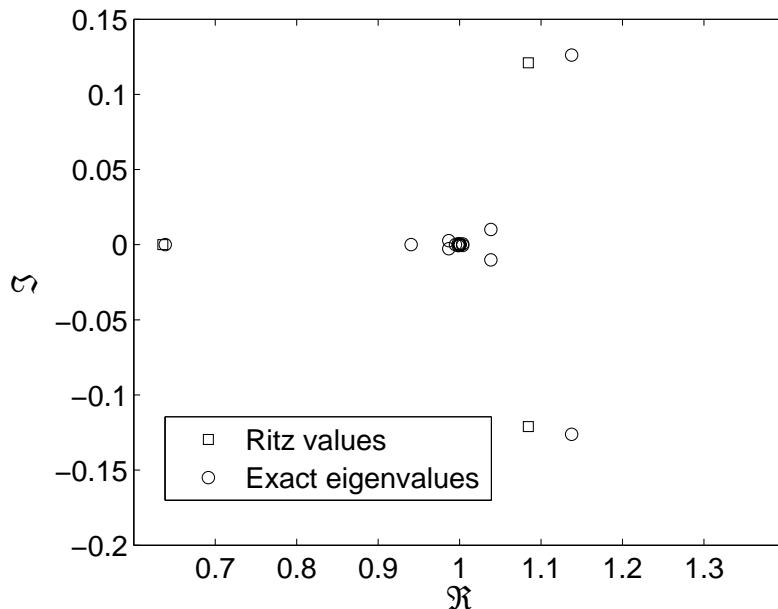
Figure 3-7: Eigenspectrum for the diffusion equation time-stepper at De = 10.0 with $\tau = 0.5$

To obtain better results for the the steady state shear viscosity and first normal stress coefficient at De = 10.0, the time stepper for the diffusion equation was treated as a black box code similar to the coarse time-stepper. The steady state results were then obtained by calling this time-stepper from a Newton-GMRES solver. This process yielded steady state shear viscosity and first normal stress coefficient in perfect agreement with those of Stewart and Sørensen [105]. The corresponding eigenspectrum at steady state is shown in Fig. 3-7, which illustrates that only 3 Arnoldi iterations were required at the last Newton step, as evident from the three Ritz values shown in the plot. It is important to note that 3 Arnoldi iterations are sufficient to yield a very good estimate for the eigenvalue farthest from unity, which is exactly the eigenvalue of interest in a stability calculation. Most importantly, however, a direct comparison of the convergence of Newton-GMRES computation (Fig. 3-8) for the diffusion equation time stepper and the coarse time-stepper constructed in this example,
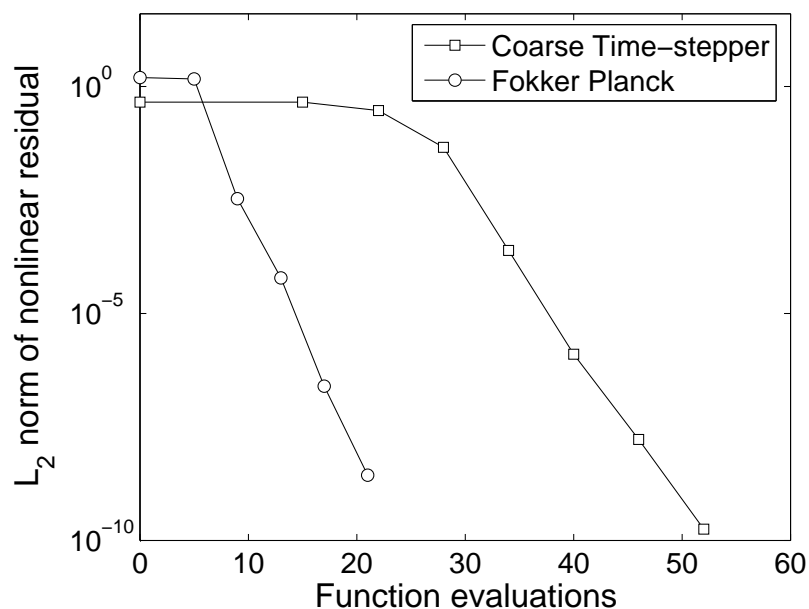
Figure 3-8: Convergence of Newton-GMRES computation of the steady state for the diffusion equation time-stepper and coarse time-stepper at De = 10.0 with $\tau = 0.5$

shows that application of Newton-GMRES solver to the Fokker Planck equation has better convergence that the coarse time-stepper.

In conclusion, this example demonstrates that if the dynamical system of interest possesses a slow manifold, one can then compute coarse steady states by choosing either a time-stepper that consists of the complete set of dynamical unknowns or by building a coarse time-stepper at a level at which one expects closure to exist, without invoking unnecessary closure approximations. This is only possible because the Jacobian matrices with either time-stepper have distinct gaps in the corresponding eigenspectrum, which can be exploited by a Newton iterative method like Newton-GMRES that essentially takes advantage of the existence of a closure, albeit and unknown one to compute the coarse steady state. Finally, the extreme eigenvalues of the dynamical problem can also be obtained readily by increasing the number of Arnoldi iterations within the Newton-GMRES solver.
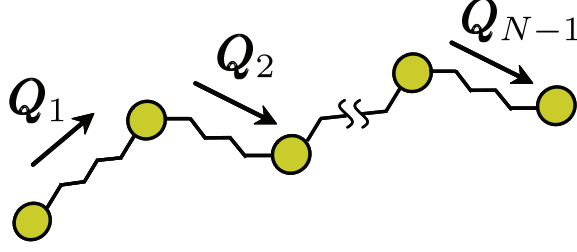
Figure 3-9: The bead spring chain model for a linear polymer molecule

3.4.2 Bead-Spring Chain Model in Steady Shear and Uniaxial Elongation

Langevin Equation

We begin with the Langevin equation for a bead spring chain consisting of N beads connected by $N-1$ springs (see Fig. 3-9). This equation describes the time evolution of the connector vectors $\boldsymbol{Q}_i$ $(i = 1, \ldots, N-1)$ of the chain as

$$\frac{d\boldsymbol{Q}_i}{dt} = \boldsymbol{\kappa} \cdot \boldsymbol{Q}_i - \frac{1}{\zeta} \sum_{j=1}^{N-1} A_{ij} \boldsymbol{F}_j^{(c)} + \sqrt{\frac{2kT}{\zeta}} \left(\frac{d\boldsymbol{W}_{i+1} - d\boldsymbol{W}_i}{dt} \right) \qquad (3.47)$$

where A_{ij} is the Rouse matrix, $\boldsymbol{\kappa} = \boldsymbol{\nabla}\boldsymbol{v}^T$, ζ is the isotropic drag coefficient, $\boldsymbol{W}_\nu(t)$ is the Wiener process that accounts for the Brownian force experienced by bead ν, and $\boldsymbol{F}_j^{(c)}$ is the connector force in spring j given by $\boldsymbol{F}_j^{(c)} = \dfrac{H\boldsymbol{Q}_j}{1 - \dfrac{Q_j^2}{Q_{j,0}^2}}$. This equation is equivalent to the Fokker-Planck equation for the phase-space distribution function [83]. Here we have used the FENE force law with spring constant H. We now define the following dimensionless variables, where the superscript * denotes variables with dimensions

$$\boldsymbol{Q} = \frac{\boldsymbol{Q}^*}{\sqrt{kT/H}}$$
$$t = \frac{t^*}{\lambda_1}$$
$$\boldsymbol{\kappa} = \frac{\boldsymbol{\kappa}^*}{U/L} \qquad (3.48)$$
$$\boldsymbol{W} = \frac{\boldsymbol{W}^*}{\sqrt{\lambda_1}}$$

103

In these definitions $\lambda_1 = \dfrac{\zeta}{8H \sin^2 \frac{\pi}{2N}}$ is the longest Rouse relaxation time, whereas U and L are the characteristic velocity and length scales for the flow problem. In addition, we also define the maximum extensibility parameter for each chain segment given by $b_j = \dfrac{HQ_{j,0}^2}{kT}$ and rewrite the Langevin equation as,

$$\frac{d\boldsymbol{Q}_i}{dt} = \mathrm{De}\,\boldsymbol{\kappa} \cdot \boldsymbol{Q}_i - \frac{1}{\alpha_1} \sum_{j=1}^{N-1} A_{ij} \frac{\boldsymbol{Q}_j}{1 - \frac{Q_j^2}{b_j}} + \frac{1}{\alpha_2}\left(\frac{d\boldsymbol{W}_{i+1} - d\boldsymbol{W}_i}{dt}\right) \qquad (3.49)$$

where $\alpha_1 = 8 \sin^2 \frac{\pi}{2N}$, $\alpha_2 = 2 \sin \frac{\pi}{2N}$, and $\mathrm{De} = \frac{\lambda_1 U}{L}$ is the Deborah number for the flow. Forward time integration of the stochastic differential in Eq. 3.49 to create an ensemble of trajectories for the polymer molecules is at the core of Brownian Dynamics simulation method for studying the dynamics of complex fluids.

Numerical integration algorithm

Due to the use of random numbers to represent the Wiener process in the Langevin equation, there is always the possibility that the forward Euler integration algorithm may result in unrealistic chain segment extensions that add up to more than the maximum possible contour length of the chain. While this could be avoided through an algorithm that rejects unrealistic moves for the chain, the generation of unnecessary random numbers and the complementary limitation of the time-step for such an algorithm leads to a simulation with a large computational cost. As a result, we use a predictor-corrector based scheme, in which no trajectory is rejected due to an implicit treatment of the connector force in a given segment, while also allowing for larger time steps than those possible with the Euler scheme.

Predictor Step In formulating the predictor step, we use backward Euler approximation for the spring force in segment i, and forward Euler for the spring force in all other segments. With this approximation, we obtain the following expression for

the predicted connector vector,

$$\left[1 + \frac{2\Delta t}{\alpha_1\left(1 - \frac{\hat{Q}_i^2}{b_i}\right)}\right]\hat{Q}_i = \bar{Q}_i + \left[\text{De }\boldsymbol{\kappa} \cdot \bar{Q}_i - \frac{1}{\alpha_1}\sum_{j=1,j\neq i}^{N-1} A_{ij}\frac{\bar{Q}_j}{1 - \frac{\bar{Q}_j^2}{b_j}}\right]\Delta t$$

$$+ \frac{1}{\alpha_2}(\Delta\bar{W}_{i+1} - \Delta\bar{W}_i) \tag{3.50}$$

where $\bar{Q}_i$ and $\bar{W}_i$ are the initial connector vector and random numbers, while $\hat{Q}_i$ is the predicted value. As evident from the form of the above expression, we must solve a cubic equation for $\hat{Q}_i$ due to the implicit treatment of the corresponding force term. It can be shown the this cubic equation has a real root less than $\sqrt{b_i}$.

Corrector Step For the corrector step we use a modification of a second order Adams-Moulton scheme for the spring force in segment i. Given an ordinary differential equation, $\frac{dy}{dt} = f(t, y)$, the second order Adams-Moulton scheme yields

$$y_{n+1} = y_n + \Delta t\left[\frac{1}{2}f(t_n, y_n) + \frac{1}{2}f(t_{n+1}, y_{n+1})\right] \tag{3.51}$$

This is an implicit scheme that uses an average of the function at time t_n and t_{n+1} to compute the update. In our formulation, we treat the spring force in segment i implicitly, while using the predictor result to compute the average of the hydrodynamic term and the contribution from spring forces in all other segments. We thus have

$$\left[1 + \frac{\Delta t}{\alpha_1\left(1 - \frac{Q_i^2}{b_i}\right)}\right]Q_i = \bar{Q}_i + \frac{\text{De}}{2}\left[\boldsymbol{\kappa} \cdot \hat{Q}_i + \boldsymbol{\kappa} \cdot \bar{Q}_i\right]\Delta t$$

$$- \frac{1}{2}\left[\frac{1}{\alpha_1}\sum_{j=1,j\neq i}^{N-1} A_{ij}\left[\frac{\hat{Q}_j}{1 - \frac{\hat{Q}_j^2}{b_j}} + \frac{\bar{Q}_j}{1 - \frac{\bar{Q}_j^2}{b_j}}\right]\right]\Delta t \tag{3.52}$$

$$- \frac{1}{\alpha_1}\frac{\bar{Q}_i}{1 - \frac{\bar{Q}_i^2}{b_i}}\Delta t + \frac{1}{\alpha_2}(\Delta\bar{W}_{i+1} - \Delta\bar{W}_i)$$

This equation is also a cubic equation for the connector vector update Q_i at the next time step. It must be noted that the random numbers generated for the predictor

step are reused in the corrector step.

Coarse Time-stepper

The combination of Eqs. 3.50 and 3.52 is sufficient to formulate a black-box code that can evolve the conformation of the bead-spring chain over a specified time horizon. However, we still need to choose a set of coarse variables that may then be used to construct a coarse time-stepper. The inspiration for the coarse set comes from the Kramer's expression used to evaluate the polymer contribution to the fluid stress tensor [9]

$$\boldsymbol{\tau}_p = \sum_{j=1}^{N-1} \boldsymbol{\tau}_{p,j} = \sum_{j=1}^{N-1} \left(\boldsymbol{\delta} - \left\langle \boldsymbol{F}_j^{(c)} \boldsymbol{Q}_j \right\rangle \right) \tag{3.53}$$

where $\langle \cdot \rangle$ is the ensemble average and the total contribution is a sum over the contributions from each chain segment. If we choose the polymer contribution to the stress tensor as the coarse variable, Eq. 3.53 would then constitute the restriction step. However, the inverse of this or the lifting operator is clearly not unique, since this would involve constructing an ensemble of conformations consistent with the total contribution to the stress tensor. To help with the choice of the lifting step we, therefore, look at the macroscopic quantities one would measure in a rheological experiment in the laboratory to validate the Brownian dynamics simulation.

In this section we consider the bead-spring chain undergoing steady shear and steady uniaxial elongation flow. For steady shear flow, one can measure three material functions, namely the viscosity η, and the first and second normal stress coefficients, Ψ_1 and Ψ_2, respectively. For steady shear flow, $v_x = \dot{\gamma}y$, $v_y = 0$, and $v_z = 0$, these materials functions can be obtained from $\tau_{p,xy}$, $\tau_{p,xx} - \tau_{p,yy}$, and $\tau_{p,yy} - \tau_{p,zz}$, whereas for steady uniaxial elongation flow, $v_x = -\frac{\dot{\epsilon}}{2}x$, $v_y = \frac{\dot{\epsilon}}{2}y$, and $v_z = \dot{\epsilon}z$, we can only obtain one material function, the extensional viscosity $\bar{\eta}$ from $\tau_{p,zz} - \tau_{p,xx}$. If the stochastic simulation consisted of a single spring, i.e. an elastic dumbbell, these components of the polymer contribution to the stress tensor would serve as the natural choice for the coarse set. Hence, it seems reasonable to choose contributions from the chain segments for these same components of the stress tensor as the coarse set for our

106

problem.

Interestingly, if we choose to express chain segment conformation in cartesian coordinates, we will need to solve for three unknowns $\{Q_{x,j}, Q_{y,j}, Q_{z,j}\}$ in order to construct a chain segment conformation. For the steady shear flow problem, this should be trivial since each chain segment contributes three variables to the coarse set. On the contrary, the same is not true for the steady elongation flow, where the three unknowns $\{Q_{x,j}, Q_{y,j}, Q_{z,j}\}$ must be constructed from a single coarse variable, $(\tau_{p,zz} - \tau_{p,xx})_j$. However, for steady elongation flow, one would expect chain segments to align primarily in the z direction. Hence, as a first approximation one may choose to set $\{Q_{y,j}, Q_{z,j}\}$ to zero.

So far, we have not addressed the issue of initializing an ensemble of segment conformations since we do not know the corresponding distribution function. For the work presented here, we assume that the distribution function is a delta function such that all components of the ensemble are identical. Hence, the distribution function is given by

$$
\begin{aligned}
f^{N-1} &= \prod_{j=1}^{N-1} f_j(Q_{x,j}, Q_{y,j}, Q_{z,j}) \\
&= \prod_{j=1}^{N-1} \delta(Q_{x,j} - x_j)\delta(Q_{y,j} - y_j)\delta(Q_{z,j} - z_j)
\end{aligned}
\tag{3.54}
$$

where $\{x_j, y_j, z_j\}$ are the lifted values of the microscopic variables $\{Q_{x,j}, Q_{y,j}, Q_{z,j}\}$. This introduces an unknown error in the lifting step in addition to the approximation $\{Q_{y,j}, Q_{z,j}\} = \{0, 0\}$ for uniaxial elongation. Table 3.4 summarizes the discussion for the lifting steps for steady shear and steady uniaxial elongation flows, where it is understood that the microscopic unknowns are given by $\{x_j, y_j, z_j\}$ for $j = 1, 2, \ldots, N-1$.

Results

We used the lifting steps summarized in Table 3.4 and the restriction step given by Eq. 3.53 to construct a coarse time-stepper for a bead-spring chain consisting of 6 beads with a total maximum extensibility of $b = 120$. For the Brownian dynamics

Flow Type	Coarse Variables	Lifting Step
Steady shear	$(\tau_{yx})_j$ $(\tau_{xx} - \tau_{yy})_j$ $(\tau_{yy} - \tau_{zz})_j$	$\dfrac{x_j^2 y_j^2}{1 - (x_j^2 + y_j^2 + z_j^2)/b_j} = (\tau_{yx})_j$ $\dfrac{y_j^2 - x_j^2}{1 - (x_j^2 + y_j^2 + z_j^2)/b_j} = (\tau_{xx} - \tau_{yy})_j$ $\dfrac{z_j^2 - y_j^2}{1 - (x_j^2 + y_j^2 + z_j^2)/b_j} = (\tau_{yy} - \tau_{zz})_j$
Uniaxial elongation	$(\tau_{zz} - \tau_{xx})_j$	$x_j = 0, \ y_j = 0, \ \dfrac{-z_j^2}{1 - x_j^2/b} = (\tau_{zz} - \tau_{xx})_j$

Table 3.4: The lifting step for the free-draining bead spring chain model in steady shear and uniaxial elongation flows
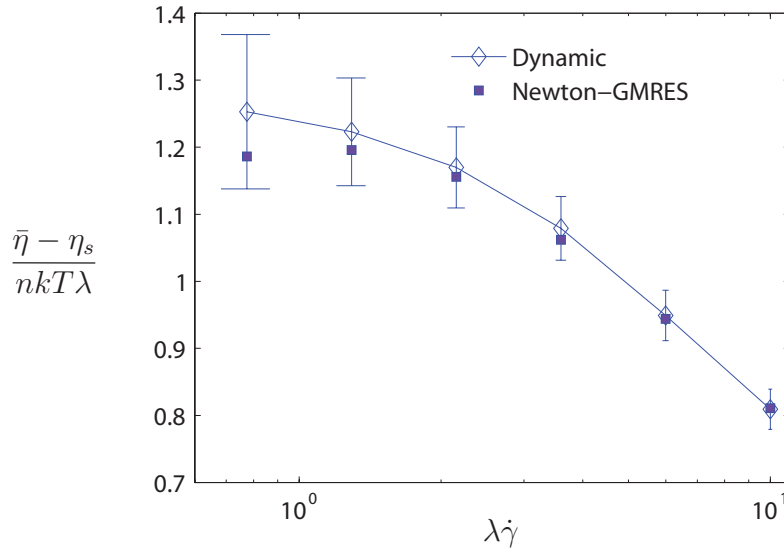
Figure 3-10: Variation of shear viscosity with dimensionless shear rate $\lambda\dot{\gamma}$. The error bars denote one unit of standard error at steady state as computed from Brownian dynamic simulation.
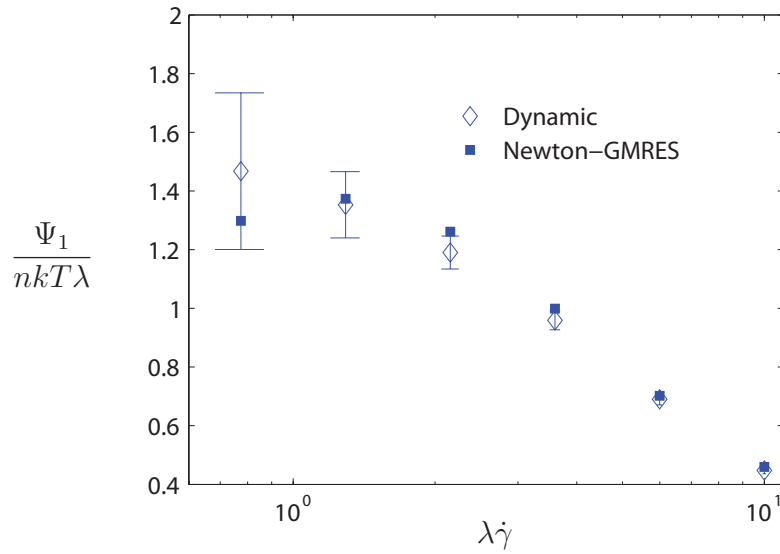
Figure 3-11: Variation of first normal stress coefficient with dimensionless shear rate $\lambda\dot{\gamma}$. The error bars denote one unit of standard error at steady state as computed from Brownian dynamic simulation.
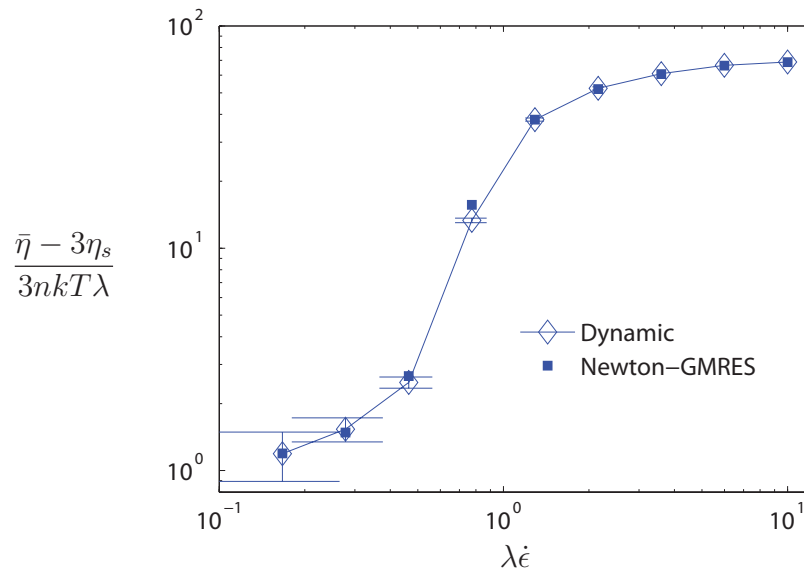
Figure 3-12: Variation of extensional viscosity with dimensionless extension rate $\lambda\dot{\epsilon}$. The error bars denote one unit of standard error at steady state computed from Brownian dynamic simulation.

simulator, we chose an ensemble size of 1000 with a time-step of $\Delta t = 0.01$. Steady state results were obtained by time integrating the Brownian dynamics simulator to $t_{\mathrm{final}} = 10$, while the time-horizon of the coarse time-stepper was set to $\tau = 1.0$. The steady state results for several values of the dimensionless shear and extension rates were computed from direct simulation and compared with steady state results obtained by making calls to the coarse time-stepper from a Newton-GMRES solver.

For steady shear flow, the profiles for the steady state shear viscosity and first normal stress coefficient as a function of dimensionless shear rate are shown in Figs. 3-10 and 3-11, respectively. It can be observed that there is excellent agreement between the results of the direct simulation and Newton-GMRES, such that the steady state computed from Newton-GMRES is within the standard error of the steady state result from the detailed time-stepper. The ensemble size of 1000 was found to be the minimum ensemble size necessary in order to converge with the Newton-GMRES solver. This situation was not remedied by increasing the time-horizon of the coarse time-stepper. This suggests that since Newton-GMRES estimates the action of the unknown Jacobian of the closed description by calling the coarse time-stepper, the latter must return sufficiently accurate estimates when called from nearby initial conditions.

For steady uniaxial elongational flow, the profile for the extensional viscosity as a function of dimensionless extension rate is shown in Fig. 3-12. Once again we find excellent agreement between the steady state computed from Newton-GMRES solver and direct simulation for the entire range of dimensionless extension rates, with perfect agreement for $\lambda \dot{\epsilon} > 1$. More importantly, the results extend to dimensionless extension rates lower than the dimensionless shear rates that were studied for the steady shear flow problem.

In conclusion, we find that the coarse time-stepper for a stochastic simulator can indeed be enabled to yield macroscopic stationary states, provided the underling stochastic simulator yields macroscopic quantities with small variance. This requirement should be easy to appreciate when considering that we are trying to estimate a steady state by using a simulator that does not have a "true" microscopic steady

state.

3.5 The Finite Element Method

The finite element method is a type of weighted residual method used to obtain approximate solutions for a wide class of boundary value problems. In particular, the approximate solution is represented as an expansion in a convenient (and finite) set of linearly-independent basis function with unknown coefficients. Substituting the expansion in the governing ordinary or partial differential equation results in an error, called the residual. In order to determine the unknown coefficients the residual is orthogonalized against a set of linearly-independent basis functions. While there are several sets of functions against which one may orthogonalize, choosing the same basis functions as the ones in the original expansion provides one way of finding the coefficients. This is known as the Galerkin approach, or the Galerkin finite element method.

Spatial discretization of the conservation of mass and momentum or the constitutive equation via the Galerkin finite element method yields a set of algebraic or ordinary differential equations. Since this is the primary task of computational rheology, we describe the Galerkin finite element method for spatial discretization by considering the standard diffusion equation in one spatial dimension. This problem is representative of Stokes flow of a Newtonian fluid in a channel, which is considered next. The equations for the Newtonian fluid are then adapted into the one-dimensional discrete elastic-viscous split-stress gradient (DEVSS-G) formulation, which is constructed by the introduction of the velocity gradient interpolant and a constitutive equation for the polymer contribution to the stress tensor. In particular, we will only consider the steady problem, as the method can be easily extended to the unsteady problem with a time integration method of choice.

In addition to discussion of the Stokes problem, numerical methods appropriate for hyperbolic problems are also discussed. This is relevant as the constitutive descriptions considered in this thesis are hyperbolic in nature. First, it is shown why

the standard Galerkin approach fails for the hyperbolic problem. This is followed by a short description of the discontinuous Galerkin method for hyperbolic problems and details of how to deal with the convective term encountered in various constitutive descriptions for the polymer contribution to the fluid stress. It is important to note that the details provided in this section are by no means comprehensive when trying to understand the finite element method and only serve to illustrate how the method is used for simulating complex viscoelastic flows. To learn further details about the method, the reader should refer to more general texts [45, 90].

3.5.1 The diffusion equation

Consider the two point boundary value problem for the unknown $u(x)$ on the domain $0 \leq x \leq 1$

$$-\frac{d^2 u}{dx^2} = f \tag{3.55}$$

with boundary conditions

$$u(0) = 0 \tag{3.56}$$

$$\frac{du}{dx}\bigg|_{x=1} = 0 \tag{3.57}$$

This problem can be solved by integrating Eq. 3.55 twice and using the boundary conditions in Eqs. 3.56 and 3.57. An equivalent formulation for the problem is to find a function $u \in V$ such that

$$a(u, v) = (f, v) \qquad \forall v \in V \tag{3.58}$$

where the functionals $a(.,.)$ and $(.,.)$ are defined as

$$a(u, v) \equiv \int_0^1 \frac{du}{dx}\frac{dv}{dx}dx \tag{3.59}$$

$$(f, v) \equiv \int_0^1 fvdx \tag{3.60}$$

and the function space V is defined as

$$V = \{v : v \in C^0 \text{ on } [0, 1], v(0) = 0\}$$

that is V is a function space consisting of continuous functions, C^0, on the domain $[0, 1]$ such that $v(0) = 0$. The two formulations can be shown to be equivalent by rewriting $a(u, v)$ as

$$a(u, v) = -\int_0^1 v \frac{d^2u}{dx^2} dx + v \frac{du}{dx}\Big|_0^1$$

and subtracting (f, v) to get

$$a(u, v) - (f, v) = 0 = -\int_0^1 v \left(\frac{d^2u}{dx^2} + f\right) dx + v \frac{du}{dx}\Big|_0^1 \qquad (3.61)$$

If a solution has been found to the boundary value problem in Eq. 3.55, then it can be seen that the integrand in Eq. 3.61 is zero along with the last term due to the requirement that $v(0) = 0$ and the boundary condition $\dfrac{du}{dx}\Big|_{x=1} = 0$.

The above argument demonstrates that the solution of the "weak formulation" of Eq. 3.58 is equivalent to the classical or "strong formulation" of Eqs. 3.55 to 3.57. The weak form of any differential equation is constructed by multiplying the differential equation by a test function, v, and then integrating over the spatial domain. Boundary conditions are enforced according to their type. Dirichlet boundary conditions like Eq. 3.56 are handled by the choice of the function space V such that it contains only those functions that satisfy the boundary condition, whereas Neumann boundary conditions like that in Eq. 3.57 are enforced through the boundary integral term (the last term in Eq. 3.61). Such boundary conditions are also referred to as "natural" boundary conditions.

Minimization principle

The model boundary value problem can also be formulated as a minimization problem to find $u \in V$ such that

$$F(u) \leq F(v) \qquad \forall v \in V \qquad (3.62)$$

where the linear functional F is defined as

$$F(v) \equiv \frac{1}{2}a(v, v) - (f, v). \tag{3.63}$$

To show that a solution u for Eq. 3.55 satisfies Eq. 3.63, we choose a function $w = u + v$ such that w also belongs to the function space V. Substituting this into Eq. 3.63 yields

$$\begin{aligned}
F(w) = F(u + v) &= \frac{1}{2}a(u + v, u + v) - (f, u + v) \\
F(w) &= \frac{1}{2}a(u, u) + \frac{1}{2}a(v, v) + [a(u, v) - (f, v)] - (f, u)
\end{aligned} \tag{3.64}$$

The term in the square brackets is zero, which yields the final result that

$$F(w) = F(u) + \frac{1}{2}a(v, v) \geq F(u). \tag{3.65}$$

Hence, solving the minimization problem in Eq. 3.63 provides a solution u to the weak formulation. The minimization problem can be understood more clearly by defining $w = u + \varepsilon v$ with $w, v \in V$ and defining a new function $g(\varepsilon)$ such that

$$g(\varepsilon) \equiv F(w) = F(u + \varepsilon v) = \frac{1}{2}a(u, u) + \varepsilon a(u, v) + \frac{\varepsilon^2}{2}a(v, v) - (f, u) - \varepsilon(f, v) \tag{3.66}$$

If the functional F is minimized by the function u, then the function g has a minimum at $\varepsilon = 0$ with $\left.\frac{dg}{d\varepsilon}\right|_{\varepsilon=0} = 0$. Hence

$$\left.\frac{dg}{d\varepsilon}\right|_{\varepsilon=0} = 0 = a(u, v) - (f, v) \tag{3.67}$$

which is exactly the weak formulation of Eq. 3.58. The ability to write Eq. 3.58 as a minimization problem is useful when obtaining the Galerkin approximation to the conservation of momentum equation.

Ritz-Galerkin Approximation

The spatial discretization of boundary value problems can be formulated by applying the Ritz-Galerkin approximation, where the infinite dimensional function space V is replaced by a finite dimensional subspace $V_h \subset V$, so that the weak formulation changes to finding $u_h \in V_h$ such that

$$a(u_h, v_h) = (f, v_h) \qquad \forall v_h \in V_h \tag{3.68}$$

The functions in V_h can be written as $v_h(x) = \sum_i c_i \phi_i(x)$ where $\{\phi_i(x)\}$ define a set of linearly independent basis functions that span the function space V_h. The task of finding a solution to Eq. 3.68 is then reduced to a linear algebra problem

$$\boldsymbol{A}\boldsymbol{u_h} = \boldsymbol{b} \tag{3.69}$$

where $A_{ij} \equiv a(\phi_i, \phi_j)$, $\boldsymbol{u_h}$ is the vector of coefficients in the expansion $u_h(x) = \sum_j u_{h,j}\phi_j(x)$, and $b_i \equiv (f, \phi_i)$. Because the basis functions $\{\phi_i\}$ are linearly independent, Eq. 3.69 has a unique solution.

In general the choice of the approximation space V_h is dictated by the form of $a(u, v)$ and (f, v). For the diffusion equation, the weak formulation only requires that products of the gradients of u and v and the functions f and v be L_2-integrable. The most general V_h under these conditions is the space of all functions whose derivatives up to the first order are in L_2. However, this space does not take into account the boundary conditions. The functions in V_h must be restricted to have zero values on the boundary as well. In the finite element method, the space V_h consists of low degree polynomials defined on a finite number of subintervals, I_j, or elements of the original domain, $[0, 1]$. Common approximation spaces include piecewise linear and piecewise quadratic functions on each element. For the diffusion equation, the function space V is continuous, so the approximation space V_h should have C^0 continuity as well. However, for other equations, continuity at the element boundaries is not required.

The piecewise linear and piecewise quadratic approximation spaces are defined as

$$V_h = \left\{ v : v \in C^0 \text{ on } [0,1], v|_{I_j} \in \Pi_1, v(0) = 0 \right\} \tag{3.70}$$

and

$$V_h = \left\{ v : v \in C^0 \text{ on } [0,1], v|_{I_j} \in \Pi_2, v(0) = 0 \right\} \tag{3.71}$$

where Π_n is the set of all real polynomial whose degrees do not exceed n. Here $v|_{I_j}$ represent the restriction of the function v to the subinterval or element I_j. If $\{x_j\}$, for $j = 1, \ldots, n$ are the nodes of the finite element mesh, then a function v_i in V_h can be associated with each node x_j so that the family of functions v_i satisfies the following condition

$$v_i(x_j) = \delta_{ij} \tag{3.72}$$

where δ_{ij} is the Kronecker delta and a basis which satisfies Eq. 3.72 is called a nodal basis.

3.5.2 The momentum balance for Stokes flow

Having considered the finite element formulation for the diffusion equation, it becomes relatively straightforward to consider the corresponding formulation for Stokes flow of a Newtonian fluid in one spatial dimension. For fully developed flow, the momentum equation is given by

$$-\frac{d^2u}{dx^2} + \frac{dp}{dy} = f \tag{3.73}$$

where u is the flow velocity in the y direction, $\dfrac{dp}{dy}$ the corresponding pressure drop, and f is a body force such as gravity. For boundary conditions, we consider symmetry boundary condition at the center of the channel and no-slip at the wall, i.e.

$$\left. \frac{du}{dx} \right|_{x=0} = 0 \tag{3.74}$$

and

$$u(1) = 0. \tag{3.75}$$

If f and the pressure drop are specified, then the method described for the diffusion equation can be applied directly to find an approximate solution to this problem. Post-processing of the solution can then yield the volumetric flow, if so desired.

However, if the volumetric flow rate is specified instead, the pressure drop must also be determined as part of the weak formulation. One way to address this problem is to define a functional to be minimized like in Eq. 3.63 that takes into account the flow rate constraint. One can construct such a functional by introducing the pressure drop as a Lagrangian multiplier in the functional defined previously, Eq. 3.63. This yields a functional

$$\Lambda(u, \lambda) = F(u) - \lambda\Big(\frac{Q}{2} - \int_0^1 u \, dx\Big) \tag{3.76}$$

which is then minimized by a solution u for the velocity and λ for the pressure drop, which now appears as a Lagrange multiplier. Since the multiplier is a real constant, we now seek to minimize the functional Λ with respect to perturbations $v \in V$ and $c \in \Re$ in velocity and pressure drop, respectively. Following the procedure described previously, we define the function

$$
\begin{aligned}
g(\varepsilon, \delta) &= \Lambda(u + \varepsilon v, \lambda + \delta c) = F(u + \varepsilon v) - (\lambda + \delta c)\Big(\frac{Q}{2} - \int_0^1 (u + \varepsilon v) \, dx\Big) \\
&= \frac{1}{2}a(u, u) + \varepsilon a(u, v) + \frac{\varepsilon^2}{2}a(v, v) - (f, u) - \varepsilon(f, v) \\
&\quad - (\lambda + \delta c)\Big(\frac{Q}{2} - \int_0^1 (u + \varepsilon v) \, dx\Big)
\end{aligned}
\tag{3.77}
$$

This leads to the minimization conditions

$$\frac{dg}{d\varepsilon}\Big|_{\delta=0} = 0 = a(u, v) - (f, v) + \lambda \int_0^1 v \, dx \qquad \forall v \in V \tag{3.78}$$

$$\frac{dg}{d\delta}\Big|_{\varepsilon=0} = 0 = c\Big(\frac{Q}{2} - \int_0^1 u \, dx\Big) \qquad \forall c \in \Re \tag{3.79}$$

Application of the Ritz-Galerkin approximation to this formulation yields the solution to the momentum equation.

Failure of viscous formulation in $\beta \to 0$ limit

While the finite element formulation just presented for the momentum balance is sufficient to obtain a solution for a Newtonian fluid, it fails when applied to the momentum balance which incorporates polymer contribution to the fluid stress tensor. This can be understood clearly by considering the momentum balance for Stokes flow

$$\boldsymbol{\nabla} \cdot (\boldsymbol{\tau} + p\boldsymbol{\delta}) = 0 \tag{3.80}$$

where $\boldsymbol{\tau} = -\eta_s \dot{\boldsymbol{\gamma}} + \boldsymbol{\tau_p}$ is the total fluid stress. Substituting this expression into Eq. 3.80 yields

$$-\beta \nabla^2 \boldsymbol{u} + \boldsymbol{\nabla} \cdot \boldsymbol{\tau_p} + \boldsymbol{\nabla} p = 0 \tag{3.81}$$

where $\beta \equiv \eta_s/\eta_0$ is the dimensionless solvent viscosity. A quick look at Eq. 3.81 suggests that any finite element formulation for the momentum balance must be solvable in the $\beta \to 0$ limit for simulation of viscoelastic flows. Here it will be shown that the finite element formulation presented previously for the Newtonian fluid will be unsuitable in the $\beta \to 0$ limit and a different formulation must therefore be constructed.

To illustrate this, consider the one-dimensional version of Eq. 3.81 along with a Newtonian constitutive equation for the polymer contribution to the fluid stress. This yields the following system of equations

$$-\beta \frac{d^2 u}{dx^2} + \frac{d\tau_p}{dx} + \lambda = 0 \tag{3.82}$$

$$\tau_p = -(1-\beta)\frac{du}{dx} \tag{3.83}$$

$$\frac{Q}{2} = \int_0^1 u \, dx \tag{3.84}$$

Using the result presented in Eqs. 3.78 and 3.79 the corresponding finite element

formulation is

$$\beta a(u_h, v_h) + \left(\frac{d\tau_{ph}}{dx}, v_h\right) + (\lambda, v_h) = 0 \qquad \forall v_h \in V_h$$

$$(\tau_{ph}, s_h) + (1 - \beta)\left(\frac{du}{dx}, s_h\right) = 0 \qquad \forall s_h \in S_h \qquad (3.85)$$

$$\left(\frac{Q}{2} - \int_0^1 u\, dx, c\right) = 0 \qquad \forall c \in \Re$$

where $V_h = \{v : v \in \Pi_2, v(1) = 0\}$ and $S_h = \{s : s \in \Pi_1\}$. This is called the viscous formulation where the elliptic term in Eq. 3.81 is simply replaced by $a(u_h, v_h)$. Since the scaling with β is retained, the viscous formulation is singular in the limit $\beta \to 0$. This can be demonstrated with a simple case where only a single element is defined on the domain $x \in [0, 1]$ with $x_i = \{0, \frac{1}{2}, 1\}$ for $i = 1, 2$, and 3. The nodal bases $\{\psi_i\}$ and $\{\phi_i\}$ for Π_1 and Π_2, respectively, are given by

$$\psi_1 = 1 - x$$
$$\psi_2 = x$$
$$\phi_1 = 2(x - 1)\left(x - \frac{1}{2}\right) \qquad (3.86)$$
$$\phi_2 = 4x(1 - x)$$
$$\phi_3 = 2x\left(x - \frac{1}{2}\right)$$

Using these bases with the viscous formulation yields the following system of linear algebraic equations for the coefficients u_{hi} and τ_{phi} in the basis function expansions for the velocity and stress

$$\begin{pmatrix} A & B & C \\ D & E & 0 \\ C^T & 0 & 0 \end{pmatrix} \begin{pmatrix} u_h \\ \tau_{ph} \\ \lambda \end{pmatrix} \begin{pmatrix} 0 \\ 0 \\ \frac{Q}{2} \end{pmatrix} \qquad (3.87)$$

where $\boldsymbol{u}_h \equiv [u_{h1}, u_{h2}, u_{h3}]^T$ and $\boldsymbol{\tau}_{ph} \equiv [\tau_{ph1}, \tau_{ph2}]^T$ are the vectors of coefficients in the expansion for velocity and polymer contribution to the stress tensor. The submatrices

119

in Eq. 3.87 are defined as

$$
\begin{aligned}
A_{ij} &\equiv a(\phi_i, \phi_j) & i,j &= 1,2,3 \\
B_{ij} &\equiv \left(\phi_i, \frac{d\psi_j}{dx}\right) & i &= 1,2,3; \; j = 1,2 \\
C_i &\equiv (\phi_i, 1) & i &= 1,2,3 \\
D_{ij} &\equiv \left(\psi_i, \frac{d\phi_j}{dx}\right) & i &= 1,2; \; j = 1,2,3 \\
E_{ij} &\equiv (\psi_i, \psi_j) & i,j &= 1,2
\end{aligned}
\tag{3.88}
$$

In this linear system $u_h \in \Pi_2$ instead of $u_h \in V_h$. The latter condition can be met by imposing the essential boundary condition, Eq. 3.75 by zeroing the third row of the matrix in Eq. 3.87 and placing a one on the diagonal. The final form of Eq. 3.87 with imposition of the essential boundary condition and computed inner products becomes

$$
\begin{pmatrix}
\frac{7\beta}{3} & -\frac{8\beta}{3} & \frac{\beta}{3} & -\frac{1}{6} & \frac{1}{6} & \frac{1}{6} \\
-\frac{8\beta}{3} & \frac{16\beta}{3} & -\frac{8\beta}{3} & -\frac{2}{3} & \frac{2}{3} & \frac{2}{3} \\
0 & 0 & 1 & 0 & 0 & 0 \\
-\frac{5(1-\beta)}{6} & \frac{2(1-\beta)}{3} & \frac{1-\beta}{6} & \frac{1}{3} & \frac{1}{6} & 0 \\
-\frac{1-\beta}{6} & -\frac{2(1-\beta)}{3} & \frac{5(1-\beta)}{6} & \frac{1}{6} & \frac{1}{3} & 0 \\
\frac{1}{6} & \frac{2}{3} & \frac{1}{6} & 0 & 0 & 0
\end{pmatrix}
\begin{pmatrix}
u_{h1} \\ u_{h2} \\ u_{h3} \\ \tau_{ph1} \\ \tau_{ph2} \\ \lambda
\end{pmatrix}
=
\begin{pmatrix}
0 \\ 0 \\ 0 \\ 0 \\ 0 \\ \frac{Q}{2}
\end{pmatrix}
\tag{3.89}
$$

Solving this linear system leads to the correct solution for the boundary value problem,

$$
\begin{aligned}
u_h(x) &= \frac{3Q}{4}(1 - x^2) \\
\tau_{ph} &= (1 - \beta)\frac{3Q}{2} \\
\lambda &= -\frac{3Q}{2}
\end{aligned}
\tag{3.90}
$$

However, the determinant of the matrix in Eq. 3.89 is equal to $-4\beta/7$, so the viscous formulation is singular for $\beta = 0$. This simple example demonstrates that the viscous formulation cannot be used for discretization when using a model where the solvent viscosity is zero. It is important to note that this result has nothing to do with the

constitutive equation used for the polymer contribution to the stress tensor. Instead the result demonstrates that the elliptic term in the momentum balance must be retained in the $\beta \to 0$ limit.

Alternative formulations and DEVSS-G

Several alternative formulations have been proposed and used in the literature for the momentum balance Baaijens [4] that retain the elliptic term. For purposes of discussion only the Elastic-Viscous Split Stress (EVSS) method of Rajagopalan et al. [88] and the Discrete Elastic-Viscous Split Stress (DEVSS) formulation of Guenette and Fortin [46] are discussed here.

In the EVSS formulation the polymer contribution to the stress tensor is split into viscous and elastic parts

$$\boldsymbol{\tau}_p = -(1-\beta)\dot{\boldsymbol{\gamma}} + \boldsymbol{\Sigma} \tag{3.91}$$

to yield a modified momentum balance

$$-\nabla^2 \boldsymbol{u} + \boldsymbol{\nabla} \cdot \boldsymbol{\Sigma} + \boldsymbol{\nabla}p = 0 \tag{3.92}$$

In this new formulation the term $\nabla^2 \boldsymbol{u}$ is no longer scaled with β but requires rewriting the constitutive equation in terms of the elastic stress $\boldsymbol{\Sigma}$. This often leads to an equation more complicated that the original constitutive equation. For example, the upper convected Maxwell model becomes

$$\boldsymbol{\Sigma} + \lambda[\boldsymbol{\Sigma}_{(1)} - (1-\beta)\dot{\boldsymbol{\gamma}}_{(1)}] = -(1-\beta)\dot{\boldsymbol{\gamma}} \tag{3.93}$$

where the term $\dot{\boldsymbol{\gamma}}_{(1)}$ contains second order derivatives of the velocity, similar to the elliptic operator in the momentum equation. In a finite element formulation this term would, therefore, require a boundary condition on the entire boundary of the computational domain, which is not appropriate for a hyperbolic equation like Eq. 3.93. For this reason, Rajagopalan et al. [88] introduced a piecewise linear, continuous

interpolant for each ij component of the rate of strain tensor such that

$$(\{\dot{\boldsymbol{\gamma}}_h - (\boldsymbol{\nabla}\boldsymbol{u}_h + \boldsymbol{\nabla}\boldsymbol{u}_h^T)\}_{ij}, s_h) = 0 \qquad \forall s_h \in S_h \tag{3.94}$$

This interpolant is then used in the constitutive equation 3.93 for calculation of the term $\dot{\boldsymbol{\gamma}}_{(1)}$. Brown et al. [13] introduced a slight modification to this called the EVSS-G (Elastic-Viscous Stress Split Gradient) formulation where the momentum balance remained unchanged as Eq. 3.92 but the gradient of the velocity is interpolated instead of the rate of tensor such that

$$(\{\boldsymbol{G}_h - \boldsymbol{\nabla}\boldsymbol{u}_h\}_{ij}, s_h) = 0 \qquad \forall s_h \in S_h \tag{3.95}$$

The components of the interpolant $\boldsymbol{G}_h$ are also chosen to be piecewise linear and continuous, but in the EVSS-G formulation, the interpolant is used to evaluate both $\dot{\boldsymbol{\gamma}}_{(1)}$ and $\boldsymbol{\Sigma}_{(1)}$. Both these formulations have been used extensively with the UCM and Oldroyd-B models Owens and Phillips [85] but they prove difficult to use with more complicated constitutive equations, such as FENE-P model from kinetic theory of polymers. Instead, Guenette and Fortin [46] proposed substituting Eq. 3.91 into Eq. 3.92 to obtain

$$-\nabla^2 \boldsymbol{u} + \boldsymbol{\nabla}\cdot[\boldsymbol{\tau}_p + (1-\beta)(\boldsymbol{G}+\boldsymbol{G}^T)] + \boldsymbol{\nabla}p = 0 \tag{3.96}$$

such that the interpolant $\boldsymbol{G}_h$ is used in the original constitutive equation. This has proven to be the most successful numerical formulation in viscoelastic fluid dynamics [91, 4] when used in conjunction with a suitable formulation for the constitutive equation. Revisiting the one-dimensional momentum balance that failed in the $\beta \to 0$ limit (Eq. 3.85), the following formulation is obtained for DEVSS-G method on a sin-

gle element

$$a(u_h, v_h) + \left(\frac{d\tau_{ph}}{dx}, v_h\right) + (1 - \beta)\left(\frac{dG_h}{dx}, v_h\right) + (\lambda, v_h) = 0 \qquad \forall v_h \in V_h$$

$$(\tau_{ph}, s_h) + (1 - \beta)\left(G_h, s_h\right) = 0 \qquad \forall s_h \in S_h$$

$$(G_h, s_h) - \left(\frac{du_h}{dx}, s_h\right) = 0 \qquad \forall s_h \in S_h \qquad (3.97)$$

$$\left(\frac{Q}{2} - \int_0^1 u\,dx, c\right) = 0 \qquad \forall c \in \Re$$

Here it is assumed that the function space for G_h is the same as that for τ_{ph}. Computing the necessary inner products in Eq. 3.97 yields the final system

$$
\begin{pmatrix}
\frac{7}{3} & -\frac{8}{3} & \frac{1}{3} & \frac{1}{6}(-1+\beta) & \frac{1-\beta}{6} & -\frac{1}{6} & \frac{1}{6} & \frac{1}{6} \\
-\frac{8}{3} & \frac{16}{3} & -\frac{8}{3} & -\frac{2}{3}(1-\beta) & \frac{2(1-\beta)}{3} & -\frac{2}{3} & \frac{2}{3} & \frac{2}{3} \\
0 & 0 & 1 & 0 & 0 & 0 & 0 & 0 \\
\frac{5}{6} & -\frac{2}{3} & -\frac{1}{6} & \frac{1}{3} & \frac{1}{6} & 0 & 0 & 0 \\
\frac{1}{6} & \frac{2}{3} & -\frac{5}{6} & \frac{1}{6} & \frac{1}{3} & 0 & 0 & 0 \\
0 & 0 & 0 & \frac{1-\beta}{3} & \frac{1-\beta}{6} & \frac{1}{3} & \frac{1}{6} & 0 \\
0 & 0 & 0 & \frac{1-\beta}{6} & \frac{1-\beta}{3} & \frac{1}{6} & \frac{1}{3} & 0 \\
\frac{1}{6} & \frac{2}{3} & \frac{1}{6} & 0 & 0 & 0 & 0 & 0
\end{pmatrix}
\begin{pmatrix}
u_{h1} \\ u_{h2} \\ u_{h3} \\ \tau_{ph1} \\ \tau_{ph2} \\ G_{h1} \\ G_{h2} \\ \lambda
\end{pmatrix}
=
\begin{pmatrix}
0 \\ 0 \\ 0 \\ 0 \\ 0 \\ 0 \\ 0 \\ \frac{Q}{2}
\end{pmatrix} \qquad (3.98)
$$

The determinant of the matrix in Eq. 3.98 is equal to $-1/81$, which shows that with the DEVSS-G formulation the discrete form of the momentum balance in nonsingular for all values of β. This formulation is, therefore, used in all calculations done with the momentum balance in this thesis.

One final point to consider is the choice of function spaces when constructing the finite element formulation for the momentum balance in more than one spatial dimension. The approach is similar to what has been presented so far where an appropriate functional to be minimized is defined for the momentum balance with the continuity equation serving as the Lagrangian constraint rather than a constraint on the flow rate. The resulting conditions from the minimization of this functional allows for direct solution for the pressure and velocities. However, when applying the Ritz-

Galerkin approximation, certain requirements on the function spaces for the velocity and pressure must be met in order to obtain a unique solution to the momentum balance. These requirements are given by the inf-sup or Babuška-Brezzi condition [3]. Without providing details, it is sufficient to state that the function spaces used for the one-dimensional problem (Eqs. 3.70 and 3.71) satisfy this condition. Details can be obtained from the work of Fortin et al. [38] who performed a rigorous analysis of the DEVSS-G formulation from a generalized Babuška-Brezzi theory.

3.5.3 Hyperbolic PDEs

In addition to solution of the momentum balance, any viscoelastic flow simulation must also consist of an appropriate treatment of the constitutive equation for polymer contribution to the stress tensor. As discussed already, the constitutive equations are typically either in the form of continuum-like evolution equations for average quantities describing molecular conformations, or require direct solution of the Fokker-Planck equation describing the distribution function for molecular orientations or stochastic simulation of individual molecule trajectories. All these descriptions yield partial differential equations that are hyperbolic in nature. This section demonstrates why the standard Galerkin method fails for linear hyperbolic problems, and how to treat the convective term in these constitutive equations with the stable and convergent discontinuous Galerkin method.

Galerkin approximation for hyperbolic equations

For purposes of discussion we will consider a linear hyperbolic equation

$$C + \boldsymbol{v} \cdot \boldsymbol{\nabla} C = f \tag{3.99}$$

which is defined on a domain Ω with boundary Γ with a forcing function f. The inflow boundary of Ω is defined as Γ_{inflow} and is defined as the portion of Γ with outward unit normal $\boldsymbol{n}$ where the inequality $\boldsymbol{v} \cdot \boldsymbol{n} < 0$ is satisfied. Additionally, the velocity field is assumed to be divergence free, i.e. $\boldsymbol{\nabla} \cdot \boldsymbol{v} = 0$. The significance of this

assumption will become clear shortly. We also introduce a a new inner product and norm in addition to the inner product of Eq. 3.60 and the standard L_2-norm

$$\langle u, w \rangle \equiv \oint_\Gamma (\boldsymbol{n} \cdot \boldsymbol{v}) u w \, ds \tag{3.100}$$

$$|w| = \langle w, w \rangle^{\frac{1}{2}} \tag{3.101}$$

where Eq. 3.100 represents a line integral in $\Re^2$. If we now multiply Eq. 3.99 by a test function C and integrate over the domain Ω in $\Re^2$ we obtain

$$(C, C) + (\boldsymbol{v} \cdot \boldsymbol{\nabla} C, C) = (f, C) \tag{3.102}$$

The inner product between a test function w and the convective term in Eq. 3.99 can be simplified to

$$\int_\Omega (\boldsymbol{v} \cdot \boldsymbol{\nabla} C) w \, dA = \int_\Omega \boldsymbol{\nabla} \cdot (\boldsymbol{v} C w) \, dA - \int_\Omega (\boldsymbol{\nabla} \cdot \boldsymbol{v}) C w \, dA - \int_\Omega (\boldsymbol{v} \cdot \boldsymbol{\nabla} w) C \, dA$$
$$= \oint_\Gamma (\boldsymbol{n} \cdot \boldsymbol{v}) C w \, ds - \int_\Omega (\boldsymbol{v} \cdot \boldsymbol{\nabla} w) C \, dA \tag{3.103}$$

This results allows for rewriting Eq. 3.102 as

$$(C, C) + \frac{1}{2} \langle C, C \rangle = (f, C) \tag{3.104}$$

Since C is a solution of the original partial differential equation Eq. 3.99, an expression can be obtained for the right hand side of Eq. 3.104 by using the following equality

$$(\boldsymbol{v} \cdot \boldsymbol{\nabla} C, \boldsymbol{v} \cdot \boldsymbol{\nabla} C) = (f - C, f - C)$$
$$= (f, f) - 2(f, C) + (C, C). \tag{3.105}$$

Substituting the expression for (f, C) in Eq. 3.104 yields the bounds on the value of C and on its gradient in the streamwise direction in terms of the norm of the forcing function f

$$|C|^2 + \|C\|^2 + \|\boldsymbol{v} \cdot \boldsymbol{\nabla} C\|^2 = \|f\|^2 \tag{3.106}$$

In trying to obtain a solution to Eq. 3.99 by using the standard Galerkin finite element method, we get the following formation

$$(C_h, w_h) + (\boldsymbol{v} \cdot \boldsymbol{\nabla} C_h, w_h) = (f, w_h) \qquad \forall w_h \in W_h \tag{3.107}$$

where the function space $W_h \equiv \{w : w \in C^0(\Omega), w = 0 \text{ on } \Gamma\}$. The corresponding form of Eq. 3.104 is now

$$(C_h, C_h), \frac{1}{2} \langle C_h, C_h \rangle = (f, C_h) \tag{3.108}$$

where we can no longer simplify the right hand side of Eq. 3.108 as before because the solution C_h only satisfies Eq. 3.99 weakly. Instead, we use the Schwarz' inequality

$$(f, C_h) \leq (f, f)(C_h, C_h) \tag{3.109}$$

to obtain the following condition on the norm

$$|C_h|^2 + \|C_h\|^2 \leq \|f\|^2 \|C_h\|^2 \tag{3.110}$$

For problems with smooth solutions, this formulation of the model hyperbolic problem leads to approximate solutions with good convergence properties since the norm of the solution is bounded by the norm of the forcing function. However, if the solution has sharp gradients, the approximate solution does not control the error in the gradient of the solution in the streamwise direction. When sharp gradients occur, the solution C_h over-estimates the magnitude of the gradient in order to minimize the error in C_h, and because the functions in the approximating function space W_h are continuous, the overshoot in the gradient leads to large oscillations within the surrounding elements. This deficiency can be alleviated by either introducing a term which controls the gradient, for e.g. numerical diffusion, or by relaxing the requirement that C_h be continuous. This is primary reason for considering the discontinuous Galerkin method for solution of hyperbolic constitutive equations.

The Discontinuous Galerkin Method

The discontinuous Galerkin (DG) method was first introduced by Reed and Hill [91] and has evolved considerably since then, gaining significant popularity in the last decade and a half. The primary reasons for its popularity include some of the main advantages of the finite element method over classical finite volume and finite difference methods, such as the ability to obtain solutions of arbitrarily high order of accuracy by choosing the approximating polynomials of suitable order or the ability to handle complicated geometries. More importantly, however, the DG method is highly parallelizable since the approximating elements are discontinuous and decoupled, which leads to matrices of the same size as the number of degrees of freedom inside a given element. This means that the matrices can be computed and inverted once and for all. In addition, the method can easily handle mesh-adaptivity strategies without taking into account the continuity restrictions typical of conforming finite element methods. This is of critical importance in hyperbolic problems given the complexity of the structure of the discontinuities [21].

Even though the theoretical and computational development of the method occurred in the framework of linear hyperbolic systems and ordinary differential equations [45] significant developments have taken place in its use with parabolic problems and the numerical approximation of viscoelastic flows. During the evolution of the method, it was first extended to nonlinear hyperbolic problems using implicit schemes, which were later adapted to explicit schemes known as Runge-Kutte DG or RKDG [22]. Following this important development with nonlinear hyperbolic problems, Bassi and Rebay [6] proposed an extension of DG for the discretization of compressible Navier-Stokes. The resulting methods were highly parallelizable and of high-order accuracy. This work was generalized with the introduction of the local discontinuous Galerkin (LDG) method of Cockburn and Shu [23] who proved both stability and high-order accuracy of the method. An excellent review of these methods can be found in the text by Cockburn et al. [21].

127

Ritz-Galerkin Approximation In the standard Galerkin method the unknown function, say u, is approximated by piecewise continuous functions defined on each element of the discretized mesh. Hence, the discretization of u, denoted by u_h is continuous. In contrast, in a discontinuous Galerkin finite element method, piecewise continuous functions are defined on the element such that the value of the approximating function at a node when approached from the left or right is not continuous. This is shown in Fig. 3-13 for piecewise linear basis functions.

Despite this main difference, the steps in a continuous or DG discretization are the same. We first derive the weak formulation by multiplying the equation by an arbitrary test function and integrate over the domain of validity. This is followed by expanding the unknown function in each element in a series in terms of a finite number of basis functions. Each basis function has compact support within each element (see Fig. 3-14), that is the basis functions are only nonzero locally within an element including the element boundary, and zero elsewhere. This expansion is then substituted into the weak formulation and the test functions are chosen to be the same as the basis functions. Finally, the integrals in the weak formulation are evaluated using a local or reference coordinate system (also known as isoparametric coordinates) (see Fig. 3-15) to yield the discretized weak formulation, which is typically a linear or nonlinear algebraic system.

For the purpose of describing the finite element approximation using discontinuous basis functions, we will consider the one-dimensional hyperbolic equation

$$\frac{\partial C}{\partial t} + \frac{\partial (vC)}{\partial x} = -KC \tag{3.111}$$

which describes the conservation of a chemical species being swept by flow in the x direction with velocity v and consumed in a first order reaction with rate constant K. Since solution to hyperbolic problems require the specification of an initial condition and an appropriate boundary condition that takes into account the propagation of information, proper specification of the term vC, which represents a flux, on element boundaries is essential for communication between adjacent elements. This can be

seen by considering the weak form of the convective term in Eq. 3.111

$$\int_\Omega \frac{\partial(vC)}{\partial x}\phi_i\,dx = vC\phi_i\Big|_\Gamma - \int_\Omega (vC)\frac{\partial \phi_i}{\partial x}\,dx \qquad (3.112)$$

which shows that the weak formulation requires the specification of the flux on elemental boundaries, such that it is consistent when viewed from either the upstream or downstream element. There are several options that may be considered. One may choose either the upstream or downstream flux or a combination, however, it makes most sense to consider the upstream flux for an element since information travels along "characteristics" or in the streamwise direction. A more rigorous explanation of this choice can be found in the text by Cockburn et al. [21].

While this is sufficient to solve the problem, it is not always convenient to use such a formulation as it requires additional book keeping for element orientation and fluxes. This is particularly demanding for problems in more than one dimension. As a result, we will now look at a different formulation that replaces the weak form of the convective term with an appropriate correction on all inflow sides. Let us reconsider the weak form of the convective term in three dimension such that the flux vC is replaced by a flux f

$$\int_{\Omega_e} (\boldsymbol{\nabla} \cdot \boldsymbol{f})\phi_i\,dV = -\int_{\Omega_e} (\boldsymbol{f} \cdot \boldsymbol{\nabla}\phi_i)\,dV + \int_{\Gamma_e} \phi_i \boldsymbol{f} \cdot d\boldsymbol{A} \qquad (3.113)$$

It is convenient to define a flux $\boldsymbol{f}^{\,\text{in}}$ as the flux computed interior to an element, and opposite to the outward unit normal direction on the element boundary, whereas $\boldsymbol{f}^{\,\text{ex}}$ denotes the flux computed exterior to an element in the direction of the unit normal on the element boundary. Additionally, we divide the boundary of an element into non-overlapping subsets that are considered inflow and outflow boundaries such that

$$\Gamma_{e,\,\text{in}} \equiv \Gamma_e : \boldsymbol{n} \cdot \boldsymbol{v} < 0 \qquad (3.114)$$

$$\Gamma_{e,\,\text{out}} \equiv \Gamma_e : \boldsymbol{n} \cdot \boldsymbol{v} \geq 0 \qquad (3.115)$$

This allows us to rewrite the surface integral in Eq. 3.113 as a sum of integrals over

the inflow and outflow boundaries such that

$$
\begin{aligned}
\int_{\Gamma_e} \phi_i \boldsymbol{f} \cdot d\boldsymbol{A} &= \int_{\Gamma_{e,\,\mathrm{in}}} \phi_i \boldsymbol{f} \cdot d\boldsymbol{A} + \int_{\Gamma_{e,\,\mathrm{out}}} \phi_i \boldsymbol{f} \cdot d\boldsymbol{A} \\
&= \int_{\Gamma_{e,\,\mathrm{in}}} \phi_i \boldsymbol{f}^{\,\mathrm{ex}} \cdot d\boldsymbol{A} + \int_{\Gamma_{e,\,\mathrm{out}}} \phi_i \boldsymbol{f}^{\,\mathrm{in}} \cdot d\boldsymbol{A}
\end{aligned}
\tag{3.116}
$$

where the flux on the inflow boundary is evaluated from the upstream side external to the element, and the flux on the outflow boundary is also evaluated on the upstream side, which is within the element. We can also rewrite the first term on the right hand side of Eq. 3.113 as

$$
-\int_{\Omega_e} (\boldsymbol{f} \cdot \boldsymbol{\nabla}\phi_i)\, dV = -\int_{\Omega_e} (\boldsymbol{f}^{\,\mathrm{in}} \cdot \boldsymbol{\nabla}\phi_i)\, dV
\tag{3.117}
$$

where flux is evaluated within the element as differentiation has been passed onto the local basis functions. Combining Eqs. 3.116 and 3.117 we get

$$
\int_{\Omega_e} (\boldsymbol{\nabla} \cdot \boldsymbol{f})\phi_i\, dV = -\int_{\Omega_e} (\boldsymbol{f}^{\,\mathrm{in}} \cdot \boldsymbol{\nabla}\phi_i)\, dV + \int_{\Gamma_{e,\,\mathrm{in}}} \phi_i \boldsymbol{f}^{\,\mathrm{ex}} \cdot d\boldsymbol{A} + \int_{\Gamma_{e,\,\mathrm{out}}} \phi_i \boldsymbol{f}^{\,\mathrm{in}} \cdot d\boldsymbol{A}
\tag{3.118}
$$

We now add and subtract the term $\displaystyle\int_{\Gamma_{e,\,\mathrm{in}}} \phi_i \boldsymbol{f}^{\,\mathrm{in}} \cdot d\boldsymbol{A}$ from the right hand side of Eq. 3.118 to get

$$
\begin{aligned}
\int_{\Omega_e} (\boldsymbol{\nabla} \cdot \boldsymbol{f})\phi_i\, dV = & -\int_{\Omega_e} (\boldsymbol{f}^{\,\mathrm{in}} \cdot \boldsymbol{\nabla}\phi_i)\, dV + \int_{\Gamma_{e,\,\mathrm{in}}} \phi_i \boldsymbol{f}^{\,\mathrm{ex}} \cdot d\boldsymbol{A} \\
& + \int_{\Gamma_{e,\,\mathrm{out}}} \phi_i \boldsymbol{f}^{\,\mathrm{in}} \cdot d\boldsymbol{A} + \int_{\Gamma_{e,\,\mathrm{in}}} \phi_i \boldsymbol{f}^{\,\mathrm{in}} \cdot d\boldsymbol{A} - \int_{\Gamma_{e,\,\mathrm{in}}} \phi_i \boldsymbol{f}^{\,\mathrm{in}} \cdot d\boldsymbol{A}.
\end{aligned}
\tag{3.119}
$$

The third and fourth terms on the right hand side of Eq. 3.119 can be rewritten as $\displaystyle\int_{\Gamma_e} \phi_i \boldsymbol{f}^{\,\mathrm{in}} \cdot d\boldsymbol{A}$ leading to the simplification

$$
\begin{aligned}
\int_{\Omega_e} (\boldsymbol{\nabla} \cdot \boldsymbol{f})\phi_i\, dV &= -\int_{\Omega_e} (\boldsymbol{f}^{\,\mathrm{in}} \cdot \boldsymbol{\nabla}\phi_i)\, dV + \int_{\Gamma_e} \phi_i \boldsymbol{f}^{\,\mathrm{in}} \cdot d\boldsymbol{A} + \int_{\Gamma_{e,\,\mathrm{in}}} \phi_i [\boldsymbol{f}^{\,\mathrm{ex}} - \boldsymbol{f}^{\,\mathrm{in}}] \cdot d\boldsymbol{A} \\
&= \int_{\Omega_e} (\boldsymbol{\nabla} \cdot \boldsymbol{f}^{\,\mathrm{in}})\phi_i\, dV + \int_{\Gamma_{e,\,\mathrm{in}}} \phi_i [\boldsymbol{f}^{\,\mathrm{ex}} - \boldsymbol{f}^{\,\mathrm{in}}] \cdot d\boldsymbol{A}
\end{aligned}
$$

$$
\tag{3.120}
$$

130
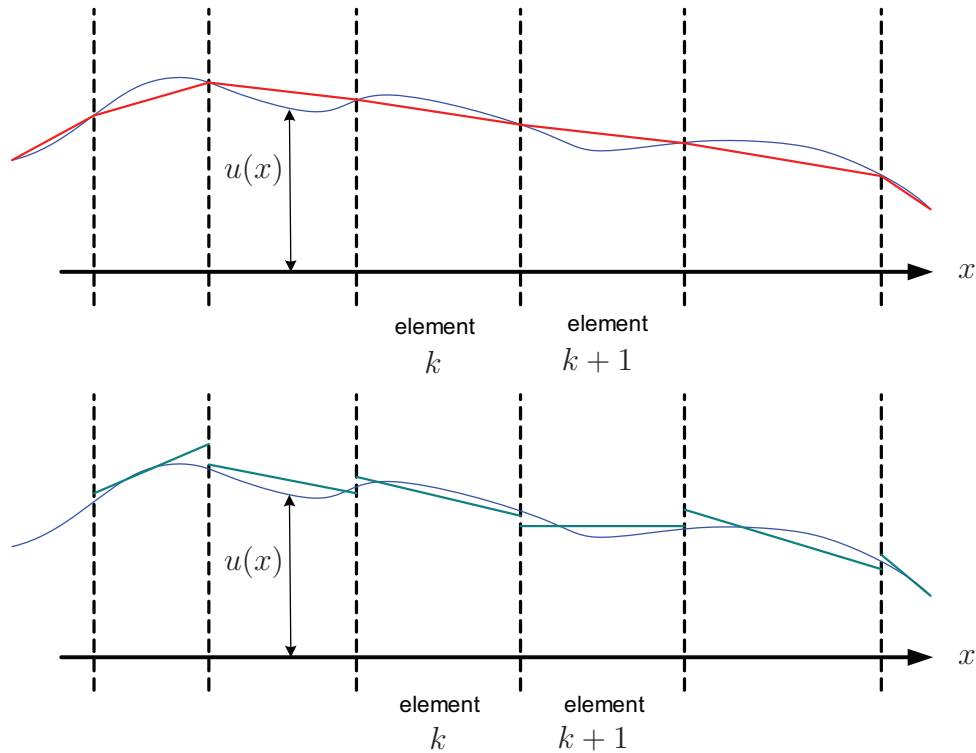
Figure 3-13: In a continuous Galerkin finite element method, the unknown function $u = u(x)$ is approximated globally in a continuous manner (top figure). In contrast, in a discontinuous Galerkin finite element method, the unknown $u = u(x)$ is approximated globally in a discontinuous manner and locally in each element in a continuous way (bottom figure). In this example the approximating basis are piecewise linear functions.

This final result is at the heart of most DG implementations, where the convective term is replaced by an evaluation of the flux within the element along with a jump term across the inflow boundary of the element. This formulation is used for the convective terms appearing in this thesis.

3.6   Bifurcation Analysis

The methods described so far allow the computation of a single stationary solution for a given parameter value and its associated linear stability using the Arnoldi process. However, one is often interested in learning how the qualitative nature of these solutions change across a range of parameters. Bifurcation analysis is the mathemat-
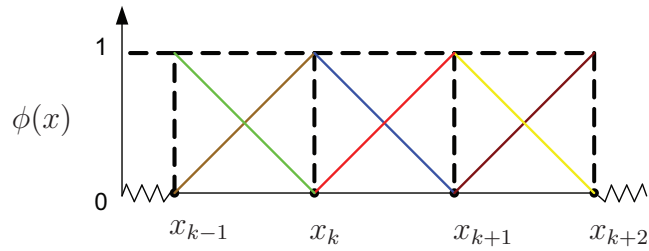
Figure 3-14: Global picture of discontinuous linear basis functions, emphasizing the lack of overlap between basis functions across element boundaries
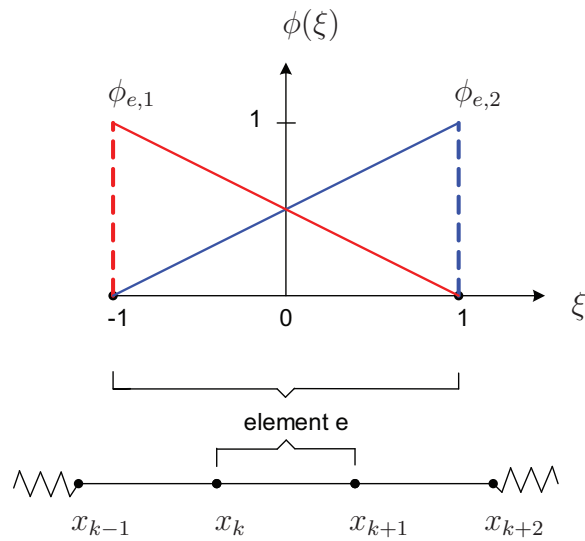
Figure 3-15: Linear discontinuous basis functions local to element k, shown in isoparametric coordinates. These basis functions are non-zero only within element k.

ical study of understanding how the long-term behavior (equilibria/fixed points or periodic orbits) of a dynamical system varies as a function of some bifurcation parameter. Here we will consider the standard dynamical system consisting of ordinary differential equations to discuss the basic principles underlying continuation and homotopy methods, and provide one specific example called the "predictor–corrector" method that has been used in this thesis to perform bifurcation analysis. Finally, we will argue that the resulting equations are particularly amenable for solution with Newton iterative methods.

We are concerned with finding solutions of the equation

$$\boldsymbol{f}(\boldsymbol{x}; \mu) = \boldsymbol{0} \tag{3.121}$$

over a range of parameter values, $\mu = [\mu_0, \mu_f]$, such that both $\boldsymbol{f}$ and $\boldsymbol{x}$ are vectors of length n, and $\boldsymbol{f}$ is assumed to be continuously differentiable everywhere in $\mathbb{R}^n$. Here $\boldsymbol{f}$ represents the right hand side of a system of ordinary differential equations that may not be known explicitly. We also assume that for the initial parameter value of μ_0, we are able to solve the equation using Newton's method with a sufficiently good initial guess. For example, a parameter value of zero, may lead to an equation that is easy to solve or one for which the solution is known. Once we have the solution at the initial parameter value, we can use this as an initial guess to solve the equation for the next parameter value until we have obtained the entire solution curve. This is an idea imported from the general class of methods known as *homotopy* methods, where one solves a complex equation by starting with a simple equation for which the solution is known or easy to calculate, followed by a relaxation of the simplifications step by step, such that the solution of each equation serves as an initial guess to the following more complicated equation [98].

As an example consider the case where the problem is easy to solve at $\mu = \mu_0$ due to a good initial guess. We can then immediately introduce a new real parameter λ

that varies in $0 \leq \lambda \leq 1$, such that

$$\mu(\lambda) = (1 - \lambda)\mu_0 + \lambda\mu_f \tag{3.122}$$

With this our problem is modified to generating a solution path $\boldsymbol{x}(\lambda)$ where

$$\boldsymbol{f}(\boldsymbol{x}(\lambda); \mu(\lambda)) = \boldsymbol{0}$$

Starting with $\lambda = 0$ and solution $\boldsymbol{x}(0)$ we can obtain the solution at $\delta\lambda$ if we have an expression for $d\boldsymbol{x}/d\lambda$. This can be done easily via a Taylor expansion for small $\delta\lambda$

$$\begin{aligned}
\boldsymbol{f}(\boldsymbol{x}(\lambda + \delta\lambda); \mu(\lambda + \delta\lambda)) = {} & \boldsymbol{f}(\boldsymbol{x}(\lambda); \mu(\lambda)) + \left(\frac{\partial \boldsymbol{f}}{\partial \boldsymbol{x}^T}\right)\left(\frac{d\boldsymbol{x}}{d\lambda}\right)\delta\lambda \\
& + \left(\frac{\partial \boldsymbol{f}}{\partial \mu}\right)\left(\frac{d\mu}{d\lambda}\right)\delta\lambda + \mathcal{O}(\delta\lambda^2)
\end{aligned} \tag{3.123}$$

Since

$$\boldsymbol{f}(\boldsymbol{x}(\lambda + \delta\lambda); \mu(\lambda + \delta\lambda)) = \boldsymbol{f}(\boldsymbol{x}(\lambda); \mu(\lambda)) = \boldsymbol{0}$$

we obtain

$$\frac{d\boldsymbol{x}}{d\lambda} = -\left(\frac{\partial \boldsymbol{f}}{\partial \boldsymbol{x}^T}\right)^{-1}\frac{\partial \boldsymbol{f}}{\partial \mu}\frac{d\mu}{d\lambda} \tag{3.124}$$

3.6.1 Principal tasks in a continuation method for bifurcation analysis

The above approach captures the essence of a *continuation* method where one generates a chain of solutions at a finite number of parameter values by framing a homotopy method as an initial value problem. However, this approach should also be able to detect and capture the richness of the bifurcation diagram that may exist for Eq. 3.121. An example of this is presented in Fig. 3-16. First, it is not unusual to have more than one solution existing at a given value of the parameter. The solution arrived at by a given solution method can, therefore, depend sensitively on the initial guess supplied to the method. In other words, the branch traced out by the continuation method

134

will depend on where the initial solution converges. Also, if two solution branches are close to each other, the parameter step size for the method must be sufficiently small to converge to the same solution branch.

Second, one can see that Eq. 3.124 works fine as long as the Jacobian of the function, $\partial \boldsymbol{f}/\partial \boldsymbol{x}^T$ is non-singular. Values of the parameter at which all eigenvalues of the Jacobian are non-zero are termed *regular* points. If one eigenvalue of the Jacobian is zero at a given point, it is then termed either as a *turning* point or a *simple stationary bifurcation* point. At a turning point the solution curve turns back upon itself in parameter space as shown in Fig. 3-16. If such a point is present, ranges of parameter space may exist in which no steady-state solution exists. On the other hand, a stationary bifurcation point is characterized by intersection of two branches of stationary solutions that have two distinct tangents. With continuation methods that aim to trace out a single solution branch, turning points can be handled naturally, while stationary bifurcation points are not. This is because even though the matrix $\boldsymbol{f}_{\boldsymbol{x}} = \partial \boldsymbol{f}/\partial \boldsymbol{x}^T$ is singular or rank deficient for both type of bifurcations, the augmented matrix $(\boldsymbol{f}_{\boldsymbol{x}}|\boldsymbol{f}_{\mu})$, where $\boldsymbol{f}_{\mu} = \partial \boldsymbol{f}/\partial \mu$, is full rank. For further details see §2.5 of Seydel [98]. As a result, using a continuation method one can easily trace a solution branch around a turning point. If needed, one can also add a method to check for stability of the computed solutions. An example of this would be branch A in Fig. 3-16 containing both stable and unstable solutions. In addition, if one is interested in computing branch B given that branch A has already been computed, this can be done with a branch switching algorithm that provides one point on branch B, after which the entire branch can be easily computed via continuation.

Given the nature of solutions that may arise, any parameter study of Eq. 3.121 must consist of a (1) continuation method for tracing out smooth branches of Eq. 3.121 while checking for stability, and a (2) method for switching from one branch to another with or without the option of calculating the branch point itself. In what follows we will restrict ourselves to "predictor-corrector" type continuation methods, which have been used successfully in many scientific and engineering applications and constitute the most time-consuming part of any such study. Methods for branch switching will
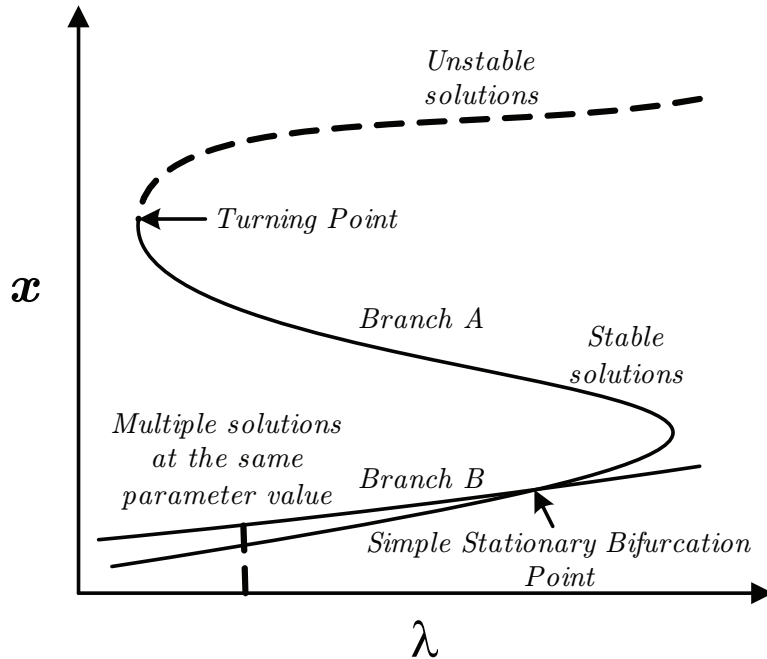
Figure 3-16: Schematic description of solution families, bifurcations and limit points

not be presented but further details can be obtained from the text by Seydel [98].

3.6.2 Predictor-Corrector Method

Assuming one solution on the branch for Eq. 3.121 has been computed, say $(\boldsymbol{x}_0; \mu_0)$, our task is to then compute further solutions on the branch,

$$(\boldsymbol{x}_1; \mu_1), (\boldsymbol{x}_2; \mu_2), \ldots$$

until one reaches the target point μ_f. With predictor-corrector methods the jth continuation step starts from a solution $(\boldsymbol{x}_j; \mu_j)$ and attempts to calculate the solution $(\boldsymbol{x}_{j+1}; \mu_{j+1})$ in two steps:

$$(\boldsymbol{x}_j; \mu_j) \xrightarrow{\text{predictor}} (\bar{\boldsymbol{x}}_{j+1}; \bar{\mu}_{j+1}) \xrightarrow{\text{corrector}} (\boldsymbol{x}_{j+1}; \mu_{j+1})$$

where the predictor $(\bar{\boldsymbol{x}}_{j+1}; \bar{\mu}_{j+1})$ is not a solution of Eq. 3.121 (see Fig. 3-17). The distance between two consecutive solutions is called the step size or step length and
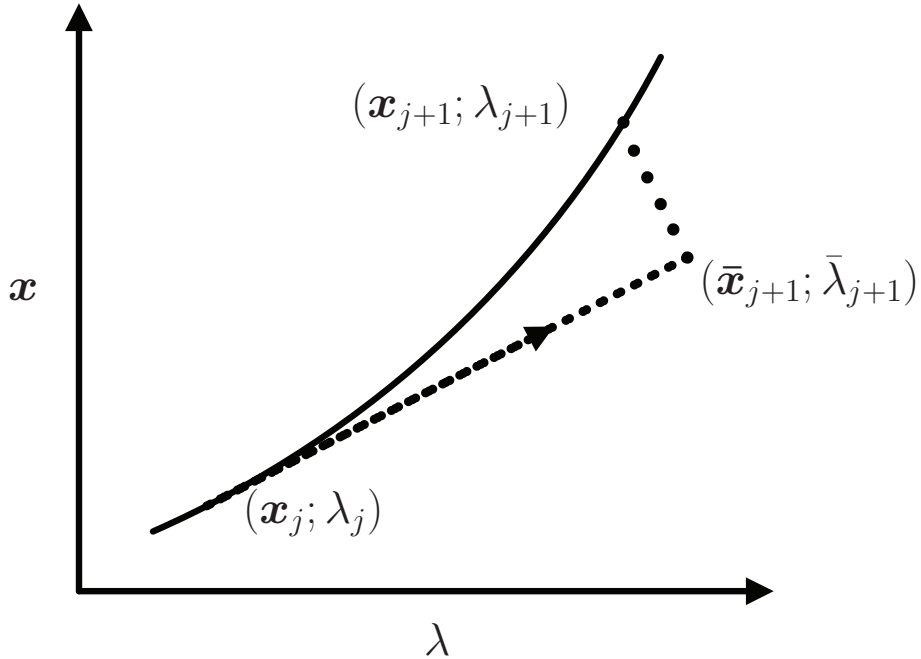
Figure 3-17: Schematic for the predictor-corrector method

is generally unknown a priori. In addition to Eq. 3.121, we also need a relationship that identifies the location of a solution on the branch in terms of a curve parameter. This relationship is different from the one introduced earlier to express μ in terms of λ (Eq. 3.122). Specifically we will look at arc-length s, which has been used extensively in literature and does not pose any problems with turning points [98]. While a robust continuation method incorporates predictor and corrector steps along with a parametrization strategy, and a step length control algorithm, we will focus on a simple tangent predictor combined with an iterative corrector method that uses a fixed step size arc-length parametrization.

Parametrization

We begin by introducing a new parametrization of the solution curve, where both $\boldsymbol{x}$ and λ are considered to be functions of the arclength parameter s, such that $\boldsymbol{x} = \boldsymbol{x}(s)$ and $\lambda = \lambda(s)$. Once λ is known, the original parameter for the problem, μ, can be readily obtained using Eq. 3.122. For a particular value of s, the system $\boldsymbol{f}(\boldsymbol{x};\lambda) = \boldsymbol{0}$

137

consists of n equations for the $n + 1$ unknowns $(\boldsymbol{x}; \lambda)$. The additional scalar equation needed to find the unknowns $(\boldsymbol{x}; \lambda)$ is provided by a relationship for the change in the path length as we move along the solution curve in $(\boldsymbol{x}; \lambda)$ space by an amount $\delta\boldsymbol{x}$ and $\delta\lambda$. This is given by

$$(\delta s)^2 = (\delta\lambda)^2 + \delta\boldsymbol{x} \cdot \delta\boldsymbol{x} \tag{3.125}$$

and results in the following extended system

$$\boldsymbol{F}(\boldsymbol{x}, \lambda; s) = \begin{pmatrix} \boldsymbol{f}(\boldsymbol{x}; \lambda) \\ (\boldsymbol{x} - \boldsymbol{x}_j) \cdot (\boldsymbol{x} - \boldsymbol{x}_j) + (\lambda - \lambda_j)^2 - (s - s_j)^2 \end{pmatrix} = \boldsymbol{0} \tag{3.126}$$

where $(\boldsymbol{x}_j; \lambda_j)$ is the solution previously calculated during continuation at arclength s_j. Solving Eq. 3.126 with a generic solver for nonlinear equations provides the solution curve at discretized arclengths with a spacing of $\Delta s = s - s_j$. This spacing or step size is generally fixed in a given calculation.

While it is sufficient to solve the system in Eq. 3.126 to obtain the solution curve, the calculation is not guaranteed to move in a unique direction along the curve and requires solution of a nonlinear system for each discretized arclength. We can avoid these extra computations by employing a predictor-corrector scheme, where Newton iterations of Eq. 3.126 are not invoked if the predicted result, $(\bar{\boldsymbol{x}}_{j+1}; \bar{\mu}_{j+1})$, is sufficiently close to the solution branch or used alternatively as an initial guess for corrector iterations. The latter case involves application of Newton's method to $\boldsymbol{f}(\boldsymbol{x}; \lambda) = \boldsymbol{0}$ with the imposition of an appropriate side condition on the iterations. In most instances, these iterations can be made more efficient by using results from the predictor step.

Tangent Predictor

It was shown in §3.6 that given the derivatives of Eq. 3.121 we can reduce the problem of obtaining the solution curve to an ordinary differential equation. Most predictor methods, and specifically the tangent predictor, is based on this idea of using the

138

solution at $s = s_j$ to obtain an explicit Euler update to the solution such that

$$\begin{pmatrix} \bar{\boldsymbol{x}}_{j+1} \\ \bar{\lambda}_{j+1} \end{pmatrix} = \begin{pmatrix} \boldsymbol{x}_j \\ \lambda_j \end{pmatrix} + \begin{pmatrix} \left.\dfrac{d\boldsymbol{x}}{ds}\right|_{s_j} \\ \left.\dfrac{d\lambda}{ds}\right|_{s_j} \end{pmatrix} \Delta s \tag{3.127}$$

To solve for $\left.\dfrac{d\boldsymbol{x}}{ds}\right|_{s_j}$ and $\left.\dfrac{d\lambda}{ds}\right|_{s_j}$, which form the components of the vector tangent to the solution curve, we use the following Taylor expansion in δs

$$\begin{aligned}
\boldsymbol{f}(\boldsymbol{x}(s + \delta s); \mu(s + \delta s)) = {} & \boldsymbol{f}(\boldsymbol{x}(s); \mu(s)) + \left(\frac{\partial \boldsymbol{f}}{\partial \boldsymbol{x^T}}\right)\left(\frac{d\boldsymbol{x}}{ds}\right)\delta s \\
& + \left(\frac{\partial \boldsymbol{f}}{\partial \mu}\right)\left(\frac{d\mu}{d\lambda}\right)\left(\frac{d\lambda}{ds}\right)\delta s + \mathcal{O}(\delta s^2)
\end{aligned} \tag{3.128}$$

to obtain the linear system

$$\left(\frac{\partial \boldsymbol{f}}{\partial \boldsymbol{x^T}}\right)\bigg|_{s_j} \frac{d\boldsymbol{x}}{ds} + \left(\frac{\partial \boldsymbol{f}}{\partial \mu}\frac{d\mu}{d\lambda}\right)\bigg|_{s_j} \frac{d\lambda}{ds} = \boldsymbol{0} \tag{3.129}$$

As already mentioned, we are guaranteed a solution to this problem as long as the matrix $(\boldsymbol{f_x}|\boldsymbol{f_\lambda})$ is of rank n. However, the length and orientation of the tangent vector are still undetermined, and a normalization condition must be imposed for the tangent vector to get a unique solution. One way of doing this is to use the equation

$$\boldsymbol{c}^T \begin{bmatrix} \dfrac{d\boldsymbol{x}}{ds} \\ \dfrac{d\lambda}{ds} \end{bmatrix} = 1 \tag{3.130}$$

where $\boldsymbol{c}$ is some vector not perpendicular to the tangent. Traditional methods use $\boldsymbol{c} = \boldsymbol{e}_k$ where $\boldsymbol{e}_k$ is the $(n+1)$-dimensional unit vector with all elements equal to zero except the kth, which equals unity. Beers [7] suggests using a randomly generated vector as it is highly unlikely to ever be perpendicular to the tangent. This yields the

139

final linear system

$$
\begin{bmatrix}
\left(\dfrac{\partial \boldsymbol{f}}{\partial \boldsymbol{x}^T}\right)\Big|_{s_j} & \left(\dfrac{\partial \boldsymbol{f}}{\partial \mu}\dfrac{d\mu}{d\lambda}\right)\Big|_{s_j} \\
\cdots & \boldsymbol{c}^T & \cdots
\end{bmatrix}
\begin{bmatrix}
\dfrac{d\boldsymbol{x}}{ds} \\
\dfrac{d\lambda}{ds}
\end{bmatrix}
=
\begin{bmatrix}
\boldsymbol{0} \\
1
\end{bmatrix}
\tag{3.131}
$$

where we enforce the following check to ensure that we are moving in a consistent direction in $(\boldsymbol{x}; \lambda)$ space

$$
\begin{bmatrix}
\dfrac{d\boldsymbol{x}}{ds} \\
\dfrac{d\lambda}{ds}
\end{bmatrix}
\cdot
\begin{bmatrix}
\boldsymbol{x}_j - \boldsymbol{x}_{j-1} \\
\lambda_j - \lambda_{j-1}
\end{bmatrix}
\geq 0
\tag{3.132}
$$

Before proceeding to corrector iterations, it may be useful to check if the predicted result is sufficiently close to the solution curve with the criterion

$$
\|\boldsymbol{f}(\bar{\boldsymbol{x}}_{j+1}; \bar{\lambda}_{j+1})\| \leq \delta_{\text{tol}}
$$

This check can save unnecessary corrector iterations along "flat" segments of the solution branch provided a sufficiently small step size is being used to perform continuation.

Corrector Step

To construct a robust corrector step, it is helpful to consider one step of the Newton iteration for the nonlinear system $\boldsymbol{f}(\boldsymbol{x}; \lambda) = \boldsymbol{0}$. This yields

$$
\left(\dfrac{\partial \boldsymbol{f}}{\partial \boldsymbol{x}^T}\right)\Big|_{(\boldsymbol{x}^k; \lambda^k)} \Delta \boldsymbol{x}^k + \left(\dfrac{\partial \boldsymbol{f}}{\partial \mu}\dfrac{d\mu}{d\lambda}\right)\Big|_{(\boldsymbol{x}^k; \lambda^k)} \Delta \lambda^k = -\boldsymbol{f}(\boldsymbol{x}^k; \lambda^k)
$$
$$
\boldsymbol{x}^{k+1} = \boldsymbol{x}^k + \Delta \boldsymbol{x}^k, \qquad \lambda^{k+1} = \lambda^k + \Delta \lambda^k
\tag{3.133}
$$

with the initial guess given by

$$
(\boldsymbol{x}^0; \lambda^0) = (\bar{\boldsymbol{x}}_{j+1}; \bar{\lambda}_{j+1})
$$

As with the predictor step, this is a system of n equations in $n + 1$ unknowns $(\Delta\boldsymbol{x}^k; \Delta\lambda^k)$ and requires an additional equation to parameterize the course of corrector iterations. By requiring that the iterations be perpendicular to the tangent computed in the predictor step we can append the necessary equation

$$\left[\frac{d\boldsymbol{x}^T}{ds} \;\; \frac{d\lambda}{ds}\right] \begin{bmatrix} \Delta\boldsymbol{x}^k \\ \Delta\lambda^k \end{bmatrix} = 0$$

to converge to a solution $(\boldsymbol{x}_{j+1}; \lambda_{j+1})$ as shown in Fig. 3-17, where circles represent subsequent iterations of the correct step. More importantly, for small Δs, the algorithm can be made more efficient by reusing the derivatives computed in the predictor step to yield a linear system

$$\begin{bmatrix} \left.\left(\dfrac{\partial \boldsymbol{f}}{\partial \boldsymbol{x}^T}\right)\right|_{s_j} & \left.\left(\dfrac{\partial \boldsymbol{f}}{\partial \mu}\dfrac{d\mu}{d\lambda}\right)\right|_{s_j} \\[2mm] \dfrac{d\boldsymbol{x}^T}{ds} & \dfrac{d\lambda}{ds} \end{bmatrix} \begin{bmatrix} \Delta\boldsymbol{x}^k \\ \Delta\lambda^k \end{bmatrix} = \begin{bmatrix} -\boldsymbol{f}(\boldsymbol{x}^k; \lambda^k) \\ 0 \end{bmatrix} \tag{3.134}$$

It must be noted that while the right hand side of Eq. 3.134 is updated in each corrector iteration, the matrix on the left hand side is factorized only once and reused in subsequent iterations. The iterations are terminated with the criterion

$$\|\boldsymbol{f}(\boldsymbol{x}^k; \lambda^k)\| \leq \delta_{\text{tol}}$$

where δ_{tol} is a tolerance set at the beginning of the iterations.

The components of the predictor–corrector scheme can be modified as needed, with the exception of parametrization strategy, to solve the problem at hand. Since the predictor step provides a prediction by computing a tangent to the solution curve, it is less susceptible to failure in comparison to the corrector step that may become too expensive as the dimensionality of the system is increased or when the derivatives computed in the predictor step cannot be reused. This problem can be avoided by employing iterative methods such as GMRES to determine an approximate solution of Equation 3.134. As mentioned previously, one main advantage of such methods is

that they are always implemented as matrix-free methods, since only matrix-vector products, rather than details of the matrix itself (in our case the matrix on the left hand side of Equation 3.134) are needed to implement the method. Additionally, in this problem, the eigenvalues of the matrix in Equation 3.134 are dominated by those of the Jacobian $\boldsymbol{f_x}$, which is the Jacobian of the coarse time-stepper. As a consequence, we would expect iterative methods like GMRES to rapidly converge to a solution for the corrector step.

Chapter 4

Using Newton-GMRES for Viscoelastic Flow Time-steppers

The majority of publications in computational rheology have been based on a macroscopic approach that utilizes constitutive equations inspired by kinetic theory. This approach invariably requires the use of closure approximations in the derivation of the constitutive models, which can have a significant qualitative impact on predictions of such simulations. However, the recent, complementary approach of hybrid simulations circumvents the need for a closure approximation by directly coupling the macroscopic equations of change with a microscopic kinetic theory model. In doing so, the polymer contribution to the stress tensor is evaluated at each material point by solving the associated Fokker-Planck equation or equivalent stochastic differential equation and evaluating appropriate averages of the distribution function. To date, available stochastic and Fokker-Planck hybrid techniques have been implemented for kinetic theory models that have relatively few configurational degrees of freedom [109, 57]. In addition, while previous studies [102, 103] of simulating complex flows with hybrid methods have employed dynamic simulators to converge to steady states and perform linear stability analysis, there is no simple method for performing bifurcation analysis without reverting to long-time simulations. This is primarily due to the unavailability of closed equations to which existing numerical techniques for bifurcation analysis may be applied.

In this chapter, we use the mathematical framework presented in Chapter 3 to converge a dynamic simulation from kinetic theory of polymeric liquids to steady states and perform stability analysis without invoking closure approximations. We will first present an overview of the approach and argue why coarse-grained models of kinetic theory are appropriate for its application. This will be followed by three examples: (1) the equilibrium behavior of the Doi model with the Onsager excluded volume potential, (2) pressure-driven flow of a dilute solution of non-interacting rigid dumbbells in a planar channel, and (3) pressure-driven flow of non-interacting rigid dumbbells through a planar channel with a linear array of equally spaced cylinders. In the first example we demonstrate the existence of a compact spectrum of eigenvalues for the Jacobian matrix associated with a well studied model from kinetic theory of polymeric liquids. More importantly, we illustrate the ability to obtain stationary states and perform stability/bifurcation analysis of the Doi model with the more realistic Onsager excluded volume potential. With the second set of examples we show that the method may also be used in the context of a hybrid simulation of a non-homogeneous flow without any significant modification to the simulation algorithm. Although in this chapter we focus on converging to stable stationary states in order to facilitate comparison with dynamic simulations, the results are very encouraging both for incorporation of higher numbers of configurational degrees of the freedom for the kinetic theory models and for performing stability/bifurcation analyses with hybrid simulations.

4.1   Time-steppers and Newton-GMRES

Hybrid methods for simulating complex viscoelastic flows directly employ models from kinetic theory for capturing the polymeric contribution to the stress tensor without obtaining a closed form expression for the stress tensor. This approach leads to a dynamical system or "time-stepper" of the form

$$\frac{d\boldsymbol{x}}{dt} = \boldsymbol{f}(\boldsymbol{x}; \mu),$$

(4.1)

where $\boldsymbol{x}$ represents the state of the system and μ is a parameter of the problem. For our work, where closed form constitutive models cannot be written, the state of the system is a set of moments of the underlying conformational distribution function. These could be obtained either from the conformational distribution function or from ensemble averaging of polymer conformations computed by using stochastic models. Given the state of the system at a moment in time, the time-stepper allows determination of the state at a later moment. For the hybrid simulations of interest here, a closed form expression for $\boldsymbol{f}(\boldsymbol{x}, \mu)$ is not available. The action of the time-stepper can only be determined with a "black-box" simulation.

4.1.1 Steady State Solutions

We propose recasting the time-stepper as a fixed point solver for the nonlinear system

$$\boldsymbol{x} - \Phi_T(\boldsymbol{x}; \mu) \equiv \boldsymbol{F}(\boldsymbol{x}; \mu) = \boldsymbol{0} \qquad \boldsymbol{F} : \mathbb{R}^N \to \mathbb{R}^N, \tag{4.2}$$

where $\boldsymbol{F}$ is assumed to be continuously differentiable everywhere in $\mathbb{R}^N$ and

$$\Phi_T(\boldsymbol{x}; \mu) = \boldsymbol{x} + \int_0^T \boldsymbol{f}(\boldsymbol{x}(t'); \mu) \, dt', \tag{4.3}$$

is the result of integration of Eq. 4.1 for time T with initial condition $\boldsymbol{x}$. The key idea is to be able to evaluate $\boldsymbol{F}(\boldsymbol{x}; \mu)$ through calls to the time-stepper rather than a closed expression for $\boldsymbol{f}(\boldsymbol{x}; \mu)$. Once we have formulated the system in Eq. 4.2, we can then apply Newton's method to converge to steady states of the system. Doing so requires, at the kth step, the solution of the linear Newton equation for step $\boldsymbol{s_k}$

$$\boldsymbol{F_x}(\boldsymbol{x}_k)\boldsymbol{s}_k = -\boldsymbol{F}(\boldsymbol{x}_k), \tag{4.4}$$

where $\boldsymbol{x_k}$ is the current approximate solution and $\boldsymbol{F_x}$ is the Jacobian of the system. Since the system in Eq. 4.4 is inevitably large due to discretization of a PDE or a model with large number of degrees of freedom, we revert to methods of large scale computational linear algebra. To this end we employ GMRES, which is an iterative

linear solver for determining an approximate solution of Eq. 4.4. GMRES belongs to the general class of Krylov subspace methods that approximately solve linear systems of the form $\boldsymbol{Ay} = \boldsymbol{b}$ by minimizing the norm of the residual $\boldsymbol{r} = \boldsymbol{b} - \boldsymbol{Ay}$. One main advantage of such methods is that they are always implemented as matrix-free methods, since only matrix-vector products, rather than details of the matrix itself (in our case the Jacobian $\boldsymbol{F_x}$) are needed to implement the method. This is in contrast to direct methods, which require that the computation, storage, and cost of factorizing the Jacobian not be excessive.

More importantly, such methods perform best if the eigenvalues of $\boldsymbol{F_x}$ are in a few tight clusters [113, 15]. This is observed in the context of hybrid simulations of complex viscoelastic flows, in which time-steppers evolve a microscopic description of the system, whereas the interest of the computational rheologist lies with prediction of macroscopic properties (such as stress) that depend on certain low order moments of the microscale model. In fact, closed constitutive models are always written in terms of a few moments of the underlying microscale model by assuming that the remaining higher-order moments quickly become functionals of a few, lower-order, slow "master" moments [59]. This occurs over timescales that are short compared to the macroscopic observation timescales. It is this separation of timescales that leads to the few tight clusters of the eigenvalues of $\boldsymbol{F_x}$.

4.1.2 Stability

The stability of a steady state $\boldsymbol{x}^*$ of Eq. 4.1 can be determined from the n eigenvalues $(\sigma_i, i = 1, \ldots, N)$ of the unavailable Jacobian $\boldsymbol{f_x}(\boldsymbol{x}^*; \mu)$. Since we compute the steady state from Eq. 4.2, we note that the Jacobian $\boldsymbol{F_x}(\boldsymbol{x}^*; \mu)$ also has N eigenvalues that can be expressed as $\nu_i = 1 - e^{\sigma_i T}$. For a stable steady state, the σ_i must all lie in the left half of the complex plane. The term $e^{\sigma_i T}$ in the expression for ν_i transforms these stable eigenvalues to within a unit disc centered at the origin. Hence, the stability criterion can be expressed as $|1 - \nu_i| < 1$. It should be noted that the neutrally stable eigenvalue of 0 for the dynamical system corresponds to an eigenvalue of 1 for the system in Eq. 4.4.

4.1.3 Continuation

The task of performing continuation also fits into this framework in the form of an augmented system that contains the appropriate continuation algorithm. For example, for pseudo-arclength continuation we add an additional arclength parameter s and write the augmented system as

$$\boldsymbol{G}(\boldsymbol{x}(s), \mu(s), s) = \begin{pmatrix} \boldsymbol{F}(\boldsymbol{x}(s), \mu(s)) \\ \dfrac{d\boldsymbol{x}}{ds} \cdot (\boldsymbol{x} - \boldsymbol{x}_j) + \dfrac{d\mu}{ds}(\mu - \mu_j) - (s - s_j) \end{pmatrix}, \qquad (4.5)$$

where $(\boldsymbol{x}_j, \mu_j)$ represents a solution previously calculated during continuation at arclength s_j. This formulation does not require any modification to the Newton-GMRES method. More importantly, assuming that the long-term dynamics of the timestepper are dictated by p slow moments, where $p \ll N$, it can be shown that the GMRES iteration for Eq. 4.4 will converge in at most $p + 1$ iterations, whereas for continuation the dimension of the slow subspace of moments increases from p to at most $p + 2$. For a detailed convergence analysis the reader is referred to the work of Kelley et al. [55].

To illustrate the use of the method described above, we first present the Doi model from kinetic theory of polymeric liquids in Section 4.2 to demonstrate the existence of a compact spectrum of eigenvalues for the linearized system in Eq. 4.4. We then exploit this property not only to converge to both stable and unstable stationary states but also to perform continuation to construct the bifurcation diagram without invoking any closure approximations. This is followed in Section 4.3 by a set of examples to demonstrate that we can also employ Newton-GMRES to obtain stationary states of a hybrid simulation in which a linear diffusion equation for the conformational distribution function of rigid rods is coupled with the macroscopic conservation of mass and momentum equations in two spatially non-homogeneous flows.

4.2   Equilibrium Bifurcation Diagram of the Doi Model with the Onsager Excluded Volume Potential

The Doi diffusion equation [26] coupled with suitable representations of the interbody excluded volume potential has been used to study problems involving rigid, rodlike nematic polymers (e.g., liquid crystalline polymers). In the absence of flow, the orientation distribution function $f(\boldsymbol{u}, t)$ for a spatially homogeneous solution of rigid rods with infinite aspect ratio follows the diffusion equation given by

$$\frac{\partial f}{\partial t} = \frac{1}{6\lambda} \frac{\partial}{\partial \boldsymbol{u}} \cdot \left[\frac{\partial f}{\partial \boldsymbol{u}} + \frac{f}{kT} \frac{\partial V(\boldsymbol{u})}{\partial \boldsymbol{u}} \right], \tag{4.6}$$

where $\boldsymbol{u}$ is the radial unit vector in spherical coordinates, kT is the Boltzmann factor, λ is the rotational time constant of a rigid rod, and $V(\boldsymbol{u})$ is a mean field interaction potential. In this study we use the Onsager mean field potential

$$V(\boldsymbol{u}) = U kT \int |\boldsymbol{u} \times \boldsymbol{u}'| f(\boldsymbol{u}', t) \, d\boldsymbol{u}', \tag{4.7}$$

where U is the dimensionless potential intensity.

For this work we choose to study the scalar structure parameter S, which represents a scalar measure of the degree of order of the sample, as a function of the dimensionless potential U. The structure parameter is defined as $S = \left[\frac{9}{2}(\boldsymbol{S} \cdot \boldsymbol{S}) : \boldsymbol{S} \right]^{\frac{1}{3}}$, in which the structure tensor $\boldsymbol{S} = \langle \boldsymbol{u}\boldsymbol{u} \rangle - \frac{\boldsymbol{\delta}}{3}$, $\langle \boldsymbol{u}\boldsymbol{u} \rangle = \int \boldsymbol{u}\boldsymbol{u} f(\boldsymbol{u}) \, d\boldsymbol{u}$ and $\boldsymbol{\delta}$ is the unit tensor.

For real-valued f satisfying $f(\boldsymbol{u}) = f(-\boldsymbol{u})$ we substitute a spherical harmonic expansion for the distribution function into Eq. 4.6 such that

$$f(\boldsymbol{u}, t) = \sum_{\substack{l=0 \\ l=\text{even}}}^{\infty} \sum_{m=-l}^{m=+l} a_l^m(t) P_l^m c_m + b_l^m(t) P_l^m s_m, \tag{4.8}$$

where P_l^m are the Legendre polynomials $P_l^m(\cos\theta)$, $c_m = \cos m\phi$, and $s_m = \sin m\phi$. Normalization of f, $\int f(\boldsymbol{u})d\boldsymbol{u} = 1$, yields $a_0^0 = (4\pi)^{-1} \forall\ t$, whereas $a_l^{-m} = (-1)^m a_l^m$, and $b_l^{-m} = (-1)^m b_l^m$ for all $m \geq 0$. Truncating the expansion in Eq. 4.8 at a certain level, M, and using the orthogonality property of spherical harmonics transforms Eq. 4.6 into a set of first-order ODEs for the spherical harmonic coefficients a_l^m and b_l^m. This system of ODEs resembles Eq. 4.1 and can be recast as a "black-box" simulator of the form of Eq. 4.3, such that it takes a set of spherical harmonic coefficients and returns the evolved coefficients after a specified time interval. Approximate models of such a system are often written for the evolution of the structure tensor $\boldsymbol{S}$ or the second moment $\langle\boldsymbol{uu}\rangle$ of the distribution function by invoking various closure approximations for the fourth moment. By choosing the complete set of spherical harmonic coefficients as defining the state of the system, we capture the full distribution function without any closure approximation in terms of the second moment, which is equivalent to writing the above system in terms of just the a_2^m and b_2^m coefficients. Moreover, as we will show next, this system exhibits a compact spectrum of eigenvalues that suggests a closure, albeit an unknown one, that need not be invoked when using the framework of Section 4.1.

Before proceeding further, we must first address the degeneracy in the problem with regards to the nematic states that bifurcate from the trivial isotropic state. The nematic state of the system is characterized by a director vector that corresponds to the peak in the orientation distribution function. For the equilibrium problem being studied, this director is rotationally degenerate. Therefore, we restrict the director based on the work of Gopinath et al. [42, 43] by setting all $l = $ odd and b_l^m coefficients to zero when initializing the time-stepper. This restriction does not alter the prediction of the structure parameter or the stability of the computed steady state. It only prevents the continuation algorithm from exploring states with the same value of S that differ by a rotation. Even if this restriction were removed, the time-stepper based algorithm would converge to the correct steady state. However, due to the inherent degeneracy in the problem, the associated director vector would be non-unique. For our simulations we set $M = 10$, $T = 0.1\lambda$, and $\mu = U$ and use
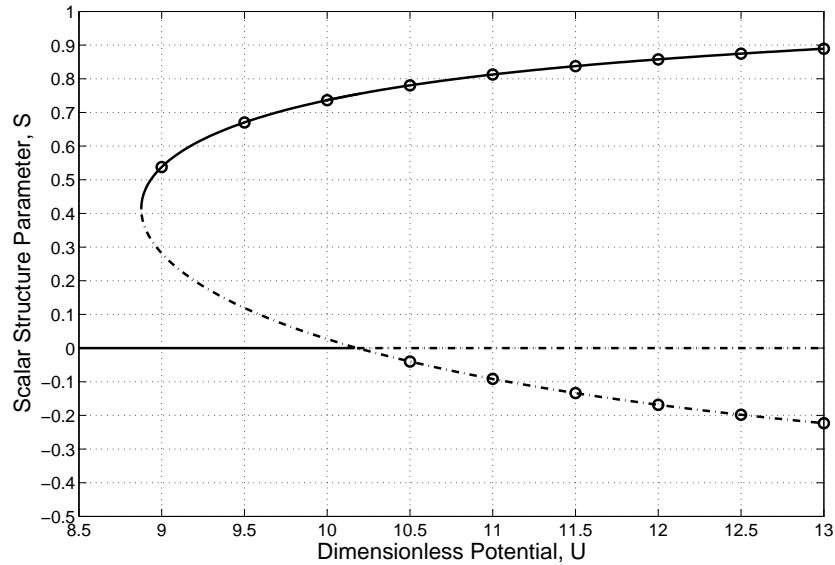
Figure 4-1: Equilibrium phase diagram for the Doi model with the Onsager excluded volume potential. The nematic branches bifurcate from the critical point $U_c \doteq 10.19$ for the Doi equation. The turning point on the $S > 0$ branch occurs at $U \doteq 8.87$. $(-)$ Stable, $(- \cdot -)$ unstable, $(\circ)$ data from Gopinath et al. [42].

pseudo-arclength continuation to trace the solution branches. Excluding the odd and b_l^m coefficients, we obtain a set of 20 real, first order ODEs. A fourth-order Runge-Kutta scheme was used to formulate the time-stepper with a time-step size of 0.005λ. Starting with the prolate $(S > 0)$ steady state solution at $U = 13$ the curve shown in Fig. 4-1 was obtained via continuation. For the purpose of comparison, we also show the the results obtained by Gopinath et al. [42] in which isolated integrations to steady state were used. In Fig. 4-1, solid lines represent stable stationary solutions whereas dashed lines are unstable stationary solutions. Two solution branches (one isotropic and the other nematic) cross at a transcritical bifurcation point, $U_c = 10.19$. This is in excellent agreement with the prediction of $U_c = 32/\pi$ from linear stability analysis [42]. A turning point is obtained on the nematic $S > 0$ branch at $U = 8.87$. Thus, for $U < 8.87$ only a stable isotropic phase is predicted, whereas for $8.87 < U < 10.19$, one stable isotropic solution, and two nematic solutions (one stable and the other unstable) are predicted. Both these solutions are prolate. For $U > 10.19$ three

150

solutions coexist: a stable prolate nematic solution ($S > 0$), an unstable isotropic solution ($S = 0$), and an unstable oblate nematic solution ($S < 0$).

$U = 12$	$U = 8.877$
0.0495	0.0202
0.0579	0.1176
0.0663	0.1599
0.1048	0.2011
0.2623	0.6141
0.4949	0.9967

Table 4.1: List of five eigenvalues, $|1 - \nu_i|$, farthest from 0 on the prolate branch ($T = 0.1\lambda$)

In Table 4.2 we present a list of the five eigenvalues $|1 - \nu_i|$ that are farthest from zero. For a parameter value such as $U = 12$ that is far from the turning point, we see that most of the eigenvalues are close to zero except for three at approximately 0.1, 0.2 and 0.5. The fact that most of the eigenvalues are clustered around zero allows GMRES to converge to the steady state. Increasing T would improve GMRES performance as more eigenvalues approach zero, but this would occur at the cost of longer simulation time for the Doi model. For the second parameter value $U = 8.877$, which lies near the turning point, we see that eigenvalues start leaving the cluster at zero, though they still exist in distinct groups with the largest eigenvalue approaching the unit circle. The change in stability at the turning point corresponds to the crossing over the boundary of the unit circle of this largest eigenvalue. The corresponding eigenmode in configuration space is shown in Fig. 4-2.
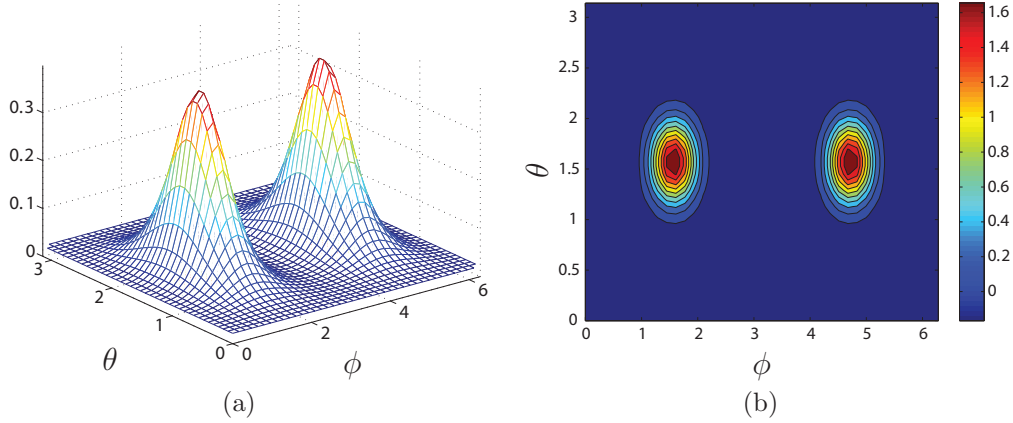
Figure 4-2: (a) Distribution function and (b) contour plot for the eigenmode corresponding to the most dangerous eigenvalue of 0.9967 (Table 1) at $U = 8.877$. The distribution function was computed with $M = 10$.

4.3 Pressure-Driven Flow of Non-Interacting Rigid Dumbbells In a Planar Channel and Through a Planar Channel with a Linear Array of Cylinders

To demonstrate that a hybrid simulation can be cast in the framework of Section 4.1 we study pressure-driven flow of a dilute solution of non-interacting rigid dumbbells both in an infinitely wide planar channel and through an infinitely wide planar channel with an infinite linear array of cylinders oriented perpendicular to the flow direction and equally spaced along the centerline in the flow direction. We solve the momentum (Eq. 4.9) and continuity (Eq. 4.10) equations for the velocity and pressure fields in the Stokes limit, whereas the polymeric contribution to the stress tensor $\boldsymbol{\tau_p}$ (Eq. 4.11) is computed from the moments of the orientational distribution function obtained by solving the diffusion equation for rigid rods (Eq. 4.12). We thus use

$$\beta \boldsymbol{\nabla} \cdot (\boldsymbol{\nabla v} + \boldsymbol{\nabla v^T}) - \boldsymbol{\nabla} p - \boldsymbol{\nabla} \cdot \boldsymbol{\tau_p} = 0, \tag{4.9}$$

$$\boldsymbol{\nabla} \cdot \boldsymbol{v} = 0, \tag{4.10}$$

152

$$\boldsymbol{\tau_p} = \frac{1-\beta}{\frac{\lambda V}{L}} \Big(\boldsymbol{\delta} - 3 \langle \boldsymbol{uu} \rangle - 6(\frac{\lambda V}{L}) \, \boldsymbol{\kappa} : \langle \boldsymbol{uuuu} \rangle \Big), \tag{4.11}$$

$$\frac{\partial f}{\partial t} + \boldsymbol{v} \cdot \boldsymbol{\nabla} f = \frac{1}{6\lambda} (\frac{\partial}{\partial \boldsymbol{u}} \cdot \frac{\partial}{\partial \boldsymbol{u}}) f - \frac{\partial}{\partial \boldsymbol{u}} \cdot ([\boldsymbol{\kappa} \cdot \boldsymbol{u} - \boldsymbol{\kappa}{:}\boldsymbol{uuu}]) f, \tag{4.12}$$

where $f = f(\boldsymbol{r}, \boldsymbol{u}, t)$, $\beta = \eta_s/\eta_0$ (ratio of solvent to solution zero-shear-rate viscosity), $\boldsymbol{\kappa} = \boldsymbol{\nabla} \boldsymbol{v}^T$, and V and L are the characteristic velocity and length scales. The momentum and continuity equations are solved with the Discrete Elastic Viscous Split Stress - Gradient (DEVSS-G) formulation of Szady et al. [110] through introduction of a new variable $\boldsymbol{G} = \boldsymbol{\nabla} \boldsymbol{v}$, whereas the discontinuous Galerkin (DG) method is used to solve the diffusion equation. For the planar channel and the planar channel with a linear array of cylinders, the strength of the flow is characterized by the Deborah number, $\mathrm{De} = \frac{3\lambda Q}{L^2}$, and the Weissenberg number, $\mathrm{We} = \frac{\lambda \langle v \rangle}{L}$, respectively, where Q is the flow rate per unit width of the channel and $\langle v \rangle$ is the average velocity.

4.3.1   Weak Form of the Diffusion Equation

The PDE for the distribution function for polymer conformations (Eq. 4.12) is first rewritten in the form

$$\frac{\partial f}{\partial t} + \boldsymbol{v} \cdot \boldsymbol{\nabla} f = \frac{1}{6\lambda} \nabla_{\boldsymbol{u}}^2 f + \boldsymbol{\Gamma}(\boldsymbol{u}, \boldsymbol{\kappa}) f, \tag{4.13}$$

where

$$\boldsymbol{\Gamma}(\boldsymbol{u}, \boldsymbol{\kappa}) = \big[3(\boldsymbol{\kappa} : \boldsymbol{uu}) - \boldsymbol{\kappa} : \boldsymbol{u} \frac{\partial}{\partial \boldsymbol{u}} \big].$$

We then solve this time dependent PDE by using a spherical harmonic-Galerkin method to discretize the equation in orientation space ($\boldsymbol{u}$ or θ, ϕ), and the discontinuous Galerkin method to discretize the equation in physical space. The DG method uses basis functions that are discontinuous across element boundaries. Each basis function is associated with a node within an element, such that it has a value of unity at its own node and a value of zero at all other nodes. Outside the element under consideration, the basis function is identically zero. This decouples the problem on every element from that on every other element, so that the problem can be solved

element by element. It is important to note that the element-by-element solution can only be carried out if the solution on the inflow element has already been computed. Two options are available: either the elements are solved according to their ordering along a streamline or the problem is solved in a time-dependent context, treating the convection term $(\boldsymbol{v} \cdot \boldsymbol{\nabla} f)$ explicitly. We reject the first option, since it involves computing an element ordering for every new flow field. The second option allows us to obtain maximum benefit of the elemental decoupling that results from the DG method.

We use the following expansion for f

$$f(\boldsymbol{r},\theta,\phi,t) = \sum_i^{\# \text{ of nodes}} \sum_{n=0}^{M} \sum_{m=0}^{n} f_{n,1i}^m(t)\Psi_{DG,i}(\boldsymbol{r})P_n^m c_m + f_{n,2i}^m(t)\Psi_{DG,i}(\boldsymbol{r})P_n^m s_m. \quad (4.14)$$

The $\Psi_{DG,i}(\boldsymbol{r})$ are discontinuous basis functions for physical space, and M denotes some level of truncation for the expansion in orientation space. We designate $f^k(\boldsymbol{r},\boldsymbol{u}) = f(\boldsymbol{r},\boldsymbol{u},t^k)$ as the value of f at time $t = t_0 + k\Delta t$. Since it is computationally efficient to avoid performing a matrix inversion for each element at each time-step, all operators that vary in space or time are treated explicitly. Only the diffusion operator in orientation space $(\nabla_{\boldsymbol{u}}^2)$ is treated implicity.

Introducing test/weight functions $\Psi_{DG,j}P_s^l c_l$ and $\Psi_{DG,j}P_s^l s_l$ along with time discretization leads to the following weak form over an element A

$$\int_A \int_{\boldsymbol{u}} \left(1 - \frac{\Delta t}{6\lambda}\nabla_{\boldsymbol{u}}^2\right) f^k \Psi_{DG,j} \begin{Bmatrix} P_s^l c_l \\ P_s^l s_l \end{Bmatrix} d\boldsymbol{u}\, dA =$$

$$\Delta t \int_A \int_{\boldsymbol{u}} \boldsymbol{\Gamma}(\boldsymbol{u},\boldsymbol{\kappa}) f^{k-1} \Psi_{DG,j} \begin{Bmatrix} P_s^l c_l \\ P_s^l s_l \end{Bmatrix} d\boldsymbol{u}\, dA + \int_A \int_{\boldsymbol{u}} f^{k-1} \Psi_{DG,j} \begin{Bmatrix} P_s^l c_l \\ P_s^l s_l \end{Bmatrix} d\boldsymbol{u}\, dA$$

$$- \Delta t \int_A \int_{\boldsymbol{u}} (\boldsymbol{v} \cdot \boldsymbol{\nabla} f^{k-1}) \Psi_{DG,j} \begin{Bmatrix} P_s^l c_l \\ P_s^l s_l \end{Bmatrix} d\boldsymbol{u}\, dA$$

$$- \Delta t \int_{\delta A^-} \int_{\boldsymbol{u}} (\boldsymbol{n} \cdot \boldsymbol{v})[f^e - f^i]^{k-1} \Psi_{DG,j} \begin{Bmatrix} P_s^l c_l \\ P_s^l s_l \end{Bmatrix} d\boldsymbol{u}\, dl. \quad (4.15)$$

In this formulation the weak form of the convective term, $\int_A \left(\boldsymbol{v} \cdot \boldsymbol{\nabla} f \right) \Psi_{DG} \, dA$, has been expressed as the sum of an area integral over the element and a line integral involving the jump in f across the inflow element boundary

$$\int_A \left(\boldsymbol{v} \cdot \boldsymbol{\nabla} f \right) \Psi_{DG} \, dA = \int_A \left(\boldsymbol{v} \cdot \boldsymbol{\nabla} f^i \right) \Psi_{DG} \, dA + \int_{\delta A^-} (\boldsymbol{n} \cdot \boldsymbol{v}) [f^e - f^i] \Psi_{DG} \, dl, \quad (4.16)$$

such that f^e and f^i represent the external value of f convected into the element A from the adjacent upstream element and the internal elemental value, respectively, and δA^- represents the inflow boundary. It is this line integral that conveys information in a streamwise direction and embodies all the communication between the element of interest and the 'upstream' elements. This inclusion of a 'jump' term at the inflow boundary alone serves the same purpose as do the various types of upwinding schemes used in solution of hyperbolic PDEs.

4.3.2 Parallelization

The DG formulation yields equations that are local to the generating element without dependence on neighboring elements. The only exception is the need to obtain boundary data from its neighbors. This renders the problem particularly well suited for parallelization. For pressure-driven flow solved on a two-dimensional rectangular domain, each element only needs boundary information from the upstream element. The physical domain is decomposed uniformly among processors, such that each processor solves the distribution function on only one subdomain. With this decomposition, the steps for the parallel computation are:

1. Processor 0 computes the velocity and pressure fields or solves the $\boldsymbol{v} - p - \boldsymbol{G}$ problem in the entire domain. The computation of the flow field is cheaper than solving for the distribution function.

2. Processor 0 then sends the nodal velocity in each subdomain to the appropriate processor.

3. Each processor integrates the diffusion equation by one time step on each ele-

| lower boundary of processor 2 |
| upper boundary of processor 1 |
| **Computational domain**
of Processor 1 |
| lower boundary of processor 1 |
| upper boundary of processor 0 |
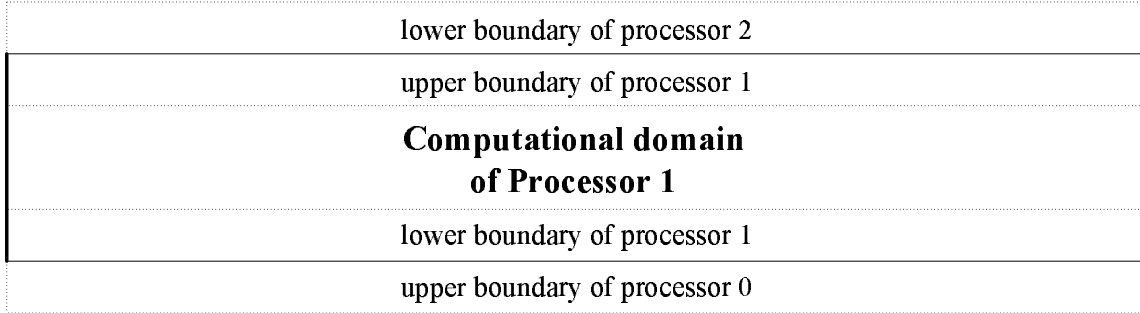
Figure 4-3: Computational domain for processor 1 with boundaries that communicate with adjacent processors

ment within its subdomain in order to update the distribution function f and polymeric contribution to the stress $\boldsymbol{\tau_p}$.

4. Each processor then sends and receives the solution of the diffusion equation to and from other processors that share a common boundary. This is shown in Fig. 4-3 for processor 1, which solves the diffusion equation on subdomain 1. Once processor 1 has updated the solution for f in its domain, it sends the the new solution for f on its upper boundary to processor 2 and receives the corresponding solution for f on the lower boundary of processor 2. A similar communication is also performed at the lower boundary of processor 1. This communication is essential in order to deal with flows in which streamlines are not parallel to the x-axis or there is a small upwinding term from elements that reside on other processors.

5. Processors 1 to n-1 then send the $\boldsymbol{\tau_p}$ information to processor 0, which computes nodal averages from adjacent elements and updates the flow field.

6. Steps 1 through 5 are repeated until convergence to steady state.

A flow chart for the parallel computation is presented in Fig. 4-4.
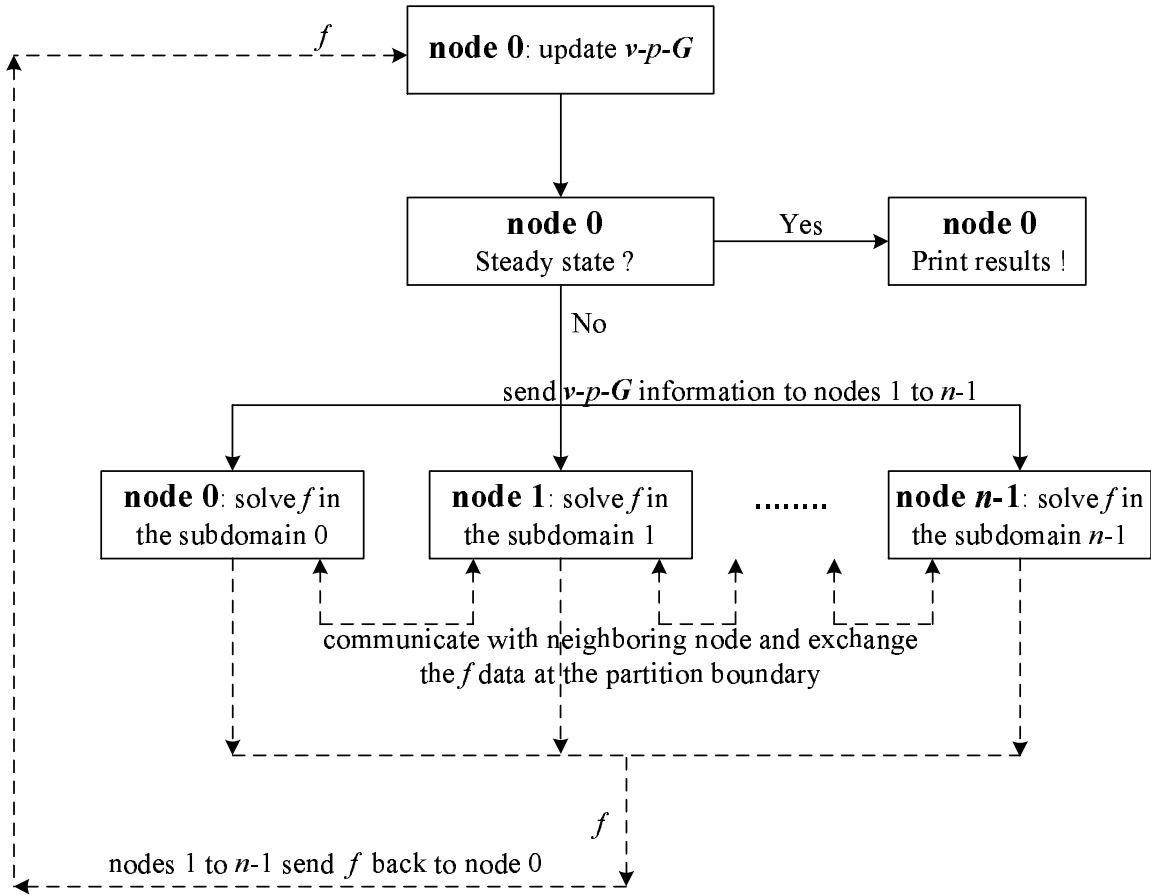
Figure 4-4: Flowchart for problem parallelization on nodes of a computational cluster
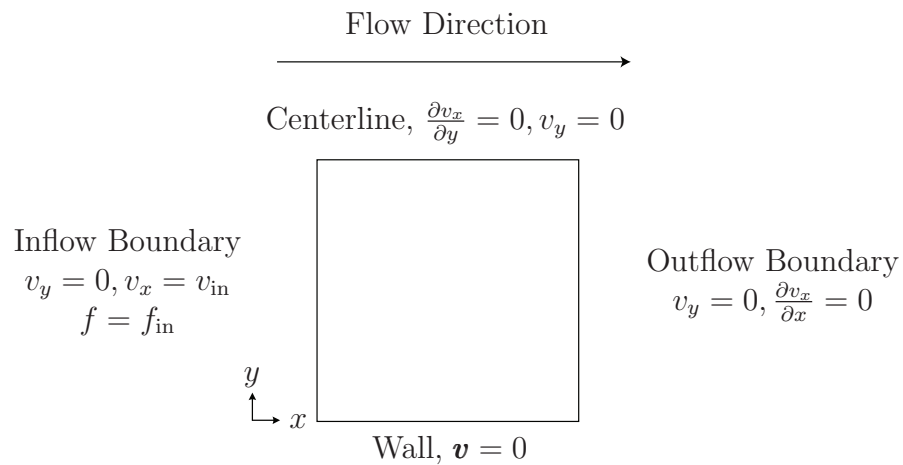
Figure 4-5: Computational domain and boundary conditions for flow through an infinitely wide planar channel
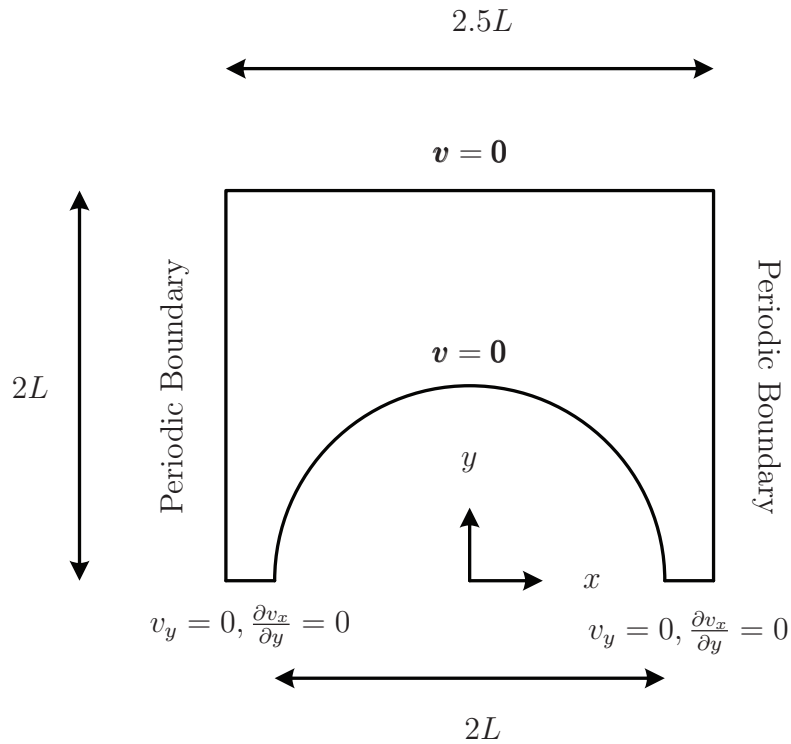
Figure 4-6: Computational domain and boundary conditions for flow around a linear array of cylinders in a planar channel. Since the cylinders are placed periodically along the centerline of the channel and since the flow is assumed symmetric about the midplane of the channel, computation is restricted to the unit cell shown. The cylinders have radius L and the cylinder–to–cylinder spacing is $2.5L$

4.3.3 Boundary conditions

The boundary conditions and the computational domain for the planar channel and the channel with linear array of cylinders are shown in Figs. 4-5 and 4-6, respectively. For the planar channel the computational domain has length and width equal to the characteristic length scale of the geometry with a flow rate specified at the inlet, $x = 0$. As a result, the hyperbolic character of the diffusion equation in physical space requires boundary conditions on the distribution function to be imposed at the inflow boundary only. The one-dimensional, fully-developed ($\boldsymbol{v} \cdot \boldsymbol{\nabla} \boldsymbol{f} = 0$) diffusion equation is, therefore, solved at the inflow boundary yielding an essential boundary condition for the solution of the diffusion equation in the bulk flow. Similarly for velocity, the one–dimensional momentum equation is solved at the inflow boundary by using the one–dimensional solution of the diffusion equation. The inflow velocities obtained from this solution furnish essential boundary conditions for the bulk flow problem. The x-component of the velocity at the outflow boundary is assumed to be fully-developed, whereas a no–slip boundary condition is imposed at the wall, and a symmetry boundary condition is imposed at the centerline.

For flow through the channel with a linear array of cylinders, the problem is solved on a periodic domain of length $2.5L$, which is also the inter-cylinder spacing, by specifying the dimensionless pressure drop across the domain. Here the characteristic length L is taken to be the radius of the cylinder. No–slip boundary conditions are imposed on the cylinder and the channel wall ($y = 2L$) along with symmetry boundary conditions at $y = 0$.

4.3.4 Newton-GMRES wrapper

Given that we have a dynamic simulator for the viscoelastic flow problem, we can then wrap it in a Newton-GMRES solver to obtain the steady state of the system. This can be achieved by treating the time-stepper as a black box integrator that takes a given distribution function for the flow domain and returns an evolved distribution function, $f^{(T)}$, after integration over time horizon T. In doing so, the integrator
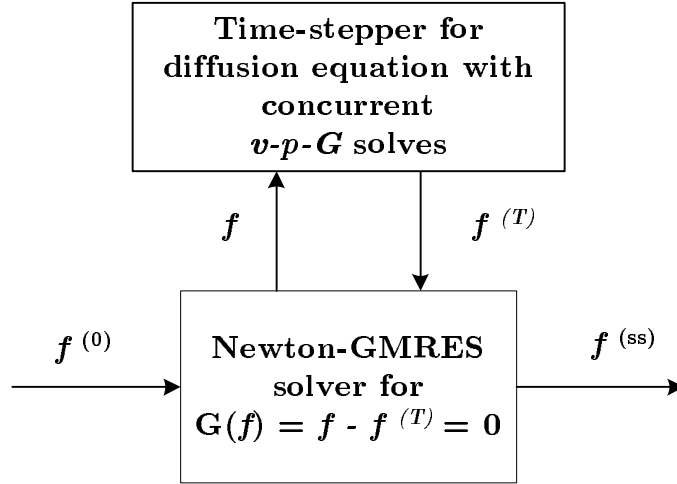
Figure 4-7: Newton-GMRES solver for viscoelastic flow time-stepper

computes consistent flow fields at each intermediate time-step, which is built into the integrator. The task of the Newton-GMRES solver then is to solve for the steady state $f^{(ss)}$ of the nonlinear system $G(f) = f - f^{(T)} = 0$ given an initial guess $f^{(0)}$. A schematic diagram of the method is shown in Fig. 4-7.
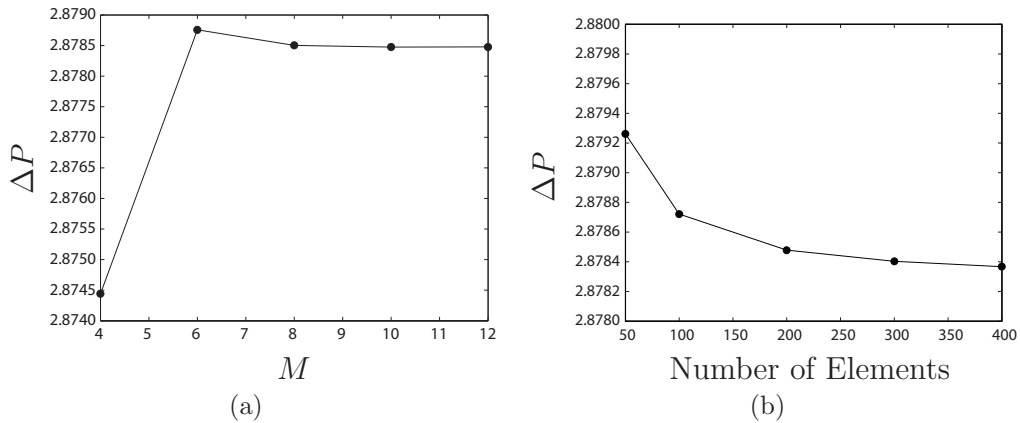
Figure 4-8: Pressure drop across channel as a function of (a) distribution function truncation parameter M (200 element mesh), and (b) mesh size with $M = 12$
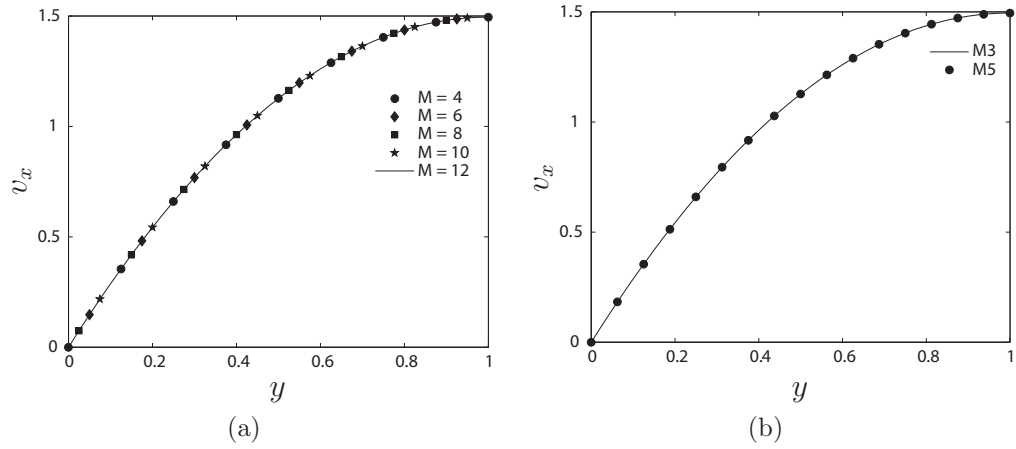
Figure 4-9: Velocity profile for varying (a) distribution truncation parameter M (200 element mesh), and (b) mesh size (M3 = 200 elements, M5 = 400 elements) with $M = 12$
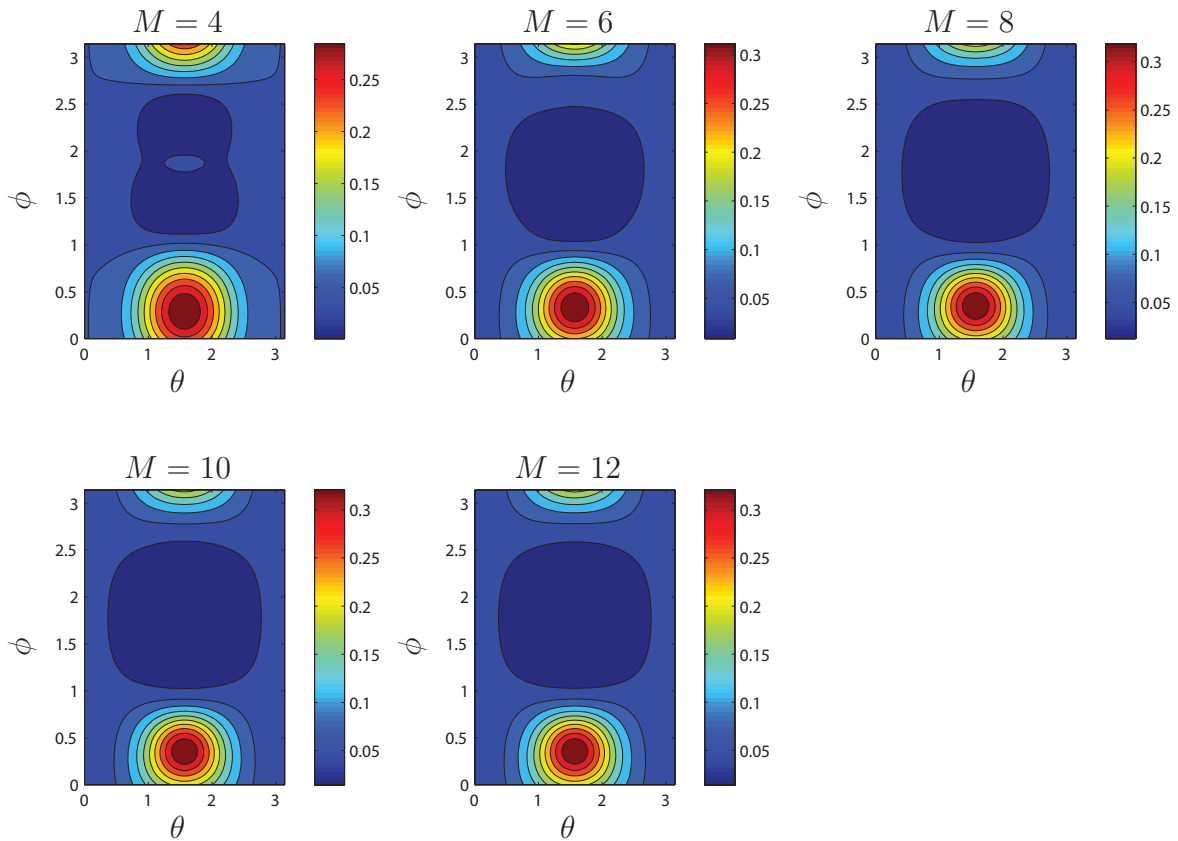
Figure 4-10: Contour plots for the distribution function at $y = 0.2$ as a function of the truncation parameter M for a 200 element mesh.
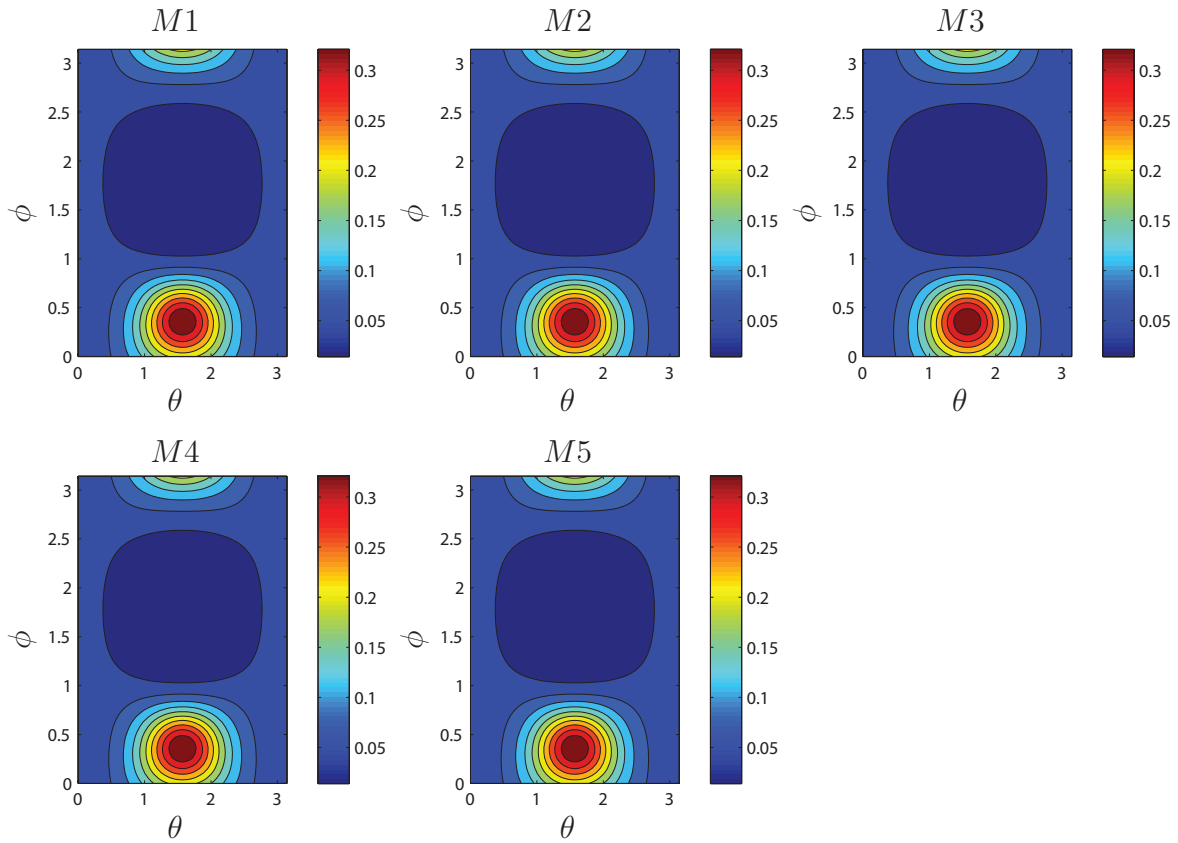
Figure 4-11: Contour plots for the distribution function at $y = 0.2$ as a function of mesh size ($M1 = 50$ elements, $M2 = 100$ elements, $M3 = 200$ elements, $M4 = 300$ elements, $M5 = 400$ elements) with $M = 12$.
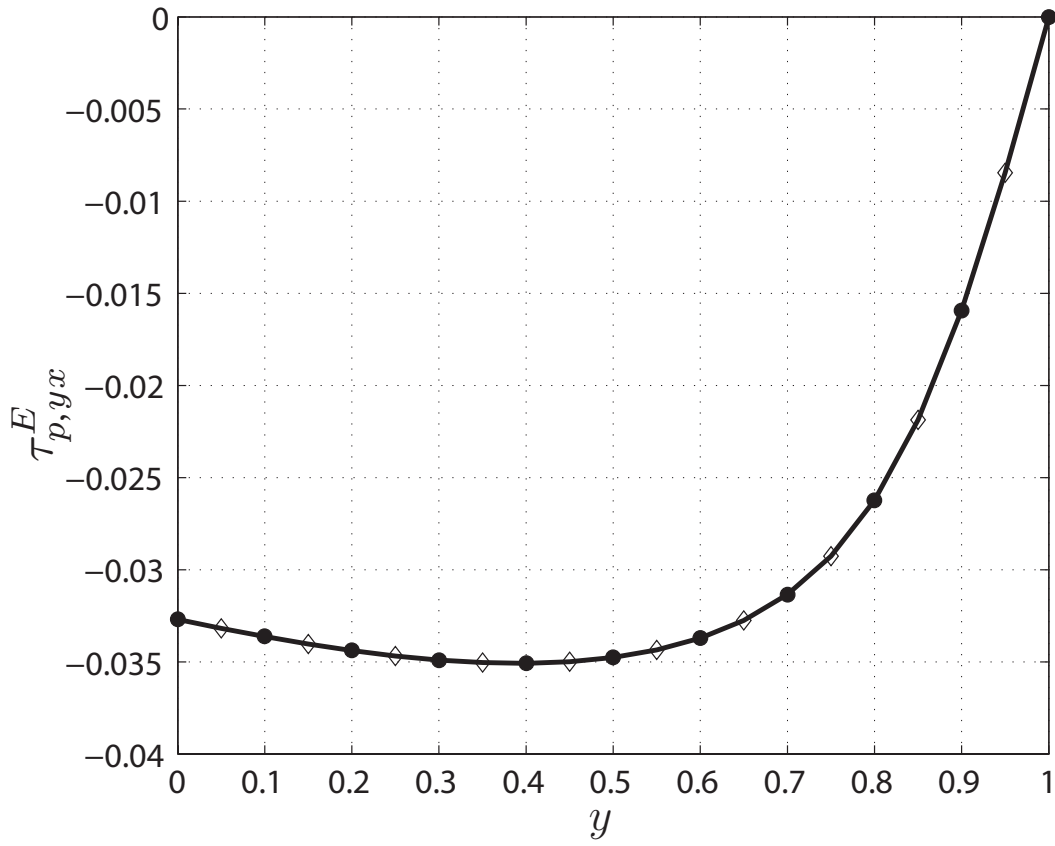
Figure 4-12: Steady state of $\tau_{p,yx}^E = \frac{-3(1-\beta)}{\lambda V/L} \langle u_y u_x \rangle$ with $\beta = \eta_s/\eta_o = 0.9$, De $= 3.0$, $T = \lambda$, and $\Delta t = 0.05\lambda$. $(-)$ Solution obtained from dynamic simulation. Solution obtained from Newton-GMRES simulation at $(\bullet)$ $x = 0.2$, and $(\diamond)$ $x = 0.8$.
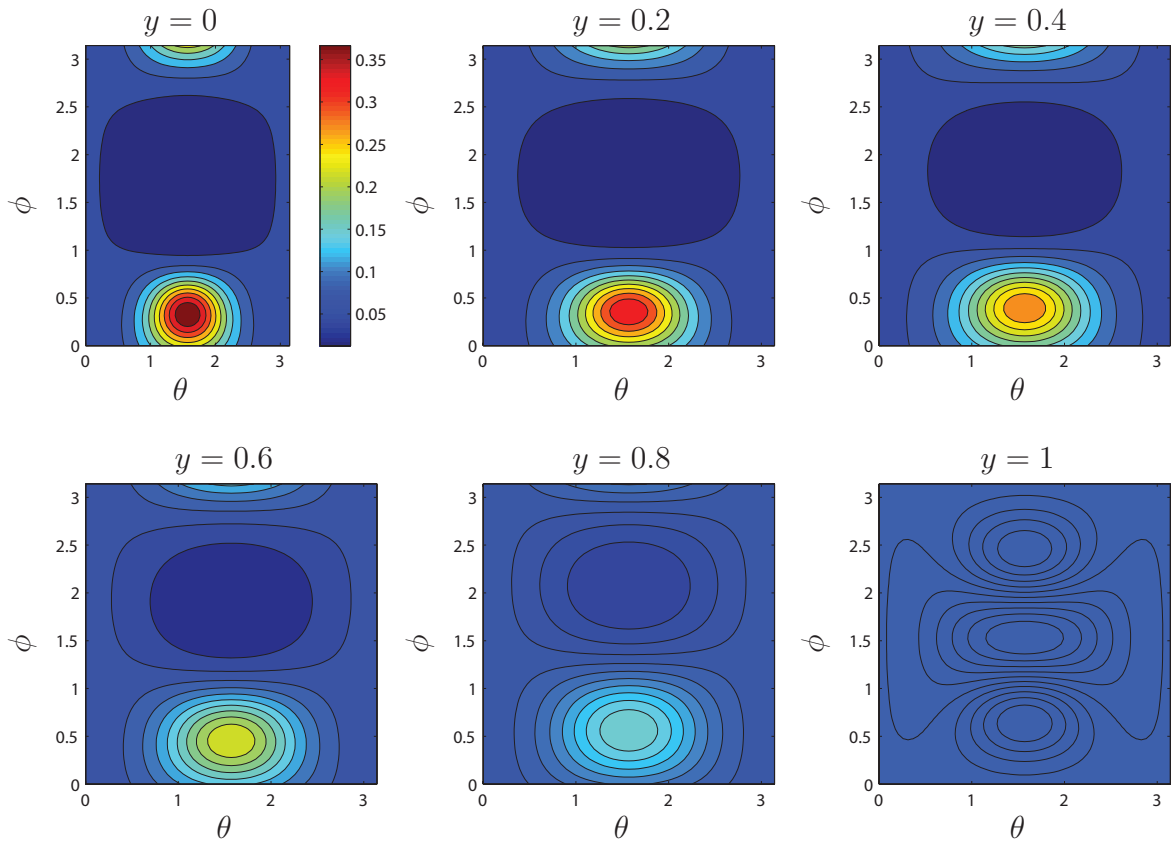
Figure 4-13: Contour plots for the distribution function across the channel, with wall at $y = 0$ and centerline at $y = 1$
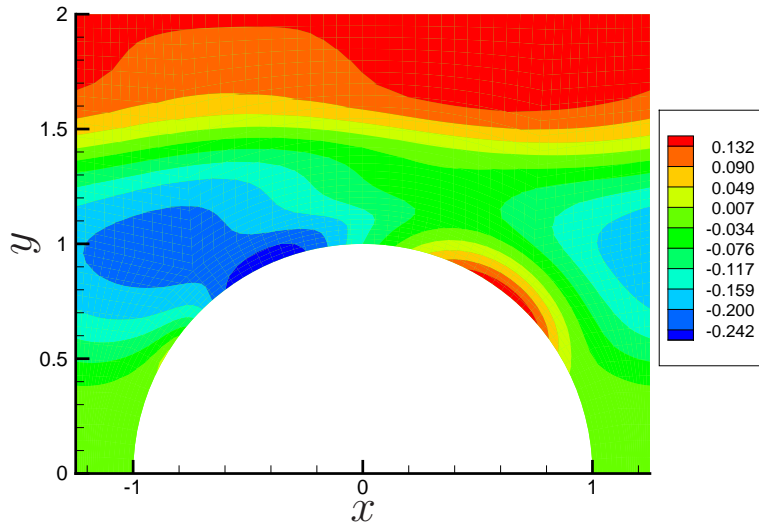
(a) Dynamic Simulation
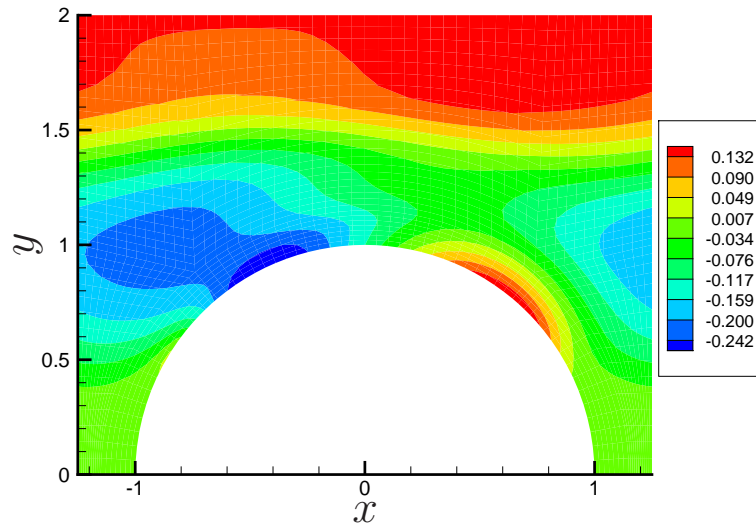
(b) Newton-GMRES Simulation

Figure 4-14: Steady state of $\tau_{p,yx}^E$ for $\beta = 0.59$, $\Delta P = 9$, and We $= 0.5201$

4.3.5 Results

Convergence in physical and configuration space

To demonstrate convergence in both configuration and physical space, the dynamic simulation was run for the planar channel at De $= 3.0$ and with $\beta = 0.9$. A stable time-step of $\Delta t = 0.05\lambda$ was chosen, while steady state was defined as the point at which the L_2 norm of the change in the distribution function was below 10^{-8}. The steady-state pressure drop and velocity profile are shown as a function of the distribution function truncation parameter, M, and mesh size in Figs. 4-8 and 4-9, respectively. It can be observed that the steady state pressure drop converges in both configuration and physical space whereas there is no change in streamline velocity with either mesh size or truncation parameter M. This is most probably due to the large value of β used in this study. Additionally, Figs. 4-10 and 4-11 show that the distribution function near the wall also converges with M and the mesh size. These results suggest that it is sufficient to use $M = 12$ and a 200 element mesh to obtain converged results, since the error in the pressure drop for the 200 element mesh relative to the 400 element mesh is only approximately 0.03%.

Planar Channel

For the planar channel the time-horizon of the Newton-GMRES solver was set to $T = \lambda$, with convergence defined by $\frac{\|G(f)\|_2}{\|G(f^{(0)})\|_2} < 10^{-8}$. An isotropic distribution function was chosen both as an initial condition and initial guess for the dynamic and Newton-GMRES simulations, respectively. The polymer contribution to the stress tensor consists of both elastic and viscous components. In Fig. 4-12, the steady state of the yx component of the elastic part of the polymer contribution to the stress tensor, $\boldsymbol{\tau_p^E} = \frac{1-\beta}{\lambda V/L}(\boldsymbol{\delta} - 3\langle\boldsymbol{uu}\rangle)$, is shown as a function of y for two values of x. There is excellent agreement between the steady states computed from the dynamic and Newton-GMRES simulations. We also plot the steady–state distribution function across the channel in Fig. 4-13 to demonstrate the degree of alignment with varying shear rate across the channel. As expected, the distribution function is peaked near

the wall ($y = 0$) and is nearly isotropic, $f = 1/4\pi$, near the symmetry plane ($y = 1$).

Linear Array of Cylinders in a Planar Channel

The steady–state results of dynamic and Newton-GMRES simulations were also compared for flow through a planar channel with a linear array of cylinders. Previously, Liu et al. [70] have presented results for the flow of flexible polymer solutions through this geometry at $\beta = 0.59$ and We $= 0.5$ and 2.0. They describe the polymer solutions with the Giesekus model, the finitely extensible, nonlinear elastic dumbbell model with Peterlin's approximation (FENE-P), and the FENE dumbbell model of Chilcott-Rallison (CR). These three constitutive equations can be derived from kinetic theory models of dilute polymer solutions; the latter two invoke closure approximations in their derivations. Because Liu et al. [70] show stresses only for We $= 0.5$, we chose this value of We for our simulations. We run both the dynamic and Newton–GMRES simulations at We $= \lambda \langle v \rangle / L = 0.5201$ and $\beta = 0.59$ for a qualitative comparison of polymeric contribution to the stress tensor with the results of Liu et al. [70].

For this study we used a 1896 element mesh, a stable time-step of $\Delta t = 0.01\lambda$, and a dimensionless pressure drop of $\Delta P = 9$ to obtain converged results. An isotropic distribution function was once again chosen as the initial condition for the dynamic simulation and as the initial guess for the Newton–GMRES solver, whereas the time–horizon was set to $T = \lambda$. The steady state for $\tau_{p,yx}^{E}$ obtained from both the dynamic simulation and Newton-GMRES solver is shown in Fig. 4-14. Once again excellent agreement is observed between the solutions of the dynamic and Newton-GMRES simulations. In addition, there is good qualitative agreement with the results of Liu et al. [70](cf. Fig. 21 in that reference). First, flow for an inter–cylinder spacing of $2.5L$ is characterized by the development of a recirculation region between adjacent cylinders with small fluid velocity and velocity gradient. This results in stresses that are near equilibrium, in contrast with a larger inter–cylinder spacing where polymer molecules along the centerline of the geometry are far from equilibrium. Second, the largest stresses exist at the solid boundaries in the gap between the cylinder and the channel wall where the flow is shear dominated with the extrema occurring up- and

down-stream of $x = 0$.

Most importantly, however, in contrast with the planar channel, which is an in-homogeneous flow in one dimension, this geometry represents a complex, inhomogeneous flow in two spatial dimensions, demonstrating the applicability of the method to hybrid simulations of general complex flows. With either geometry, the Newton-GMRES solver obtains the steady state of the problem by computing the function $G(f)$ (cf. Fig. 4-7), which is obtained from running the "black-box" dynamic simulation, without any modification, over a short time horizon. For the example problems presented here, the main goal was to demonstrate that the framework introduced in this thesis can enable a hybrid simulation to converge to steady state. The steady state computed here is a stable steady state as it is also accessible via a dynamic simulation. However, these results when combined with those presented in Section 4.2 indicate that the method presented in this thesis may also be used to obtain unstable steady states and to perform bifurcation analysis of a viscoelastic flow.

4.4   Conclusions

In this chapter we have presented a method to enable dynamic simulators or time-steppers from kinetic theory to obtain stationary states and perform stability/bifurcation analysis. The separation in the time scales of evolution of kinetic theory moments leads to a linearization with a compact spectrum of eigenvalues. This allows the use of matrix-free iterative methods to locate steady states and perform continuation/bifurcation analysis of the unavailable closed-form macroscopic system. We demonstrate this, first by obtaining the equilibrium bifurcation diagram for the structure parameter for the unclosed Doi-model with the Onsager excluded volume potential. We show that most of the eigenvalues of the linearized system lie in a tight cluster about zero, with only a few eigenvalues leaving this cluster near a fold bifurcation.

The second set of examples involve dynamic hybrid implementations of pressure-driven flow of non-interacting rigid dumbbells in a planar channel and through a

planar channel with a linear array of equally spaced cylinders. We show that short bursts of a state-of-the-art parallel implementation with the discontinuous Galerkin method can be used to obtain steady states of the system with our method. Most importantly, we did not have to modify the hybrid simulation algorithm, which indicates that such an approach can be quickly adapted to other state-of-the-art simulators. In addition, since the method requires only short bursts of a viscoelastic timestepper, it presents a feasible approach of studying macroscopic flows through hybrid simulations that incorporate more configurational degrees of freedom in the kinetic theory description. Finally, these results are particularly encouraging, as the method presented in this thesis, contrary to previous methods, also allows for convergence to unstable steady states, opening up the possibility of performing stability/bifurcation analysis of viscoelastic flows via hybrid timesteppers.

Chapter 5

Flow Induced Transitions in a Hard-Rod Suspension

Flow induced aligning of rigid rod suspensions occurs in many forms and variations in manufacturing processes as well as in nature. A specific example which is of theoretical and practical significance is a liquid crystal polymeric (LCP) suspension - the state of which is usually described by a Fokker-Planck like equation for the distribution function - the Doi-Hess diffusion supplemented with a suitable excluded volume interaction potential [81, 97, 63, 64, 96, 67, 76, 73, 74, 2, 20] equation or by simpler lower-dimensional closed versions [31, 1, 94, 93, 36, 35, 115]. Equilibrium base states of such homogeneous suspensions at rest possess symmetries and degeneracies which the imposition of flow destroys, and it is of critical importance to understand and characterize changes in the modes of alignment seen in response to imposed flow. Such studies can then be extended to understand realistic inhomogeneous suspensions.

A homogeneous suspension of hard rods with fore-aft symmetry moving around purely due to Brownian motion in an ideal solvent can be described in the mean field limit by the Doi-Hess diffusion equation. When the concentration of the rods is very dilute, inter-rod interactions are negligible and the distribution function characterizing rod alignment relaxes to a constant - the isotropic value. In the semi-dilute and concentrated regimes, rod-rod interactions can be modeled using potentials based on excluded volume interactions. Typical forms of these are the Onsager potential and

the Maier-Saupe potential [81, 97, 74]. Analysis of the equilibrium problem indicates that there exists a critical concentration of rods, or equivalently a critical dimensionless potential strength, $U = U_{\mathrm{IN}}$ beyond which the isotropic state is no longer stable. Instead for $U > U_{\mathrm{IN}}$, the rods tend to align along a mean direction - termed the director which can be arbitrary. The steady distribution function for this nematic state is uniaxial and characterized by two parameters - the scalar structure factor and the director vector that indicates the mean direction of rod alignment. There are no persistent time-dependent states in the equilibrium problem, as there is just one time scale - the inverse of the diffusion coefficient. In the presence of flow, however, there is competition between the tendency to align due to the potential and align in the direction of the flow. The strength of the flow is measured in terms of a dimensionless shear rate, G, given by the ratio of the shear rate to the diffusivity. This competition determines whether steady or unsteady states are seen.

There is a wealth of information on the effect of shearing on the alignment of rods in homogeneous suspensions. At the same time much remains to be elucidated. Bifurcation studies of Doi-Hess diffusion [63, 64, 96, 67, 73, 36, 35, 37, 19] have been performed over a range of rod concentrations as well as shear rates. The emphasis has been mainly on moderate to large flow strengths with a view to understanding specifically the route from periodic states to chaotic states. Both Maier-Saupe [73, 74, 36, 35, 37] and Onsager excluded volume potentials [67, 42] have been considered - again for moderate to large shear rates, for which rich bifurcation maps with a multitude of stationary and time-periodic states exist. Transition to chaotic behavior, shear-induced biaxiality, Hopf-Poincaré bifurcations from in-plane tumbling to out of plane wagging oscillations, frequency locking in oscillatory shear have all been explored in these papers.

The complementary low flow limit, which is of interest in polymer applications and rheological studies, has only been briefly addressed in these works. In-plane, steady tumbling orbits that exist at low shear rates were calculated by Larson and Ottinger [67] using numerical solutions of the diffusion equation with the Onsager potential. The stability of these solutions to out-of-plane disturbances as well as the transition

to in-plane and out-of plane wagging modes were elucidated. Similar studies with the Maier-Saupe potential for a linear shear flow [73, 36, 35, 37] indicate that at low shear rates steady aligned solutions exist until a critical value of the concentration, after which periodic non-sinusoidal oscillations are seen. In spite of the detailed and illuminating nature of these studies, questions still remain to be resolved. The nature of the bifurcation leading to loss of steady solutions and dependence of this critical point (at which periodic orbits are born) on the flow rate and on the aspect ratio of the rods has not been fully explored. It has been suggested that the tumbling orbits arise from a global homoclinic bifurcation - but investigations of the amplitude and frequency of these to confirm this are lacking. A part of the reason for this is that most computations have been done for $G > 10^{-1}$ - while going to much lower values is indicated to discern the true behavior as $G \to 0$. Perhaps a more serious issue is that all studies treat the concentration as a fixed parameter and vary the shear rate. This approach unfortunately prevents a clear evaluation of the role played by shear in unfolding the equilibrium solution map and birthing new solutions. In the parlance of bifurcation theory, the role played by shear as an imperfection is yet to be elucidated completely in the weak shear flow analysis of the full Doi-Hess equation. A recent step towards this has been the asymptotic analysis of Zhou and Wang [117] wherein the solutions to the 2-D Doi Hess equation are analyzed for infinite aspect ratio rods and $G \ll 1$. We will treat their paper as a benchmark to validate our numerical technique. Our results are consistent with their asymptotic results and extends the solutions known to finite aspect ratio values.

More detailed analyses of the $G \to 0$ limit also exist for lower dimensional approximations to the full diffusion equations using a modified Landau-deGennes (LDG) [1] and and alternative closed model [19]. Although it is well known that solutions to these models can yield predictions at variance with results from the full diffusion equations, it is nevertheless very instructive to study these in detail. These studies have posited the existence of tumbling in-plane solutions that are stable to out of plane disturbances with orbital periods that depend inversely on the shear rate parameter. Unfortunately, the LDG model predicts un-physical structure parameter

values; and, in addition, it is unclear how the parameters in the LDG model relate to those in the diffusion equation. It is therefore important to analyze the full equations without resorting to closed forms. This enables us to discriminate and identify effects caused by the closure and/or the lower dimensionality of the models. Furthermore, the general formalism allows us to study bifurcations and all states, steady and periodic, in terms of just three parameters that arise physically: the strength of the inter-rod potential, the shear rate, and the aspect ratio of the rods.

In this chapter we discuss the change in the equilibrium properties induced due to a weak shearing flow - the strength of the flow being characterized by the dimensionless shear rate G. Specifically, we focus on the bifurcation from steady to time-periodic tumbling state of hard-rod liquid crystals for $0 < G \ll 1$. For this purpose we have chosen a physically relevant yet simple model, wherein high aspect ratio rigid rods undergo steady shear flow while begin restricted to lie in the plane defined by the velocity gradient. Unlike previous studies using low dimensional closed form models, we consider the unclosed diffusion equation with a Maier-Saupe type excluded volume potential as the starting point for our analysis and perform numerical continuation and spot calculations to identify steady and unsteady solution states. These calculations are supplemented by asymptotic theory wherever possible. Calculations are performed for the range $10^{-4} \leq G \leq 10^{-1}$, which are much smaller shear rates than addressed previously. By computing the scaling of the frequency and amplitude of these time-periodic solutions in the weak shear flow limit, we are able to characterize correctly the nature of the bifurcation. In addition, we also investigate the effects of finite aspect ratio in detail to discern general trends and scalings. Finally, we demonstrate how our results are consistent with or sometimes differ from results from lower dimensional closed form models and comment on extensions to the full 3-D case.

From an applications perspective, characterization of complex fluids and crystallizing polymers typically requires the measurement of the elastic and viscous properties using a cone and plane viscometer or a Couette cell and subjecting the sample to steady or oscillating shearing and extensional flows. The measured torques and forces are related to the material properties of the sample. In this instance it would

be interesting to understand the difference in measured properties between steady and periodic shearing especially in the limits of small and large shear rates. Recent work builds on previous experimental and theoretical work to address this question in the framework of closed models [2, 1, 37, 19]. The current work may thus be looked at as the base work needed to be accomplished before consideration of the effects of oscillatory shear flow.

5.1 Theoretical framework

Previous studies on both the diffusion equation [67, 36, 35, 115] and on the LDG/closed models [1, 19] show that in-plane tumbling orbits are stable to out of plane disturbances over a range of parameter values. It is thus possible to learn about the birth of these orbits by studying a restricted 3-D diffusion equation, one which considers purely in-plane modes. With this in mind, we proceed to the formulation of the governing equations for the 2-D Doi-Hess diffusion model. We choose to represent the inter-rod potential via the Maier-Saupe form, but the results are easily extended to cover the Onsager potential as well; detailed forms needed for this change are in [42, 43].

5.1.1 Governing equations for the 2-D model

The particles comprising the homogeneous dispersion are modeled as rigid rods of length L and width d, with the aspect ratio, $r \equiv L/d \gg 1$, and the suspension is subjected to a homogeneous shear flow $\mathbf{v} = \Gamma y e_x$. All rods are assumed to lie in places parallel to that defined by the velocity gradient. In the mean-field approximation it suffices to consider one test particle in a mean potential due to the other rods, and the one-particle orientation distribution function $f(\mathbf{u}, t)$ is sufficient to characterize the suspension. The orientation of a test rod is specified by the unit vector $\mathbf{u} \equiv \cos\theta \mathbf{e_x} + \sin\theta \mathbf{e_y}$ with θ being the polar angle. Assuming a constant rotational diffusivity, we

can write the Doi diffusion equation in two dimensions [63, 64, 73],

$$\partial_t f + \partial_{\mathbf{u}} \cdot (\mathbf{u}_t f) = D_r \partial_{\mathbf{u}} \cdot (\partial_{\mathbf{u}} f + f(k_B T)^{-1} \partial_{\mathbf{u}} V_{ev}) \tag{5.1}$$

with V_{ev} being the excluded volume potential measured in units of $k_b T$ and $\mathbf{u}_t$ the rate at which $\mathbf{u}$ changes due to the shear flow given by $(u_i)_t = \omega_{ij} u_j + p(\dot{\gamma}_{ij} u_j - \dot{\gamma}_{jk} u_j u_k u_i)$. Here, $p = (a^2 - 1)/(a^2 + 1)$ is a shape factor with a being the aspect ratio of the particles and $\boldsymbol{\omega} = (\boldsymbol{\nabla}\mathbf{v} - \boldsymbol{\nabla}\mathbf{v}\dagger)/2$ and $\dot{\boldsymbol{\gamma}} = (\boldsymbol{\nabla}\mathbf{v} + \boldsymbol{\nabla}\mathbf{v}\dagger)/2$ are the antisymmetric and symmetric parts of the velocity gradient tensor $\boldsymbol{\nabla}\mathbf{v}$. Let us define the average of a quantity, $\mathbf{X}(\mathbf{u})$, as $\langle\mathbf{X}\rangle \equiv \int \mathbf{X}(\mathbf{u}) f(\mathbf{u}) d\mathbf{u}$. The distribution function satisfies the normalization condition, $\langle 1 \rangle = 1$. If the excluded volume intermolecular potential is assumed to be of the Maier-Saupe type, then we have $V_{ev}(\mathbf{u}) = -2U k_B T \langle \mathbf{uu} \rangle : \mathbf{uu}$, U being a phenomenological constant proportional to the concentration of rods. Using $\partial_{\mathbf{u}} = \mathbf{t}\partial_\theta$, $\mathbf{t}$ being the tangent vector, we can write the following evolution equation for f in terms of the angle $\theta \in (0, \pi)$,

$$\partial_\tau f + G\Phi_s[f] = \partial_\theta^2 f + U\Phi_{ev}[f], \tag{5.2}$$

the forcing term due to the shear being

$$\Phi_s[f] = -fp\sin 2\theta + p\cos^2\theta(\partial_\theta f) - \frac{(p+1)}{2}(\partial_\theta f), \tag{5.3}$$

and the excluded volume potential term is of the Maier-Saupe form and given by

$$\Phi_{ev}[f] = 2\cos 2\theta(-\alpha_1 \partial_\theta f + 2f\alpha_2) + 2\sin 2\theta(\alpha_2 \partial_\theta f + 2f\alpha_1). \tag{5.4}$$

Here, $\tau = tD_r$ is a scaled time, $\alpha_1 = \langle \sin 2\theta \rangle$, $\alpha_2 = \langle \cos 2\theta \rangle$ and $G = \Gamma/D_r$ is a dimensionless shear rate. Note that substituting $p = 1$ in the previous equation reduces it to the evolution equation derived earlier [73].

Three dimensionless parameters arise in Eqs. 5.2, 5.3, and 5.4 - p, U and G. Note that p and G arise as two independent combinations pG and p. The forcing

term due to shear is linear in f whereas the interaction term due to the Maier-Saupe approximation to the hard rod potential is quadratic in f. The dimensionless potential strength U is proportional to the concentration of rods, c, and the excluded area for two rods (since we have a 2-D system). In reality the interaction term has additional terms that also depend on the aspect ratio - however these are found to be an order of magnitude smaller than the leading term and can be neglected. In any case, the Maier-Saupe potential is itself an approximation to the actual hard rod interaction; and thus we choose to treat the parameter U as a phenomenological parameter that may be related to the concentration of the rods and geometry. The analysis here may be extended to more general excluded volume potentials such as the Onsager potential [81, 67, 42, 43] in 2-D and 3-D[1].

5.1.2 Eigenfunction expansion in Fourier modes and evolution equations

The orientational distribution function, f, is real and π periodic due to fore-aft symmetry of the rods. That is $f(\theta, \tau) = f(\theta + \pi, \tau)$. For a non-isotropic solution, two physically significant parameters characterize the state of the suspension. These are the scalar structure factor that denotes the extent of orientation around the average direction of the rods, $S \equiv (\alpha_1^2 + \alpha_2^2)^{1/2}$, and the angle the director makes with e_x given by $\alpha = (1/2) \tan^{-1} (\alpha_1/\alpha_2)$. Note that one can define a symmetric, traceless structure tensor, $\mathbf{S} = \langle \mathbf{uu} \rangle - (1/2)\boldsymbol{\delta}$. In three dimensions, this tensor has five independent elements whereas in two dimensions it has two independent elements, S_{11} and S_{12} with $S_{22} = -S_{11}$ and $S_{21} = S_{12}$. Thus, the diagonal form of this matrix in two dimensions remains traceless and has eigenvalues that are equal in magnitude

---

[1]To obtain a more general form for the excluded volume interaction for arbitrary aspect ratio rods in 3-D, consider two rigid rods aligned in directions $\mathbf{u}$ and $\mathbf{u}'$ with centers of mass located at $\mathbf{r}_m$ and $\mathbf{r}'_m$. The potential is zero if the two rods are not in contact and is infinite if they try to cross or touch each other. Thus the repulsive potential may be written as $\nu_P(\mathbf{u}, \mathbf{u}', \mathbf{r}_m, \mathbf{r}'_m)$. We fix the orientations of the two rods and the center of mass of one of them. The second rod is now moved and the volume inaccessible to it due to the presence of the first is estimated as $V_P(\mathbf{u}, \mathbf{u}') = -(1/V) \int d\mathbf{r}_m \int d\mathbf{r}'_m F_M(\mathbf{u}, \mathbf{u}', \mathbf{r}_m, \mathbf{r}'_m)$ where the Mayer function F_M is given by $F_M = \exp(-\nu_P(\mathbf{u}, \mathbf{u}', \mathbf{r}_m, \mathbf{r}'_m) - 1)$. For two spherocylinders with length L and diameter D, for instance, we get $V_P(\mathbf{u}, \mathbf{u}') = L^2 D |\mathbf{u} \times \mathbf{u}'| + 4D^3/3\pi + 2\pi L D^2$.

with opposite signs, say λ and $-\lambda$. Thus one anticipates two equilibrium states in 2-D, with scalar structure factor, S and $-S$. Note also that the isotropic state in 2-D resembles the oblate nematic in 3-D wherein the rods are arranged randomly in planes perpendicular to the director. The nematic state in 2-D does not directly map onto a nematic state in 3-D. However, the nature of the solutions and their dynamical nature do bear a resemblance to corresponding solutions obtained from 3-D with the rods constrained to rotate in the plane of shear.

Guided by the periodicity and forms of the governing equations, we write $f(\theta, \tau) = A_0(\tau) + \sum_{m=1}^{\infty}(A_m(\tau)e^{2im\theta} + A_{-m}(\tau)e^{-2im\theta})$. Since f is constrained to be real, this implies an equivalent form for f,

$$f(\theta, \tau) = f_0 + \sum_{m=1}^{\infty} a_m(\tau)\cos(2m\theta) + \sum_{m=1}^{\infty} b_m(\tau)\sin(2m\theta), \tag{5.5}$$

where f_0 corresponds to the isotropic solution, $\partial_\tau f_0 = 0$ and $\partial_\theta f_0 = 0$. Normalization then yields $f_0 = \pi^{-1}$. Note that $\alpha_1 = b_1\pi/2$ and $\alpha_2 = a_1\pi/2$. The evolution of modes a_m and b_m is obtained by substituting Eq. 5.5 into Eq. 5.2 and taking suitable inner-products. For $m \geq 2$ this yields

$$\frac{da_m}{d\tau} = -4m^2 a_m + \frac{mG}{2}(-pb_{m-1} + 2b_m - pb_{m+1}) + m\pi U\{a_1(a_{m-1} - a_{m+1})$$
$$- b_1(b_{m-1} + b_{m+1})\} \tag{5.6}$$

$$\frac{db_m}{d\tau} = -4m^2 b_m + \frac{mG}{2}(pa_{m-1} - 2a_m + pa_{m+1}) + m\pi U\{b_1(a_{m-1} + a_{m+1})$$
$$+ a_1(b_{m-1} - b_{m+1})\} \tag{5.7}$$

The $m = 1$ modes evolve according to

$$\frac{da_1}{d\tau} = -4a_1 + \frac{G}{2}(2b_1 - pb_2) + \pi U\{a_1(\frac{2}{\pi} - a_2) - b_1 b_2\} \tag{5.8}$$

$$\frac{db_1}{d\tau} = -4b_1 + \frac{G}{2}(p\frac{2}{\pi} - 2a_1 + pa_2) + \pi U\{b_1(\frac{2}{\pi} + a_2) - a_1 b_2\} \tag{5.9}$$

We note that in the time dependent, $G = 0$ evolution problem, starting with an

initial state with $b_k(\tau = 0) = 0$ results in $b_k(\tau > 0) = 0$. That is when $G = 0$, solutions with modes $b_{k \geq 1} = 0$ form an invariant subspace [42, 43]. This result can be used to find scaling relationships of these coefficients with k and U. The base nematic state can be written in terms of the set $(a_k^{\mathrm{N}}, 0)$ for $k \geq 1$. Setting all $b_k = 0$ and seeking a steady nematic solution yields a recursion relationship for $a_{k \geq 2}^{\mathrm{N}}$, namely $4k[\pi U a_1^{\mathrm{N}}]^{-1} a_k^{\mathrm{N}} = (a_{k-1}^{\mathrm{N}} - a_{k+1}^{\mathrm{N}})$. The equation for the first mode yields $0 = -4a_1^{\mathrm{N}} + \pi U(a_1^{\mathrm{N}}(2\pi^{-1} - a_2^{\mathrm{N}}))$ and thus we find that when $a_1^{\mathrm{N}} \neq 0$, the second mode is independent of a_1^{N}. Analysis yields $a_2^{\mathrm{N}} = 2/\pi(1 - 2/U)$, $a_3^{\mathrm{N}} = a_1^{\mathrm{N}} - 16(U - 2)(\pi^2 U^2 a_1^{\mathrm{N}})^{-1}$, and $a_4^{\mathrm{N}} = 2\pi^{-1} - 16(\pi U)^{-1} + 192(U - 2)\pi^{-3} U^{-3}(a_1^{\mathrm{N}})^{-2}$. The value of a_1^{N} is obtained from the implicit integral equation. These results imply that as $U \to \infty$, a_1^{N}, a_2^{N}, a_3^{N} and a_4^{N} all tend to $2/\pi$. This is not surprising and implies that as $U \to \infty$, a finite mode representation up to $k = k_\infty$ modes yields

$$f_0(\theta, U \to \infty | k_\infty) \sim \frac{1}{\pi} + \frac{2}{\pi} \sum_{k=1}^{k_\infty} \cos{(2k\theta)} = \frac{\sin{(M\theta)}}{\pi \sin \theta}.$$

where $M = (2k_\infty + 1)$. In the vicinity of small θ, expanding the denominator about θ and taking the limit of infinite terms indicates that $f(\theta, U \to \infty)$ approaches a delta function peaked at $\theta = 0$ as is to be expected, viz., $f_0(\theta, U \to \infty) \sim \lim_{M \to \infty} \sin{(M\theta)}(\pi \sin \theta)^{-1} = \delta(0)$. The peak at $\theta = 0$ is also accompanied by a peak at $\theta = \pi$ due to circular symmetry.

5.1.3 Numerical methodology

The ODEs for the Fourier coefficients a_m and b_m can be expressed as a single system $d_\tau \boldsymbol{x} = \boldsymbol{f}(\boldsymbol{x}, \mu_\alpha, \mu^*)$ where $\boldsymbol{x} = \{a_m, b_m\}$ for $m = 1, \ldots, N$, μ_α denotes the set of parameters held constant, and μ^* is the parameter which is used to continue solution branches. For the purpose of tracing out stationary solution branches of this system, we introduce an additional arclength parameter s and employ arclength continuation. The kth solution along a branch is calculated by solving the augmented system

$$\boldsymbol{g}(\boldsymbol{x}_k(s), \mu_k^*(s), s) = 0 =$$

$$\begin{pmatrix} \boldsymbol{f}(\boldsymbol{x}_k(s), \mu_k^*(s)) \\ \sum_i (\boldsymbol{x}_{i,k} - \boldsymbol{x}_{i,k-1})^2 + (\mu_k^* - \mu_{k-1}^*)^2 - (s_k - s_{k-1})^2 \end{pmatrix} \quad (5.10)$$

The continuation was performed over the provided parameter space (μ_0^*, μ_f^*) by first solving the system $\boldsymbol{f}(\boldsymbol{x}, \mu^*) = 0$ at the initial starting value, $\mu^* = \mu_0^*$, followed by a modified predictor-corrector continuation algorithm, where corrector iterations were replaced with Newton-GMRES iterations. For the first and subsequent nonlinear solves we used absolute and relative tolerances of 10^{-6} to terminate iterations, whereas solutions produced by the predictor iterations were accepted for $\|\boldsymbol{f}(\boldsymbol{x}_k, \mu_k^*)\|_2 < 10^{-6}$. The continuation algorithm was finally terminated at the final value $\mu_k^* \geq \mu_f^*$. For each computed solution, the eigenvalues of the Jacobian of Eq. 5.10 were calculated to determine stability. For the simulations carried out in this chapter we chose $N = 10$. Higher values of N gave practically identical results for the parameter ranges studied.

5.2   The base states $p = 1$

We begin by summarizing the characteristics of the base states given by the limiting cases $(G = 0, p = 1)$ (no flow) and $(U = 0, p = 1)$ (no interaction potential). These results provide convenient starting points for the discussion of more general cases.

When $G = 0$ the suspension of rods becomes aligned by an Isotropic-Nematic (IN) transition beyond a critical concentration U_{IN}. The director, or the average orientation of the rods, is arbitrary, since there is no intrinsically preferred direction. Anticipating that the solution is uniaxial about the director, we find that the base state depends on $\mathbf{u}$ and the director $\mathbf{n}$ through the functional form $f_0(\mathbf{u} \cdot \mathbf{n})$. We now choose to consider solutions with the director aligned such that $\alpha_1 = 0$. All other solutions may then be obtained by suitably rotating this base canonical solution [2]. Then we have $f_0(\theta, \tau) = \exp\left(U\alpha_2 \cos(2\theta)\right)\left(\int_0^\pi \exp\left(U\alpha_2 \cos(2\theta)\right) d\theta\right)^{-1}$, so that

---

[2] Consider rotating the director by a small angle $\boldsymbol{\varphi}$ so that $\mathbf{n}$ goes to $\mathbf{n} + \boldsymbol{\varphi} \times \mathbf{n}$. However, since $f_0 = f_0(\mathbf{u} \cdot \mathbf{n})$ and $f_0^R = f_0(\mathbf{u} \cdot (\mathbf{n} + \boldsymbol{\varphi} \times \mathbf{n}))$ both satisfy $\partial_\mathbf{u} \cdot (\partial_\mathbf{u} f + f(k_B T)^{-1} \partial_\mathbf{u} V_{ev}[f]) = 0$, it follows that to leading order in $\boldsymbol{\varphi}$, $\Psi[\boldsymbol{\varphi} \cdot (\mathbf{n} \times \partial f_0 / \partial \mathbf{n})] = 0$ where Ψ is the linearized operator corresponding to the right side of Eq. 5.1. This implies that the steady solutions have a neutral eigenvalue $\lambda_R = 0$, which corresponds to rotating the director. The eigenvector is just $\boldsymbol{\varphi} \cdot (\mathbf{n} \times \partial f_0 / \partial \mathbf{n})$. Rotating the director while keeping the distribution about the director fixed thus constitutes a soft mode. In

$\alpha_2 = S_0^N(U)$ is given by,

$$\alpha_2 = S_0^N = \frac{\int_0^\pi \cos\left(2\theta\right) \exp\left(U\alpha_2 \cos\left(2\theta\right)\right) d\theta}{\int_0^\pi \exp\left(U\alpha_2 \cos\left(2\theta\right)\right) d\theta} \tag{5.11}$$

Solving this implicit equation for $S_0^N(U)$ yields the equilibrium curve indicated as a solid line in Fig. 5-1 (a). For $U < U_{\rm IN} = 2$, the isotropic solution is stable and is the only equilibrium solution. For $U > U_{\rm IN}$, the isotropic branch constitutes an unstable equilibrium solution, the only stable solution being a prolate nematic branch. The bifurcating nematic branch arises from the isotropic branch via a supercritical pitchfork bifurcation, as expected from the symmetries of the structure tensor $\mathbf{S}$. This implies that $\hat{U} \equiv U - U_{\rm IN}$ satisfies $\hat{U}(-S_0^N) = \hat{U}(S_0^N)$. A simple asymptotic expansion using this yields for $0 < S_0^N \ll 1$,

$$\hat{U} \approx (S_0^N)^2 + \frac{5}{6}(S_0^N)^4 + \frac{19}{24}(S_0^N)^6 + \frac{143}{180}(S_0^N)^8 \tag{5.12}$$

which is plotted in Fig. 5-1 (a) as the dashed line. A linear stability analysis of Eqs. (8) and (9) shows that the $m = 1$ modes have growth rates that become positive for $U > 2$. The eigenvalues corresponding to the $m \geq 2$ modes remain negative and do not change sign. Fig. 5-1 (b) compares the computed and predicted Fourier coefficients for the nematic state with the director parallel to the x-axis. As can be seen, we have excellent agreement. In the limit $(U = 0,\ p = 1)$, only one stable stationary aligned solution branch is found. The scalar structure factor increases with increasing shear rate, and the director orientation approaches the shearing direction $\boldsymbol{e}_x$. This is shown in Fig. 5-1 (c). There is no bifurcation observed in this scenario. This result may be compared with that for a general 2-D symmetric potential flow field as seen for example when the rods are subjected to planar elongation flow $(\boldsymbol{v} = \dot{\epsilon}\,\boldsymbol{e}_x - \dot{\epsilon}\,\boldsymbol{e}_y)$. The distribution function in this case has the form $f_0 = J^{-1} \exp\left(\dot{\boldsymbol{\gamma}} : \mathbf{uu}/2\right)$, J being a normalizing factor, $\gamma \equiv (\dot{\boldsymbol{\gamma}} : \dot{\boldsymbol{\gamma}})^{1/2}$ a characteristic strength of the field and θ being

---

other words, there is no energy penalty due to the rotation as long as the shape of f and the value of S_0^N are kept constant. In terms of the Fourier coefficients, setting all the $b_k = 0$ for $k \geq 1$ is equivalent to pinning the director and removing this rotational degeneracy.
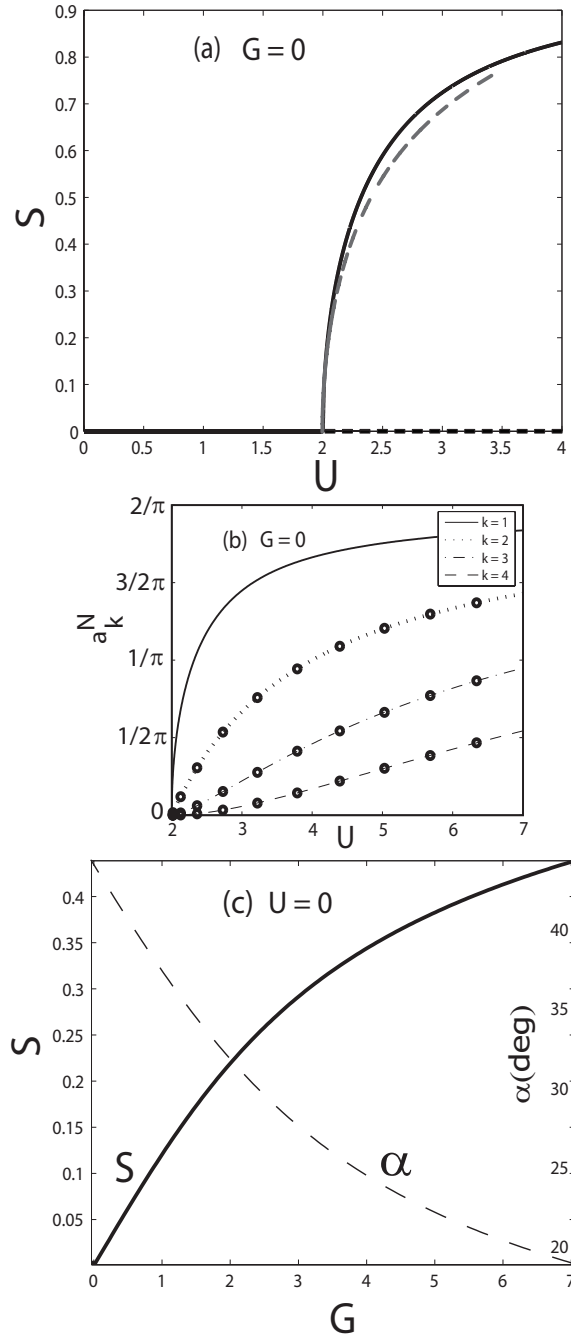
Figure 5-1: (a) Equilibrium bifurcation diagram for $G = 0$. At $U = 2$ a pitchfork bifurcation occurs. The asymptotic expression for $0 < S_0^N \ll 1$ is the dashed line. (b) The first four coefficients characterizing the nematic state with $b_k = 0 \; \forall \; k \geq 1$. The lines represent computed results whereas the the symbols are analytical predictions. (c) Variation of the structure parameter S and the director angle α with G.

the angle made by the rod with $\boldsymbol{e}_x$. Taking averages, we find that $\langle \sin 2\theta \rangle = 0$ while the structure factor $S(U = 0) = \langle \cos 2\theta \rangle \approx \gamma/4$. The linearity of the equations in γ imply a well behaved solution and a structure factor that smoothly varies as γ increases from zero. Thus there is no bifurcation for $U = 0$. Results for small shear rates also show that as $\gamma \to 0$, the angle of alignment is exactly $\pi/4$ with the axis of flow and the structure factor is approximately linear in the shear rate.

5.3 Results of computations: The effects of weak shearing on the equilibrium bifurcation map

Imposition of weak shearing has two main ramifications: First weak shearing acts as an imperfection pinning the director (thus removing the degeneracy) and unravels the pitchfork bifurcation. The breaking up of the pitchfork results in two steady states, one stable and the other unstable. Imposition of shearing also breaks the I-N bifurcation at $U = U_{\mathrm{IN}}$ into stable and unstable nematic branches separated by a gap (that vanishes in the limit $G = 0$) with no persistent isotropic states. This effect is seen for both $p = 1$ and $p < 1$. Second, for a given shear rate $0 < G \ll 1$, steady solutions are lost beyond a critical value of $U = U_{\mathrm{L}}(G, p)$. Instead for $U > U_{\mathrm{L}}(G, p)$, we obtain periodic solutions with a frequency and amplitude incommensurate with the requirements for a Hopf bifurcation. This suggests that the periodic tumbling orbits arise from a global bifurcation that cannot be discerned from a simple linear stability analysis about the limit point.

5.3.1 Steady aligned nematic solutions at small shear rates

Weakly aligned states as perturbations to the isotropic branch and breakup of the pitchfork

We first focus on the para-nematic states with $0 < S \ll 1$ induced for small shear rates. These states may be looked at as small perturbations to the isotropic state due to imposition of shearing. Two branches of these exist for arbitrary p : a steady,

weakly aligned, stable branch for $0 < U \ll U_{\text{IN}}$ and a steady, weakly aligned but unstable branch for $U \gg U_{\text{IN}}$. The form of the stable and unstable nematic branches are illustrated in Fig. 5-2 (a) for $p = 1$ and $G = 10^{-2}$ and $G = 10^{-1}$. Fig. 5-3 (a) shows a typical bifurcation curve for $G = 10^{-3}$ and various values of $p < 1$. Note that as either $G \to 0$ or $p \to 0$, these weakly aligned branches collapse onto the isotropic branch. As one approaches U_{IN} either from lower or higher values of U, the degree of alignment increases rapidly as seen in the closeup in Fig. 5-2 (b) and also observed near $U = 2$ in Fig. 5-3 (a).

The weak perturbation to the isotropic state imposed by the shear flow can be easily calculated by means of a simple regular perturbation analysis so long as $|(U - U_{\text{IN}})/U_{\text{IN}}| \gg 1$. Consider the equations for the expansion coefficients (a_k, b_k) in the limit where $0 < G \ll 1$. Define $f = f_0 + Gf^{(1)} + G^2 f^{(2)}$, $(a_k, b_k) = (a_k^{(0)}, b_k^{(0)}) + G(a_k^{(1)}, b_k^{(1)}) + G^2(a_k^{(2)}, b_k^{(2)}) = (a_k^{(0)}, b_k^{(0)}) + G(a_k^*, b_k^*)$ such that $(a_k^{(0)}, b_k^{(0)}) = 0$ for $k \geq 1$ characterizes the isotropic state. Linearizing the no-flow $(G = 0)$ evolution equation for (a_1, b_1) about this isotropic state indicates that these modes become unstable at $U_{\text{IN}} = 2$ with growth rates $\lambda_1^{(0)} = (2U - 4)$. The growth rates for (a_k, b_k) when $k \geq 2$ and $G = 0$ are $\lambda_m^{(0)} = -4m^2$. Thus the eigenvalues occur in pairs of two as anticipated by the form of the expansion chosen. Continuing with the regular perturbation, we obtain at $O(G)$, the equations $da_1^{(1)}/d\tau = 2a_1^{(1)}(U-2)$ and $db_1^{(1)}/d\tau = 2b_1^{(1)}(U - 2) + p/\pi$. These not only imply that the steady base state is given by $(a_1^{(1)}, b_1^{(1)}) = (0, -p(2\pi)^{-1}(U - 2)^{-1})$, but also show that this perturbed solution is unstable for $U > 2$ and stable for $U < 2$ with no solution at $U = 2$. The higher modes are all zero, that is $(a_{k\geq2}^{(1)}, b_{k\geq2}^{(1)}) = (0, 0)$. Continuing to $O(G^2)$, we have $da_1^{(2)}/d\tau = 2(U - 2)a_1^{(2)} + b_1^{(1)}$ and $db_1^{(2)}/d\tau = 2(U - 2)b_1^{(2)}$, which yield the steady solution, $(a_1^{(2)}, b_1^{(2)}) = (b_1^{(1)}(2 - U)^{-1}/2, 0)$ valid so long as $(U - 2) \neq 0$. The $a_2^{(2)}$ mode follows $da_2^{(2)}/d\tau = -16a_2^{(2)} - pb_1^{(1)} - 2\pi U(b_1^{(1)})^2$ which implies the steady solution $a_2^{(2)} = -p^2(16\pi(U - 2)^2)^{-1}$. The complementary mode $b_2^{(2)} = 0$ and all higher modes $(a_{k\geq3}^{(2)}, b_{k\geq3}^{(2)}) = (0, 0)$. Using these results we obtain the asymptotic value of S when
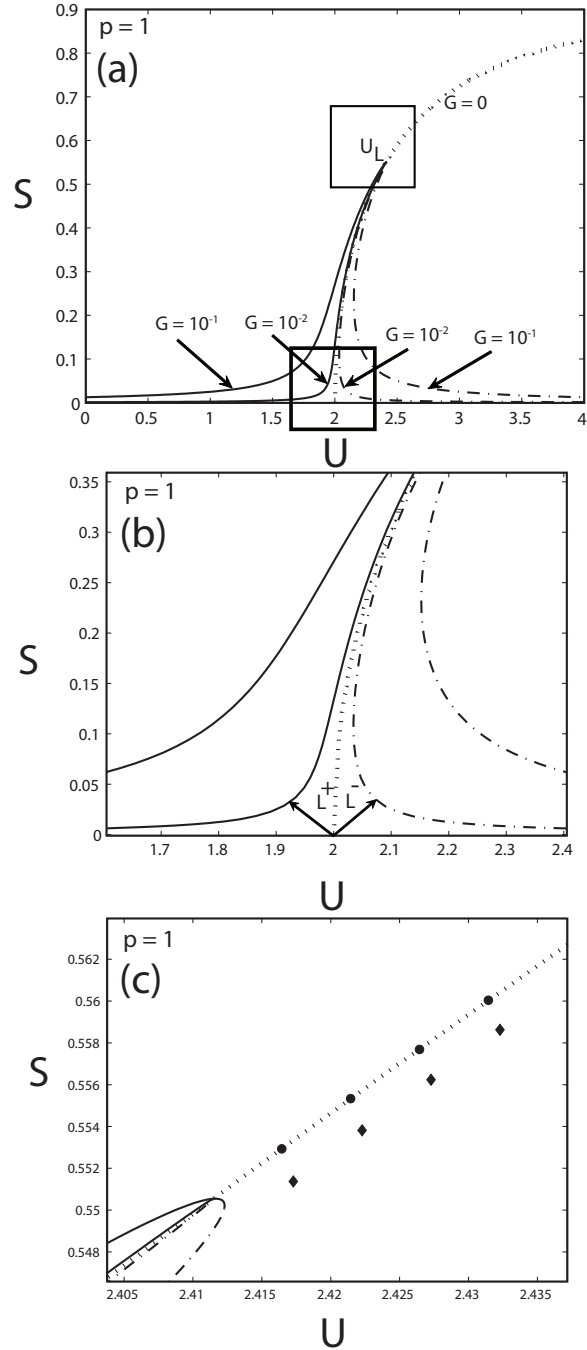
Figure 5-2: The effect of weak shear flow on the $G = 0$ bifurcation map for $p = 1$. (a) For $G \ll 1$, the pitchfork bifurcation at $U = 2$ vanishes. The two steady branches, one stable the other unstable, meet at the limit point, $U = U_{\mathrm{L}}(G, p = 1)$. (b) For $0 < G \ll 1$, the area around the critical point U_{IN} exhibits a gap in which no steady solutions exist. (c) For $U > U_{\mathrm{L}}$ no steady solutions are seen. Stable, periodic solutions, indicated by the solid symbols, exist with $O(1)$ amplitude approximately equal to $S_0^N(U_{\mathrm{L}})$ close to the limit point. As $G \to 0$, the two steady branches meet at a singular point.
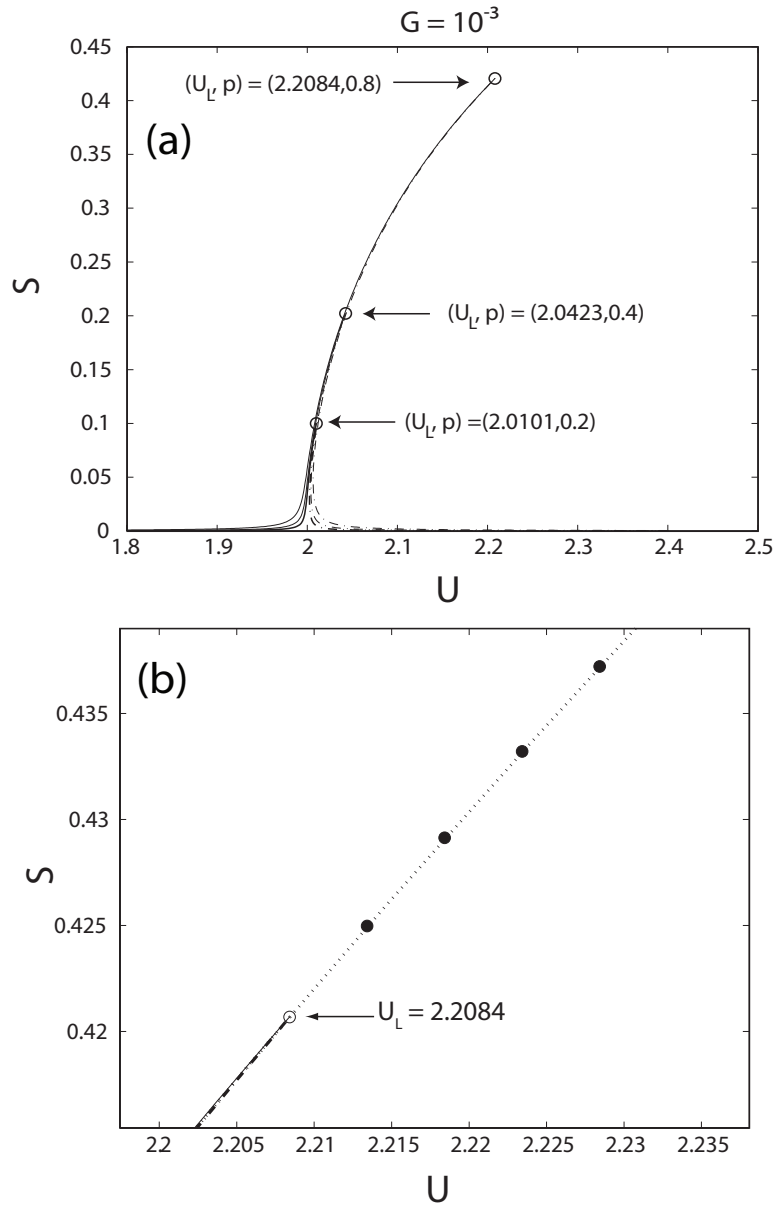
Figure 5-3: Illustration of the effect of weak shear flow on the $G = 0$ bifurcation map for $p < 1$. The $G = 0$, $p < 1$ bifurcation diagram is identical to the $p = 1$ case. (a) Variation of structure factor with dimensionless potential intensity for varying shape factor and (b) close up of the transition from steady to tumbling behavior at $G = 10^{-3}$ and $p = 0.8$. The solid and dashed curves represent stable and unstable solutions, respectively, whereas the dotted curve corresponds to the $G = 0$ solution. The hollow symbols mark the limit point while the filled symbols correspond to unsteady but stable solutions.

$0 < G \ll 1$ and $|U - 2|/2 \gg 1$, namely

$$S \approx \frac{Gp}{4|U-2|}(1 + \frac{G^2}{8|U-2|^2}) + O(G^3 p). \tag{5.13}$$

This expression is physically consistent with the observation that as $p \to 0$, the structure parameter goes to zero. Similarly, as $G \to 0$, $S \to 0$ as well, indicating that the base state tends to an isotropic state. Finally note that when $U \to 0$ and $G > 0$, the structure factor $S > 0$, a result consistent with the $U = 0$ base state calculations of the previous section.

A close up of the region around the I-N transition point $U_{\text{IN}} = 2$ for non-zero values of G shown in Fig. 5-2 (b) for $p = 1$ suggests that shear flow acts as a small perturbation unfolding the pitchfork bifurcation into stable and unstable para-nematic branches. A gap develops close to the critical point around which no persistent perturbations of the isotropic state exist. Both the steady, weakly aligned states are seen to *move away* from $U = 2$ as indicated schematically by L^+ and L^- in Fig. 5-2(b). The behavior also persists for smaller values of p suggesting that the asymptotic expansion developed previously ceases to be valid. The extent of the gap is seen to depend on both G (with p fixed) and p (with G fixed) as is seen from Fig. 5-3(a). The scaling of widths $|L^+|$ and $|L^-|$ for which there are no small amplitude, $O(G)$ perturbed solutions can be estimated by a different perturbation analysis, in a manner analogous to that in [96] and [37, 117]. We treat G as a parameter on which the curves $U(G)$ and $S(G)$ vary. Thus the bifurcation map of S vs. U represents a phase plot in which G is implicit. Solvability (marginal stability) and consistency criteria are used then to evaluate scalings for the perturbed solutions. Repeating their analysis indicates that these gaps scale as $G^{2/3}$ for $0 < G \ll 1$.

Highly aligned steady solutions: perturbations from the equilibrium nematic state

Examination of the nematic branches at moderate values of S for both $p = 1$ and $p < 1$ (Figs. 2(a) and 3(a)) show that both the stable branches exist up to the

limit point; the two (stable and unstable) steady branches are arbitrarily close to the equilibrium nematic branch and collapse onto it at $G = 0$. The branches seem to meet at a limit point $U = U_L(G, p)$ rather sharply. This is seen very clearly in Fig. 5-2 (c), for instance, when comparing the curves for $G = 10^{-1}$ and $G = 10^{-2}$. The smaller the value of G, the more dramatic the collapse as illustrated in Fig. 5-4 (a). As already discussed, the equilibrium nematic state is degenerate due to the lack of an intrinsic direction; and thus the eigenvalues characterizing the equations linearized about the nematic branch possess a zero eigenvalue. Imposition of shearing essentially destroys this, and the zero eigenvalue attains a non-zero value. We expect that this eigenvalue value is negative on the stable nematic, positive on the unstable branch, and exactly zero at the limit point where the two meet. The stable, steady branch in effect turns around and becomes the unstable steady branch. The smaller the value of G or p, the sharper the turn.

The dramatic collapse is perhaps the clearest illustration of symmetry breaking in this system. To obtain some insight into the nature of these steady branches, we consider a perturbation about the nematic state, characterized by the set of coefficients $(a_k, b_k) = (a_k^N, 0)$. Consider the expansion for $U_c = 2 \ll U \ll U_L(G, p)$ and $0 < G \ll 1$, such that to leading order $S = S_0^N + O(G)$. We choose $a_k = a_k^N + G a_k^{(1)}$ and $b_k = G b_k^{(1)}$. We seek steady non-trivial solutions $(a_k^{(1)}, b_k^{(1)})$. Expanding the equations to $O(G)$ yields $a_2^{(1)} = (\pi U a_1^N)^{-1}(2(U - 2) - \pi U a_2^N) a_1^{(1)} = \beta_{2,1} a_1^{(1)} = 0$. For $k \geq 2$

$$\frac{4k}{\pi U}\left(\frac{a_k^{(1)}}{a_1^N}\right) = (a_{k-1}^{(1)} - a_{k+1}^{(1)}) + \frac{4k}{\pi U}\left(\frac{a_1^{(1)}}{a_1^N}\right)\left(\frac{a_k^N}{a_1^N}\right). \tag{5.14}$$

The form of these equations also suggests that one can write in general $a_k^{(1)} = \beta_{k,1} a_1^{(1)}$. Fixing the first mode fixes all the modes. Note that the equations do not involve any $b_k^{(1)}$ modes; this is because we are essentially considering only small terms linear in G. This decoupling is similar to that seen for $G = 0$. However, when one considers the $b_k^{(1)}$ terms, a different scenario emerges. We find

$$b_2^{(1)} = \frac{1}{2\pi U a_1^N}\left(2\frac{p}{\pi} - 2a_1^N + pa_2^N\right) + b_1^{(1)}(2(U - 2) + \pi U a_2^N)$$

188
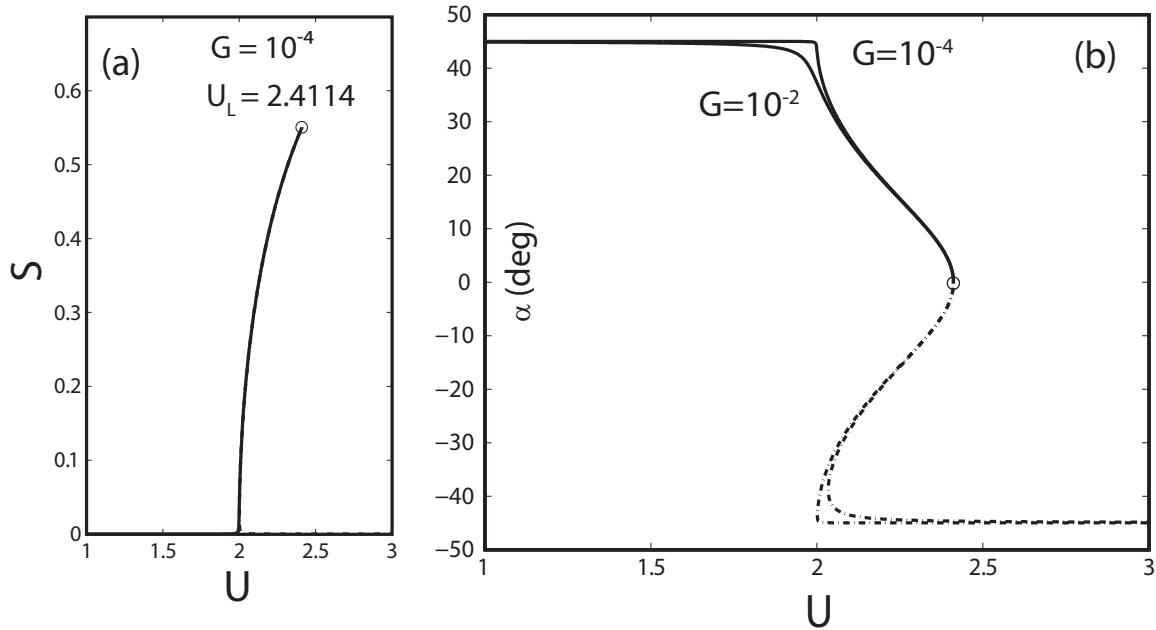
Figure 5-4: (a) Enlargement of the collapse of the stable and unstable nematic branches as $G \to 0$. The two branches essentially lie on top of each other. For $G > 0$, the unraveling of the symmetry in the equilibrium state results in the two solutions. (b) Variation of the director angle with U when G is very small. Note that as the critical limit point is reached beyond which steady solutions cease to exist, the director angle approaches zero. The stable branch tends to an angle of $+\pi/4$ for $U \ll U_{\text{IN}}$ whereas the unstable steady branch tends to $-\pi/4$ for $U \gg U_{\text{IN}}$.

and for $k \geq 2$,

$$b_k^{(1)} = \frac{1}{8k}(p(a_{k-1}^N + a_{k+1}^N) - 2a_k^N)$$

$$+ \frac{\pi U}{4k}(b_1^{(1)}(a_{k-1}^N + a_{k+1}^N) + a_1^N(b_{k-1}^{(1)} - b_{k+1}^{(1)})).$$

For a non-trivial steady solution to exist, at least one of these coefficients has to be non-zero. We note that even if $b_1^{(1)} = 0$, $b_2^{(1)}$ is not zero. This indicates that we do not have any subspace of steady solutions wherein only $a_k^{(1)}$ modes exist. Since then $(a_k, b_k) \approx (a_k^N, Gb_k^{(1)})$, the flow breaks the degeneracy and symmetry associated with the invariant subspace of equilibrium solutions.

5.3.2 Limit point and loss of steady solutions at moderate to large alignment

A very important feature of the branches that emerge from our calculations is the loss of steady - both stable and unstable solutions - by the formation of a limit point seen in Fig. 5-2 (a) and in more detail in Fig. 5-2 (c) for $p = 1$. Similar features exist for $p < 1$. The steady, stable nematic aligned family turns back at the limit point, $U = U_L(G, p)$, and returns along a descending curve. These two independent solution branches superimpose and become indistinguishable as $G \rightarrow 0$. The superposition is very sharp, leading to a cusp like behavior at the limit point. For example, Fig. 5-2 (a) shows the curves for $G = 10^{-1}$ and $G = 10^{-2}$, and the result for the even smaller value $G = 10^{-4}$ is illustrated in Fig. 5-4 (a).

In order to understand the stability characteristics of these two branches we plot the angle made by the director with the flow axis as a function of U, which is shown in Fig. 5-4 (b). It is seen that the transition from stable to unstable solutions marks the change in sign of the director orientation from positive to negative with respect to e_x. As $G \rightarrow 0$, the rods in the steady nematic branch orient at an angle $+\pi/4$ to the flow axis, whereas those in the unstable branch are oriented at $-\pi/4$ degrees. A negative α is unstable as the flow imposes a clockwise moment on the rods that is largest when they are in the negative orientation. As the critical limit point is approached,

$U \rightarrow U_{\mathrm{L}}(G,p)$, the angle made by the rods approaches $\alpha = 0$ denoting that the point is neutrally stable. In Figs. 5-5 (a) and 5-5 (b) we plot $U_{\mathrm{L}}(G, p = 1)$ and second show how $U_L(G, p)$ varies as p changes for fixed G. In general, keeping G fixed and decreasing p pushes the limit point monotonically to lower values of U. Specifically, $U_L(G \ll 1, p \rightarrow 0) \rightarrow U_{\mathrm{IN}}$. The trend for fixed p, say $p = 1$, and varying G is as seen in Fig. 5-5 (a). Let us start, for example, at $G = 10^{-2}$ and $p = 1$. When we move to higher values of G, there is a region over which the limit point roughly has the same value, and then $U_L(G, 1)$ is seen to slowly increase with increasing G. As we move in the other direction towards smaller values of G, the value of the critical point tends towards a finite value that is p dependent. Specifically $U_{\mathrm{L}}(G \rightarrow 0, p \rightarrow 1) \rightarrow 2.4114...$ This value is in excellent agreement with previous asymptotic estimates of the limit point [117]. Note that our numerical calculations also suggest that the limiting value is actually an excellent approximation to values of up to $G \sim O(10^{-1})$.

5.3.3   Onset of periodic solutions via global bifurcation

For a small, but constant value of G, we find no steady solutions for $U > U_{\mathrm{L}}(G, p)$. Instead, periodic, non-sinusoidal oscillations in the coefficients are observed. These periodic orbits emanate from the limit point and correspond to tumbling modes where the rods rotate continuously but with a fixed mean structure parameter. The average value of S for these stable, time-dependent solutions is approximately $S_0^N(U)$.

Examples of such states are presented in Fig. 5-6 ($p = 1$) and Fig. 5-7 ($p = 0.8$). The periodic orbits for $G = 10^{-2}$ were computed at 2.5114. Under these conditions the simulation had to be run for up to 5000 rotational relaxation times in order to capture a few periods of the structure factor. Figs. 5-6 and 5-7 illustrate the limit cycle observed by plotting the first two Fourier modes, a_1 and b_1, representing the two independent components, S_{11} and S_{12}, of the structure tensor. A short transient is seen after which the components attain their unsteady but stable values. The scalar structure factor fluctuates about a mean that has value approximately equal to $S_0^N(U)$ close to $U_L(G, p)$ with variations that are $O(G)$ (see Fig. 5-8 (b)) and periodic with period $T_p = \omega_T^{-1} \sim O(G^{-1})$. The qualitative forms of the periodic trajectories
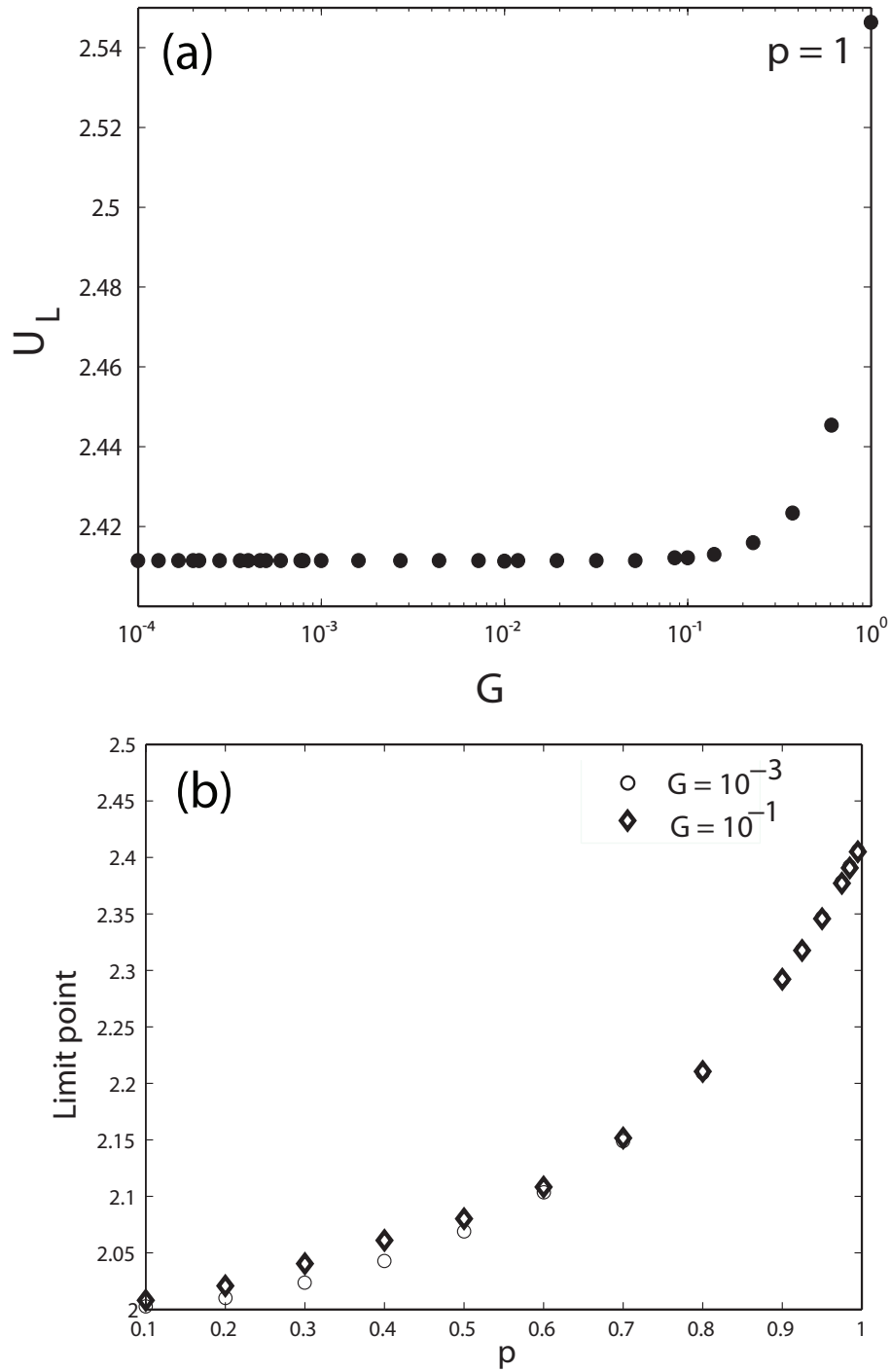
Figure 5-5: (a)The variation of critical potential intensity where steady solutions are lost, $U = U_L$, with G is shown for $p = 1$. As $G \to 0$, the limit point asymptotically approaches the value 2.4114. (b) Effect of finite aspect ratio for $p < 1$. The variation of critical potential intensity with shape factor is now shown.
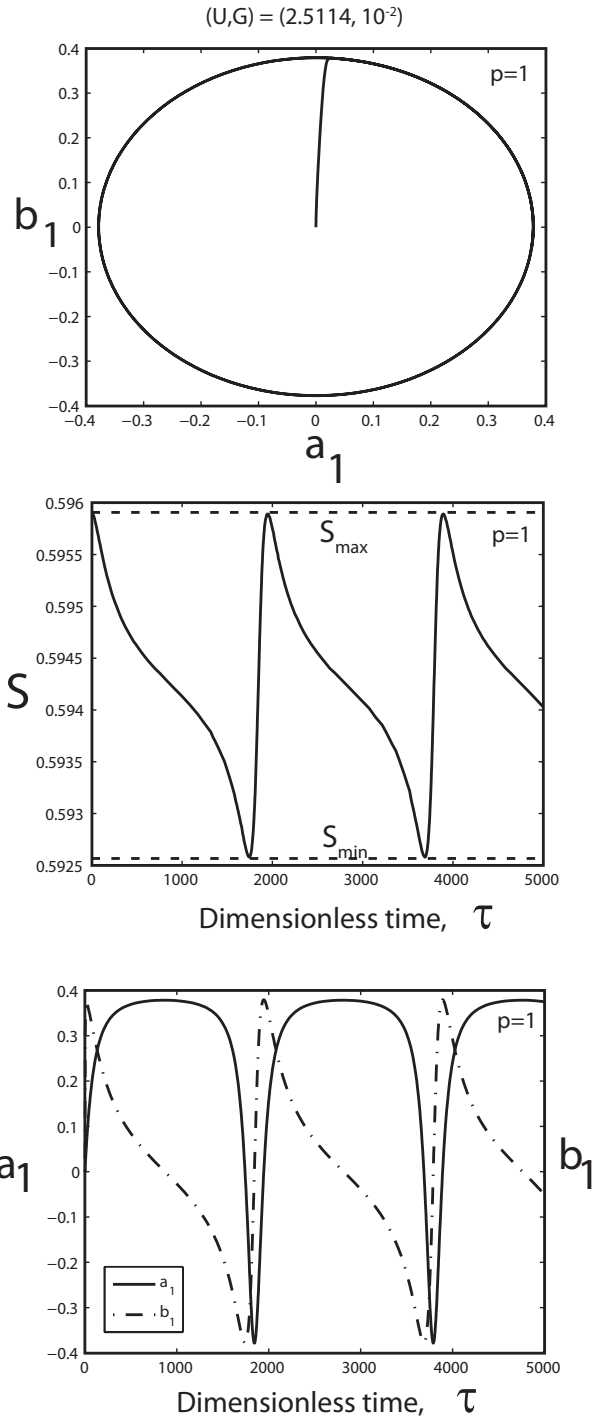
Figure 5-6: The nature of the periodic solutions for $p = 1$ including the limit cycle for the periodic state, tumbling behavior for the structure factor, and the first two non-zero Fourier modes, a_1 and b_1.
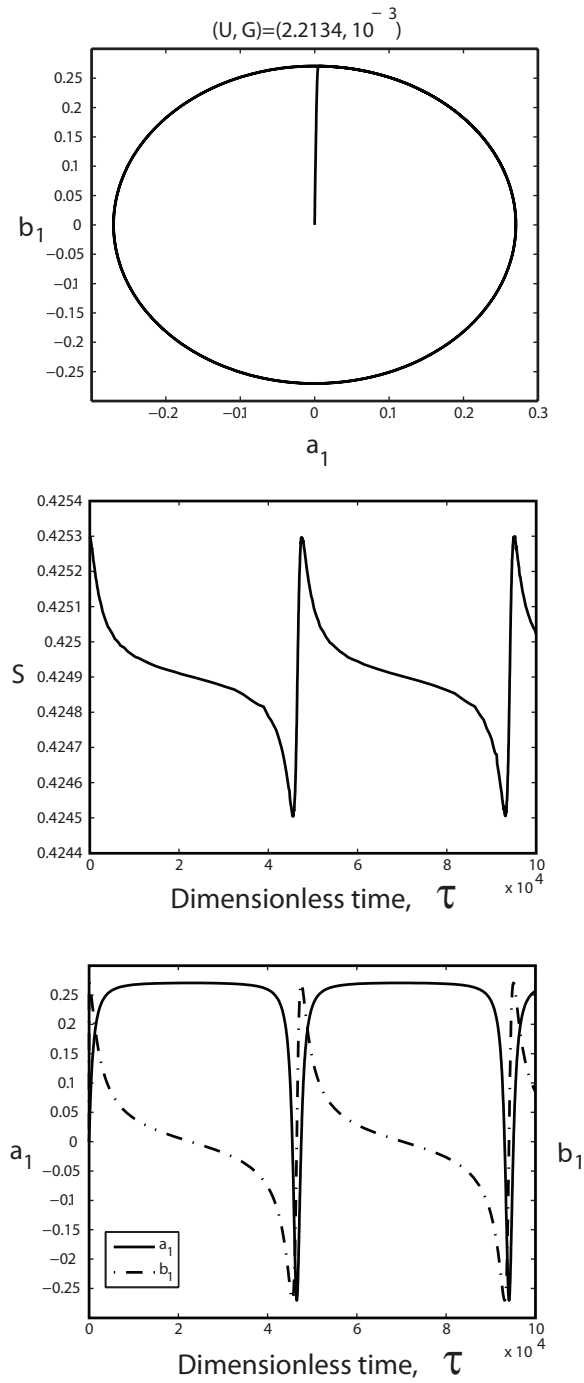
Figure 5-7: Nature of the periodic solutions for a finite aspect ratio corresponding to $p = 0.8$.

do not change much for $0 \ll p < 1$.

From the nature of the periodic solutions, we deduce that they correspond to tumbling behavior rather than wagging behavior for the rod director. In the wagging state, the director oscillates between two angles whereas for tumbling, the director rotates continuously. The two Fourier modes, a_1 and b_1, represent averages of the cosine and sine of the polar angle θ and hence provide a measure of the average orientation of a test rod placed in the shear flow. Consider Fig. 5-6 (c). During one period of the oscillation, a_1 remains positive for majority of the period, while b_1 changes sign from positive to negative. This is followed by a quick transition to negative and then positive values for a_1 as it goes through zero twice, while b_1 only goes through zero once in the quick transition before completing the period. During the first transition, the test rod slowly rotates past $\boldsymbol{e}_x$, as α changes sign from positive to negative. In this transition, the cosine remains positive while the sine goes through zero. In the second transition, the rods quickly rotate across $-\boldsymbol{e}_y$ since the clockwise moment on the rods is largest once they rotate cross $\boldsymbol{e}_x$. This behavior is repeated as the rod continues to tumble.

As $U \to [U_L(G, p)]^+$, the tumbling solutions have increasingly larger periods. In addition, the oscillations emerge with finite amplitude at the limit point. Although this is sufficient to eliminate the possibility that the critical point marks a Hopf bifurcation to periodic solutions, the spectrum of eigenvalues evaluated on the stable branch(es) shows that only a single eigenvalue is close to crossing the imaginary axis. This is contrary to the typical scenario for a Hopf bifurcation where the real part of a complex conjugate pair of eigenvalues with non-zero imaginary part passes through the imaginary axis. Furthermore, the eigenspectrum seems also to rule out a homoclinic bifurcation, a distinguishing feature of which is a complex conjugate pair of eigenvalues with zero imaginary parts crossing the imaginary axis. Therefore, we characterize the bifurcation by analyzing numerical results for the amplitude and frequency of the time-periodic states as a function of the distance from criticality ($U - U_L$). This is shown in Figs. 5-8 (a) and 5-8 (b). As the critical point is approached, the amplitude of the oscillation stays $O(1)$ while the frequency decreases like $|U -$
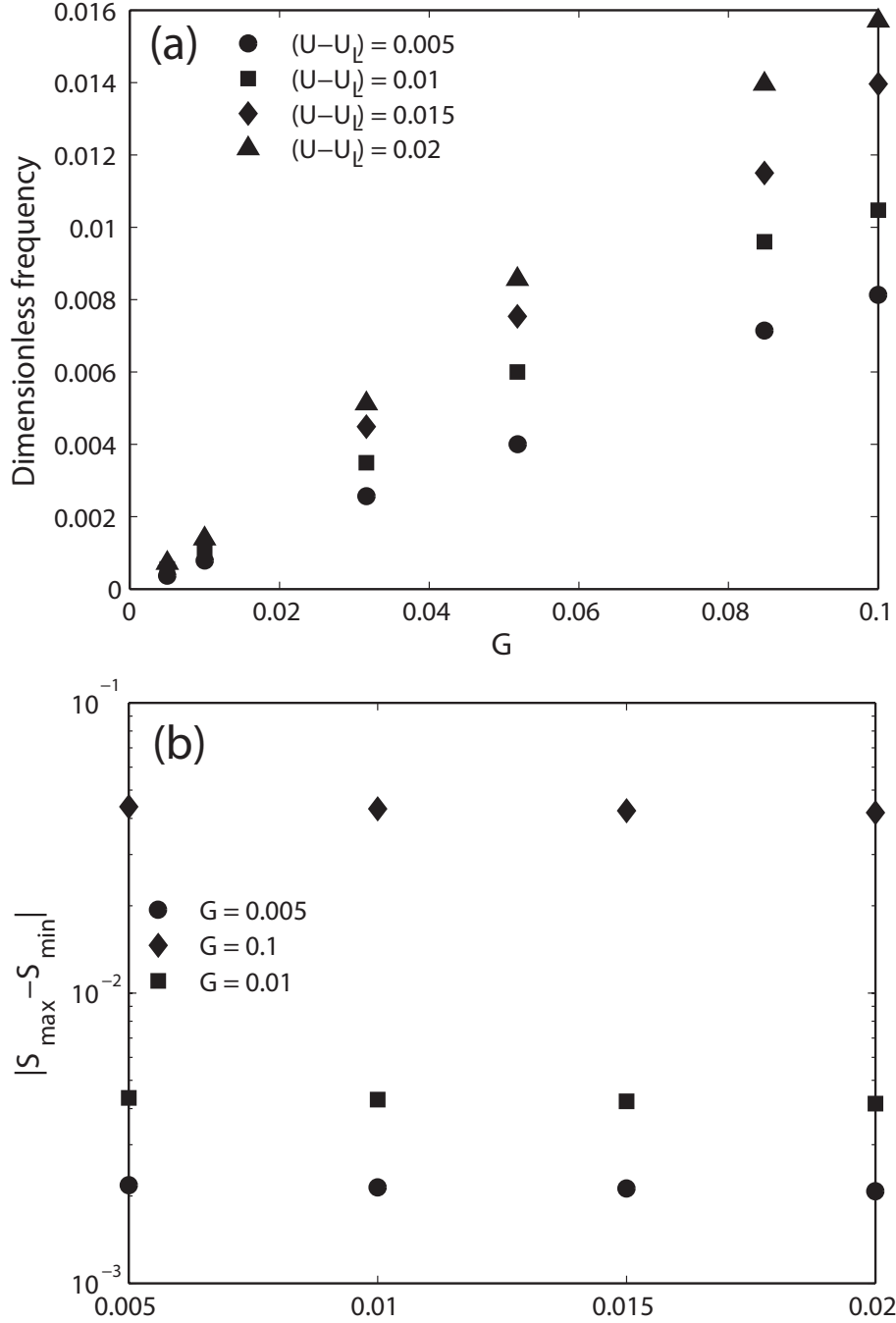
Figure 5-8: Frequency and amplitude scalings for bifurcating periodic solutions for $p = 1$, $U > U_L(G, p)$. Part (a) suggests that the frequency is of the form $\omega_T \sim G^\alpha$ where $\alpha > 1$ with a slope dependent on the potential. The amplitude of oscillations at onset does not go to zero as one approaches the critical limit point; it remains $O(S_0^N(U_L))$. This rules out the possibility that tumbling is born via a Hopf-Poincaré bifurcation, consistent with analysis of the eigenvalue spectrum. The variations in the structure factor, $S_{\max} - S_{\min}$, is $O(G)$.
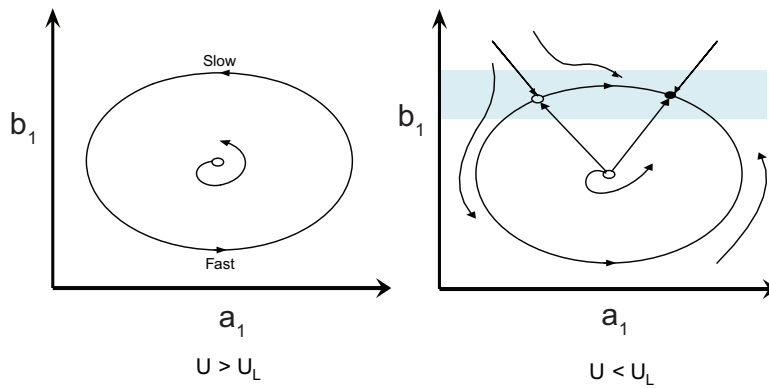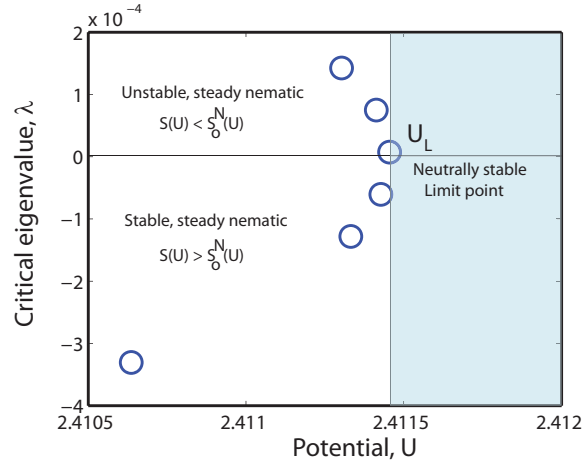
Figure 5-9: (a) The variation of the critical eigenvalue for $G = 10^{-2}$ and $p = 1$ near $U = U_L$ as we move from the stable to the unstable steady nematic branch through the limit point. At $\lambda = 0$ and $U = U_L$, a stable, periodic branch of solutions is born. (b) Schematic diagram of the bifurcation scenario that gives rise to the periodic, tumbling orbits for a prototypical two-dimensional system. The limit cycle develops a bottleneck as $U \to U_L^+$, resulting in oscillations with larger and larger periods. At $U = U_L$ the period becomes infinite as a pseudo-fixed point appears in the phase portrait. For $U < U_L$ the fixed point splits into a saddle point and a stable node that are characterized by the sign of the most critical eigenvalue.
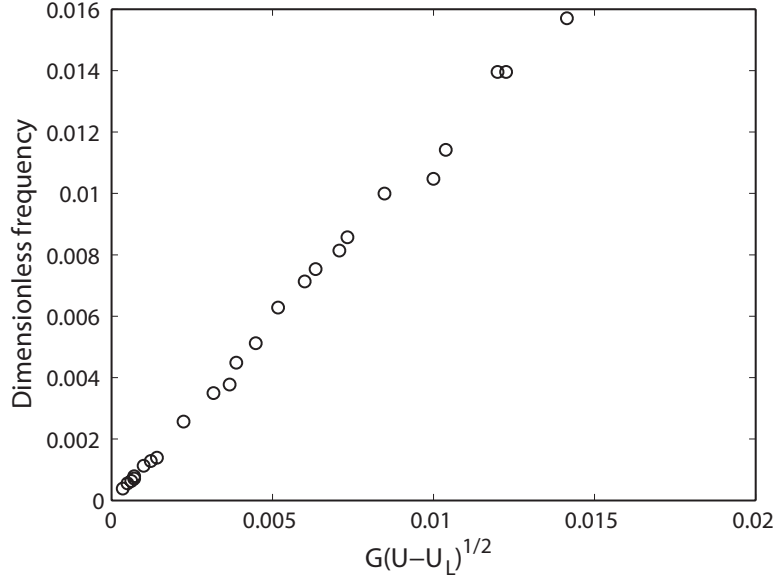
Figure 5-10: Collapse of the frequency, ω_T, associated with the tumbling orbits close to criticality when $p = 1$ and $U > U_L(G, p)$. Rescaling of the numerical results indicates that $\omega_T \sim G(U - U_L)^{\frac{1}{2}}$, which is consistent with the scaling for a global infinite period bifurcation in two-dimensions.

$U_L(G, p)|^\rho$ with $\rho \approx 0.49$. This scaling is obtained through a power law fit for the three values of G shown in the plots (see Fig. 5-10) and suggests that the time-periodic states arise because of an infinite-period global bifurcation at the limit point.

The infinite period bifurcation is characterized by the collision of a stable node and a saddle point in phase space that results in a stable limit cycle, or vice versa. This is exactly the case in this problem, where we have stable periodic solutions or a limit cycle in phase space for $U > U_L$, and as U decreases through U_L we obtain both stable and unstable stationary solutions. This change in the phase space is shown in Fig. 5-8 (b) for a prototypical two-dimensional system [106]. As already demonstrated through numerical simulations, the limit cycle develops a bottleneck as $U \to (U_L)^+$ resulting in oscillations with larger and larger periods. At $U = U_L$ the period becomes infinite as a pseudo-fixed point appears in the phase portrait. For $U < U_L$ the fixed point splits into a saddle point and a stable node that are characterized by the sign of the most critical eigenvalue.

5.4 Summary and concluding remarks

The results of our bifurcation analysis of the *full, unclosed* equations can be compared to scaling results obtained by analysis of lower dimensional approximations. We focus on results obtained for the LDG form [1] by Alonso, Wheeler and Sluckin and for the Doi-Hess mesoscopic tensor model [19] coupling structure factor variations to director dynamics. The two give similar scaling predictions, and so we choose to revisit the Doi-Hess tensor model as it is closer in form and spirit to the full diffusion equation we have investigated.

The Doi-Hess closed form equations (DHC) for the 3-D form of the equations [19] involve the parameters N (the dimensionless potential), p, and the shear flow parameter Pe $\propto G$. The equilibrium nematic structure parameter for this form is given by $S_c = (1 + 3\sqrt{1 - 8/(3N)})/4$ so that the I-N bifurcation now occurs at $N = 3$ with a turning point (which is not present in our system) seen at $N = 8/3$. Note that the oblate nematic state in 3-D $(-1/2 < S_c < 0)$ corresponds to the isotropic state in 2-D. Any connecting orbits between the 2-D isotropic $U > U_{\text{IN}}$ and the 2-D prolate nematic state are to be compared to the orbits connecting the 3-D oblate $(-1/2 < S_c < 0)$ and the 3-D prolate $(S_c > 0)$ states. With this in mind, let us compare our results with those obtained by asymptotic analysis of the DHC equations. We note that the tumbling states have a structure factor that is to leading order $O(S_0^N(U))$ and $O(S_0^N(U_L))$ close to $U = U_L$ with the first order corrections to this being $O(G)$ that vary on a time scale given by the slow time scale of $O(\omega_T t)$. These compare very favorably to the DHC results (cf. Eqs. (2)-(5) in [19]). Note that the slow time scale characterizing the tumbling orbits is found to be (in terms of our parameters) $\omega_T = (G/2\pi)(1 - S_c(N)^2)^2\sqrt{1 - \lambda_0^2} \equiv (G/2\pi)\Psi(N, p)$, which is consistent with the scaling for the exact model in terms of the G dependence. The tumbling parameter $\lambda_0(N, p) = (p/3)(1 + 2/S_c(N))$ introduces the dependence on the aspect ratio; and thus for $p = 1$, we have $\lambda_0(N, 1) = (1 + 2/S_c(N))/3$.

To conclude, we have presented a detailed numerical study of the shear induced transition from steady to in-plane periodic states of a suspension of rods in the low

shear rate limit. The 2-D Doi-Hess diffusion equation with a Maier-Saupe excluded volume potential was used to model the interactions between rods. It is shown that flow breaks the degeneracy and symmetry of the nematic state at equilibrium, yielding both stable and unstable solution branches that exist arbitrarily close to the equilibrium solution. Results are also presented from asymptotic analysis for the perturbation to the isotropic and nematic solutions in the weak shear flow limit around the equilibrium isotropic-nematic transition. These asymptotic results show that no solutions exist in a gap of $O(G^{1/2})$ around the transition point. Analysis of numerical solutions obtained via continuation and spot calculations strongly suggests the birth of periodic orbits at the critical potential strength, $U = U_L$, via an infinite period bifurcation. This is supported by a study of the eigenspectrum of the stationary solutions near the limiting potential. We find that the eigenspectrum of the model closely resembles the eigenspectrum of a prototypical two-dimensional system that exhibits an infinite period bifurcation. However, this does not guarantee that a single, two-variable constitutive equation exists that can elucidate the complete set of solutions for the diffusion equation. Limited results were also obtained earlier in our group for the full 3-D problem by using wavelet methods [80]. Although the calculations are still in their preliminary stages it is heartening to note that the numerical results for the full 3-D $G \ll 1$ shear flow problem are consistent with what has been obtained in this chapter.

Chapter 6

Predicting Onset of Draw Resonance for Isothermal Fiber-spinning with Hybrid Simulators

6.1 Introduction

The fiber spinning process involves drawing a molten polymer as a liquid fiber following extrusion from an orifice to form continuous synthetic fibers of very small diameters, typically on the order of 100μm and smaller. The small diameters are achieved by stretching the molten polymer before solidifying in air or in a quench bath and wounding on a spool. In addition to forming fibers of small diameters, the process also leads to development of morphological features that depend on the extent and rate of drawing. This is of particular importance in the spinning of anisotropic polymeric fluids, such as liquid crystals, that yield products with highly anisotropic properties. As such, the events that occur in the drawing region are the most significant in determining the ultimate properties of the fiber. For example, ultra high molecular weight high density polyethylene fibers with high degree of orientation in

the axial direction can have the stiffness of steel with current fiber-spinning technology [82].

One of the major concerns during fiber spinning are the instabilities that arise during drawing. Usually there is an upper limit to the speed of extrusion or a lower limit on the length of the drawing region beyond which the filament breaks. More generally, however, the rheological properties of the polymer melt in the drawing region are such that a uniform fiber cannot be drawn into the solidification process. This phenomenon typically manifests itself as periodic fluctuations in the diameter of the drawn fiber and an accompanying oscillation in the tension at the take-up point. This latter instability, also known as draw resonance, has been studied extensively in a number of theoretical and experimental investigations. Kase and Matsuo [53] and Matovich and Pearson [78] were the first to derive the correct equations for the fiber-spinning process and used them to study the onset of draw resonance instability of inelastic fluids. They predicted a minimum ratio of the take-up and extrusion speeds beyond which the Newtonian fluid was unstable to infinitesimal disturbances. While their results were in excellent agreement with experimental data for the isothermal spinning of low molecular weight polymers that have small relaxation times and viscosities independent of deformation rate, the results could not be extended to spinning of polymer melts that exhibit high stress levels and velocity profiles that are linear compared to those predicted by inelastic fluid analysis.

The first major publication to address these limitations was the work of Fisher and Denn [33] who studied the mechanics of isothermal fiber-spinning with the shear-thinning White-Metzner model. They were able to predict both the onset of draw resonance and a second stable region at high draw ratios, which was in agreement with the data of Ishihara and Kase [50] for PET. Following this work other constitutive equations were also used to model the fiber-spinning process, most notably the multimode Phan-Thien Tanner model [86], which has multiple relaxation times for modeling a real polymeric liquid. Finally, Gupta et al. [47] were able to use the one-dimensional equations for the fiber-spinning process to successfully model spinning data for a dilute solution of polyisobutylene in polybutene with the Oldroyd-B

constitutive equation. It was shown that for a given value of the draw ratio and viscoelasticity, as measured by the ratio of solvent viscosity to total solution viscosity, there is a maximum for the Deborah number beyond which no solution exists.

The purpose of this chapter is to obtain the onset of draw resonance and the transition to second region of stability at high draw ratios for the Oldroyd-B model by using the time-stepper based approach to stability and bifurcation analysis. In particular, the fiber-spinning process for the Oldroyd-B constitutive equation is modelled as a hybrid simulation that couples the conservation of mass and momentum in the isothermal fiber spinning model to a stochastic simulation for the Brownian configuration fields of the Hookean dumbbell model from polymer kinetic theory. For the degree of viscoelasticity used for the model, the values of Deborah number presented in this chapter cover the possible range. This chapter is organized as follows. We begin by developing the equations for isothermal fiber-spinning of polymeric solutions and recast them in a form suitable for solution with a general constitutive equation. This is followed by a presentation of the Oldroyd-B constitutive equation and the stochastic differential equation for the Hookean dumbbell model, their numerical discretization, corresponding weak formulations for obtaining a finite element solution, and the necessary boundary conditions. The chapter concludes with results for the steady state solutions, comparison of the leading eigenvalues of the Oldroyd-B model with their approximations, and bifurcation analysis as obtained from the time-stepper approach.

6.2 Spinning Equations

A schematic diagram of the fiber spinning process is shown in Fig. 6-1, where the origin of the cylindrical coordinate system is placed just downstream of the point of maximum extrudate swell. This position corresponds to a point where the velocity and stress profiles are assumed to be independent of the radial position. To further simplify analysis, it is assumed that the fiber is isothermal and that no shear or normal stresses act on the boundary of the fiber. To develop the spinning equations, we now
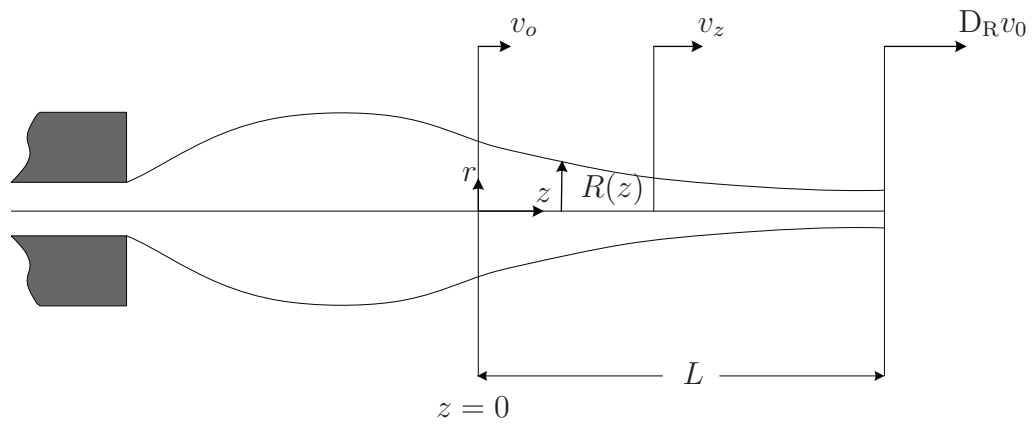
Figure 6-1: Schematic diagram of the fiber spinning process in the post-extrusion die region
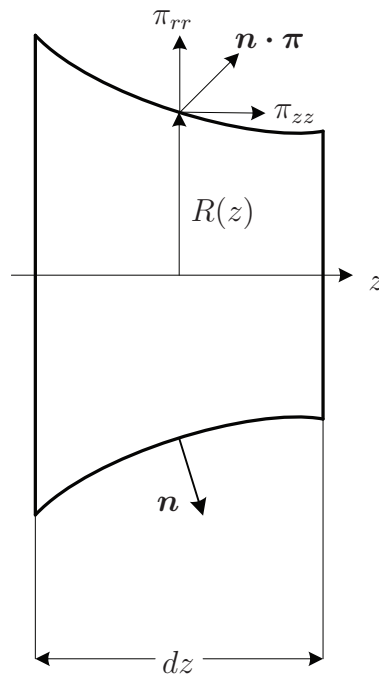
Figure 6-2: Differential element of a fiber during spinning

consider a differential element of the fiber, as shown in Fig. 6-2, with local radius $R(z,t)$, unit outward normal vector $\boldsymbol{n}$, and total stress tensor $\boldsymbol{\pi}$. The components of the normal vector $\boldsymbol{n}$ are given by the geometry of the fiber as

$$n_r = \left[1 + \left(\frac{\partial R}{\partial z}\right)^2\right]^{-1/2} \tag{6.1}$$

$$n_z = -\frac{\partial R}{\partial z}\left[1 + \left(\frac{\partial R^2}{\partial z}\right)\right]^{-1/2} \tag{6.2}$$

By neglecting the effect of the ambient fluid and surface tension, the stress boundary condition on the surface is given by

$$\boldsymbol{\pi} \cdot \boldsymbol{n} = \boldsymbol{0} \tag{6.3}$$

which in component form can be written as

$$0 = (\boldsymbol{\pi} \cdot \boldsymbol{n})_r = \pi_{rr}n_r + \pi_{rz}n_z \tag{6.4}$$

$$0 = (\boldsymbol{\pi} \cdot \boldsymbol{n})_z = \pi_{zr}n_r + \pi_{zz}n_z \tag{6.5}$$

Due to the fact that the fiber is being pulled in the z direction, a finite shear stress is obtained at the free surface, given by

$$\pi_{rz} = -\frac{n_z}{n_r}\pi_{zz} = \frac{\partial R}{\partial z}\pi_{zz} \tag{6.6}$$

This result may seem contradictory with the assumption that there is only atmospheric pressure exerting a force on the free surface. However, this can be resolved by considering that even though π_{rz} is a shear stress, it is not a shear stress in the free surface as it does not lie in the plane of the free surface. Instead, it is a shear stress in the cylindrical coordinate surface shown in Fig. 6-2.

With this result, we can write the momentum balance in the axial direction

$$0 = \frac{1}{r}\frac{\partial}{\partial r}(r\pi_{rz}) + \frac{\partial \pi_{zz}}{\partial z} \tag{6.7}$$

205

where we have neglected inertia and gravity. Since we have assumed $v_z = v_z(z,t)$, we integrate each term in Eq. 6.7 across the fiber cross-section

$$\int_0^R \frac{1}{r}\frac{\partial}{\partial r}(r\pi_{rz})r\,dr = R\pi_{rz}\Big|_R = R\pi_{zz}\frac{\partial R}{\partial z}$$

and

$$\int_0^R \frac{\partial \pi_{zz}}{\partial z}r\,dr = \frac{\partial}{\partial z}\int_0^R \pi_{zz}r\,dr - \pi_{zz}R\frac{\partial R}{\partial z} = \frac{1}{2}\frac{\partial \pi_{zz}}{\partial z}R^2$$

to obtain

$$0 = \frac{2}{R}\frac{\partial R}{\partial z}\pi_{zz} + \frac{\partial \pi_{zz}}{\partial z} \tag{6.8}$$

This can be simplified further to

$$\frac{\partial}{\partial z}(A\pi_{zz}) = 0 \tag{6.9}$$

where $A(z,t) = \pi R(z,t)^2$ is the cross-section area of the fiber. As for π_{rr} we use Eqs. 6.4 and 6.6 to write

$$\pi_{rr} = \left(\frac{\partial R}{\partial z}\right)^2\pi_{zz} \qquad \text{at } r = R(z,t) \tag{6.10}$$

Since there is no significant radial flow we might expect no strong radial variation of stress. This combined with the approximation that the radius of the fiber does not change rapidly, that is $\frac{dR}{dz} \ll 0$, a reasonable approximation is that $\pi_{rr} \approx 0$. Consequently, π_{zz} in Eq. 6.9 is replaced with $\pi_{zz} - \pi_{rr} = \tau_{zz} - \tau_{rr}$, which is the first normal stress to yield the final form of the momentum balance

$$\frac{\partial}{\partial z}[A(\tau_{zz} - \tau_{rr})] = 0 \tag{6.11}$$

In addition to the momentum balance, we can also write the mass balance for an incompressible fluid, which reads

$$\frac{\partial A}{\partial t} + \frac{\partial}{\partial z}(Av_z) = 0 \tag{6.12}$$

206

In Eqs. 6.11 and 6.12, the variables z, v_z, t, A, and stress have been made dimensionless with respect to the length L, the initial velocity v_0 at $z = 0$, time scale L/v_0, initial area, and $\eta_0 v_0 / L$, where $\eta_0 = \eta_s + \eta_p$ and η_s and η_p are the solvent and polymer contributions to the zero shear rate viscosities, respectively. The formulation in Eqs. 6.11 and 6.12 was initially proposed by Kase and Matsuo [53] and Matovich and Pearson [78], and used subsequently by several authors to study the fiber spinning process for various constitutive models. In this study, however, we will rewrite Eq. 6.11 with the DEVSS-G formulation and focus on the Oldroyd-B constitutive equation and its kinetic theory equivalent, the dilute solution of Hookean dumbbells.

For the DEVSS-G formulation, we introduce a new variable, G, for the velocity gradient such that

$$G - \frac{\partial v_z}{\partial z} = 0 \tag{6.13}$$

and write the rr and zz components of the stress tensor as

$$\tau_{zz} = -2\frac{\partial v_z}{\partial z} + 2(1 - \beta)G + \tau_{p,\,zz} \tag{6.14}$$

$$\tau_{rr} = \frac{\partial v_z}{\partial z} - (1 - \beta)G + \tau_{p,\,rr} \tag{6.15}$$

where $\beta = \eta_s / \eta_0$, and $\tau_{p,\,zz}$ and $\tau_{p,\,rr}$ are the polymer contributions to the stress components τ_{zz} and τ_{rr}, respectively. The new formulation for the problem, excluding the constitutive equations, is then

$$
\begin{aligned}
\frac{\partial A}{\partial t} &= -v_z \frac{\partial A}{\partial z} - A\frac{\partial v_z}{\partial z} \\
0 &= \frac{\partial A}{\partial z}\left[-3\frac{\partial v_z}{\partial z} + 3(1 - \beta)G + (\tau_{p,\,zz} - \tau_{p,\,rr})\right] \\
&\quad + A\left[-3\frac{\partial^2 v_z}{\partial z^2} + 3(1 - \beta)\frac{\partial G}{\partial z} + \frac{\partial}{\partial z}[\tau_{p,\,zz} - \tau_{p,\,rr}]\right] \\
0 &= G - \frac{\partial v_z}{\partial z}
\end{aligned}
\tag{6.16}
$$

Before proceeding to the evolution equations for the Oldroyd-B model and its kinetic theory equivalent, the Hookean dumbbell, it is important to mention that while we will be able to couple the Oldroyd-B constitutive equations directly with

the system in Eq. 6.16, the Hookean dumbbell model will be described by a stochastic differential equation for the molecular configuration. This description when coupled with Eq. 6.16 will result in a hybrid simulation for the fiber-spinning process. More importantly, in order to use this hybrid simulation to obtain steady states and perform stability and bifurcation analysis, we will need to build a coarse time-stepper for evolution of the polymer contribution to the stress tensor.

6.2.1 Oldroyd-B model

The Oldroyd-B constitutive equation in tensor form reads as

$$\boldsymbol{\tau} + \lambda_1 \boldsymbol{\tau}_{(1)} = -\eta_0 \left[\dot{\boldsymbol{\gamma}} + \lambda_2 \frac{\partial \dot{\boldsymbol{\gamma}}}{\partial t} \right] \tag{6.17}$$

where λ_1 and λ_2 are the relaxation and retardation times and $\boldsymbol{\tau}_{(1)}$ is the upper convected derivative of $\boldsymbol{\tau}$. By decomposing the stress tensor into a Newtonian solvent contribution and polymer contribution as before, such that $\boldsymbol{\tau} = -\eta_s \dot{\boldsymbol{\gamma}} + \boldsymbol{\tau}_p$ and noting that $\lambda_2/\lambda_1 = \eta_s/\eta_0$ leads to the following equation for the polymer contribution to the stress tensor

$$\boldsymbol{\tau}_p + \lambda_1 \boldsymbol{\tau}_{p,(1)} = -\eta_p \dot{\boldsymbol{\gamma}} \tag{6.18}$$

which in dimensionless form reads as

$$\boldsymbol{\tau}_p + \mathrm{De}\boldsymbol{\tau}_{p,(1)} = -(1-\beta)\dot{\boldsymbol{\gamma}} \tag{6.19}$$

where $\mathrm{De} = \lambda_1 v_0/L$ is the Deborah number. The zz- and rr- components of this constitutive equation are

$$\mathrm{De}\left[\frac{\partial \tau_{p,zz}}{\partial t} + v_z \frac{\partial \tau_{p,zz}}{\partial z} \right] = -2(1-\beta)G - \tau_{p,zz} + 2\mathrm{De}G\tau_{p,zz} \tag{6.20}$$

$$\mathrm{De}\left[\frac{\partial \tau_{p,rr}}{\partial t} + v_z \frac{\partial \tau_{p,rr}}{\partial z} \right] = (1-\beta)G - \tau_{p,rr} - \mathrm{De}G\tau_{p,rr} \tag{6.21}$$

Eqs. 6.20 and 6.21 are hyperbolic, partial differential equations that must be solved along with Eq. 6.16 and appropriate boundary conditions to obtain a transient solu-

tion to the fiber-spinning problem. In particular, such a simulation will constitute a time-stepper for the Oldroyd-B model that will be called for short time-horizons to obtain steady states and perform stability and bifurcation analysis. Details of this will be presented in Section 6.3.1.

6.2.2 Hookean dumbbell model

The molecular configuration of the Hookean dumbbell is represented by continuous, Eulerian fields that evolve according to the following stochastic differential equations

$$dQ_{z,i} = \left[-v_z \frac{\partial Q_{z,i}}{\partial z} + GQ_{z,i} - \frac{1}{2\mathrm{De}} Q_{z,i} \right] dt + \sqrt{\frac{dt}{\mathrm{De}}} dW_{z,i} \qquad (6.22)$$

$$dQ_{r,i} = \left[-v_z \frac{\partial Q_{r,i}}{\partial z} - \frac{G}{2} Q_{r,i} - \frac{1}{2\mathrm{De}} Q_{r,i} \right] dt + \sqrt{\frac{dt}{\mathrm{De}}} dW_{r,i} \qquad (6.23)$$

where the configuration variables $Q_{z,i}$ and $Q_{r,i}$ are functions of both space and time, whereas the standard Wiener processes $W_{z,i}$ and $W_{r,i}$ are functions of time only. For a given velocity field v_z and corresponding velocity gradient G, Eqs. 6.22 and 6.23 can be used to evolve an ensemble of N_f configuration fields, for $i = 1, \ldots, N_f$, in time over the entire computational domain. In a standard transient simulation, these fields are initialized from the equilibrium distribution of Hookean dumbbells, with the same value for each field over the entire computational domain. The polymer contribution to the stress tensor is then obtained at the end of the simulation by using Kramers expression for the stress tensor.

For the simulation carried out in this chapter, however, it is necessary to be able to initialize the configuration fields such that they are consistent with a specified initial macroscopic field for $\tau_{p,zz}$ and $\tau_{p,rr}$. Such an initialization is then followed by evolution of the configuration fields for a short time horizon, and subsequent averaging to obtain the updated stress fields. This procedure yields a simulation cast in the form of the coarse time-stepper, where we obtain the evolution of the macroscopic stress fields over a short time horizon by invoking a stochastic simulation of configuration fields. Clearly, the important step in this procedure is the lifting step for constructing an

initial ensemble of configuration fields consistent with the macroscopic stress. This is accomplished by assuming that all fields are equivalent, and only vary in space to be consistent with the spatial profile of the macroscopic stress. As such, each configuration field is given by

$$Q_{z,i} = \sqrt{1 - \frac{\text{De}}{1 - \beta} \tau_{p,zz}} \tag{6.24}$$

$$Q_{r,i} = \sqrt{1 - \frac{\text{De}}{1 - \beta} \tau_{p,rr}} \tag{6.25}$$

for $i = 1, \ldots, N_f$. This lifting step is basically a rearrangement of the Kramers expression by assuming that all configuration fields are identical.

An important computational issue with stochastic simulation is the reduction of statistical error through the method of control variates [114]. This is accomplished by calculating the evolution of an ensemble of configuration fields, $\hat{Q}_{z,i}$ and $\hat{Q}_{r,i}$ at quiescent conditions that have the same initial condition and are subjected to the same random noise as the original configuration field variables $Q_{z,i}$ and $Q_{r,i}$. This leads to a modification of the Kramers expression for obtaining the macroscopic stress field at the end of each stochastic simulation and represents the restriction step in the coarse time-stepper approach. The new expression used to obtain the macroscopic stress field is given by

$$\tau_{p,zz} = \frac{1 - \beta}{\text{De}} \frac{1}{N_f} \sum_{i=1}^{N_f} \left(\hat{Q}_{z,i} \hat{Q}_{z,i} - Q_{z,i} Q_{z,i} \right) \tag{6.26}$$

$$\tau_{p,rr} = \frac{1 - \beta}{\text{De}} \frac{1}{N_f} \sum_{i=1}^{N_f} \left(\hat{Q}_{r,i} \hat{Q}_{r,i} - Q_{r,i} Q_{r,i} \right) \tag{6.27}$$

The coarse time-stepper when combined with Eq. 6.16 yields a dynamical system for the evolution of the fiber-spinning problem. As such, the Oldroyd-B model and the stochastic differential equation for evolution of the configuration fields are identical in that they describe the same molecular model. However, they are analyzed by two different approaches, namely the continuum and hybrid simulation methods. The

only modification introduced to the hybrid simulation is to recast the evolution of the polymer contribution to the stress tensor as a coarse time-stepper. With an appropriate numerical discretization described in the next section, we will see that the resulting simulation can be used to compute stationary solutions and perform stability analysis with Newton-GMRES.

6.3   Problem Formulation

The transient simulation of the fiber-spinning process is carried out by decoupling the solution of the momentum equation from the update of the cross-sectional area of the fiber and the polymer contribution to the stress tensor. In particular, given an initial condition for A, $\tau_{p,zz}$, and $\tau_{p,rr}$, we first solve for v_z and G, followed by an update of A, $\tau_{p,zz}$, and $\tau_{p,rr}$ over one time step. The process is then repeated for a specified time horizon. While A is updated using Eq. 6.12, the polymer contribution to the stress tensor is obtained either through Eqs. 6.20 and 6.21 for the Oldroyd-B model or a coarse time-stepper for the Hookean dumbbell model that uses Eqs. 6.22 and 6.23 to evolve the molecular conformation. We describe the numerical discretization of these equations next.

6.3.1   Numerical discretization

The partial differential equations for the fiber-spinning process are solved by discretizing the computational domain $z \in [0,1]$ into N elements and time domain $t \in [0, T_f]$ in N_T steps. We then use the finite element method to discretize spatially the mass and momentum balances and the equation for the velocity gradient G. Continuous, quadratic basis functions ϕ_i are used for A and v_z, whereas continuous linear basis functions ψ_i are used for G. In contrast, the polymer contributions to the stress tensor, $\tau_{p,zz}$ and $\tau_{p,rr}$, and configuration fields, $Q_{z,i}$ and $Q_{r,i}$, are discretized in space by using the discontinuous Galerkin method with local linear discontinous basis functions $\psi_{\mathrm{DG},l}$. For time-discretization all terms are treated explicitly to yield the following algorithm

1. Given A^k, $\tau_{p,zz}^k$, $\tau_{p,rr}^k$, and the initial guess v_z^k and G^k, update the velocity and velocity gradient by solving the following nonlinear problem for the weak formulation

$$
0 = \int_0^1 \Bigg(\frac{\partial A^k}{\partial z} \Bigg[-3\frac{\partial v_z^{k+1}}{\partial z} + 3(1-\beta)G^{k+1} + (\tau_{p,zz}^k - \tau_{p,rr}^k) \Bigg]
$$
$$
+ A^k \Bigg[-3\frac{\partial^2 v_z^{k+1}}{\partial z^2} + 3(1-\beta)\frac{\partial G^{k+1}}{\partial z} + \frac{\partial}{\partial z}[\tau_{p,zz}^k - \tau_{p,rr}^k] \Bigg] \Bigg) \phi_i \, dz \qquad (6.28)
$$
$$
0 = \int_0^1 \Big(G^{k+1} - \frac{\partial v_z^{k+1}}{\partial z} \Big) \psi_i \, dz
$$

2. Given the new velocity field update the area as follows

$$
\int_0^1 A^{k+1}\phi_i \, dz = \int_0^1 A^k \phi_i \, dz - \Delta t \int_0^1 \Big(v_z^{k+1}\frac{\partial A^k}{\partial z} + A^k \frac{\partial v_z^{k+1}}{\partial z} \Big) \phi_i \, dz \qquad (6.29)
$$

3. Update the polymer contributions to the stress tensor for the Oldroyd-B model by using the following weak formulations over each element $[z_j, z_{j+1}]$ of the domain

$$
\int_{z_j}^{z_{j+1}} \mathrm{De}\tau_{p,zz}^{k+1}\psi_{\mathrm{DG},l} \, dz = \int_{z_j}^{z_{j+1}} \mathrm{De}\tau_{p,zz}^k \psi_{\mathrm{DG},l} \, dz
$$
$$
+ \Delta t \int_{z_j}^{z_{j+1}} \Big(-2(1-\beta)G^{k+1} - \tau_{p,zz}^k + 2\mathrm{De}G^{k+1}\tau_{p,zz}^k - v_z^{k+1}\frac{\partial \tau_{p,zz}^k}{\partial z} \Big) \psi_{\mathrm{DG},l} \, dz +
$$
$$
\begin{cases} v_z^{k+1}\Big|_{z_j} > 0 : \Delta t\mathrm{De}[\psi_{\mathrm{DG},l}v_z^{k+1}(\tau_{p,zz}^{k,\mathrm{ex}} - \tau_{p,zz}^{k,\mathrm{in}})]\Big|_{z_j} \\[2mm] v_z^{k+1}\Big|_{z_{j+1}} < 0 : -\Delta t\mathrm{De}[\psi_{\mathrm{DG},l}v_z^{k+1}(\tau_{p,zz}^{k,\mathrm{ex}} - \tau_{p,zz}^{k,\mathrm{in}})]\Big|_{z_{j+1}} \end{cases} \qquad (6.30)
$$

$$
\int_{z_j}^{z_{j+1}} \mathrm{De}\tau_{p,rr}^{k+1}\psi_{\mathrm{DG},l} \, dz = \int_{z_j}^{z_{j+1}} \mathrm{De}\tau_{p,rr}^k \psi_{\mathrm{DG},l} \, dz
$$
$$
+ \Delta t \int_{z_j}^{z_{j+1}} \Big((1-\beta)G^{k+1} - \tau_{p,rr}^k - \mathrm{De}G^{k+1}\tau_{p,rr}^k - v_z^{k+1}\frac{\partial \tau_{p,rr}^k}{\partial z} \Big) \psi_{\mathrm{DG},l} \, dz +
$$
$$
\begin{cases} v_z^{k+1}\Big|_{z_j} > 0 : \Delta t\mathrm{De}[\psi_{\mathrm{DG},l}v_z^{k+1}(\tau_{p,rr}^{k,\mathrm{ex}} - \tau_{p,rr}^{k,\mathrm{in}})]\Big|_{z_j} \\[2mm] v_z^{k+1}\Big|_{z_{j+1}} < 0 : -\Delta t\mathrm{De}[\psi_{\mathrm{DG},l}v_z^{k+1}(\tau_{p,rr}^{k,\mathrm{ex}} - \tau_{p,rr}^{k,\mathrm{in}})]\Big|_{z_{j+1}} \end{cases} \qquad (6.31)
$$

or for the Hookean dumbbell model, lift $\tau_{p,zz}^k$ and $\tau_{p,rr}^k$ to a consistent ensemble of molecular configurations $\{Q_{z,i}^k, Q_{r,i}^k\}$ that are then evolved using the following weak formulations

$$
\int_{z_j}^{z_{j+1}} Q_{z,i}^{k+1}\psi_{\mathrm{DG},l}\,dz = \int_{z_j}^{z_{j+1}} Q_{z,i}^k\psi_{\mathrm{DG},l}\,dz
$$

$$
+ \Delta t \int_{z_j}^{z_{j+1}} \left[-v_z^{k+1}\frac{\partial Q_{z,i}^k}{\partial z} + G^{k+1}Q_{z,i}^k - \frac{1}{2\mathrm{De}}Q_{z,i}^k \right]\psi_{\mathrm{DG},l}\,dz
$$

$$
+\Delta W_{z,i}\int_{z_j}^{z_{j+1}}\psi_{\mathrm{DG},l}\,dz + \begin{cases} \left. v_z^{k+1}\right|_{z_j} > 0 : \Delta t[\psi_{\mathrm{DG},l}v_z^{k+1}(Q_{z,i}^{k,\mathrm{ex}} - Q_{z,i}^{k,\mathrm{in}})]\Big|_{z_j} \\[2ex] \left. v_z^{k+1}\right|_{z_{j+1}} < 0 : -\Delta t[\psi_{\mathrm{DG},l}v_z^{k+1}(Q_{z,i}^{k,\mathrm{ex}} - Q_{z,i}^{k,\mathrm{in}})]\Big|_{z_{j+1}} \end{cases}
$$

$$(6.32)$$

$$
\int_{z_j}^{z_{j+1}} Q_{r,i}^{k+1}\psi_{\mathrm{DG},l}\,dz = \int_{z_j}^{z_{j+1}} Q_{r,i}^k\psi_{\mathrm{DG},l}\,dz
$$

$$
+ \Delta t \int_{z_j}^{z_{j+1}} \left[-v_z^{k+1}\frac{\partial Q_{r,i}^k}{\partial z} - \frac{G^{k+1}}{2}Q_{r,i}^k - \frac{1}{2\mathrm{De}}Q_{r,i}^k \right]\psi_{\mathrm{DG},l}\,dz
$$

$$
+\Delta W_{r,i}\int_{z_j}^{z_{j+1}}\psi_{\mathrm{DG},l}\,dz + \begin{cases} \left. v_z^{k+1}\right|_{z_j} > 0 : \Delta t[\psi_{\mathrm{DG},l}v_z^{k+1}(Q_{r,i}^{k,\mathrm{ex}} - Q_{r,i}^{k,\mathrm{in}})]\Big|_{z_j} \\[2ex] \left. v_z^{k+1}\right|_{z_{j+1}} < 0 : -\Delta t[\psi_{\mathrm{DG},l}v_z^{k+1}(Q_{r,i}^{k,\mathrm{ex}} - Q_{r,i}^{k,\mathrm{in}})]\Big|_{z_{j+1}} \end{cases}
$$

$$(6.33)$$

For the Hookean dumbbell simulation, another ensemble of equilibrium configurations $\{\hat{Q}_{z,i}^k, \hat{Q}_{r,i}^k\}$ are also initialized that have the same initial configuration as $\{Q_{z,i}^k, Q_{r,i}^k\}$. These are then subjected to the same Wiener process and evolved according to a similar weak form with v_z^{k+1} and G^{k+1} equal to zero. The evolved configurations for the flow field and quiescent state are then used to evaluate the updated stress field, $\tau_{p,zz}^{k+1}$ and $\tau_{p,rr}^{k+1}$, by using Eqs. 6.26 and 6.27.

4. Repeat steps 1–3 with A^{k+1}, $\tau_{p,zz}^{k+1}$, $\tau_{p,rr}^{k+1}$, v_z^{k+1}, and G^{k+1} until $t = T_f$.

In the discontinuous Galerkin method, the weak form of the advection term has been replaced with the sum of an integral over the element $[z_j, z_{j+1}]$ and a jump

term that is only evaluated at inflow boundaries. Specifically, terms labelled $\tau_{p,rr}^{k,\text{ex}}$ are evaluated upstream of a given element while terms labelled $\tau_{p,rr}^{k,\text{in}}$ are evaluated within the element itself. If a boundary, z_j or z_{j+1} is not an inflow boundary, the jump term at that boundary is equal to zero. Also, in the weak formulation for the Hookean dumbbell configuration, the same Wiener process ($\Delta W_{z,i}$ or $\Delta W_{r,i}$) is applied to all points in space. In writing the weak formulation for the dumbbell configuration, the Wiener process has been scaled by $\sqrt{\Delta t/\text{De}}$ (cf. Eqs. 6.22 and 6.23).

6.3.2   Boundary and Initial Conditions

In order to evolve the fiber-spinning equations along with the constitutive descriptions for the Oldroyd-B model or the Hookean dumbbell model, we need four spatial boundary conditions. The conditions at $z = 0$ are not clear due to the unknown behavior of the upstream flow, including the die swell. In an experimental situation, the flow rate is generally given but the initial area is unknown because of the extrudate swell and uncertainty as to the precise location of the coordinate origin. Hence, it is customary to specify the velocity and area at $z = 0$. In this work we set $v_z(0) = 1$ and $A(0) = 1$, which sets the flow rate. In principle these boundary conditions should only be valid at steady state, but following previous work [33] we assume that these hold at all times for both transient and steady fiber-spinning.

The downstream boundary conditions are easier to specify, as the velocity at the take-up device can be fixed. Here it is assumed that the fiber is quenched directly onto the take-up roll at $z = 1$. By defining the draw ratio D_R as the ratio of the take-up velocity to the initial velocity, the boundary condition for the velocity is then $v_z(1) = \text{D}_\text{R}$.

Finally, we need to establish boundary conditions for the polymer contributions to the stress tensor. As such, both $\tau_{p,zz}$ and $\tau_{p,rr}$ or their difference cannot be specified at $z = 0$ since that would fix the tension in the fiber. For a fixed flow rate, the take-up velocity and force cannot both be specified; for a fixed take-up velocity we must accept whatever tension is necessary to draw the fiber. It is therefore customary to set the ratio τ_{rr}/τ_{zz} at $z = 0$. While this ratio is -0.5 over the entire filament for a

Newtonian fluid, for a viscoelastic fluid, it depends on the tension in the fiber, which, of course, depends on the solution. Finite element calculations of Keunings et al. [58] have shown that this ratio monotonically goes from -0.5 to 0 at the point where the stresses become radially uniform, as the tension in the fiber is increased. Also, it has been shown that the fiber-spinning equations presented here are insensitive to this stress ratio as long as it is in the range from -0.5 to 0 [24].

In this work, at $z = 0$ we evolve the fully developed versions of the equations for the polymer contributions to the stress tensor for the Oldroyd-B model and stochastic differential equations for N_f Hookean dumbbell configurations for the inlet velocity gradient. These are given by

$$\text{De}\frac{\partial \tau_{p,\,zz}^0}{\partial t} = -2(1-\beta)G - \tau_{p,\,zz}^0 + 2\text{De}G\tau_{p,\,zz}^0 \tag{6.34}$$

$$\text{De}\frac{\partial \tau_{p,\,rr}^0}{\partial t} = (1-\beta)G - \tau_{p,\,rr}^0 - \text{De}G\tau_{p,\,rr}^0 \tag{6.35}$$

and

$$dQ_{z,\,i}^0 = \left[GQ_{z,\,i}^0 - \frac{1}{2\text{De}}Q_{z,\,i}^0\right]dt + \sqrt{\frac{dt}{\text{De}}}dW_{z,\,i} \tag{6.36}$$

$$dQ_{r,\,i}^0 = \left[-\frac{G}{2}Q_{r,\,i}^0 - \frac{1}{2\text{De}}Q_{r,\,i}^0\right]dt + \sqrt{\frac{dt}{\text{De}}}dW_{r,\,i} \tag{6.37}$$

Here the ensemble $\{Q_{z,\,i}^0\}$ $\{Q_{r,\,i}^0\}$ are consistent with the polymer contributions to the stress tensor, $\tau_{p,\,zz}^0$ and $\tau_{p,\,rr}^0$ at $z = 0$ and subjected to the same Wiener process as $\{Q_{z,\,i}\}$ $\{Q_{r,\,i}\}$. The transient state of $\tau_{p,\,zz}^0$ and $\tau_{p,\,rr}^0$ or $\{Q_{z,\,i}^0\}$ $\{Q_{r,\,i}^0\}$ is then used as a Dirichlet boundary condition for Eqs. 6.30 and 6.31 or Eqs. 6.32 and 6.33. With this formulation we find that the ratio τ_{rr}/τ_{zz} varies from -0.5 to 0 over the length of the fiber, and approaches zero with increasing viscoelasticity, that is, decreasing β or increasing De.

In addition to boundary conditions, we must also set an initial condition for a transient simulation or an initial guess for obtaining the steady state with Newton-

GMRES. In either case, A, v, and G are set to the Newtonian solution, that is

$$A(z) = e^{-z \ln D_R} \tag{6.38}$$

$$v_z(z) = e^{z \ln D_R} \tag{6.39}$$

$$G(z) = \ln D_R e^{z \ln D_R} \tag{6.40}$$

while $\tau_{p,zz}$, and $\tau_{p,rr}$ are set to

$$\tau_{p,zz}(z) = -2(1-\beta)G(z) \tag{6.41}$$

$$\tau_{p,rr}(z) = (1-\beta)G(z) \tag{6.42}$$

6.3.3   Time-stepper based stability and bifurcation analysis

If we denote the finite element discretization of the field variables as a vector of unknowns $\boldsymbol{u} = [A, v_z, G, \tau_{p,zz}, \tau_{p,rr}]^T$ for $\boldsymbol{u} \in \Re^M$, then Eq. 6.16 coupled with Eqs. 6.20 and 6.21 represent a time-stepper, $\boldsymbol{\Phi}_{O,T_f}(\boldsymbol{u}; D_R)$ that can evolve the vector $\boldsymbol{u}$ over a specified time horizon T_f for a given value of the draw ratio. A similar time-stepper $\boldsymbol{\Phi}_{H,T_f}(\boldsymbol{u}; D_R)$ can also be constructed for the Hookean dumbbell model by using Eqs. 6.22 and 6.23 and the associated lifting and restriction procedures. These time-steppers can be thought of as black-boxes that provide the transient behavior of the fiber-spinning process. In order to use these black-boxes to perform stability and bifurcation analysis, we formulate the following nonlinear problems for the Oldroyd-B and Hookean dumbbell models

$$\boldsymbol{F}_O(\boldsymbol{u}; D_R) = \boldsymbol{u} - \boldsymbol{\Phi}_{O,T_f} \tag{6.43}$$

$$\boldsymbol{F}_H(\boldsymbol{u}; D_R) = \boldsymbol{u} - \boldsymbol{\Phi}_{H,T_f} \tag{6.44}$$

that can then be solved to obtain the steady state of the fiber-spinning process, $\boldsymbol{u}^*$, for a specified draw ratio.

The main advantage of this approach is that the formulation for the Hookean dumbbell model, $\boldsymbol{F}_H$ is constructed without invoking closure even though a closed

equation may be written for $\boldsymbol{F}_O$. While it is trivial to show that the Hookean dumbbell and Oldroyd models are equivalent, the approach taken so far can be easily used to study kinetic theory models that cannot be expressed in closed form. Additionally, by casting the time-stepper as a nonlinear problem, we can also trace branches of the stationary solution. This can be achieved by using a suitable continuation method, such as arclength continuation (see Section 3.6). More importantly, the stability of the computed steady states can also be obtained from such an analysis. In particular, the eigenvalues (ν_i for $i = 1, \ldots, M$) of the Jacobian $\left.\dfrac{\partial \boldsymbol{F}_H}{\partial \boldsymbol{u}}\right|_{\boldsymbol{u}^*}$ or $\left.\dfrac{\partial \boldsymbol{F}_O}{\partial \boldsymbol{u}}\right|_{\boldsymbol{u}^*}$ are related to the eigenvalues (σ_i for $i = 1, \ldots, M$) of the Jacobian of the closed model, which may not be explicitly available, by

$$\nu_i = 1 - e^{\sigma_i T_f} \tag{6.45}$$

In the current example, we can compare the eigenvalues ν_i to the exact eigenvalues σ_i since we have a closed equation for the Oldroyd-B model. Specifically, these can be obtained by writing Eqs. 6.16, 6.20, and 6.21 as

$$\boldsymbol{M}\frac{d\boldsymbol{u}}{dt} = \boldsymbol{F}(\boldsymbol{u}; D_R) \tag{6.46}$$

where

$$\boldsymbol{M} = \begin{bmatrix} \boldsymbol{A} & 0 & 0 & 0 & 0 \\ 0 & 0 & 0 & 0 & 0 \\ 0 & 0 & 0 & \boldsymbol{T}_{zz} & 0 \\ 0 & 0 & 0 & 0 & \boldsymbol{T}_{rr} \end{bmatrix} \tag{6.47}$$

such that $\boldsymbol{A}$, $\boldsymbol{T}_{zz}$, and $\boldsymbol{T}_{rr}$ are the finite element mass matrices for the mass balance and the constitutive equations, respectively. Performing a linearization of Eq. 6.46 around $\boldsymbol{u}^*$ leads to

$$\boldsymbol{M}\frac{d(\boldsymbol{u} - \boldsymbol{u}^*)}{dt} = \left.\boldsymbol{F_u}\right|_{\boldsymbol{u}^*} (\boldsymbol{u} - \boldsymbol{u}^*) \tag{6.48}$$

217

and the corresponding generalized eigenvalue problem

$$\boldsymbol{Mv} = \sigma \boldsymbol{F_u}\Big|_{\boldsymbol{u}^*} \boldsymbol{v} \qquad (6.49)$$

where σ is an eigenvalue of the dynamical system (Eq. 6.46) and $\boldsymbol{v}$ its correspond-
ing eigenvector. A steady state $\boldsymbol{u}^*$ is then a stable solution if $\Re\{\sigma_i\} < 0$. The
corresponding stability criterion for the time-stepper formulation, therefore, requires
that the eigenvalues ν_i must lie within a unit disc centered at $(1, 0)$ in the complex
plane. In our simulation, the ν_i are never all computed, as that would be a pro-
hibitively expensive simulation requiring $M + 1$ function evaluations. Instead, we
use the Newton-GMRES method to solve Eqs. 6.43 and 6.44. The advantage of this
approach is that the explicit computation of the Jacobians $\dfrac{\partial \boldsymbol{F}_H}{\partial \boldsymbol{u}}\Big|_{\boldsymbol{u}^*}$ and $\dfrac{\partial \boldsymbol{F}_O}{\partial \boldsymbol{u}}\Big|_{\boldsymbol{u}^*}$ is
never required; only matrix-vector multiplications are needed that can be performed
at low cost by calling the time-steppers m times, where $m \ll M$. Since the Newton-
GMRES solver uses the iterative Arnoldi procedure to converge to stationary states,
the Ritz values returned by this procedure provide good estimates to ν_i. In particular,
these values are very good approximations of the leading eigenvalues of the Jacobian
matrices, which are exactly the eigenvalues of interest in a stability calculation.

6.4 Results

6.4.1 Comparison of time-steppers

In order to test the numerical discretization, the time-steppers for the Oldroyd-B
and Hookean dumbbell models were evolved until $T_f = 10.0$ with $\Delta t = 10^{-4}$. A
one-dimensional mesh discretized into 20 elements of equal length was used; for the
Hookean dumbbell simulation, 500 configuration fields were employed. The draw ratio
was set to 20; and the Deborah number and β were set to 0.01 and 0.2, respectively.
The spatial profiles for A, v_z, G, $\tau_{p,zz}$, and $\tau_{p,rr}$ are shown in Figs. 6-3 and 6-4.
In these figures, the solid lines represent the solution obtained from the Oldroyd-B
time-stepper, whereas the circles represent the solution for the Hookean dumbbell

time-stepper. Given the excellent agreement between the two results, subsequent calculations to compute the stationary states and perform bifurcation analysis were done with $\Delta t = 10^{-4}$ and $N_f = 500$.

6.4.2 Steady-state results for the Oldroyd-B and Hookean dumbbell time-steppers

Given the good agreement between the two timesteppers, $\mathbf{\Phi}_{O,T_f}$ and $\mathbf{\Phi}_{H,T_f}$, the steady state for the fiber-spinning process was then obtained for a range of β and De by solving Eq. 6.44 with a Newton-GMRES solver at $\mathrm{D_R} = 20$ and time-horizon of $T_f = 0.05$. The steady-state velocity profiles thus obtained are shown in Figs. 6-5 and 6-6. A Newtonian initial guess was sufficient to converge to a solution for $\beta = 0.8$ and De = 0.03 and also for $\beta = 0.2$, and De = 0.001. The remaining solutions were obtained by using continuation in β or De from one of these solutions.

To check consistency of these solutions, steady states were also obtained by solving Eq. 6.43 for the Oldroyd-B time-stepper at selected values of β and De. The steady-state profiles for area, velocity, velocity gradient G, and the polymer contribution to the stress tensor are compared with those obtained from applying Newton-GMRES to the Hookean dumbbell time-stepper in Figs. 6-7 to 6-14. No error bars are shown for the comparison of the polymer contribution to the stress tensor, since the stochastic time-stepper $\mathbf{\Phi}_{H,T_f}$ is run with different initial conditions by the Newton-GMRES solver over a short time horizon T_f that is not sufficient to compute statistical averages. Nevertheless, there is excellent agreement between the results of the Oldroyd-B and Hookean dumbbell time-steppers. Moreover, the velocity profiles are in very good agreement with the computational results obtained by Gupta et al. [47].

6.4.3 Comparison of exact eigenvalues and Ritz values

In order to perform stability and bifurcation analyses with the Hookean dumbbell time-stepper, it is important to obtain good estimates for the leading eigenvalues of the underlying dynamical system. Since we apply a Newton-GMRES solver to the
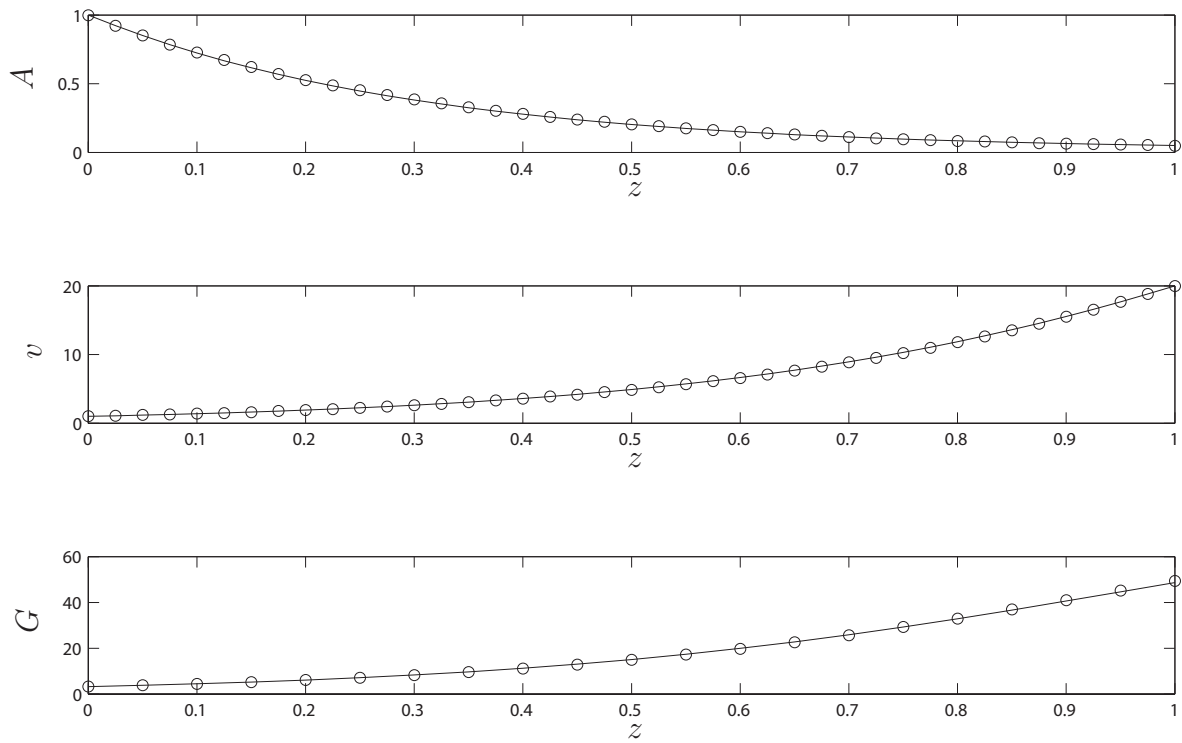
Figure 6-3: Comparison of steady-state spatial profile of area, velocity, and velocity gradient for the Oldroyd-B and Hookean dumbbell time-steppers. The solid lines and circles represent Oldroyd-B and Hookean dumbbell results, respectively. $\{\beta, \mathrm{De}, \mathrm{D_R}\} = \{0.2, 0.01, 20\}$
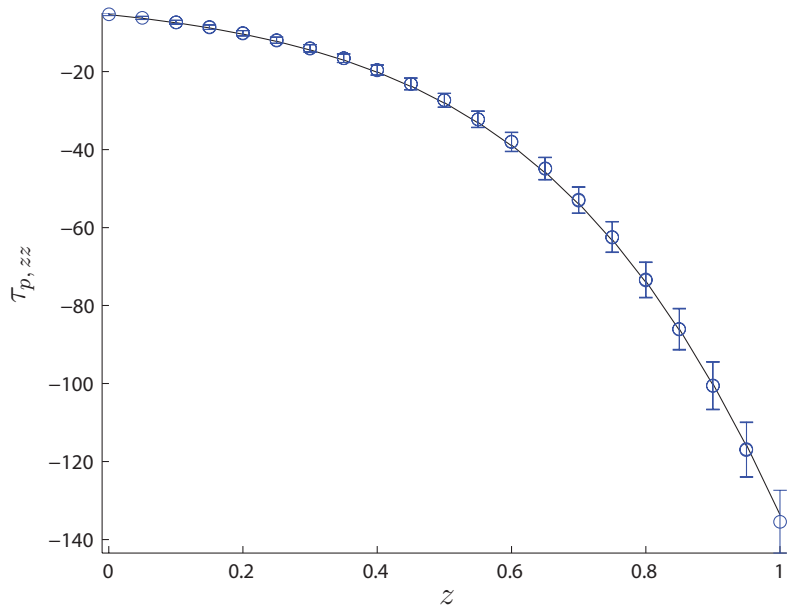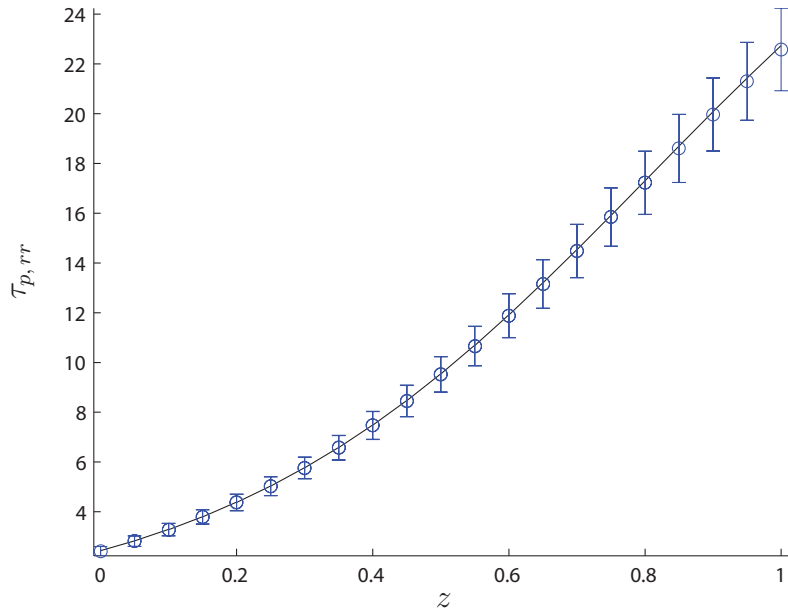
Figure 6-4: Comparison of steady state spatial profiles of (a)$\tau_{p,zz}$, and (b) $\tau_{p,rr}$ for the Oldroyd-B and Hookean dumbbell time-steppers. The length of the error bars is equal to two standard deviations of standard error in the stochastic simulation. The solid lines and circles represent Oldroyd-B and Hookean dumbbell results, respectively. $\{\beta, \mathrm{De}, \mathrm{D_R}\} = \{0.2, 0.01, 20\}$

Figure 6-5: Steady state velocity profile obtained from the Newton-GMRES solver and the Hookean dumbbell time-stepper for varying De at $\{\beta, D_R\} = \{0.2, 20\}$
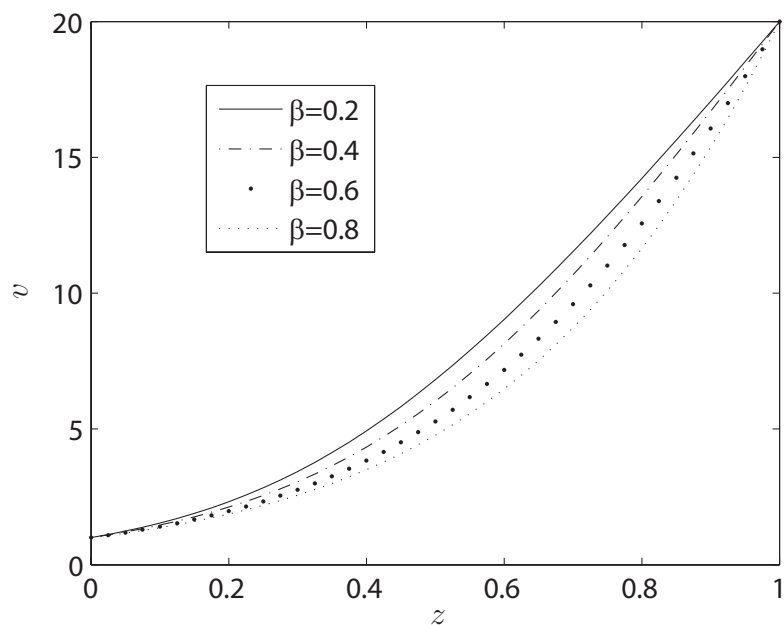
Figure 6-6: Steady state velocity profile obtained from the Newton-GMRES solver and the Hookean dumbbell time-stepper for varying β at $\{De, D_R\} = \{0.03, 20\}$

Figure 6-7: Comparison of steady state spatial profiles of area, velocity, and velocity gradient as obtained from the Newton-GMRES solver applied to Oldroyd-B and Hookean dumbbell time-steppers. The solid lines and circles represent Oldroyd-B and Hookean dumbbell results, respectively. $\{\beta, \mathrm{De}, \mathrm{D_R}\} = \{0.2, 0.01, 20\}$

Figure 6-8: Comparison of steady state spatial profiles of $\tau_{p,zz}$ and $\tau_{p,rr}$ as obtained from the Newton-GMRES solver applied to the Oldroyd-B and Hookean dumbbell time-steppers. The solid lines and circles represent Oldroyd-B and Hookean dumbbell results, respectively. $\{\beta, \mathrm{De}, \mathrm{D_R}\} = \{0.2, 0.01, 20\}$
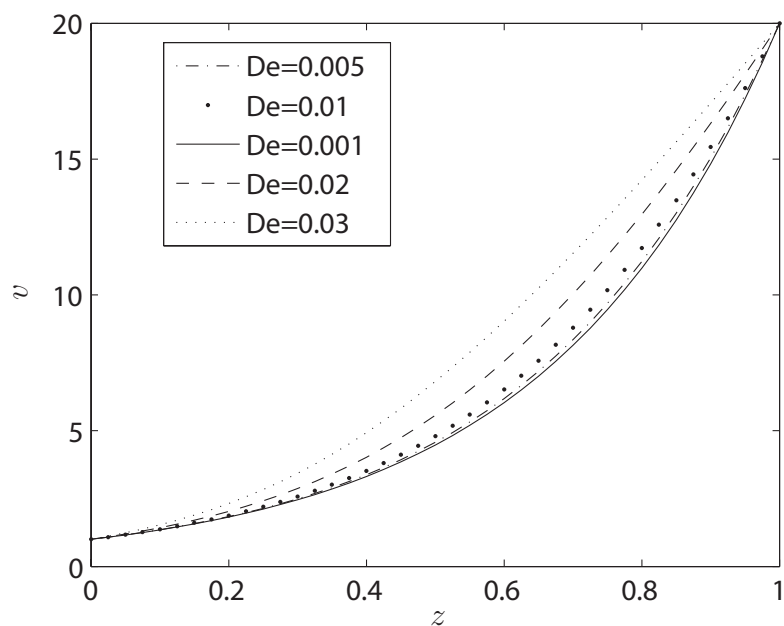
Figure 6-9: Comparison of steady state spatial profiles of area, velocity, and velocity gradient as obtained from the Newton-GMRES solver applied to the Oldroyd-B and Hookean dumbbell time-steppers. The solid lines and circles represent Oldroyd-B and Hookean dumbbell results, respectively. $\{\beta, \mathrm{De}, \mathrm{D_R}\} = \{0.2, 0.02, 20\}$

Figure 6-10: Comparison of steady state spatial profiles of $\tau_{p,zz}$ and $\tau_{p,rr}$ as obtained from the Newton-GMRES solver applied to the Oldroyd-B and Hookean dumbbell time-steppers. The solid lines and circles represent Oldroyd-B and Hookean dumbbell results, respectively. $\{\beta, \mathrm{De}, \mathrm{D_R}\} = \{0.2, 0.02, 20\}$
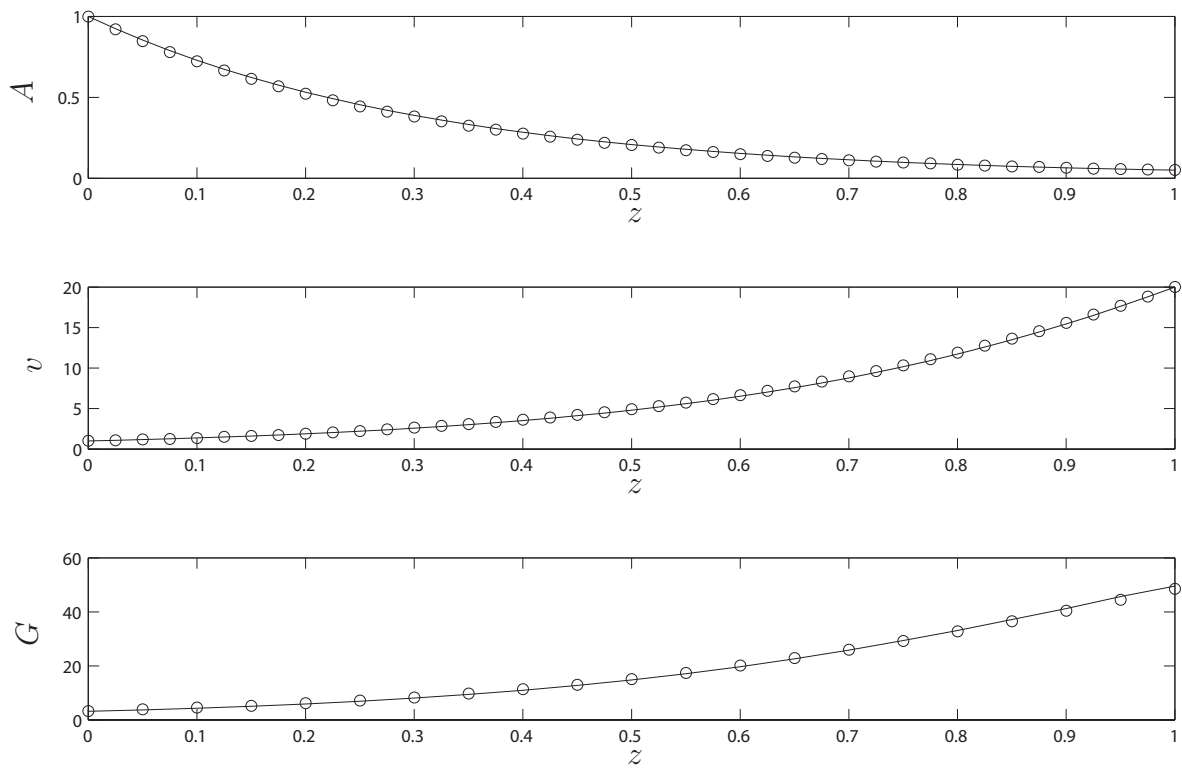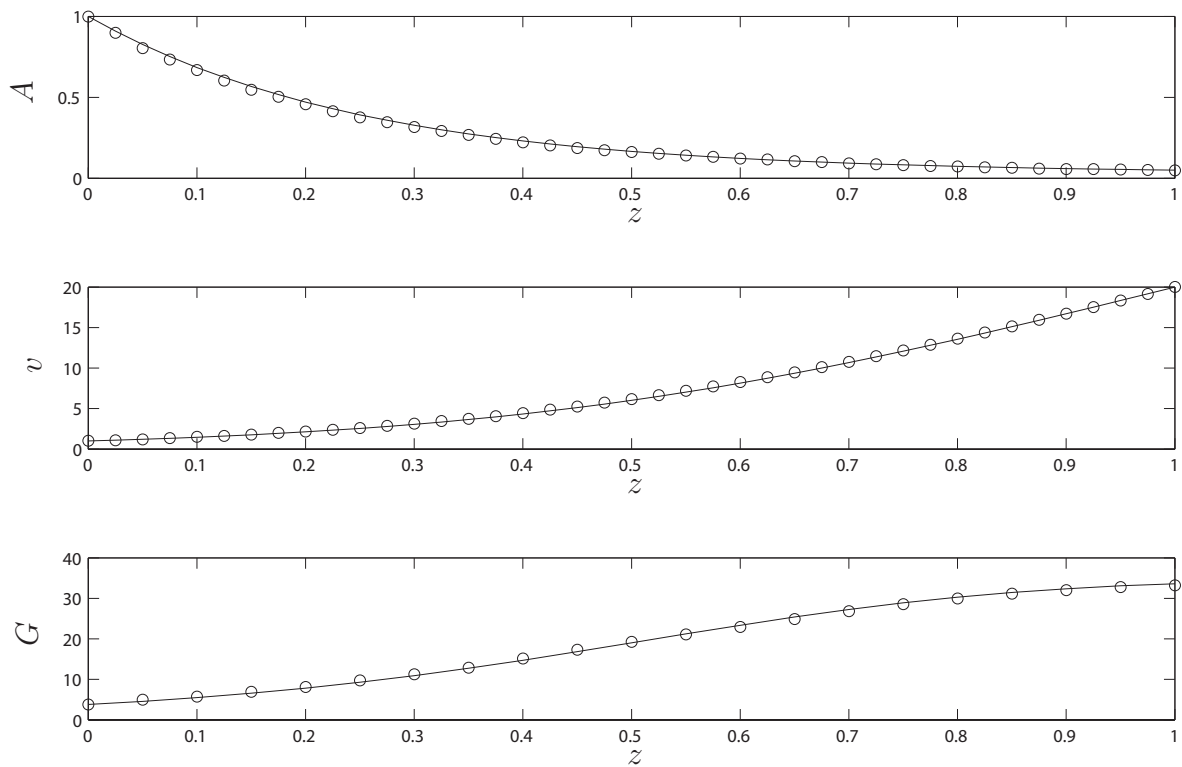
Figure 6-11: Comparison of steady state spatial profiles of area, velocity, and velocity gradient as obtained from the Newton-GMRES solver applied to the Oldroyd-B and Hookean dumbbell time-steppers. The solid lines and circles represent Oldroyd-B and Hookean dumbbell results, respectively. $\{\beta, \mathrm{De}, \mathrm{D_R}\} = \{0.4, 0.03, 20\}$
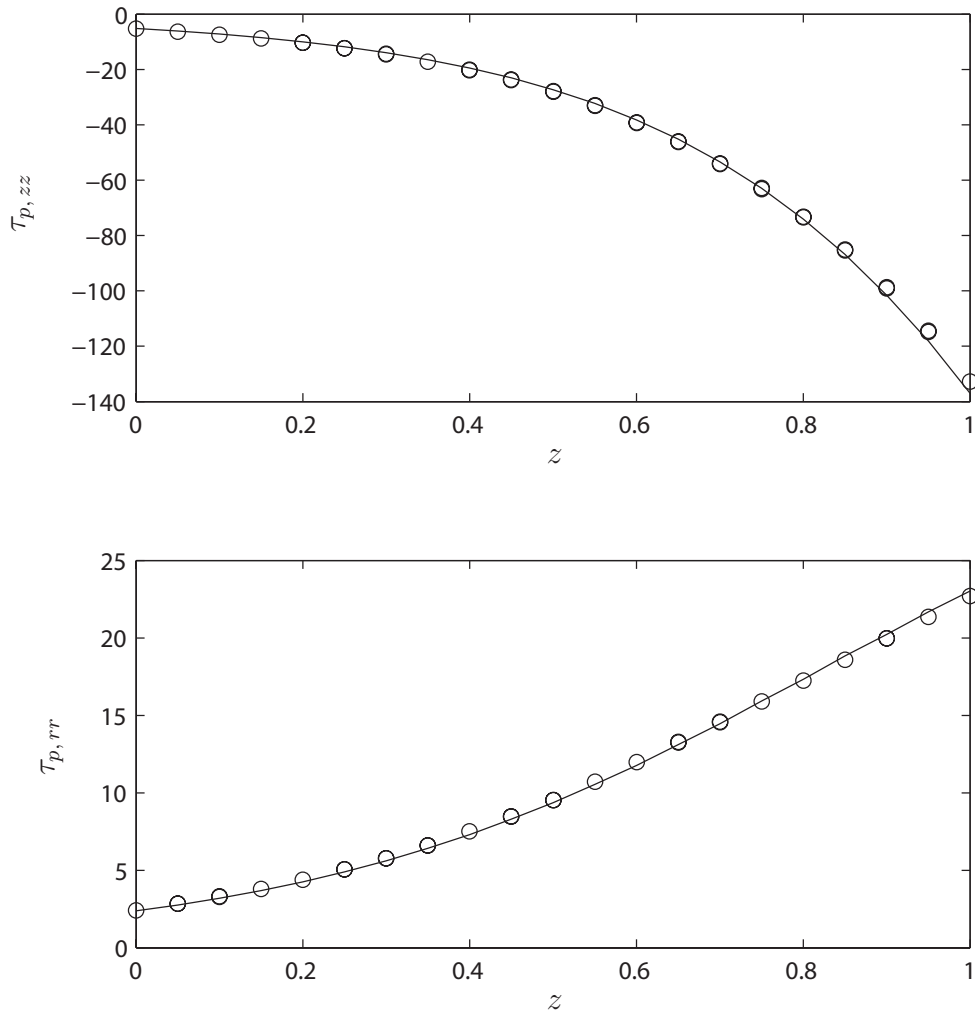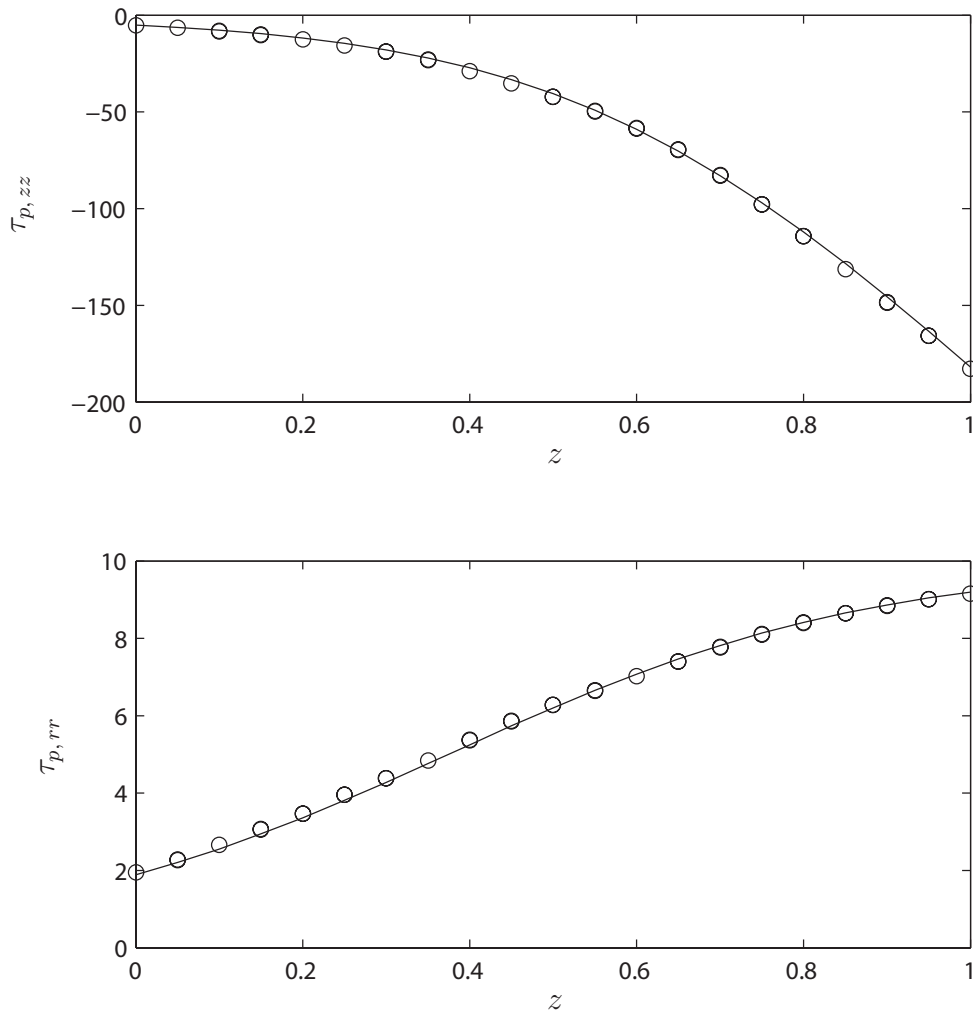
Figure 6-12: Comparison of steady state spatial profiles of $\tau_{p,zz}$ and $\tau_{p,rr}$ as obtained from the Newton-GMRES solver applied to the Oldroyd-B and Hookean dumbbell time-steppers. The solid lines and circles represent Oldroyd-B and Hookean dumbbell results, respectively. $\{\beta, \mathrm{De}, \mathrm{D_R}\} = \{0.4, 0.03, 20\}$
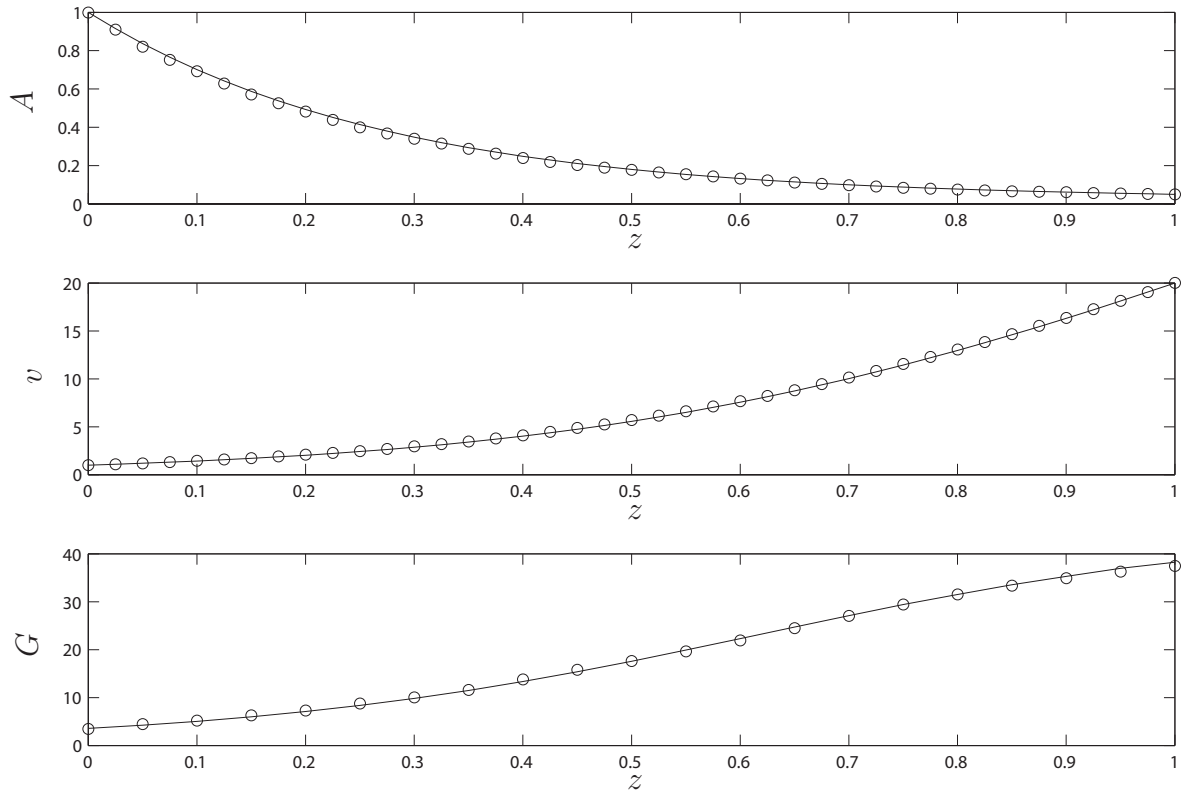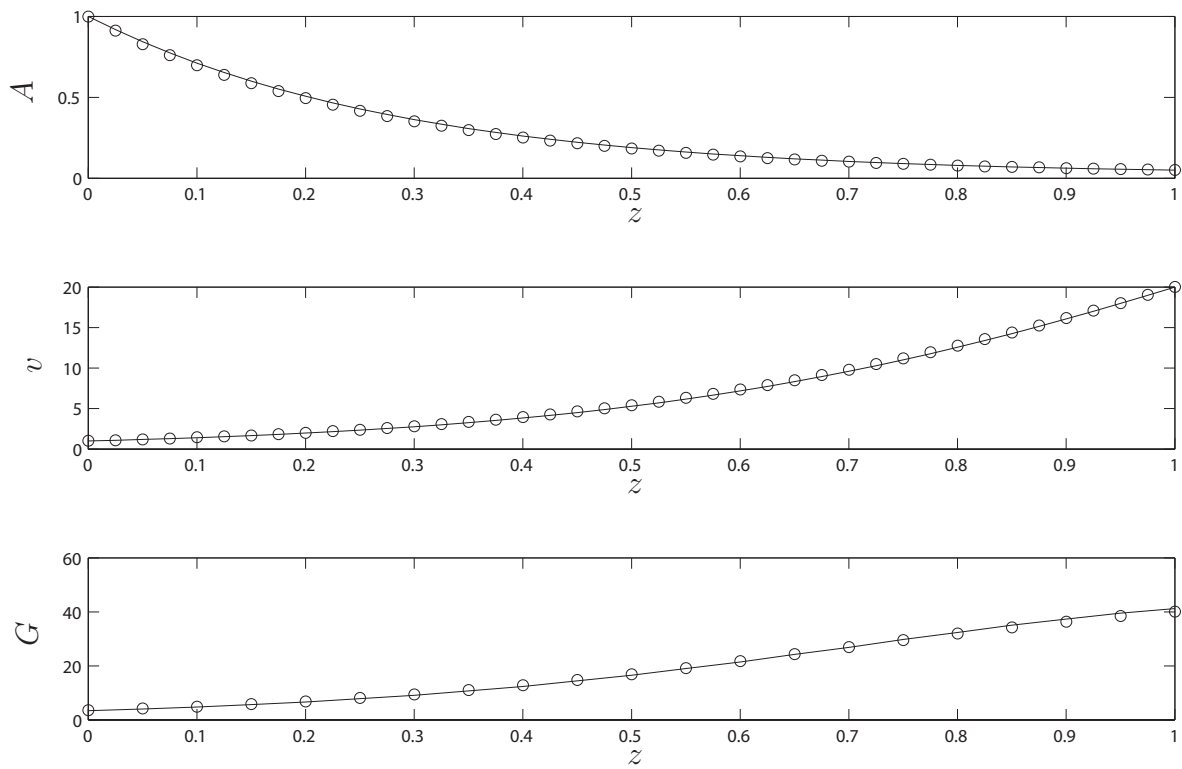
Figure 6-13: Comparison of steady state spatial profiles of area, velocity, and velocity gradient as obtained from the Newton-GMRES solver applied to the Oldroyd-B and Hookean dumbbell time-steppers. The solid lines and circles represent Oldroyd-B and Hookean dumbbell results, respectively. $\{\beta, \mathrm{De}, \mathrm{D_R}\} = \{0.6, 0.03, 20\}$
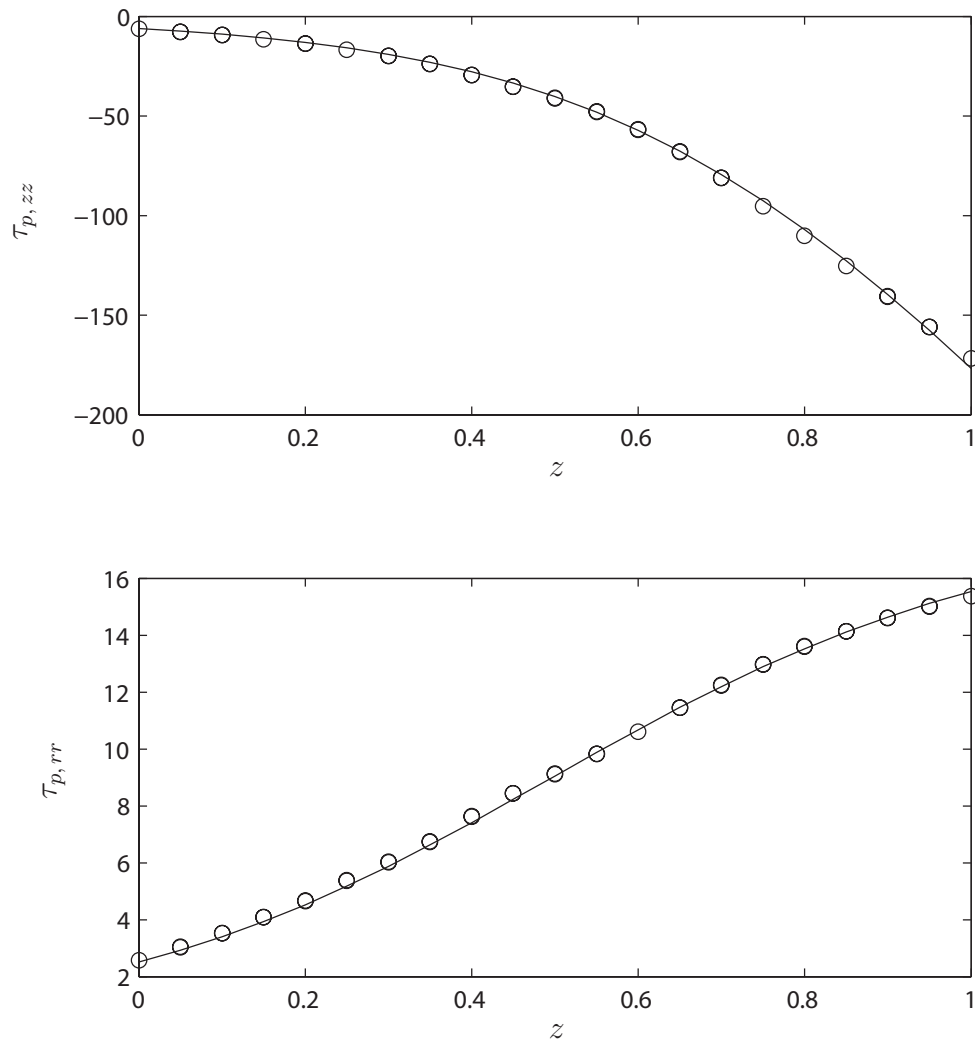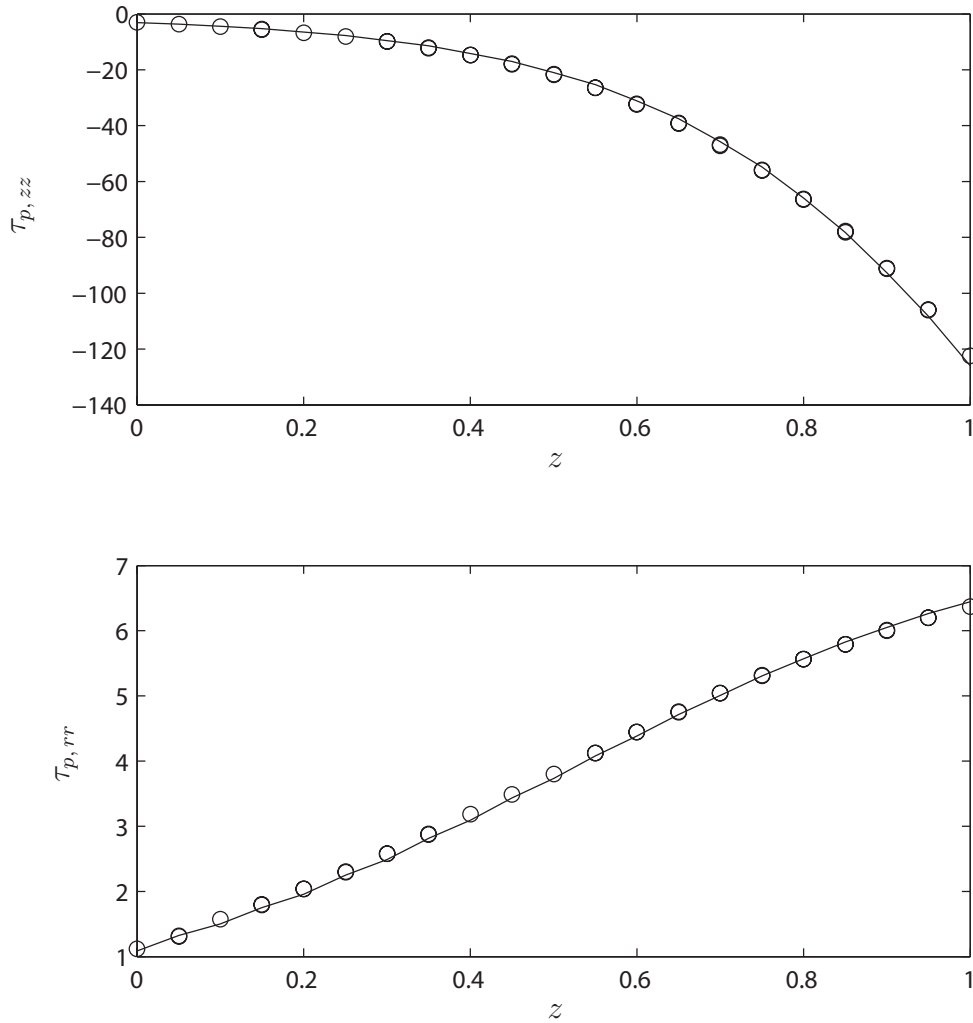
Figure 6-14: Comparison of steady state spatial profiles of $\tau_{p,zz}$ and $\tau_{p,rr}$ as obtained from the Newton-GMRES solver applied to the Oldroyd-B and Hookean dumbbell time-steppers. The solid lines and circles represent Oldroyd-B and Hookean dumbbell results, respectively. $\{\beta, \mathrm{De}, \mathrm{D_R}\} = \{0.6, 0.03, 20\}$
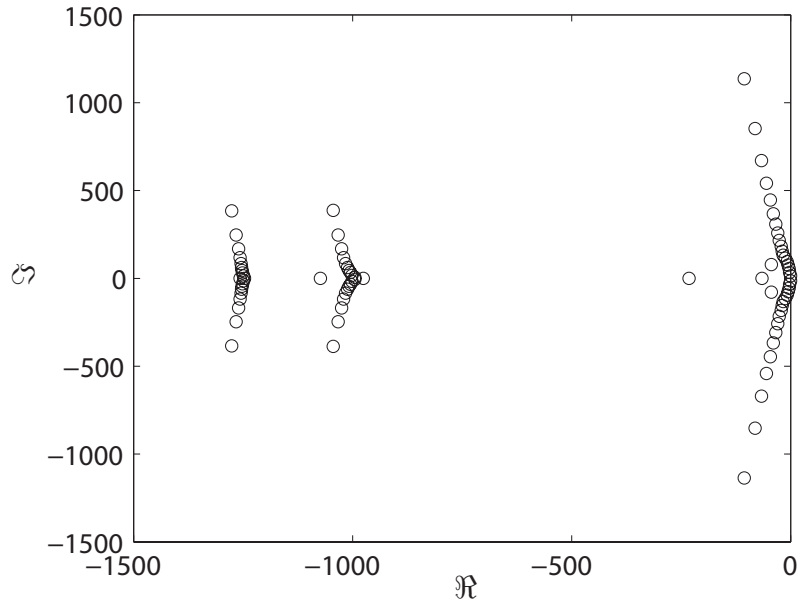
Figure 6-15: Eigenvalues of the dynamical equations for the Oldroyd-B formulation at $\{\beta, \mathrm{De}, \mathrm{D_R}\} = \{0.8, 0.001, 20\}$
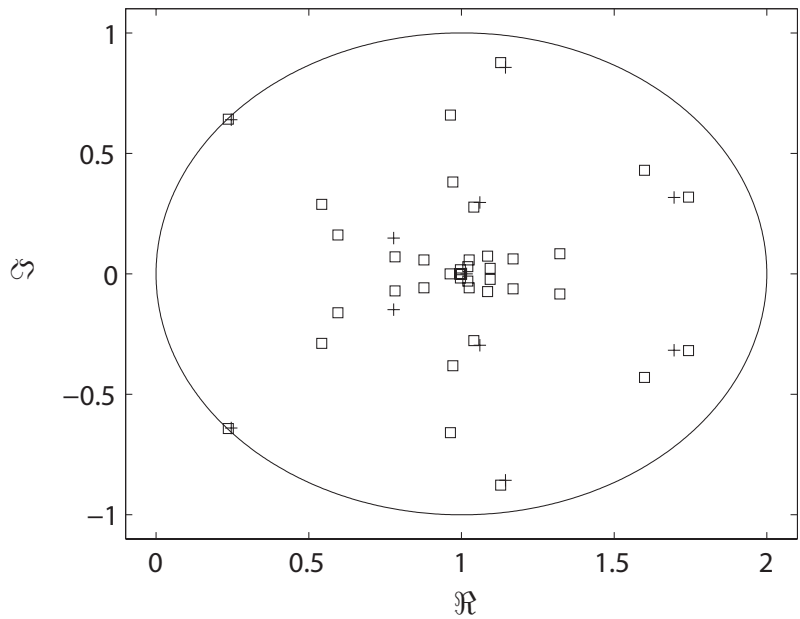
Figure 6-16: Comparison of eigenvalues ($\square$) of the dynamical equations and Ritz values ($+$) for the Oldroyd-B time-stepper. The Ritz values were obtained with a time stepping horizon of $T_f = 0.05$ at $\{\beta, \mathrm{De}, \mathrm{D_R}\} = \{0.8, 0.001, 20\}$

231
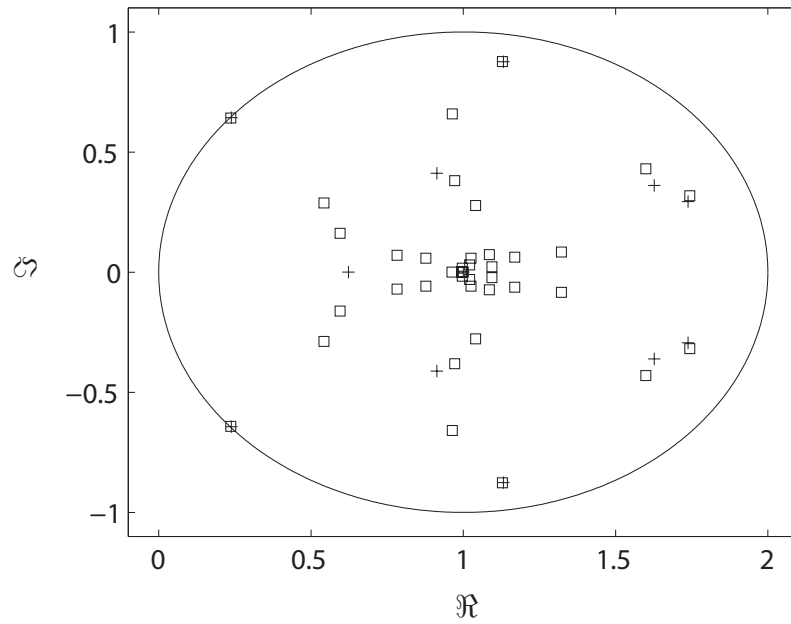
Figure 6-17: Comparison of eigenvalues ($\square$) of the dynamical equations and Ritz values ($+$) for the Hookean dumbbell time-stepper. The Ritz values were obtained with a time stepping horizon of $T_f = 0.05$ at $\{\beta, \mathrm{De}, \mathrm{D_R}\} = \{0.8, 0.001, 20\}$
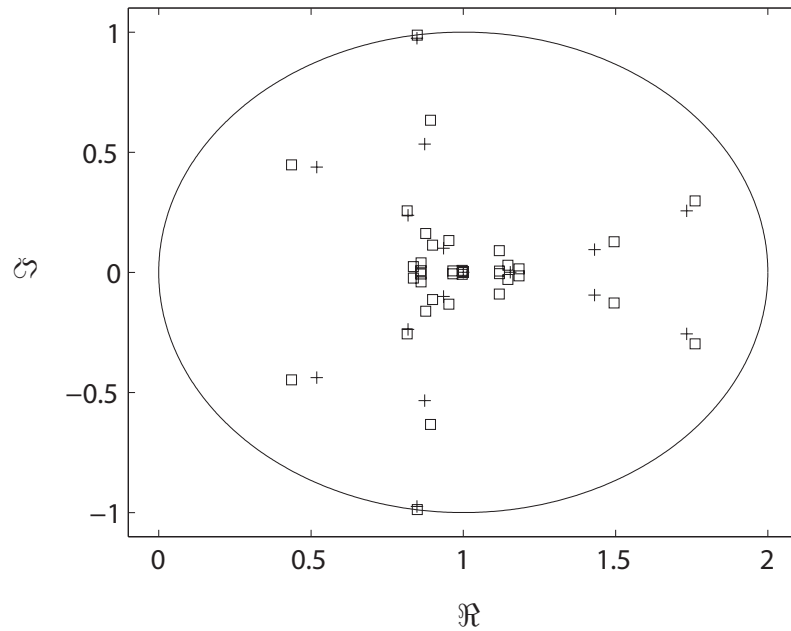
Figure 6-18: Comparison of eigenvalues ($\square$) of the dynamical equations and Ritz values ($+$) for the Hookean dumbbell time-stepper. The Ritz values were obtained with a time stepping horizon of $T_f = 0.1$ at $\{\beta, \mathrm{De}, \mathrm{D_R}\} = \{0.2, 0.001, 20\}$
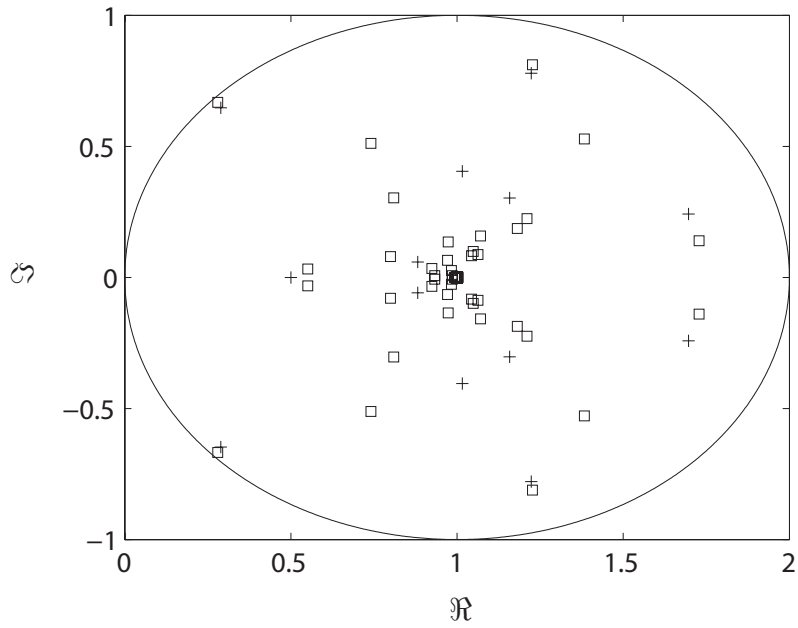
(a) $T_f = 0.05$
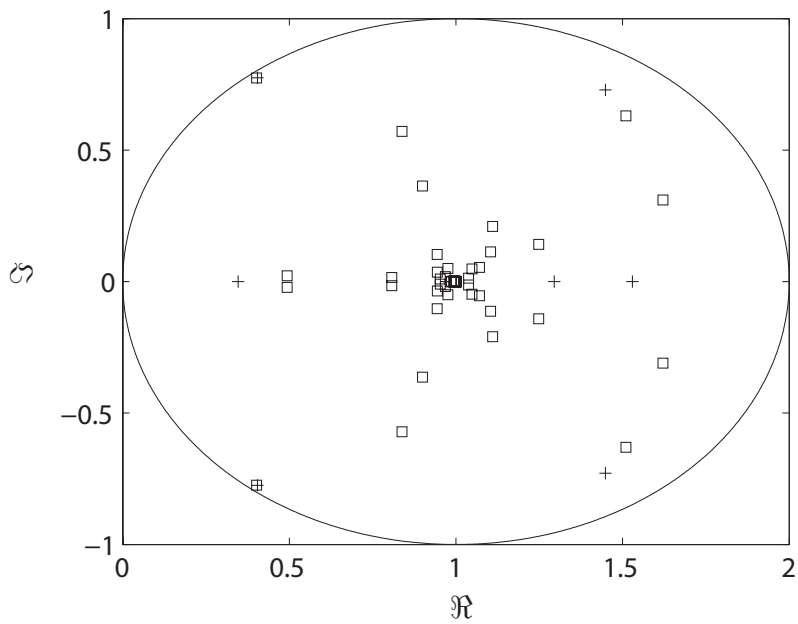
(b) $T_f = 0.06$

Figure 6-19: Comparison of eigenvalues ($\square$) of the dynamical equations and Ritz values ($+$) for the Hookean dumbbell time-stepper at $\{\beta, \text{De}, \text{D}_\text{R}\} = \{0.2, 0.01, 20\}$

Hookean-dumbbell time-stepper for the fiber-spinning process, these leading eigenvalues are approximated by Ritz values that are obtained at the last Newton iteration within a Newton-GMRES solver by computing the eigenvalues of the upper Hessenberg matrix generated by the Arnoldi procedure. Since this matrix is of low dimension, much smaller than the actual dimension of the system, the Ritz values are obtained cheaply.

We first solve the steady-state version of the dynamic formulation for the Oldroyd-B model given in Eq. 6.46. The steady state thus obtained is used to solve the generalized eigenvalue problem Eq. 6.49, which yields the eigenspectrum shown in Fig. 6-15. Since all eigenvalues lie in the left half of the complex plane, the fiber-spinning process is stable to infinitesimal perturbations at $\{\beta, \mathrm{De}, \mathrm{D_R}\} = \{0.8, 0.001, 20\}$.

In order to facilitate comparison with the approximate Ritz values obtained from the Arnoldi procedure within the Newton-GMRES solver, the eigenvalues for the dynamic formulation are then mapped to within a unit circle centered at $(1, 0)$ in the complex plane by using Eq. 6.45. The resulting eigenspectrum and the Ritz values are plotted in Figs. 6-16 and 6-17 for the Oldroyd-B and Hookean dumbbell time-steppers. In obtaining the Ritz values, the time-horizon for the Oldroyd-B and Hookean time-steppers was set to $T_f = 0.05$. It can be observed that there is very good agreement between the Ritz values and the leading transformed eigenvalues, which are exactly the eigenvalues of interest in a stability calculation. Since the Ritz values lie within the unit circle, the time-stepper formulation returns the correct stability information for the fiber-spinning process.

The effect of increasing the time-horizon to $T_f = 0.1$ on the eigenspectrum for the Hookean dumbbell time-stepper is shown next in Fig. 6-18. Increasing the time horizon results in increased clustering of the eigenvalues, which is beneficial for GMRES iterations. Once again, the agreement is excellent between the leading transformed eigenvalues and Ritz values. The benefit of increased clustering should be weighed against the cost of running the time-stepper over a longer time-horizon. For example, with the Hookean dumbbell time-stepper, increasing the time-horizon to $T_f = 0.1$ reduces the number of calls to the time-stepper by 10% when compared with the

number of calls to the time-stepper for $T_f = 0.05$. The doubling of the time-stepping horizon is, therefore, not justified for the modest descrease in number of time-stepper calls, since the agreement between the Ritz values and the leading eigenvalues is equally good for $T_f = 0.05$.

Finally, the transformed eigenvalues and the Ritz values for the Hookean dumbbell time-stepper are shown in Fig. 6-19(a) for $\{\beta, \mathrm{De}, \mathrm{D_R}\} = \{0.2, 0.01, 20\}$ with a time-horizon of $T_f = 0.05$. This case represents increased viscoelasticity and we see that once again there is good agreement between the leading eigenvalues and Ritz values, although not as good as in previous cases. However, in this particular case, increasing the time-horizon to $T_f = 0.06$ results in better agreement as shown in Fig. 6-19(b). We, therefore, use this time-horizon when obtaining bifurcation diagrams for the fiber-spinning process at these conditions.

6.4.4 Continuation in draw ratio for Hookean dumbbell time-stepper

We obtain bifurcation diagrams for the fiber-spinning process by choosing the draw ratio as the bifurcating parameter and augmenting Eq. 6.44 with the equation for arclength continuation. Here, we aim to show that we can use the time-stepper for the Hookean dumbbell model to capture draw resonance as a transition in stability of the the steady state solutions by continuing in the draw ratio. In particular, we set $\beta = 0.2$ and obtain the bifurcation diagrams at 3 different values of De to compare with previous studies.

The computed bifurcation diagrams are shown in Fig. 6-20 for De = 0.001, De = 0.01, and De = 0.011, where we plot the average velocity as a function of draw ratio. It can be observed that at the three conditions shown in Fig. 6-20, the transition from stable to unstable steady states occurs through a Hopf bifurcation, where a pair of complex conjugate eigenvalues with nonzero imaginary part cross the imaginary axis for the dynamical problem. In the case of the time-stepper formulation, this corresponds to a pair of complex conjugate eigenvalues leaving the unit circle.
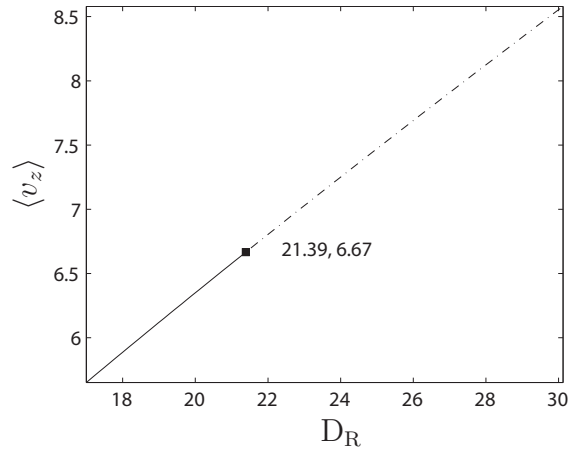
(a) De = 0.001
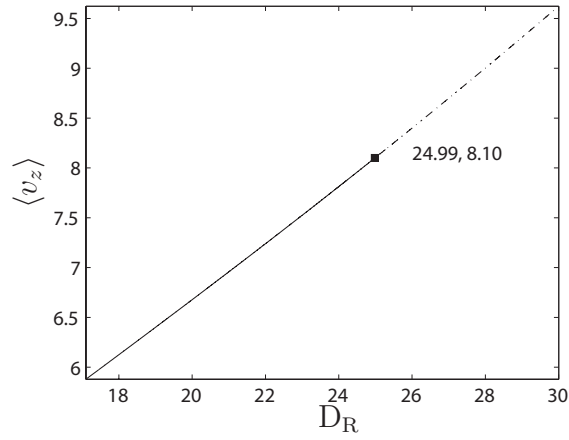
(b) De = 0.01
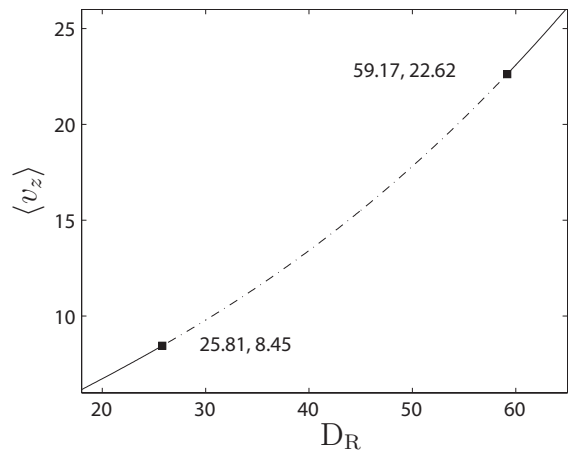
(c) De = 0.011

Figure 6-20: Bifurcation diagrams for the fiber-spinning process at $\beta = 0.2$, where the draw ratio has been used as the continuation parameter. The solid and dotted curves represent stable and unstable steady states, respectively. The solid squares mark Hopf bifurcations.

As De is increased from 0.001 to 0.011, the transition from stable to unstable steady states occurs at increasing value of the draw ratio. This is in agreement with previous studies with the Maxwell model [24], which corresponds to $\beta = 0$. Additionally, the critical draw ratio at De = 0.001 is greater than the Newtonian fluid critical draw ratio of 20.21, which is also in agreement with the linear stability analysis for a Maxwell fluid. Most importantly, however, we find that at De = 0.011 and a high draw ratio of 59.17 the fiber-spinning process regains stability to infinitesimal disturbances. Similar results were obtained by Fisher and Denn [33] in their analysis of the draw resonance with the White-Metzner fluid. In particular, the critical draw ratios of 25.81 and 59.17 are in very good agreement with Fig. 5 in [33].

6.5   Conclusions

In this chapter we apply the time-stepper based approach for stability and bifurcation analysis to the industrially relevant fiber-spinning process. While this process has been studied extensively in the past, here we obtain well known results by constructing a hybrid simulation for the fiber-spinning process that couples the conservation of mass and momentum to the evolution of stochastic Brownian configuration fields for a model from polymer kinetic theory, and use it to compute stationary states, perform continuation in a chosen parameter, and obtain stability information. This analysis is made possible by combining Newton's method with iterative methods from numerical linear algebra that take advantage of a compact eigenspectrum for the Jacobian matrix of a nonlinear problem, which is constructed by posing a fixed point mapping for the hybrid simulation. The idea is extremely simple as it treats the hybrid simulation as a black-box routine, which is called from appropriately perturbed initial conditions for relatively short time horizons. The leading eigenvalues of the nonlinear problem are also approximated as a by-product of this procedure, allowing one to perform stability and bifurcation analysis.

The results in this chapter were obtained for a kinetic theory model for which one can write a closed constitutive equation. This closed description was important

for demonstrating the accuracy of the method; however, in building the hybrid simulation the existence of a closed form was never invoked. All the ingredients of a state-of-the-art hybrid simulation were employed in this chapter, albeit in one spatial dimension, and for the simplest kinetic theory model. When the results obtained here are combined with the results presented in previous chapters, it is clear that the approach can be easily extended to hybrid simulations of polymer kinetic theory in higher spatial dimensions and with higher number of configurational degrees of freedom.

Chapter 7

Conclusions

7.1 Summary

The area of viscoelastic flow modeling has matured considerably since its inception three decades ago, when researchers struggled to compute kinematics with simple models, such as second-order fluids and the upper-convected Maxwell model. Today, we are beginning to model three-dimensional flows and study rheological descriptions that originate from polymer kinetic theory. As such, a great deal of effort is being devoted to develop robust numerical methods for three-dimensional continuum and hybrid simulations and apply to existing numerical methods to gain further insight into rheological behavior of real materials. In particular, very detailed molecular dynamics simulations [52, 51] have now become feasible that can be used to construct more sophisticated molecular models. The models developed by theoretical rheologists can then, in principle, be implemented numerically.

An overarching goal of viscoelastic flow modeling has been the prediction of flow instabilities that occur in polymer processing operations. The standard approach for this has been to solve the finite element discretization of the conservation and constitutive equations with Newton's method or integrate the full set of nonlinear equations to steady state. The former approach, while simple in principle, can be difficult to implement for complicated constitutive descriptions, such as the adaptive length scale model of Ghosh et al. [41], and suffers from various mathematical closure

239

approximations that must be introduced to obtain closed-form constitutive equations from kinetic theory. The latter approach, however, overcomes these difficulties by employing appropriate time-discretization methods for the constitutive descriptions that decouple the flow kinematics from the terms in the constitutive equation. In particular, this approach can be easily extended to evolve models from polymer kinetic theory, with the appropriate physics, in order to obtain the steady state solution.

The standard approach to studying viscoelastic flow instabilities with these simulations then involves computing the steady state base flow followed by determination of the linear stability by solving the generalized eigenvalue problem that results from examining the evolution of small normal mode perturbations applied to the base flow. This method has been used to study both closed-form constitutive equations for the polymer contribution to stress tensor [100, 101] and stochastic descriptions from kinetic theory [102, 103]. Since closed-form constitutive equations are known to give results of doubtful validity, the work with stochastic descriptions presents a considerable improvement. Nevertheless, this approach is limited in several respects. First, the base flow stochastic simulation for polymer configuration is evolved in time with subsequent updates to the base flow stresses and the velocities at every time step even after starting the linear stability calculations. This means that the base flow variables continue to fluctuate because of the fluctuating random forces experienced by the microstructural model. This is a marked difference from traditional linear stability analysis where the base flow solution is stationary. Second, this approach requires derivation of linearized stochastic differential equations for the perturbed conformation of the microstructural model, which are evolved along with the base flow. This adds considerable analytical effort for every new microstructural model that is being studied with this approach. Finally, this approach is only suitable for testing constitutive equations by comparison with experiments at well defined operating conditions, and does not address the need of the polymer engineer who wishes to predict flow transitions and analyze instabilities in real polymer processing operations.

The work presented in this thesis addresses this primary need by enabling models from polymer kinetic theory to deliver stationary states of viscoelastic flows, report

240

their stability, and perform bifurcation analysis. This is made possible by constructing a fixed point problem for the hybrid simulations and applying Newton's method along with iterative methods, like GMRES [113], from numerical linear algebra to converge to steady states. In doing so, the hybrid simulations are treated as black-boxes that are called from appropriately perturbed initial conditions for relatively short time horizons compared to the macroscopic time horizon to achieve steady state instead of direct integration. Calling the time-steppers for short time horizon leads to a compact spectrum of eigenvalues for the Jacobian of the fixed-point problem, which is exploited by iterative methods to obtain an approximation to the Newton step within Newton's method. The approach is novel in the sense that it combines the traditional Newton's method approach to linear stability analysis with time integration schemes for hybrid simulations. The stability of the computed steady state is readily determined from the cheaply available estimates for the leading eigenvalues of the original dynamical problem, since these are produced as by-product of the Arnoldi [95] procedure within the GMRES algorithm. Standard methods for performing bifurcation analysis, such as arclength continuation, can then be applied directly to this approach to obtain critical points of the hybrid simulation.

This thesis has further demonstrated this approach on several problems ranging from kinetic theory models in homogeneous flows that represent rheological experiments, to benchmark and industrial flows of polymeric solutions. Chapter 3 presents steady–state results for two kinetic theory models: (1) the non-interacting rigid dumbbell in steady shear flow, and (2) the free-draining bead-spring chain in steady shear and uniaxial elongation flows. The results for the rigid dumbbell are in excellent agreement with previous studies [105], where it is shown that one can apply the method to both a time-stepper for the kinetic theory model of the rigid dumbbell and an equivalent time-stepper constructed for a set of coarse variables. This time-stepper, also referred to as the "coarse time-stepper" [111], provides steady–state results in better agreement with unclosed descriptions than the results of standard closure approximations for this model. In addition to computing the steady state, we also obtain the approximate eigenvalues for the problem, which are in excellent agree-

ment with the exact eigenvalues. When these eigenvalues are not in good agreement, as is the case for high Deborah number, a stricter tolerance on the Arnoldi procedure improves the agreement with few additional calls to the time-stepper.

The free draining bead-spring chain, on the other hand, is modeled through a stochastic differential equation for the conformation of the molecular model, which does not have a true steady state due to Brownian forces acting on the beads of the molecule. However, since a macroscopic steady state can be measured in a laboratory experiment, the evolution of the molecular conformation can be cast in the form of a coarse time-stepper for the macroscopic shear stresses and normal stresses, which is then used to obtain the corresponding steady state. It is shown that the steady state thus obtained is in excellent agreement with the steady state of the macroscopic stress that is obtained by directly integrating the stochastic differential equation.

Results are also presented in Chapter 4 for the bifurcation analysis of the Doi model at equilibrium with excluded volume interactions given by the highly nonlinear Onsager potential. The kinetic theory description for this model is discretized with a spherical harmonic Galerkin approximation that is then wrapped within the time-stepper framework to compute steady states, to compute their stability as given by the approximate eigenvalues, and to perform continuation in the dimensionless potential intensity. The stable and unstable stationary solution branches produced by this approach are in excellent agreement with other studies that either use spot calculations [42] or thermodynamic arguments [44].

With these encouraging results, the method is then used to obtain the steady states for the pressure-driven flow of a dilute solution of non-interacting rigid dumb-bells in a planar channel and in a planar channel with a linear array of equally spaced cylinders. The flow problem is cast in the form of a hybrid simulation that couples a DEVSS-G formulation of the conservation of mass and momentum with a spherical harmonic-Galerkin/discontinuous-Galerkin discretization of the diffusion equation for dumbbell configuration in conformation/physical space. The steady state computed from a Newton-GMRES solver applied to this hybrid simulation is in excellent agreement with that obtained by directly integrating the hybrid simulation to steady state.

For the parameter values studied, an isotropic initial guess for the distribution of rigid dumbbells conformations was sufficient to compute the steady state for the flow. More importantly, however, there is very good qualitative agreement with previous studies of Liu et al. [70] for the stress profile. Specifically, for the inter–cylinder spacing chosen in our work, the flow is characterized by the development of a recirculation region between adjacent cylinders with small fluid velocity and velocity gradient. This results in stresses that are near equilibrium, in contrast with a larger inter–cylinder spacing for which the polymer molecules along the centerline of the geometry are far from equilibrium. Second, the largest stresses exist at the solid boundaries in the gap between the cylinder and the channel wall where the flow is shear dominated with the extrema occurring up- and down-stream of cylinder midplane. Finally, these simulations show that the time-stepper based approach to steady state computation can be successfully applied to non-homogeneous flows of polymeric liquids in one and two spatial dimensions. Although the focus of this study was to converge to stable stationary states in order to facilitate comparison with the corresponding dynamic simulations, the results are very encouraging both for incorporation of higher numbers of configurational degrees of the freedom for the kinetic theory models and for performing stability and bifurcation analyses with hybrid simulations of benchmark flows.

Chapter 5 investigates the flow induced transitions from steady aligned states to periodic, tumbling states in a linear, weak shear flow for the Doi model with the Maier-Saupe excluded volume interaction potential. The analysis is slightly simplified by considering the model in two spatial dimensions. While the bifurcation analysis for the unapproximated Doi model has been carried out previously [73], the presentation in Chapter 5 focuses on the behavior in the weak shear limit. Specifically, numerical results from time-steppers, continuation methods, and local asymptotic analysis are combined to determine the effect of weak shearing, characterized by the dimensionless shear rate, on the equilibrium bifurcation diagram. It is found that the imposition of a weak shear flow has two main ramifications. First, the shear flow unravels the pitchfork bifurcation at equilibrium and results in two steady branches, one stable and

the other unstable. Second, imposition of shearing results in the loss of steady aligned solutions beyond a critical value of the dimensionless potential, the value of which depends on the dimensionless shear rate and a parameter $p \equiv (a^2 - 1)/(a^2 + 1)$, where a is the aspect ratio of the rods. Periodic, tumbling orbits with fluctuating structure parameter values characterized by an $O(1)$ mean amplitude and fluctuations of the order of the dimensionless shear rate are born at these critical points. In the weak shear flow limit, the period of these orbits scales as $G^{-1}(U - U_{\mathrm{L}})^{-1/2}$ in the vicinity of the limit point, where G is the dimensionless shear rate, U the potential intensity, and U_{L} is the critical dimensionless potential. The computations also indicate that for fixed G, decreasing the aspect ratio monotonically decreases the value of the critical potential. For rods with infinite aspect ratio, the critical point approaches a threshold of 2.4114 as the shear rate approaches zero, whereas the critical point approaches the isotropic-nematic transition point for $p \to 0$. Analysis of numerical solutions obtained via continuation and spot calculations strongly suggests the birth of periodic orbits at the critical potential via an infinite period bifurcation. This is supported by a study of the eigenspectrum of the stationary solutions near the limiting potential. It is found that the eigenspectrum of the model closely resembles the eigenspectrum of a prototypical two-dimensional system that exhibits an infinite period bifurcation. However, this does not guarantee that a single, two-variable constitutive equation exists that can elucidate the complete set of solutions for the Doi model.

Finally, Chapter 6 presents results for the onset of draw resonance and recovery of stability at high draw ratios for the isothermal fiber-spinning process. These results are obtained by constructing a hybrid simulation for the fiber-spinning process that includes a stochastic description of Hookean dumbbell configuration fields, discretized with the discontinuous Galerkin method, and the fiber-spinning model equations, discretized with the Galerkin finite element method. The resulting hybrid simulation is then wrapped in a Newton-GMRES solver to obtain steady states, compute approximate eigenvalues, and perform bifurcation analysis via arclength continuation. The steady state profiles for the fiber area, velocity, and polymer contribution to the stress tensor are in excellent agreement with previous work with the Oldroyd-B

model [47]. The approximate eigenvalues are also found to be in good agreement with the corresponding eigenvalues for the Oldroyd-B model, which allows for performing bifurcation analysis with the hybrid time-stepper. The analysis provides a critical draw ratio for transition from stable to unstable stationary solutions that increases with increasing viscoelasticity. The change of stability occurs via a Hopf bifurcation and is regained at high draw ratio, a well-known phenomenon in fiber-spinning of polymeric liquids.

7.2   Future Work

In this thesis, state-of-the-art numerical techniques were employed to discretize the conservation equations and molecular models from kinetic theory to build viscoelastic flow time-steppers. The results presented were then obtained by enabling these time-steppers to compute steady states and perform stability and bifurcation analysis, rather than improve on the numerical techniques. Hence, if a specific numerical technique is unstable or does not converge for a given flow or kinetic theory model, time-stepper based analysis cannot be expected to yield better results. Consequently, developing improved temporal schemes for the solution of the discretized equations in a viscoelastic flow model will increase the robustness of time-steppers to perform stability and bifurcation analysis and trace nonlinear qualitative behavior.

This thesis makes use of a customized parallel algorithm to solve the complex flow of the rigid dumbbell model, an inevitability in any investigation involving a hybrid simulation. While efficient use of massively parallel computers is becoming the norm, time-stepper based analysis can be exceedingly useful if implemented in parallel. The Newton-GMRES solver applied to the parallel time-stepper for the complex flow of rigid dumbbells was provided by the PETSc package [5], which includes a parallel implementation. Consequently, in order to incorporate viscoelastic flow models from kinetic theory into control algorithms that can aid the process engineer, it is imperative that time-stepper analysis and any algorithm using it be implemented in parallel.

In addition to developing more robust time-steppers and parallel algorithms, a natural extension of the work carried out in this thesis is to study the stability of two-dimensional benchmark flows with larger numbers of degree of freedom for the kinetic theory model. As a first step, one can consider the flow of FENE chains with up to 6 beads. It was shown by Ghosh [40] and Burmenko [14] that in rheometric flows the results for this model are in remarkable agreement with the Kramers chain. Transient simulations with this model were recently carried out by Koppol et al. [61] for the 4:1:4 axisymmetric contraction–expansion flow. Given that such a hybrid simulation is clearly feasible, it will be interesting to use the methods of this thesis to perform stability and bifurcation analysis of this complex flow. Moreover, results have been also been published recently for a three-dimensional flow calculation in a 4:1:4 planar contraction with a stochastic description for Hookean dumbbells [89]. While it may be computationally prohibitive to consider the flow of a bead-spring chain in a three-dimensional flow, publication of these results suggests that it will be interesting to test time-steppers based computation of the steady state for this geometry with the FENE dumbbell model.

In addition to solving complex flows, this thesis has shown that time-stepper based analysis is also effective for studying kinetic theory models in rheometric flows. This suggests that one may use time-stepper based stability and bifurcation analysis to test kinetic theory models that incorporate additional physics for polymer interactions and microstructure. Since the approach does not require closed equations, one only needs to build accurate black-box codes that describe the necessary physics in order to explore the qualitative behavior of the improved model.

Finally, the bifurcation analysis carried out in this thesis was limited to computing stationary solutions and detection of stability transitions through approximate eigenvalues. It may, therefore, be useful to improve upon this and develop algorithms for branch switching, tracing of periodic solutions, etc. This may simply require implementing standard algorithms for bifurcation analysis [98] in parallel to work with viscoelastic flow time-steppers. However, one must be careful to ensure that the number of function calls to the time-stepper or time-horizon is not increased considerably.

For the calculations performed in this thesis with standard arclength continuation, typically one or two additional function evaluations of the time-stepper were needed when compared with the calculation of the same steady state without the arclength equation. This may not be true for other algorithms of bifurcation analysis. One particular problem could arise when trying to trace branches of periodic solutions that emanate from a infinite period bifurcation point. Since computation of a periodic solution requires adding a phase constraint to the original nonlinear system in order to find the unknown period, this may lead to evolving the time-stepper over a prohibitively expensive time-horizon. As such, it may not be possible to continue on such a solution branch other than to initialize the time-stepper near the infinite period bifurcation point and simply observe the dynamic behavior of the viscoelastic flow.

Bibliography

[1] **Alonso, E. V., Wheeler, A. A., and Sluckin, T. J.** (**2003**). "Nonlinear dynamics of a nematic liquid crystal in the presence of a shear flow." *Proceedings of the Royal Society of London Series A-Mathematical Physical and Engineering Sciences*, 459(2029): 195–220.

[2] **Archer, L. A. and Larson, R. G.** (**1995**). "A Molecular Theory of Flow-Alignment and Tumbling in Sheared Nematic Liquid-Crystals." *Journal of Chemical Physics*, 103(8): 3108–3111.

[3] **Aziz, A. K. and Babuska, I.** (**1972**). *The Mathematical Foundations of the Finite Element Method with Application to Partial Differential Equations.* Academic Press.

[4] **Baaijens, F. P. T.** (**1998**). "Mixed finite element methods for viscoelastic flow analysis: a review." *Journal of Non-Newtonian Fluid Mechanics*, 79(2-3): 361–385.

[5] **Balay, S., Buschelman, K., Gropp, W. D., Kaushik, D., Knepley, M. G., McInnes, L. C., Smith, B. F., and Zhang, H.** (**2001**). "PETSc Web page." Http://www.mcs.anl.gov/petsc.

[6] **Bassi, F. and Rebay, S.** (**1997**). "A high-order accurate discontinous finite element method for the numerical solution of compressible Navier-Stokes equations." *J. Comput. Phys.*, 138: 267–279.

[7] **Beers, K. J.** (**2007**). *Numerical Methods for Chemical Engineering: Applications in Matlab.* Cambridge University Press.

[8] **Bird, R. B., Curtiss, C. F., Armstrong, R. C., and Hassager, O.** (**1987**). *Dynamics of Polymeric Liquids*, volume 1. Wiley, New York.

[9] **Bird, R. B., Curtiss, C. F., Armstrong, R. C., and Hassager, O.** (**1987**). *Dynamics of Polymeric Liquids*, volume 2. Wiley, New York.

[10] **Bird, R. B. and Wiest, J. M.** (**1995**). "Constitutive-Equations for Polymeric Liquids." *Annual Review of Fluid Mechanics*, 27: 169–193.

[11] **Boger, D. V. and Walters, K.** (**1993**). *Rheological phenomena in focus.* Elsevier, Amsterdam ; New York.

[12] **Bonvin, J. and Picasso, M.** (**1999**). "Variance reduction methods for CONNFFESSIT-like simulations." *Journal of Non-Newtonian Fluid Mechanics*, 84(2-3): 191–215.

[13] **Brown, R. A., Szady, M. J., Northey, P. J., and Armstrong, R. C.** (**1993**). "On the numerical stability of mixed finite-element methods for viscoelastic flows governed by differential constitutive equations." *Theoret. Comput. Fluid Dynamics*, 5: 77–106.

[14] **Burmenko, I.** (**2005**). *Brownian Dynamics Simulations of Fine-Scale Molecular Models.* Master's thesis, Massachusetts Institute of Technology.

[15] **Campbell, S. L., Ipsen, I. C. F., Kelley, C. T., and Meyer, C. D.** (**1996**). "GMRES and the minimal polynomial." *Bit*, 36(4): 664–675.

[16] **Chauviere, C. and Lozinski, A.** (**2004**). "Simulation of complex viscoelastic flows using the Fokker-Planck equation: 3D FENE model." *Journal of Non-Newtonian Fluid Mechanics*, 122(1-3): 201–214.

[17] **Chauviere, C. and Lozinski, A.** (**2004**). "Simulation of dilute polymer solutions using a Fokker-Planck equation." *Computers & Fluids*, 33(5-6): 687–696.

[18] **Chilcott, M. D. and Rallison, J. M.** (**1988**). "Creeping Flow of Dilute Polymer-Solutions Past Cylinders and Spheres." *Journal of Non-Newtonian Fluid Mechanics*, 29(1-3): 381–432.

[19] **Choate, E. P. and Forest, M. G.** (**2006**). "A classical problem revisited: rheology of nematic polymer monodomains in small amplitude oscillatory shear." *Rheologica Acta*, 46(1): 83–94.

[20] **Cocchini, F., Aratari, C., and Marrucci, G.** (**1990**). "Tumbling of Rodlike Polymers in the Liquid-Crystalline Phase Under Shear-Flow." *Macromolecules*, 23(20): 4446–4451.

[21] **Cockburn, B., Karniadakis, G. E., and Shu, C.-W.** (**2000**). *Dicontinuous Galerkin Methods: Theory, Computation and Applications*. Springer-Verlag.

[22] **Cockburn, B. and Shu, C. W.** (**1989**). "TVB Runge-Kutta Local Projection Discontinuous Galerkin Finite-Element Method for Conservation-Laws .2. General Framework." *Mathematics of Computation*, 52(186): 411–435. PT: J.

[23] **Cockburn, B. and Shu, C. W.** (**1998**). "The local discontinuous Galerkin finite element method for convection-diffusion equation." *SIAM J. Numer. Analysis*, 35: 2440–2463.

[24] **Denn, M. M.** (**1974**). *Stability of reaction and transport processes*. Prentice-Hall, Englewood Cliffs, N.J.

[25] **Denn, M. M.** (**2001**). "Extrusion instabilities and wall slip." *Annual Review of Fluid Mechanics*, 33: 265–287.

[26] **Doi, M.** (**1981**). "Molecular-Dynamics and Rheological Properties of Concentrated-Solutions of Rodlike Polymers in Isotropic and Liquid-Crystalline Phases." *Journal of Polymer Science Part B-Polymer Physics*, 19(2): 229–243.

[27] **Doyle, P. S., Shaqfeh, E. S. G., and Gast, A. P.** (**1997**). "Dynamic simulation of freely draining flexible polymers in steady linear flows." *Journal of Fluid Mechanics*, 334: 251–291.

[28] **Doyle, P. S., Shaqfeh, E. S. G., McKinley, G. H., and Spiegelberg, S.** (**1998**). "Relaxation of dilute polymeric solutions following extenstional flow." *Journal of Non-Newtonian Fluid Mechanics*, 76: 79–110.

[29] **Eisenstat, S. C. and Walker, H. F.** (**1996**). "Choosing the forcing terms in an inexact Newton method." *SIAM J. Sci. Comput.*, 17: 16–32.

[30] **Fan, X. J.** (**1985**). "Viscosity, 1st and 2nd Normal-Stress Coefficients, and Molecular Stretching in Concentrated-Solutions and Melts." *Journal of Non-Newtonian Fluid Mechanics*, 17(3): 251–265.

[31] **Farhoudi, Y. and Rey, A. D.** (**1993**). "Shear Flows of Nematic Polymers. 1. Orienting Modes, Bifurcations, and Steady-State Rheological Predictions." *Journal of Rheology*, 37(2): 289–314.

[32] **Feigl, K., Laso, M., and Ottinger, H. C.** (**1995**). "Connffessit Approach for Solving a 2-Dimensional Viscoelastic Fluid Problem." *Macromolecules*, 28(9): 3261–3274.

[33] **Fisher, R. J. and Denn, M. M.** (**1976**). "A Theory of Isothermal Melt Spinning and Draw Resonance." *AIChE Journal*, 22: 236–245.

[34] **Flory, P. J.** (**1989**). *Statistical mechanics of chain molecules*. Hanser Publishers; Distributed in the U.S.A. by Oxford University Press, Munich ; New York; New York.

[35] **Forest, M., Wang, Q., and Zhou, R. H.** (**2004**). "The flow-phase diagram of Doi-Hess theory for sheared nematic polymers II: finite shear rates." *Rheologica Acta*, 44(1): 80–93.

[36] **Forest, M. G., Wang, Q., and Zhou, R. H. (2004)**. "The weak shear kinetic phase diagram for nematic polymers." *Rheologica Acta*, 43(1): 17–37.

[37] **Forest, M. G., Zhou, R. H., and Wang, Q. (2004)**. "Scaling behavior of kinetic orientational distributions for dilute nematic polymers in weak shear." *Journal of Non-Newtonian Fluid Mechanics*, 116(2-3): 183–204.

[38] **Fortin, M., Guenette, R., and Pierre, R. (1997)**. "Numerical analysis of the modified EVSS method." *Comput. Methods Appl. Engrg.*, 143: 79–95.

[39] **Gear, C. W., Kaper, T. J., Kevrekidis, I. G., and Zagaris, A. (2005)**. "Projecting to a Slow Manifold: Singularly Perturbed Systems and Legacy Codes." *SIAM Journal on Applied Dynamical Systems*, 4(3): 711–732.

[40] **Ghosh, I. (2000)**. *Molecular modeling of polymer solutions using Brownian dynamics*. Ph.D. thesis, Massachusetts Institute of Technology.

[41] **Ghosh, I., Joo, Y. L., McKinley, G. H., Brown, R. A., and Armstrong, R. C. (2002)**. "A new model for dilute polymer solutions in flows with strong extensional components." *Journal of Rheology*, 46(5): 1057–1089.

[42] **Gopinath, A., Armstrong, R. C., and Brown, R. A. (2004)**. "Observations on the eigenspectrum of the linearized Doi equation with application to numerical simulations of liquid crystal suspensions." *Journal of Chemical Physics*, 121(12): 6093–6094.

[43] **Gopinath, A., Mahadevan, L., and Armstrong, R. C. (2006)**. "Transitions to nematic states in homogeneous suspensions of high aspect ratio magnetic rods." *Physics of Fluids*, 18(2): 028 102.

[44] **Green, M. J. (2007)**. *Molecular Modeling of Liquid-Crystal Polymer Phase Behavior and Dynamics*. Ph.D. thesis, Massachusetts Institute Of Technology.

[45] **Gresho, P. M. and Sani, R. L. (2000)**. *Incompressible Flow and the Finite Element Method*. John Wiley and Sons.

[46] **Guenette, R. and Fortin, M.** (**1995**). "A new mixed method for computing viscoelastic flows." *Journal of Non-Newtonian Fluid Mechanics*, 60: 27–52.

[47] **Gupta, R. K., Puszynski, J., and Sridhar, T.** (**1986**). "Steady Spinning of the Oldroyd Fluid-B .1. Theory." *Journal of Non-Newtonian Fluid Mechanics*, 21(1): 99–113.

[48] **Hinch, E. J. and Leal, L. G.** (**1976**). "Constitutive Equations in Suspension Mechanics .2. Approximate Forms for a Suspension of Rigid Particles Affected by Brownian Rotations." *Journal of Fluid Mechanics*, 76(JUL14): 187–208.

[49] **Hulsen, M. A., vanHeel, A. P. G., and vandenBrule, B. H. A. A.** (**1997**). "Simulation of viscoelastic flows using Brownian configuration fields." *Journal of Non-Newtonian Fluid Mechanics*, 70(1-2): 79–101.

[50] **Ishihara, H. and Kase, S.** (**1975**). "Studies on melt spinning. V. Draw resonance as a limit cycle." *Journal of Applied Polymer Science*, 19(2): 557–566.

[51] **Jabbarzadeh, A., Atkinson, J. D., and Tanner, R. I.** (**2000**). "Effect of the wall roughness on slip and rheological properties of hexadecane in molecular dynamics simulation of Couette shear flow between two sinusoidal walls." *Physical Review E*, 61(1): 690–699.

[52] **Jabbarzadeh, A., Atkinson, J. D., and Tanner, R. I.** (**2002**). "The effect of branching on slip and rheological properties of lubricants in molecular dynamics simulation of Couette shear flow." *Tribology International*, 35(1): 35–46.

[53] **Kase, S. and Matsuo, T.** (**1965**). "Studies on melt spinning. I. Fundamental equations on the dynamics of melt spinning." *Journal of Polymer Science Part A: General Papers*, 3(7): 2541–2554.

[54] **Kelley, C. T.** (**2003**). *Solving Nonlinear Equations wth Newton's method.* SIAM.

[55] **Kelley, C. T., Kevrekidis, I. G., and Qiao, L. (2004).** "Newton-Krylov solvers for timesteppers." Can be obtained as math/0404374 from http://www.arxiv.org.

[56] **Keunings, R. (2000).** "A Survey of Computational Rheology." *D.M. Binding and K. Walters (Eds.), British Society of Rheology*, 1: 7–14.

[57] **Keunings, R. (2004).** "MICRO-MACRO METHODS FOR THE MULTI-SCALE SIMULATION OF VISCOELASTIC FLOW USING MOLECULAR MODELS OF KINETIC THEORY." *Rheology Reviews*, pages 67–98.

[58] **Keunings, R., Crochet, M. J., and Denn, M. M. (1983).** "Profile Development in Continuous Drawing of Viscoelastic Liquids." *Industrial & Engineering Chemistry Fundamentals*, 22(3): 347–355.

[59] **Kevrekidis, I. G., Gear, C. W., and Hummer, G. (2004).** "Equation-free: The computer-aided analysis of complex multiscale systems." *AICHE Journal*, 50(7): 1346–1355.

[60] **Kiss, G. and Porter, R. S. (1978).** "Rheology of concentrated suspension of poly-γ-benzyl-glutamate." *Journal of Polymer Science, Polymer Symposium*, 65.

[61] **Koppol, A. P., Sureshkumar, R., and Khomami, B. (2007).** "An efficient algorithm for multiscale flow simulation of dilute polymeric solutions using bead-spring chains." *Journal of Non-Newtonian Fluid Mechanics*, 141(2-3): 180–192.

[62] **Kuhn, W. (1939).** *Kolliod Z.*, 87: 3.

[63] **Kuzuu, N. and Doi, M. (1983).** "Constitutive Equation for Nematic Liquid-Crystals Under Weak Velocity-Gradient Derived from a Molecular Kinetic-Equation." *Journal of the Physical Society of Japan*, 52(10): 3486–3494.

[64] **Kuzuu, N. and Doi, M. (1984).** "Constitutive Equation for Nematic Liquid-Crystals Under Weak Velocity-Gradient Derived from a Molecular Kinetic-Equation. 2. Leslie Coefficients for Rodlike Polymers." *Journal of the Physical Society of Japan*, 53(3): 1031–1038.

[65] **Larson, R. G. (1992).** "Instabilities in Viscoelastic Flows." *Rheologica Acta*, 31(3): 213–263.

[66] **Larson, R. G. (2005).** "The rheology of dilute solutions of flexible polymers: Progress and problems." *Journal of Rheology*, 49(1): 1–70.

[67] **Larson, R. G. and Öttinger, H. C. (1991).** "Effect of Molecular Elasticity on Out-Of-Plane Orientations in Shearing Flows of Liquid-Crystalline Polymers." *Macromolecules*, 24(23): 6270–6282.

[68] **Laso, M. and Ottinger, H. C. (1993).** "Calculation of Viscoelastic Flow using Molecular-Models - the Connffessit Approach." *Journal of Non-Newtonian Fluid Mechanics*, 47: 1–20.

[69] **Laso, M., Picasso, M., and Ottinger, H. C. (1997).** "2-D time-dependent viscoelastic flow calculations using CONNFFESSIT." *AICHE Journal*, 43(4): 877–892.

[70] **Liu, A. W., Bornside, D. E., Armstrong, R. C., and Brown, R. A. (1998).** "Viscoelastic flow of polymer solutions around a periodic, linear array of cylinders: comparisons of predictions for microstructure and flow fields." *Journal of Non-Newtonian Fluid Mechanics*, 77(3): 153–190.

[71] **Lozinski, A. and Chauvire, C. (2003).** "A fast solver for FokkerPlanck equation applied to viscoelastic flows calculations: 2D FENE model." *Journal of Computational Physics,*, 189(2): 607–625.

[72] **Maffettone, P. L. (1992).** "A Constitutive Equation for Monodomains of Nematic Polymers." *Journal of Non-Newtonian Fluid Mechanics*, 45(3): 339–354.

[73] **Maffettone, P. L. and Crescitelli, S.** (**1995**). "Bifurcation-Analysis of a Molecular-Model for Nematic Polymers in Shear Flows." *Journal of Non-Newtonian Fluid Mechanics*, 59(1): 73–91.

[74] **Maffettone, P. L., Sonnet, A. M., and Virga, E. G.** (**2000**). "Shear-induced biaxiality in nematic polymers." *Journal of Non-Newtonian Fluid Mechanics*, 90(2-3): 283–297.

[75] **Marrucci, G.** (**1982**). "Prediction of Leslie Coefficients for Rodlike Polymer Nematics." *Molecular Crystals and Liquid Crystals*, 72(5-6): 153–161.

[76] **Marrucci, G. and Maffettone, P. L.** (**1989**). "Description of the Liquid-Crystalline Phase of Rodlike Polymers at High Shear Rates." *Macromolecules*, 22(10): 4076–4082.

[77] **Mass, U. and Pope, S. B.** (**1992**). "Simplifying chemical kinetics: Intrinsic low-dimensional manifolds in compositional space." *Combust. Flame*, 88: 239–264.

[78] **Matovich, M. A. and Pearson, J. R. A.** (**1969**). "Spinning a Molten Threadline. Steady-State Isothermal Viscous Flows." *Industrial & Engineering Chemistry Fundamentals*, 8(3): 512–520.

[79] **Melchior, M. and Ottinger, H. C.** (**1996**). "Variance reduced simulations of polymer dynamics." *Journal of Chemical Physics*, 105(8): 3316–3331.

[80] **Nayak, R.** (**1998**). *Molecular Simulation of Liquid Crystal Polymer flow: A wavelet-Finite Element Analysis.* Ph.D. thesis, Massachusetts Institute of Technology.

[81] **Onsager, L.** (**1949**). "The effects of shape on the interaction of colloidal particles." *Ann. N.Y. Acad. Sci.*, 51: 627–659.

[82] **Osswald, T. A. and Hernndez-Ortiz, J. P.** (**2006**). *Polymer processing : modeling and simulation.* Hanser Publishers, Munich ; Cincinnati.

[83] **Öttinger, H. C.** (**1996**). *Stochastic processes in polymeric fluids.* Springer-Verlag, New York.

[84] **Öttinger, H. C. and Laso, M.** (**1992**). In "Theoretical and Applied Rheology : Proceedings of the XIth International Congress on Rheology, Brussels, Belguim, August 17-21, 1992," Elsevier, Amsterdam, Netherlands ; New York.

[85] **Owens, R. G. and Phillips, T. N.** (**2002**). *Computational rheology.* Imperial College Press, London.

[86] **Phan-Thien, N.** (**1978**). "Non-Linear Network Viscoelastic Model." *Journal of Rheology*, 22(3): 259–283.

[87] **Press, W. H., Teukolsky, S. A., Vetterling, W. T., and Flannery, B. P.** (**1992**). *NUMERICAL RECIPES in FORTRAN 77: The Art of Scientific Computing.* Cambridge University Press.

[88] **Rajagopalan, D., Armstrong, R. C., and Brown, R. A.** (**1990**). "Finite element methods for calculation of steady, viscoelastic flow using constitutive equations with a Newtonian viscosity." *Journal of Non-Newtonian Fluid Mechanics*, 36: 159–192.

[89] **Ramírez, J. and Laso, M.** (**2004**). "Micro-macro simulations of three dimensional plane contraction flow." *Modelling Simul. Mater. Sci. Eng.*, 12: 1293–1306.

[90] **Reddy, J. N.** (**1984**). *An Introduction to the Finite Element Method.* McGraw-Hill.

[91] **Reed, W. H. and Hill, T. R.** (**1973**). "Triangular mesh methods for the neutron transport equation." Technical Report LA-UR-73-479, Los Alamos Scientific Laboratory.

[92] **Rhodes, C., Morari, M., and Wiggins, S.** (**1999**). "Identification of lower order manifolds: Validating the algorithm of Maas and Pope." *Chaos*, 9(1): 108–123.

[93] **Rienäcker, G. and Hess, S. (1999)**. "Orientational dynamics of nematic liquid crystals under shear flow." *Physica A*, 267(3-4): 294–321.

[94] **Rienäcker, G., Kroger, A., and Hess, S. (2002)**. "Chaotic and regular shear-induced orientational dynamics of nematic liquid crystals." *Physica A-Statistical Mechanics and its Applications*, 315(3-4): 537–568.

[95] **Saad, Y. (2003)**. *Iterative Methods for Sparse Linear Systems, 2nd edition.* SIAM, Philadelpha, PA.

[96] **See, H., Doi, M., and Larson, R. (1990)**. "The Effect of Steady Flow-Fields on the Isotropic-Nematic Phase-Transition of Rigid Rod-Like Polymers." *Journal of Chemical Physics*, 92(1): 792–800.

[97] **Semenov, A. N. (1983)**. "Rheological Properties of a Liquid-Crystal Solution of Rod-Like Macromolecules." *Zhurnal Eksperimentalnoi i Teoreticheskoi Fiziki*, 85(2): 549–560.

[98] **Seydel, R. (1994)**. *Practical Bifurcation and Stability Analysis: From Equilibrium to Chaos.* Springer-Verlag.

[99] **Shaqfeh, E. S. G. (1996)**. "Purely elastic instabilities in viscometric flows." *Annual Review of Fluid Mechanics*, 28: 129–185.

[100] **Smith, M. D., Armstrong, R. C., Brown, R. A., and Sureshkumar, R. (2000)**. "Finite element analysis of stability of two-dimensional viscoelastic flows to three-dimensional perturbations." *Journal of Non-Newtonian Fluid Mechanics*, 93(2-3): 203–244.

[101] **Smith, M. D., Joo, Y. L., Armstrong, R. C., and Brown, R. A. (2003)**. "Linear stability analysis of flow of an Oldroyd-B fluid through a linear array of cylinders." *Journal of Non-Newtonian Fluid Mechanics*, 109(1): 13–50.

[102] **Somasi, M. and Khomami, B. (2000)**. "Linear stability and dynamics of viscoelastic flows using time-dependent stochastic simulation techniques." *Journal of Non-Newtonian Fluid Mechanics*, 93(2-3): 339–362.

[103] **Somasi, M. and Khomami, B. (2001).** "A new approach for studying the hydrodynamic stability of fluids with microstructure." *Physics of Fluids*, 13(6): 1811–1814.

[104] **Somasi, M., Khomami, B., Woo, N. J., Hur, J. S., and Shaqfeh, E. S. G. (2002).** "Brownian dynamics simulations of bead-rod and bead-spring chains: numerical algorithms and coarse-graining issues." *Journal of Non-Newtonian Fluid Mechanics*, 108(1-3): 227–255.

[105] **Stewart, W. E. and Sørensen, J. B. (1972).** "Hydrodynamic Interaction Effects in Rigid Dumbbell Suspension. II. Computations of Steady Shear Flow." *Transactions of the Society of Rheology*, 16(1): 1–13.

[106] **Strogatz, S. H. (2000).** *Nonlinear Dynamics and Chaos.* Westview Press.

[107] **Suen, J. K., Nayak, R., Armstrong, R. C., and Brown, R. A. (2003).** "A wavelet-Galerkin method for simulating the Doi model with orientation-dependent rotational diffusivity." *Journal of Non-Newtonian Fluid Mechanics*, 114(2-3): 197–228.

[108] **Suen, J. K. C. (2002).** *Multiscale simulation of viscoelastic flows: Applications to Kinetic Theory Models of Polymer Melts and Liquid Crystalline Polymers.* Ph.D. thesis, Massachusetts Institute of Technology.

[109] **Suen, J. K. C., Joo, Y. L., and Armstrong, R. C. (2002).** "Molecular orientation effects in viscoelasticity." *Annual Review of Fluid Mechanics*, 34: 417–444.

[110] **Szady, M. J., Salamon, T. R., Liu, A. W., Bornside, D. E., Armstrong, R. C., and Brown, R. A. (1995).** "A New Mixed Finite-Element Method for Viscoelastic Flows Governed by Differential Constitutive-Equations." *Journal of Non-Newtonian Fluid Mechanics*, 59(2-3): 215–243.

[111] **Theodoropoulos, C., Qian, Y. H., and Kevrekidis, I. G. (2000).** ""Coarse" stability and bifurcation analysis using time-steppers: A reaction-

diffusion example." *Proceedings of the National Academy of Sciences of the United States of America*, 97(18): 9840–9843.

[112] **Tran-Canh, D. and Tran-Cong, T. (2004)**. "Element-free simulation of dilute polymeric flows using Brownian configuration fields." *Korea-Australia Rheology Journal*, 16(1): 1–15.

[113] **Trefethen, L. N. and III, D. B. (1997)**. *Numerical Linear Algebra*. SIAM.

[114] **van den Brule, B. H. A. A., vanHeel, A. P. G., and Hulsen, M. A. (1997)**. "Brownian configuration fields: A new method for simulating viscoelastic fluid flow." *Macromolecules Symposium*, 121: 205–217.

[115] **Wang, Q. (1997)**. "Biaxial steady states and their stability in shear flows of liquid crystal polymers." *Journal of Rheology*, 41(5): 943–970.

[116] **Warner, H. R. (1972)**. "Kinetic Theory and Rheology of Dilute Suspensions of Finitely Extendible Dumbbells." *Industrial & Engineering Chemistry Fundamentals*, 11(3): 379–387.

[117] **Zhou, H. and Wang, H. Y. (2007)**. "Steady states and dynamics of 2-D nematic polymers driven by an imposed weak shear." *Communications in Mathematical Sciences*, 5(1): 113–132.